Pairing, Paramagnetism and Prethermalization in Strongly Correlated Low-Dimensional Quantum Systems

Neil Joe Robinson

Jesus College

University of Oxford

A thesis submitted for the degree of

Doctor of Philosophy

Trinity Term 2014

Pairing, Paramagnetism and Prethermalization in Strongly Correlated Low-Dimensional Quantum Systems

Neil Joe Robinson

Jesus College, University of Oxford

A thesis submitted for the degree of *Doctor of Philosophy*

Trinity Term 2014

Abstract

Quasi-one-dimensional quantum models are ideal for theoretically exploring the physical phenomena associated with strong correlations. In this thesis we study three examples where strong correlations play an important role in the static or dynamic properties of the system.

Firstly, we examine the behaviour of a doped fermionic two-leg ladder in which umklapp interactions are present. Such interactions arise at special band fillings and can be induced by the formation of charge density wave order in an array of two-leg ladders with long-range (three-dimensional) interactions. For the umklapp which arises from the half-filling of one of the bands, we show that the low-energy theory has a number of phases, including a strong coupling regime in which the dominant fluctuations are superconducting in nature. These superconducting fluctuations carry a finite wave vector – they are the one-dimensional analogue of Fulde-Ferrell-Larkin-Ovchinnikov superconductivity.

In a second example, we consider a quantum spin model which captures the essential one-dimensional physics of $CoNb_2O_6$, a quasi-one-dimensional Ising ferromagnet. Motivated by high-resolution inelastic neutron scattering experiments, we calculate the dynamical structure in the paramagnetic phase and show that a small misalignment of the transverse field can lead to quasi-particle breakdown – a surprising broadening in the single particle mode observed in experiment.

Finally, we study the out-of-equilibrium dynamics of a model with tuneable integrability breaking. When integrability is broken by the presence of weak interactions, we show that the system relaxes to a non-thermal state on intermediate time scales, the so-called "prethermalization plateau". We describe the approximately stationary behaviour in this regime by constructing a generalised Gibbs ensemble with charges deformed to leading order in perturbation theory. Expectation values of these charges are time-independent, but interestingly the charges do not commute with the Hamiltonian to leading order in perturbation theory. Increasing the strength of the integrability breaking interactions leads to behaviour compatible with thermalisation.

In each case we use a combination of perturbative analytical calculations and non-perturbative numerical computations to study the problem at hand.

Acknowledgements

It is my pleasure to thank Prof. Fabian Essler for guidance, patience, many helpful conversations and opening my eyes to the combined used of field theory and numerical calculations. I have also greatly benefited from interactions with other members of the group: Maurizio Fagotti, Imke Schneider, Bruno Bertini, Stefano Evangelisti and Thomas Veness, all of whom I thank for many useful and interesting discussions.

My thanks also go to my collaborators: Eric Jeckelmann, Alexei Tsvelik, Radu Coldea, Ivelisse Cabrera, Stefan Kehrein, Salvatore Manmana and Robert Konik, all of whom it has been a pleasure to work with. The hospitality of the department of physics at the Georg-August-Universität Göttingen and the Condensed Matter Physics and Material Science department at Brookhaven National Laboratory during research visits was greatly appreciated.

I am extremely grateful to my friends and colleagues in the condensed matter theory group and Jesus College for making Oxford a great environment to live and do research in. Particular thanks go to Curt von Keyserlingk for teaching me a great deal over the four years of being office mates, Jesada Temaismithi for being a great friend, and Fenner Harper for conversations both in and out of the pub and squash courts. My thanks also go to the department administrators: Michelle Bosher, Sarah Loving and Stephanie Shen who've been a great help throughout my time in Oxford.

I've had the great fortune to speak with many people outside of the department whilst a graduate student. In particular I would like to thank Rianne van der Berg, Joe Bhasheen, Giuseppe Brandino, Jean-Sébastien Caux, Amalia Coldea, Tetsuo Deguchi, Sebas Eliëns, Masud Haque, James Hickey, Andrew James, Austen Lamacraft, Zala Lenarčič, Charles Mathey, Misha Portnoi, Jesada Temaismithi and Maurice Rice for fruitful and interesting discussions. My sincere thanks also go to Giussepe Mussardo and Steve Simon for thoughtful examination and discussion of this thesis.

Finally and most importantly, I wish to thank my family and Christopher, for their never ending support and encouragement.

The work presented in this thesis is based upon two published papers [1, 2] and a submitted preprint [3]. My work has been supported by the EPSRC under grant EP/I032487/1 and additional travel funding has been provided by Jesus College, ICAM, CUNY, and IRSES grant QICFT.

Contents

List of Figures

List of Tables

1. Introduction

At first sight condensed matter systems are overwhelmingly complicated: a staggering number of degrees of freedom are brought together, interact with one another and, depending on the details of the material, realise phases of matters as diverse as insulators, metals, superconductors, magnets, topological insulators and fractional quantum hall fluids, to name but a few. The study of how such states of matter can emerge from "simple" theoretical models has been fruitful, and some understanding of the rich variety of phases observed in nature has been gained. However, even in the simplest models of interacting quantum systems (such as the Ising model or the Hubbard model), many questions remain unanswered and many properties of these models incalculable.

Why are interacting quantum systems so difficult to study? Perhaps the greatest difficulty in the study of such systems was eloquently described by Anderson [4] over 40 years ago

> *"The behaviour of large and complex aggregations of elementary particles, it turns out, is not to be understood in terms of a simple extrapolation of the properties of a few particles. Instead, at each level of complexity entirely new properties appear..."*

This appearance of new and distinct properties – so-called "emergent phenomena" – is perhaps the defining feature of strongly correlated systems. It can mean that the excitations in these systems bear little semblance to the constituent elements, making the study of such systems difficult and often surprising.

In the hope of getting a concrete understanding of strongly correlated systems, we turn to the study of low-dimensional quantum systems, where it has long been known that strong correlations and collective phenomena rule the roost. The archetypal

example of emergent phenomena in a condensed matter context is the "spin-charge separation" predicted in theoretical models [5, 6, 7] and observed over 30 years later in experiments [8]. Given the difficulty in studying strongly correlated systems, it is perhaps then surprising that one-dimensional quantum models are amenable to theoretical treatment: in many cases we know how to reformulate them in such a way that they become weakly interacting [6, 7] and in some special cases the quantum problem can be solved exactly [9, 10, 11, 12, 13, 14, 15].

1.1 One-dimensional quantum models

The amenability of one-dimensional quantum problems to theoretical study is due to a number of techniques which are peculiar to such theories. A special class of models, so-called "integrable models", are solvable via the Bethe ansatz [9, 10, 11, 12]. There, much progress has been made in the last 30 years determining representations of correlation functions in (non-nested) systems [12, 16] which can be efficiently evaluated numerically [17]. Examples of one-dimensional integrable systems include experimentally relevant models such as the Heisenberg (isotropic or anisotropic) magnet, the Lieb-Liniger model of delta-function interacting bosons and the Hubbard model for interacting electrons. More generally, non-integrable theories can be attacked using bosonisation and refermionisation [5, 6, 7] which maps the strongly interacting fermion problem in to a weakly interacting bosonic problem. Critical one-dimensional quantum systems (such as the Luttinger liquid or the critical transverse field Ising model) can be studied with conformal field theory [14, 15] which gives insight into critical phenomena and yields exact expressions for critical exponents and power laws of correlation functions. We are also aided by powerful numerical methods, such as the density matrix renormalisation group [18, 19], which allow us to explore problems in parameter regimes where controlled analytical techniques no longer apply.

Let us now turn our attention to specific one-dimensional quantum models that will be central to the problems studied within this thesis. In the subsequent subsections we will review these models, highlighting salient features and show that the restriction to one spatial dimension will have striking consequences, with collective excitations and emergent phenomena being at the forefront.

1.1.1 The transverse field Ising chain

The transverse field Ising chain (TFIC) is a paradigm in the study of quantum magnetism [15, 20, 21, 22, 23] and may be derived from the transfer matrix of the classical two-dimensional Ising magnet [15, 25]. The Hamiltonian is given by

$$H_I = J\sum_{\ell=1}^{L} S_\ell^z S_{\ell+1}^z + h\sum_{\ell=1}^{L} S_\ell^x, \tag{1.1}$$

where J characterises the interaction between nearest neighbour spins, h is a transverse magnetic field, L is the number of sites in the chain (we impose periodic boundary conditions) and $S_\ell^x, S_\ell^y, S_\ell^z$ are the three components of the spin operator $\mathbf{S}_\ell$. These operators obey the commutation relations $[S_\ell^\alpha, S_{\ell'}^\beta] = i\delta_{\ell,\ell'}\epsilon_{\alpha\beta\gamma}S_\ell^\gamma$ where $\epsilon_{\alpha\beta\gamma}$ is the totally antisymmetric tensor. The symmetrised combinations of the x, y components give two non-Hermitian operators $S_\ell^\pm = S_\ell^x \pm iS_\ell^y$ which act as raising and lowering operators in the local spin space: flipping the spin configuration $S^+|\downarrow\rangle = |\uparrow\rangle$, $S^-|\uparrow\rangle = |\downarrow\rangle$ or annihilating the state $S^+|\uparrow\rangle = S^-|\downarrow\rangle = 0$.

Beyond applications to quantum magnetism, the model itself was actually first introduced in 1963 as a simple model for the collective motion of hydrogen bonds in the ferroelectric KH_2PO_4 [24]. In this material, protons at each site reside in the minima of a double well (labelled by $S^z = \pm\frac{1}{2}$) and may tunnel between the two minima with amplitude h. The model was then treated semi-classically, allowing de Gennes to make predictions about neutron scattering on the compound.

The model is not exactly solvable for $D > 1$ spatial dimensions, nevertheless extensive progress was made in the 1970s in studying the properties of the TFI model using mean field theory [21] and series expansions at high temperature [26] and low temperature [27]. In the $D = 1$ case, the model becomes exactly solvable and equal-time correlators are known exactly for the ground state [20, 28, 29] and in out-of-equilibrium for quantum quenches from the ground state [30]. The calculation of dynamical correlation functions in the ground state of the TFIC remains an area of active research 45 years after the exact solution was found [31, 32, 33, 34, 35, 36].

The TFIC will form an important part of our model in Chapter 3, so we will now present the exact solution of the TFIC and the phase diagram, discussing concepts which will be useful in the presented work.

1.1.1.1 The exact solution

The exact solution of the TFIC begins with the Jordan-Wigner transformation [37]: an exact operator equivalence between spin–$\frac{1}{2}$ operators and spinless fermions

$$S^x_\ell = \frac{1}{2}\Big(1 - 2c^\dagger_\ell c_\ell\Big), \qquad S^z_\ell = \frac{1}{2}\prod_{j<\ell}\Big(1-2c^\dagger_j c_j\Big)\Big(c_\ell + c^\dagger_\ell\Big),$$

where c_ℓ ($c^\dagger_\ell$) is the spinless fermion annihilation (creation) operator on site ℓ of the chain, which obeys the anti-commutation relations $\{c_\ell, c^\dagger_{\ell'}\} = \delta_{\ell,\ell'}$, $\{c_\ell, c_{\ell'}\} = 0$. Following the Jordan-Wigner transformation the Hamiltonian becomes

$$\begin{aligned} H_I &= \frac{J}{4}\sum_\ell \Big(c^\dagger_\ell c^\dagger_{\ell+1} + c^\dagger_\ell c_{\ell+1} + c^\dagger_{\ell+1}c_\ell + c_{\ell+1}c_\ell\Big) - h\sum_\ell c^\dagger_\ell c_\ell + \frac{hL}{2} \\ &\quad -\frac{J}{4}\Big(1+e^{i\pi\hat{N}}\Big)\Big(c^\dagger_L c^\dagger_1 + c^\dagger_L c_1 + c^\dagger_1 c_L + c_1 c_L\Big), \end{aligned}$$

where $\hat{N} = \sum_{j=1}^L c^\dagger_j c_j$ is the total number operator and the final term arises from the periodic boundary conditions in the spin chain (with open boundary conditions no such term appears). The boundary term enforces *anti-periodic* (*periodic*) boundary conditions when there are an even (odd) number of fermions. For large systems the boundary term may be neglected as the corrections to the eigenvectors and eigenvalues due to it scale with L^{-1}. Hereafter we neglect the boundary term.

We proceed by Fourier transforming the fermion operators $c_\ell = \sum_k e^{ik\ell}c_k/\sqrt{L}$ and find the momentum space Hamiltonian

$$H_I = \sum_k \Big\{\Big[\frac{J}{4}\cos(k) - \frac{h}{2}\Big]\Big(c^\dagger_k c_k + c^\dagger_{-k}c_{-k}\Big) + i\frac{J}{4}\sin(k)\Big(c^\dagger_k c^\dagger_{-k} + c_{-k}c_k\Big)\Big\} + \frac{hL}{2}.$$

This can then be diagonalised by the Bogoliubov transformation

$$c_k = \cos\left(\frac{\theta_k}{2}\right)\gamma_k + i\sin\left(\frac{\theta_k}{2}\right)\gamma^\dagger_{-k}, \qquad \tan(\theta_k) = \frac{\sin(k)}{\cos(k) - \frac{2h}{J}},$$

where γ_k are new "Bogoliubov fermions". The condition on the Bogoliubov parameter θ_k arises from the condition that we have a diagonal Hamiltonian in terms of the Bogoliubov fermions, which is given by

$$H_I = \sum_k E(k)\Big(\gamma^\dagger_k\gamma_k - \frac{1}{2}\Big),$$

where the single particle dispersion is

$$E(k) = \frac{J}{2}\sqrt{1 + \Big(\frac{2h}{J}\Big)^2 - \frac{4h}{J}\cos(k)}.$$

The single particle dispersion $E(k) > 0$ and hence the ground state is easily constructed as the vacuum state for the Bogoliubov fermions $\gamma_k|0\rangle = 0$. Excited states are constructed by adding Bogoliubov fermions to the ground state.

We see that the Bogoliubov fermions γ_k are well-defined quasi-particles, with the mode occupation numbers $n_k = \gamma_k^\dagger \gamma_k$ commuting with the Hamiltonian (and forming a mutually commuting set, so this is an *integrable* model [10, 12]). These fermions are the *emergent* degrees of freedom of our model and are related in a non-local way to the spin degrees of freedom, e.g. they are collective excitations of the system.

Before discussing the ground state phase diagram, it is useful to consider two limiting cases of the TFIC and discuss the structure of the ground state and its excitations at zero temperature.

1.1.1.2 Limiting case (i): $h = 0$

In the limit of $h \to 0$, the Hamiltonian retains only the Ising spin exchange interaction $H_I(h=0) = J\sum_\ell S^z_\ell S^z_{\ell+1}$ and the ground state is formed from either parallel ($J<0$) or anti-parallel ($J>0$) neighbouring spins

$$\begin{array}{cc} J<0 & J>0 \\ \frac{1}{\sqrt{2}}\Big(|\uparrow\uparrow\ldots\uparrow\rangle \pm |\downarrow\downarrow\ldots\downarrow\rangle\Big) & \frac{1}{\sqrt{2}}\Big(|\uparrow\downarrow\uparrow\ldots\downarrow\uparrow\rangle \pm |\downarrow\uparrow\downarrow\ldots\uparrow\downarrow\rangle\Big) \end{array}$$

where $+(-)$ denotes the states with even (odd) parity under the $\mathbb{Z}_2$ global spin-inversion symmetry $S^z \to -S^z$. We have, of course, recovered the classical Ising model and the ground states correspond to the classical ferromagnetic and antiferromagnetic (Néel) states.

The excited states of the system correspond to single spin flips (with an energy cost of $J/2$ as two exchange interactions have changed from $-J/4 \to +J/4$). Adding a small magnetic field $h \ll J$ allows the domain walls to hop on the lattice, for example they may move apart:

$$|\uparrow\uparrow\uparrow\uparrow\vdots\downarrow\vdots\uparrow\uparrow\uparrow\uparrow\rangle \xrightarrow{h} |\uparrow\uparrow\uparrow\vdots\downarrow\downarrow\downarrow\vdots\uparrow\uparrow\uparrow\rangle \xrightarrow{h} |\uparrow\uparrow\vdots\downarrow\downarrow\downarrow\downarrow\downarrow\vdots\uparrow\uparrow\rangle \xrightarrow{h} \ldots.$$

Domain walls $\vdots$ thus become excitations with a well-defined momentum k and excitation energy $E(k) = J/2 - h\cos(k) + \mathcal{O}(h^2)$. The original spin flip excitation has, in some sense, "fractionalised" into two domain wall degrees of freedom which can move independently.

This fractionalisation of the spin flip into two degrees of freedom means that inelastic neutron scattering in the ordered phase shows the *two-particle* (and at higher energies, $2n$ particle) continuum of excitations [23].

1.1.1.3 Limiting case (ii): $|h| \to \infty$

In a strong transverse field, the ground state properties are dominated by the term in the Hamiltonian $H_I(|h| \to \infty) = h \sum_\ell S^x_\ell$. The resulting ground state configurations become polarised antiparallel to the transverse field direction

$$\begin{array}{cc} h < 0 & h > 0 \\ |\to\to\to \ldots \to\rangle & |\leftarrow\leftarrow\leftarrow \ldots \leftarrow\rangle, \end{array}$$

where $|\to\rangle = (|\uparrow\rangle + |\downarrow\rangle)/\sqrt{2}$. Excitations are single spin flips in the completely polarised state with energy cost $2h$. Each additional flipped spin costs energy $2h$ and hence domain walls $\vdots$ cannot move freely in this limit. The addition of a small Ising term $J \ll h$ allows the single spin flip to hop

$$|\to\to\to\vdots\leftarrow\vdots\to\to\rangle \xrightarrow{J} |\to\to\vdots\leftarrow\vdots\to\to\to\rangle \xrightarrow{J} |\to\vdots\leftarrow\vdots\to\to\to\to\rangle.$$

The single spin flip becomes a quasi-particle with momentum k and excitation energy $E(k) = h - J/2\cos(k) + \mathcal{O}(J^2)$.

As a result of individual spin flips being a good single particle excitation, inelastic neutron scattering on the TFIC in the high-field paramagnetic phase will observe the *single particle* excitation and at higher energies the multi particle continuum [23].

1.1.1.4 The ground state phase diagram

We have seen in the above two limiting cases that the nature of the ground state and the low-energy excitations are very different at low and high-field. In fact, at some intermediate field there exists a *critical point* separating the ordered state and the paramagnetic state. Ignoring boundary conditions, the field at which this phase transition occurs can be found using the Kramers-Wannier duality transformation: following Refs. [15, 23] we define Pauli matrices μ on a dual lattice:

$$\mu^x_{n+\frac{1}{2}} = \sigma^z_n \sigma^z_{n+1}, \qquad \mu^z_{n+\frac{1}{2}} = \prod_{j<n+1} \sigma^x_j.$$

Using that $(\sigma_j^a)^2 = \mathbb{1}_2$, it follows that $\mu^z_{n-\frac{1}{2}}\mu^z_{n+\frac{1}{2}} = \sigma^x_n$. The Hamiltonian can now be written in the dual form (we define $h = gJ$):

$$H_I = \frac{gJ}{2}\sum_\ell \mu^z_{\ell-\frac{1}{2}}\mu^z_{\ell+\frac{1}{2}} + \frac{J}{4}\sum_\ell \mu^x_{\ell+\frac{1}{2}} = 2g\frac{J}{4}\left[\sum_\ell \mu^z_{\ell-\frac{1}{2}}\mu^z_{\ell+\frac{1}{2}} + \frac{1}{2g}\sum_\ell \mu^x_{\ell+\frac{1}{2}}\right].$$

We now compare this to the original form of the Hamiltonian

$$H_I = \frac{J}{4}\left[\sum_\ell \sigma^z_\ell\sigma^z_{\ell+1} + \frac{g}{2}\sum_\ell \sigma^x_\ell\right] \tag{1.2}$$

and we observe a symmetry of the model under the duality transformation which implies the eigenvalues of H_I obey $E(J,g) = 2gE(J,g^{-1})$. At the critical point, the lack of a spectral gap implies the model must be self-dual, e.g. $E(J,g_C) = E(J,g_C^{-1})$, and hence $2g_C = 1$ and the critical transverse field strength is given by $h_C = J/2$. This point separates the low-field ordered phase from the high-field paramagnetic phase, as shown in Fig. 1.1.

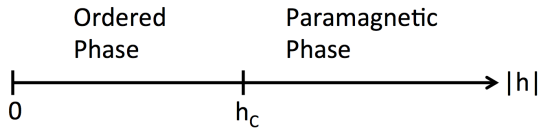

Figure 1.1: Zero-temperature phase diagram for the TFIC.

Having established the presence of a critical point separating the ordered and paramagnetic phases at zero-temperature, let us now briefly discuss the effect of temperature on the long-range order of the TFIC. At finite temperature T the ground state minimises the free-energy $F = E - TS$, where E is the energy of the state and S the entropy. Consider the long-range magnetic order of the ferromagnetic state: inserting a domain wall costs energy of $J/2$ and it may be inserted on any of the $L-1$ bonds of the L site chain. The free energy is then given by $F = J/2 - k_BT\log(L-1)$ and the insertion of domain walls minimises the free energy at any non-zero temperature for $L \to \infty$. Thus temperature melts long-range order in the one-dimensional system. More generally, the Mermin-Wagner theorem [38] tells us that a system with short range interactions in $D \leq 2$ cannot have a spontaneously broken continuous symmetry at finite temperature.

1.1.2 The Peierls insulator

Let us now turn our attention to the Peierls insulator, whose out-of-equilibrium physics will be considered in Chapter 4, alongside a closely related interacting model.

In its simplest realisation, the Peierls insulator describes spinless fermions with modulated hopping

$$H_P = -t \sum_{\ell} \Big[1 + \delta(-1)^{\ell}\Big] \Big(c_{\ell}^{\dagger} c_{\ell+1} + c_{\ell+1}^{\dagger} c_{\ell}\Big), \tag{1.3}$$

where t is the average hopping amplitude and δ is a (dimensionless) dimerisation parameter which describes the modulation of the hopping. Such dimerisation can naturally arise in a crystal structure which breaks translational invariance from one-site to two-site, as illustrated in Fig. 1.2.

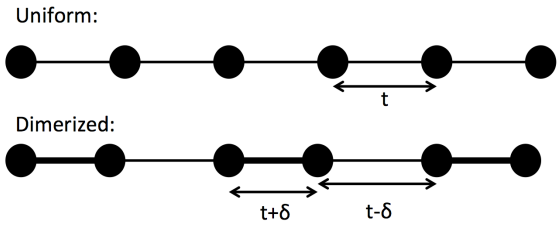

Figure 1.2: Schematic of the periodic (uniformly spaced) and dimerised crystal structures.

The Peierls insulator (1.3) is exactly solved by Fourier transformation and Bogoliubov transformation (see Eq. 4.6 onwards in Chapter 4). The resulting Hamiltonian is formed from two bands $\alpha = \pm$ separated by an energy gap of $4|\delta t|$

$$H_P = \sum_{\alpha=\pm} \sum_{k} \epsilon_{\alpha}(k,\delta) a_{\alpha}^{\dagger}(k) a_{\alpha}(k), \qquad \epsilon_{\alpha}(k,\delta) = 2\alpha t \sqrt{\delta^2 + (1-\delta^2)\cos^2(k)},$$

where the momentum k is restricted to the two-site Brillouin zone $0 < k \leq \pi$. As $\pm\epsilon_{\pm}(k, \delta \neq 0) > 0$ the ground state $|\Psi_0\rangle$ consists of a completely filled "$-$" band

$$|\Psi_0\rangle = \prod_{k>0} a_{-}^{\dagger}(k)|0\rangle,$$

where $|0\rangle$ is the fermion vacuum $a_{\alpha}(k)|0\rangle = 0$. The ground state is thus half-filled, containing $L/2$ fermions.

One surprising result [39] concerning (1.3) is that the half-filled periodic chain ($\delta = 0$) possesses an instability towards the formation of dimerisation $\delta \neq 0$.[†] This follows from a rather simple argument: the ground state energy $E_0(\delta)$ is given by

$$E_0(\delta) = 2 \int_0^{\pi/2} \mathrm{d}k \; \epsilon_{-}(k,\delta),$$

and satisfies

$$E_0(0) - E_0(\delta) = 4J \Big[\mathcal{E}(1-\delta^2) - 1\Big] > 0,$$

[†] This instability was discovered by Peierls in the early 1950s whilst preparing a text book, and was not formally published.

where $\mathcal{E}(m)$ is the complete elliptic integral of the second kind [40]. Thus it is energetically favourable for the chain to dimerise and open a gap in the spectrum, the so-called "Peierls transition" (often called the "Peierls instability"). In reality, the structural distortion pictured in Fig. 1.2 is associated with phonons – a dynamical degree of freedom. A generalisation of the Peierls insulator which treats the dynamics of the lattice distortions was used by Su, Schrieffer and Heeger (SSH) [41] to describe the behaviour of polyacetylene. The phase-diagram of the one-dimensional SSH model was later obtained by Fradkin and Hirsch [42] and interaction effects were investigated by Kivelson and Heim [43].

Interest in the Peierls transition was readily established in the 1970s with the discovery of superconductivity in quasi-one-dimensional organic compounds, observed to exhibit a Peierls transition at higher temperatures [44]. Very soon after this, the Peierls transition was also observed in quasi-one-dimensional (non-organic) metallic systems [45] and an analogous effect in spin systems was also observed [46] (the "Spin-Peierls transition"). More recently, the Peierls transition has been experimentally observed in one-dimensional gold nanowires deposited on silicon surfaces [47]. In these systems, one of the bands in the nanowire is half-filled and is observed to undergo a metal–insulator transition with accompanied lattice distortion as the temperature is lowered. In another case, where the crystal structure of the nanowire is tuned such that there is both a half-filled band *and* a one-third-filled band, Peierls transitions are observed in both bands [48] and parts of the crystal structure distort to dimerise or trimerise, respectively.

1.1.3 The Hubbard model

We finish our review of the models central to the problems presented in this thesis with the Hubbard model, which forms the basis of Chapter 2. The Hubbard model is the simplest model of interacting electrons

$$H_U = -t \sum_{\sigma=\uparrow,\downarrow} \sum_{\langle \ell,\ell' \rangle} \left(c^\dagger_{\sigma,\ell} c_{\sigma,\ell'} + c^\dagger_{\sigma,\ell'} c_{\sigma,\ell} \right) + U \sum_{\ell} n_{\uparrow,\ell} n_{\downarrow,\ell} \tag{1.4}$$

where t is the hopping amplitude, U is the interaction energy, $\langle \ell, \ell' \rangle$ denotes nearest neighbours and $n_{\sigma,\ell} = c^\dagger_{\sigma,\ell} c_{\sigma,\ell}$ is the number operator for spin σ electrons on site ℓ

of the lattice. Only the interaction between electrons sitting on the same site ℓ has been kept, with all longer range interactions neglected. This can be justified for s electrons, where the orbital radius is much smaller than the lattice spacing [49] or for d electrons in a transition metal where the s electrons screen interactions [50].

The Hubbard model (1.4) was proposed independently by John Hubbard [49], Junjiro Kanamori [50] and Martin Gutzwiller [51] in 1963, with the aim of understanding correlation effects in narrow band models (Hubbard) and the effect of interactions on ferromagnetism in transition metals (Kanamori and Gutzwiller). It was then further studied with approximate techniques in a landmark series of paper by Hubbard [52] which have had a lasting impact on the theory of solids [53].

Following these works in the 1960s, the Hubbard model has been used to study an increasingly diverse number of phenomena, from the high-temperature cuprate superconductors (see e.g. Ref. [54]) to the Mott metal-insulator transition [55] and band magnetism [56]. For all its apparent simplicity, the Hubbard model in general dimensions D is not fully solved and there are no well-controlled analytical approaches for studying the problem with $U \sim 4t$ (the region most relevant for e.g. the high–T_c cuprates). Instead, for a generic spatial dimension D one must resort to numerical studies where even the nature of the ground state phase diagram is actively debated (see for example, in two dimensions Refs. [54, 57]).

There are, however, two particular cases in which the exact solution is known. In the first case, the lattice coordination number z is taken to infinity (often called the infinite-dimensional limit) and non-trivial electron–electron correlations can be retained by taking this limit in particular way [58, 59], resulting in the "dynamical mean field theory". The other exact solution is found in the opposing limit of $z = 2$ (e.g. one spatial dimension), where Lieb and Wu [60] constructed the exact eigenstates of the Hubbard model using the Bethe ansatz [9, 10, 11, 12]. A rather complete exposition on the ground state properties and excitations of the one-dimensional Hubbard model can be found in the monograph [11]. It is on this limit that we will focus the remainder of our discussion.

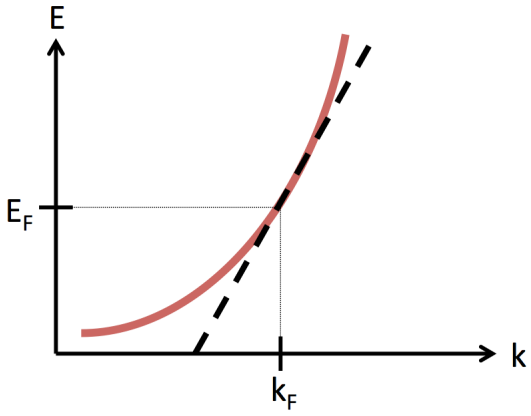

Figure 1.3: Illustration of linearisation of the spectrum (dashed black line) about the Fermi point k_F for a generic dispersion (red solid line).

1.1.3.1 Spin-charge separation in the Hubbard model

Let us begin our discussion of the one-dimensional Hubbard model by highlighting a quintessential example of emergent phenomena: the separation of spin and charge degrees of freedom. We begin by considering the Hubbard model with weak interactions at a generic filling (away from the top/bottom of the non-interacting band or commensurate fillings); the low-energy degrees of freedom occur within the vicinity of the Fermi points $\pm k_F$. Focussing on these low-energy degrees of freedom, the detailed band structure can be approximated by a linear spectrum, as shown for the right Fermi point in Fig. 1.3. This corresponds to splitting the electron into left and right moving components according to

$$c_{\sigma,\ell} \sim \sqrt{a_0}\Big[R_\sigma(x)e^{ik_F x} + L_\sigma(x)e^{-ik_F x}\Big], \tag{1.5}$$

where $R_\sigma(x)/L_\sigma(x)$ is the right/left moving fermion field with spin σ at $x = \ell a_0$ and a_0 is the lattice spacing.

Following the linearisation (1.5), the continuum limit of the one-dimensional Hubbard Hamiltonian (1.4) is

$$\begin{aligned} H_U &= v_F \int \mathrm{d}x \sum_{\sigma=\uparrow\downarrow} :\Big[iL^\dagger_\sigma(x)\partial_x L_\sigma(x) - iR^\dagger_\sigma(x)\partial_x R_\sigma(x)\Big]: \\ &+ U\int \mathrm{d}x\Big[:\Big(R^\dagger_\uparrow(x)R_\uparrow(x) + L^\dagger_\uparrow(x)L_\uparrow(x)\Big)\Big(R^\dagger_\downarrow(x)R_\downarrow(x) + L^\dagger_\downarrow(x)L_\downarrow(x)\Big): \\ &\qquad - :R^\dagger_\uparrow(x)R_\downarrow(x)L^\dagger_\downarrow(x)L_\uparrow(x): - :R^\dagger_\downarrow(x)R_\uparrow(x)L^\dagger_\uparrow(x)L_\downarrow(x):\Big], \end{aligned} \tag{1.6}$$

where $:\mathcal{O}:$ denotes normal ordering[†] of the operator $\mathcal{O}$, the first term is derived

[†]This is necessary as the linearisation of the spectrum introduces divergences into the theory,

from point-splitting (see e.g. Chapter 2 or Ref. [61]) and oscillatory terms have been suppressed by the integration over x. Here we have introduced the Fermi velocity $v_F = 2ta_0 \sin(k_F a_0)$ and we have redefined the interaction parameter $U \to U/a_0$.

To show the separation of spin and charge degrees of freedom in the Hubbard model, we proceed to bosonise [6, 7, 11, 61] the low-energy Hamiltonian.[†] The following operator identities hold in one spatial dimension [6, 7, 14]

$$R^\dagger_\sigma(x) \sim \frac{\kappa_\sigma}{\sqrt{2\pi a_0}} :e^{-i\sqrt{4\pi}\varphi_\sigma(x)}:, \qquad L^\dagger_\sigma(x) \sim \frac{\kappa_\sigma}{\sqrt{2\pi a_0}} :e^{i\sqrt{4\pi}\bar{\varphi}_\sigma(x)}:, \tag{1.7}$$

where the bosonic fields obey $[\varphi_\sigma(x), \varphi_{\sigma'}(x')] = -[\bar{\varphi}_\sigma(x), \bar{\varphi}_{\sigma'}(x')] = \mathrm{sgn}(x-x')i/4\delta_{\sigma,\sigma'}$ and $[\varphi_\sigma(x), \bar{\varphi}_{\sigma'}(x')] = i/4\delta_{\sigma,\sigma'}$ which enforce the anti-commutation of electrons with the same spin, whilst $\{\kappa_\sigma, \kappa_{\sigma'}\} = 2\delta_{\sigma,\sigma'}$ enforces the anti-commutation of electrons with different spins. The kinetic term is evaluated by point-splitting, and it follows that in terms of the bosonic fields the Hamiltonian takes the form

$$\begin{aligned} H_U &= v_F \int \mathrm{d}x \sum_{\sigma=\uparrow\downarrow} :\left[(\partial_x\varphi_\sigma)^2 + (\partial_x\bar{\varphi}_\sigma)^2\right]: + \frac{U}{\pi}\int \mathrm{d}x :\partial_x(\varphi_\uparrow + \varphi_\downarrow)\partial_x(\bar{\varphi}_\uparrow + \bar{\varphi}_\downarrow): \\ &+ \frac{2U}{(2\pi a_0)^2}\int \mathrm{d}x :\cos\left[\sqrt{4\pi}(\varphi_\uparrow - \varphi_\downarrow + \bar{\varphi}_\uparrow - \bar{\varphi}_\downarrow)\right]: \ . \end{aligned}$$

A natural basis for the bosonic fields describes spin (s) and charge (c) fluctuations:

$$\begin{aligned} \Phi_c &= \frac{1}{\sqrt{2}}\Big[\varphi_\uparrow + \varphi_\downarrow + \bar{\varphi}_\uparrow + \bar{\varphi}_\downarrow\Big], \qquad \Phi_s = \frac{1}{\sqrt{2}}\Big[\varphi_\uparrow - \varphi_\downarrow + \bar{\varphi}_\uparrow - \bar{\varphi}_\downarrow\Big], \\ \Theta_c &= \frac{1}{\sqrt{2}}\Big[\varphi_\uparrow + \varphi_\downarrow - \bar{\varphi}_\uparrow - \bar{\varphi}_\downarrow\Big], \qquad \Theta_s = \frac{1}{\sqrt{2}}\Big[\varphi_\uparrow - \varphi_\downarrow - \bar{\varphi}_\uparrow + \bar{\varphi}_\downarrow\Big], \end{aligned}$$

where Θ and Φ are conjugate fields in each sector. In this basis the low-energy effective Hamiltonian takes the simple form

$$\begin{aligned} H &= H_c + H_s, \qquad (1.8) \\ H_c &= v_c \int \mathrm{d}x : \left[K_c^{-1}(\partial_x\Phi_c)^2 + K_c(\partial_x\Theta_c)^2\right]:, \\ H_s &= v_s \int \mathrm{d}x : \left[K_s^{-1}(\partial_x\Phi_s)^2 + K_s(\partial_x\Theta_s)^2\right]: + \frac{2U}{\pi}\frac{1}{(2\pi a_0)^2}\int \mathrm{d}x :\cos(\sqrt{8\pi}\Phi_s):, \end{aligned}$$

where we have defined the Luttinger parameters

$$K_c = \frac{1}{\sqrt{1 + U/4\pi v_F}} \quad \text{and} \quad K_s = \frac{1}{\sqrt{1 - U/4\pi v_F}},$$

which may be regulated by introducing a cutoff momentum/energy or by consistent normal-ordering. Normal ordering is discussed further in Chapter 2.

[†]A full discussion of bosonisation can be found in Chapter 2, where bosonisation is used extensively.

and the velocities $v_c = v_F/K_c$, $v_s = v_F/K_s$. These parameters characterise the strength of the interactions: $K > 1$ is effective attractive interactions and $K < 1$ is the repulsive regime.[†] We see that in the low-energy effective theory the spin and charge degrees of freedom have decoupled: they even have *different* velocities. This is the phenomena of spin-charge separation, which is quite generic in one-dimensional quantum systems [6, 7]. The separation of spin and charge in the Hubbard model holds beyond the low-energy limit and applies to excitations at all energies [11].

1.1.3.2 The Luttinger liquid

The low-energy renormalisation group fixed point of the Hubbard model at generic filling (1.8) and repulsive interactions[‡] is given by a two-component Luttinger liquid [6, 11]:

$$H_{\text{fixed}} = \sum_{\alpha=c,s} \tilde{v}_\alpha \int \mathrm{d}x : \left[\tilde{K}_\alpha^{-1} (\partial_x \Phi_\alpha)^2 + \tilde{K}_\alpha (\partial_x \Theta_\alpha)^2 \right] : ,$$

where $\tilde{K}_\alpha$ is the renormalised Luttinger parameter and $\tilde{v}_\alpha$ is the renormalised excitation velocity. This can be written as a free theory by rescaling the bosonic fields $\Phi_\alpha = \sqrt{\tilde{K}_\alpha}\tilde{\Phi}_\alpha$, $\Theta_\alpha = \tilde{\Theta}_\alpha/\sqrt{\tilde{K}_d}$, giving

$$H_{\text{fixed}} = \sum_{\alpha=c,s} \tilde{v}_d \int \mathrm{d}x : \left[(\partial_x \tilde{\Phi}_\alpha)^2 + (\partial_x \tilde{\Theta}_\alpha)^2 \right] : \ .$$

As this is now a theory of free bosons, we can calculate bosonic correlation functions and hence correlation functions of the original fermions via (1.7). For example, the Green's function of right-moving spin-↑ fermions is

$$\begin{aligned} \langle R_\uparrow^\dagger(x) R_\uparrow(y) \rangle &= \frac{1}{2\pi a_0} \Bigg\langle : \exp\left[-i\sqrt{\frac{\pi}{2}} \left(\frac{\tilde{K}_c \tilde{\Phi}_c + \tilde{\Theta}_c}{\sqrt{\tilde{K}_c}} + \frac{\tilde{K}_s \tilde{\Phi}_s + \tilde{\Theta}_s}{\sqrt{\tilde{K}_s}} \right)(x) \right] : \\ &\quad \times : \exp\left[i\sqrt{\frac{\pi}{2}} \left(\frac{\tilde{K}_c \tilde{\Phi}_c + \tilde{\Theta}_c}{\sqrt{\tilde{K}_c}} + \frac{\tilde{K}_s \tilde{\Phi}_s + \tilde{\Theta}_s}{\sqrt{\tilde{K}_s}} \right)(y) \right] : \Bigg\rangle \\ &\propto \frac{1}{2\pi} \left(\frac{1}{|x-y|} \right)^{\frac{\tilde{K}_c + \tilde{K}_c^{-1} + \tilde{K}_s + \tilde{K}_s^{-1}}{4}} \end{aligned}$$

[†] The $SU(2)$ spin symmetry sets $K_s = 1$, which follows from a full renormalisation group treatment of the interaction terms.

[‡] For repulsive interactions, the cosine term in the spin sector is marginally irrelevant and gives logarithmic corrections to correlation functions, which we neglect. In the attractive case it is marginally relevant and causes a spin gap to open, in an analogous manner to the umklapp process we'll discuss in the next section.

which shows that in the presence of interactions ($K_c \neq 1$ and/or $K_s \neq 1$) the fermions acquire an *anomalous dimension*.

1.1.3.3 Half-filling and umklapp scattering

Having discussed the phenomena of spin-charge separation at generic fillings in the Hubbard model, let us now consider the case of half-filling, which will be of some relevance to Chapter 2. At a density of one electron per site, the Fermi wave vector $k_F = \pi/2$ and some of the terms dropped in (1.6) because they oscillated at $4k_F$ are no longer suppressed by integration over x. In our low-energy effective theory we must include the interaction terms

$$H_{\rm um} = -U \int \mathrm{d}x : \left[R^\dagger_\uparrow(x) R^\dagger_\downarrow(x) L_\uparrow(x) L_\downarrow(x) e^{-4ik_F x} + L^\dagger_\uparrow(x) L^\dagger_\downarrow(x) R_\uparrow(x) R_\downarrow(x) e^{4ik_F x} \right] :,$$

where $\exp(\pm 4ik_F x) = 1$. These scattering terms, which do not conserve the number of left and right movers, are known as "umklapp" interactions.[†] Importantly, at half-filling such terms connect the low-energy degrees of freedom at the Fermi points, see Fig. 1.4. This has striking consequences for the behaviour of the low-energy degrees of freedom.

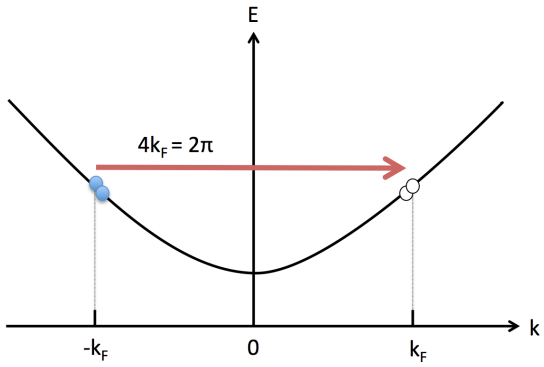

Figure 1.4: Schematic figure of umklapp scattering at half-filling, where two left movers (blue circles) scatter in to two available right moving states (white vacancies).

Bosonising the umklapp term and adding it to the Hamiltonian (1.8) we find

$$\begin{aligned} H &= v_c \int \mathrm{d}x : \left[K_c^{-1} (\partial_x \Phi_c)^2 + K_c (\partial_x \Theta_c)^2 \right] : - \frac{2U}{\pi} \frac{1}{(2\pi a_0)^2} \int \mathrm{d}x : \cos(\sqrt{8\pi}\Phi_c) : \\ &+ v_s \int \mathrm{d}x : \left[K_s^{-1} (\partial_x \Phi_s)^2 + K_s (\partial_x \Theta_s)^2 \right] : + \frac{2U}{\pi} \frac{1}{(2\pi a_0)^2} \int \mathrm{d}x : \cos(\sqrt{8\pi}\Phi_s) : , \end{aligned}$$

which shows a symmetry under changing the sign of the interaction $U \to -U$, where we recover the same theory with $c \leftrightarrow s$. The effect of the cosine terms on the low-

[†]Umklapp derives from the german word for fold/flip over, and its use in this context is due to Peierls [62].

energy effective theory can be obtained from the renormalisation group flow [11]. As was the case in the previous subsection, the spin cosine remains marginally irrelevant and the low-energy fixed point of the spin sector is a Luttinger liquid. However, in the charge sector the cosine is marginally relevant and flows to strong coupling. This then pins the bosonic field Φ_c to one of the maxima of the cosine potential and becomes an effective mass term – at energies below this mass gap, the charge degree of freedom becomes "frozen". This is the Mott metal–insulator transition [55] in the one-dimensional Hubbard model, which occurs for any $U \neq 0$.

This picture from the renormalisation group flow is consistent with the conventional large-U picture of the half-filled Hubbard model [11]: double occupancy is suppressed, but energy can be lowered by the virtual process which hops an electron onto a neighbouring site and back again. Such processes can only occur if neighbouring spins are antiparallel, leading to a low-energy effective theory (derived from second-order perturbation theory) describing the Heisenberg antiferromagnet $H_{U\gg 1} \sim J \sum_\ell \mathbf{S}_\ell \cdot \mathbf{S}_{\ell+1}$ with $J \approx 4t^2/U$. Charge fluctuations are frozen by the large onsite repulsion, but spin excitations exist and can propagate (in a similar manner to that discussed for the TFIC, Sec 1.1.1).

1.2 This thesis

In the above, we began by reviewing a number of properties of the models that we will study in this thesis. Each chapter also contains introductory technical material specific to the problems therein and motivation/background to the problem. The remainder of this thesis is laid out as follows: in Chapter 2, motivated by the apparent interplay of charge ordering and superconductivity in the enigmatic cuprate superconductors, we study the properties of the extended Hubbard model on the two-leg ladder with the addition of "umklapp-like" terms, which may arise from long range Coulomb interactions with charge order in a material. We derive the low-energy effective field theory for one such case and find the zero-temperature phase diagram. We show that such umklapp scattering can lead to phases whose dominant fluctuations are of an interesting superconducting type with finite centre of mass momentum, the one-dimensional analogue of the Fulde-Ferrell-Larkin-Ovchinnikov (FFLO) supercon-

ductivity in the absence of a magnetic field.

Following this, in Chapter 3 we move away from studying the ground state static properties and examine the equilibrium dynamical properties of a quasi-one-dimensional quantum magnet, $CoNb_2O_6$. In this, we are motivated by inelastic neutron scattering experiments which reveal an unusual "anomalous broadening" of the single particle mode in part of the Brillouin zone. We study the dynamical structure factor of an effective model for $CoNb_2O_6$, a perturbed transverse field Ising chain, using a combination of diagrammatic perturbation theory and numerical exact diagonalization on systems of up to length $L = 28$. We show that this anomalous broadening is consistent with *quasi-particle breakdown* – a many-body quantum mechanical effect induced by a small misalignment of the magnetic field in experiment.

In contrast to the previous chapter, we study the *out-of-equilibrium* dynamics of a one-dimensional quantum system in Chapter 4. We examine the effect of breaking integrability in a quantum quench by adding interactions to the Peierls insulator. When integrability is weakly broken, we show the system approaches a non-thermal quasi-stationary state at intermediate times after the quantum quench. We show that stationary values of local observables in this non-thermal state may be described by a generalised Gibbs ensemble with modified charges and we explicitly construct these charges. Interestingly, the charges are only conserved at an expectation value level – they do not commute with the Hamiltonian to the required order in perturbation theory to be conserved at an operator level. Our construction shows that when integrability breaking is weak there is still a time scale on which integrability governs the time-evolution. Following this we increase the strength of the integrability breaking and show by numerical calculations that the behaviour is consistent with thermalisation.

We finish this thesis in Chapter 5 with a brief summary of our main results and we highlight some of the open questions.

2. Finite wave vector pairing in doped two-leg ladders

2.1 Introduction and background

Umklapp processes can lead to a profound restructuring of the ground state and low-energy properties of a system. This is well illustrated by the one-dimensional Hubbard model [11] introduced in Chapter 1, where at half-filling the Fermi wave vector is $4k_F = 2\pi/a_0$ and umklapp scattering processes connect opposite Fermi points, opening a spectral gap for single-particle excitations. In a similar way, half-filled two-leg ladders are known to have a variety of insulating states as a result of umklapp scattering [63, 64, 65, 66]. In both these cases, umklapp scattering becomes relevant at a particular *commensurate* filling of one electron per site, independent of the details of the interaction. However, in multi band systems, such as the two-leg ladder, there are other sorts of umklapp scattering which will connect Fermi points at certain other band fillings, which generally *do* dependent on microscopic details of the band structure and the interactions. These types of umklapp scattering have not been well studied and it is with these umklapp processes that we will concern ourselves in this chapter.

2.1.1 Long-range Coulomb interaction and umklapp processes

One example where multi band umklapp processes may play a crucial role is the "telephone number compound" $Sr_{14-x}Ca_xCu_{24}O_{41}$ [67, 68]. X-ray scattering techniques have established the presence of a standing wave in the hole density without a significant lattice distortion in this material [67]. The simplest explanation for these findings is a crystalline state of pairs of holes [69, 70].

The physical origin of the hole crystal is likely to be the long-ranged Coulomb interaction between ladders:

$$H_{\rm int} = \sum_{i,j,k,l} V_{ij}^{kl} n_i^{(k)} n_j^{(l)},$$

where i, j label sites within each ladder and k, l are ladder indices. Generically V_{ij}^{kl} has a complicated dependence on i, j, k, l and includes effects such as screening.

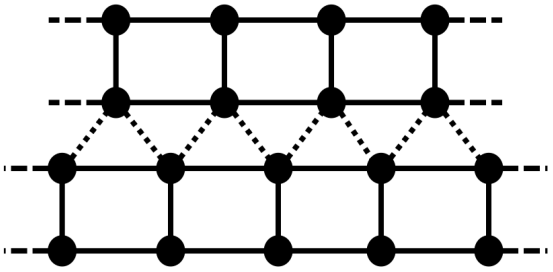

Figure 2.1: Schematic diagram of the weakly coupled ladder geometry of Ref. [70], used to model the crystal of hole pairs in $Sr_{14-x}Ca_xCu_{24}O_{41}$.

Following Almeida, Roux and Poilblanc [70], we treat the long-range Coloumb interaction in mean-field (MF), focusing on only the interactions between the nearest-neighbour (NN) ladders (see the dotted bonds in Fig. 2.1). This leads to a model of decoupled ladders subject to a self-consistent periodic potential

$$\sum_{i,j,k,l} V_{ij}^{kl} n_i^{(k)} n_j^{(l)} \xrightarrow{\rm NN} \sum_{l,i,\langle j\rangle_i} V_{ij}^{\perp} n_i^{(l)} n_j^{(l+1)} \xrightarrow{\rm MF} -\sum_{l,i} \mu_i^{(l)} n_i^{(l)}$$
$$\text{with} \quad \mu_i^{(l)} = -\sum_{\langle j\rangle_i} V_{ij}^{\perp} \langle n_j^{(l+1)} \rangle,$$

where $\langle j\rangle_i$ denotes only those sites j which are neighbours of i (denoted by dotted bonds in Fig. 2.1) . It will usually be the case that the Coulomb repulsion will be minimised by the formation of a charge density wave (CDW), that is the density will take the generic form

$$\langle n_j \rangle = n\Big[1 + \sum_{q\in S} \rho_q \cos(qj)\Big],$$

where n is the average density, ρ_q are the amplitudes of the Fourier components q of the density and S is the set of Fourier components (e.g. $2k_F$, $4k_F, \ldots$ which depend upon microscopic details and the band structure).

Let us now consider the effect of adding such terms within a single ladder. Provided that the interaction strength $V^{\perp}$ is weak in comparison to the inter-ladder hopping amplitudes, we can consider the effect of CDW formation by projecting the

new terms on to the low-energy degrees of freedom which are found in the vicinity of the Fermi points. The projection of the self-consistent periodic potential induces scattering between these degrees of freedom: in the continuum limit, we have added terms of the form

$$\int \mathrm{d}x\ \rho(x)\mu(x) = \int \mathrm{d}x \sum_{q\in S} \mu_q \cos(qx)\rho(x), \tag{2.1}$$

where $\rho(x)$ is the density operator on the ladder. This can be decomposed into its Fourier components

$$\rho(x) = \hat{\rho}_0(x) + \sum_{k\in S'} e^{ikx}\hat{\rho}_k(x), \tag{2.2}$$

where S' is the set of Fourier components for the density operator $n(x)$ (for a system of identical coupled ladders, the sets of Fourier components in each ladder will be identical, e.g. $S = S'$). The integral over x suppresses oscillatory terms:

$$\int \mathrm{d}x\ \rho(x)\mu(x) \propto \int \mathrm{d}x \sum_{k\in S'}\sum_{q\in S} \delta_{k,q}\mu_q[\hat{\rho}_k(x) + \mathrm{H.c.}].$$

In effect, we see that CDW formation has imposed a lattice on the electronic degrees of freedom which is *commensurate* with the filling (at arbitrary filling of the crystal lattice) and consequently induces umklapp scattering. In an interacting theory, an important question of current interest is what effect do such terms have on the ground state properties and excitations of ladders?

We should also note that in complete analogy with the above, umklapp processes can equally well be induced by imposing an *external* periodic potential. This has recently been demonstrated in carbon nanotubes, where a monolayer of noble gas is adsorbed on to the surface, forming a periodic structure which couples to the electronic degrees of freedom [71].

2.1.2 The Kondo-Heisenberg model (KHM)

Another case in which it is known that umklapp processes have very interesting physical consequences is the Kondo-Heisenberg model [72, 73] (KHM). The KHM is a model of spin–1/2 fermions on a two-leg ladder with *inequivalent* legs: one leg of the ladder is half-filled whilst the other has less than one electron per site. As a consequence of umklapp interactions, the half-filled leg has a large Mott gap and this

results in tunnelling between the two legs being suppressed at low energies. Virtual processes, which hop from the metallic leg to the Mott insulator and back result in an effective Heisenberg exchange interaction between the electrons in the two legs. The resulting low-energy model of such a two-leg ladder consists of a spin–1/2 Heisenberg chain (leg 1) coupled to a one-dimensional electron gas (1DEG, leg 2) through across-rung exchange interactions.

In its simplest guise, the KHM was studied extensively in Refs. [72, 73]. There, the 1DEG is taken to be non-interacting and the Hamiltonian takes the form

$$\begin{aligned} H_{\rm KHM} &= H_{\rm 1DEG} + H_{\rm Heis} + H_K, \\ H_{\rm 1DEG} &= -t\sum_{j,\sigma} c^\dagger_{j,\sigma} c_{j+1,\sigma} + \text{H.c} - \mu \sum_{j,\sigma} c^\dagger_{j,\sigma} c_{j,\sigma}, \\ H_{\rm Heis} &= J_H \sum_j \mathbf{S}_j \cdot \mathbf{S}_{j+1}, \\ H_K &= J_K \sum_{j,a} S^a_j \Big[c^\dagger_{j,\sigma} (\frac{1}{2}\tau^a)_{\sigma\sigma'} c_{j,\sigma'} \Big], \end{aligned}$$

with S^a_j the $a = x, y, z$ component of the spin operator $\mathbf{S}_j$ on site j of the spin chain leg and τ^a are the $a = x, y, z$ Pauli matrices. For $J_H, t \gg J_K$ the continuum limit can be taken for the 1DEG and the Heisenberg chain; for the generic case of the Fermi momentum of the 1DEG being incommensurate with lattice the low-energy field theory is given by ($H = \int \mathrm{d}x \mathcal{H}$)

$$\begin{aligned} \mathcal{H}_{\rm 1DEG} &= \sum_{\alpha=c,s} \frac{v_\alpha}{2} \Big[K_\alpha (\partial_x \theta_\alpha)^2 + \frac{1}{K_\alpha} (\partial_x \phi_\alpha)^2 \Big], \\ \mathcal{H}_{\rm Heis} &= \frac{\tilde{v}_s}{2} \Big[(\partial_x \tilde{\theta}_s)^2 + (\partial_x \tilde{\phi}_s)^2 \Big], \\ \mathcal{H}_K &= \frac{J_K}{8\pi} \Big[(\partial_x \phi_+)^2 - (\partial_x \phi_-)^2 \Big] \\ &\quad + \frac{\tilde{J}_K}{2(\pi a)^2} \cos(\sqrt{4\pi}\theta_-) \Big[\cos(\sqrt{4\pi}\phi_-) + \cos(\sqrt{4\pi}\phi_+) \Big], \end{aligned} \tag{2.3}$$

where the low-energy degrees of freedom are bosonic fields satisfying $[\phi_a(x), \partial_x \theta_a(x')] = i\delta(x - x')$, K_α (v_α) is the Luttinger parameter (velocity) of the α boson in the 1DEG, $\tilde{v}_s$ is the velocity of the spin boson in the Heisenberg chain and J_K, $\tilde{J}_K$ are interaction parameters. The fields $\phi_{c,s}$ describe charge (c) and spin (s) spin fluctuations in the 1DEG, with Luttinger parameter K_a and excitation velocity v_a ($a = c, s$). The spin degrees of freedom in the Heisenberg chain are represented by the bosonic field $\tilde{\phi}_s$ and

the Luttinger parameter $\tilde{K}_s$ and spin velocity $\tilde{v}_s$. The across rung "Kondo" interaction couples the spin degrees of freedom in the two legs of the ladder and is most conveniently expressed in terms of the symmetric/antisymmetric fields $\phi_\pm = (\phi_s \pm \tilde{\phi}_s)/\sqrt{2}$ and $\theta_\pm = (\theta_s \pm \tilde{\theta}_s)/\sqrt{2}$. The process for deriving the above low-energy field theory in terms of bosonic fields, *bosonisation*, will be discussed in detail later in the chapter.

When $J_K < 0$ (ferromagnetic across rung interaction) the renormalisation group (RG) flow of the Hamiltonian is to weak coupling and one recovers a three-component Luttinger liquid where correlation functions can be calculated in the conventional manner, see Sec. 1.1.3.2. When $J_K > 0$, the non-interacting fixed point is no longer stable and the RG flow is to strong coupling [74] and a phase in which the charge degree of freedom remains gapless and a spin gap is established (this can be seen in a number of ways: (i) the term $\cos(\sqrt{4\pi}\theta_-)\cos(\sqrt{4\pi}\phi_+)$ flows to strong coupling, pinning θ_- and ϕ_+; (ii) Sikkema, Affleck and White [74] showed that the spin sector of the KHM at generic filling is equivalent to a zig-zag spin ladder and established a gap using numerics (DMRG); (iii) in the limit that the spin velocities in the two legs are identical, the model realises the spin sector of the $SU(2)$ Thirring model [72], known to have a gap through RG arguments [74]).

Having established that there are two accessible phases in the KHM, it is natural to ask what is the predominant order in the phase? For example, is there superconducting order $\Delta \propto R^\dagger_\uparrow L^\dagger_\downarrow + L^\dagger_\uparrow R^\dagger_\downarrow$ or CDW order $\hat{\mathcal{O}}_{\text{CDW}} \propto R^\dagger_\uparrow L_\uparrow + R^\dagger_\downarrow L_\downarrow + \text{H.c.}$ in the 1DEG? Here one must be careful as the Mermin-Wagner theorem [38] tells us that it is not possible to break a continuous symmetry of a one-dimensional quantum model. Clearly order parameters break just such a symmetry (Δ breaks the $U(1)$ charge conservation symmetry, whilst $\mathcal{O}_{CDW}$ breaks the two $U(1)$ symmetries reflecting conservation of L/R movers). Instead, we study the two-point correlation functions of order parameters and use that the slowest decaying two-point functions correspond to the *most divergent* susceptibilities, which would be stabilised into true long-range order in a *quasi*-one-dimensional material by weak 3D couplings [6].

The strong coupling phase was studied analytically by Zachar and Tsvelik in Ref. [72], where they found that the conventional singlet pairing order parameter Δ and the $2k_F$ CDW order parameter $\hat{\mathcal{O}}_{\text{CDW}}$ are incoherent (the two point functions of

these operators decay exponentially). They showed that there are gapless modes of a "composite nature" which mix degrees of freedom on the spin chain and in the 1DEG, for example $\hat{\mathcal{O}}_{c-SP} \propto R^\dagger_\alpha(\underline{\boldsymbol{\tau}}\tau^y)_{\alpha\beta}L^\dagger_\beta \cdot \mathbf{S}$, where R/L are right/left moving fermion fields in the 1DEG.

More recently, Berg, Fradkin and Kivelson [73] used density matrix renormalisation group (DMRG) calculations to show that there is also quasi-long-range superconductivity in the KHM. This superconducting order is not the usual singlet superconductivity (which is incoherent), but has wavenumber π and is "bond centred"

$$\Delta_\pi(j) = \frac{1}{2}(-1)^j\left(c^\dagger_{j,\uparrow}c^\dagger_{j+1,\downarrow} - c^\dagger_{j,\downarrow}c^\dagger_{j+1,\uparrow}\right). \tag{2.4}$$

This rather surprising result constitutes an example of the 1D Fulde-Ferrell-Larkin-Ovchinnikov (FFLO) state [75] in the *absence* of a magnetic field. Through this example, we see that umklapp scattering can have a profound effect on the properties of the system – in the KHM we realise an unconventional form of superconductivity and interesting types of composite order due umklapp scattering opening a Mott gap and the subsequent RG flow of the low-energy theory being to strong coupling.

2.1.3 This chapter

This chapter is organised as follows. In Section 2.2 we introduce the lattice model that we study, derive the low-energy effective field theories in the "band" and "chain" limits of the Hamiltonian and discuss how we account for the external periodic potential. In Section 2.3 we consider the a particular umklapp process (the "$4k_b$ umklapp") in both band and chain representations of the model. By means of renormalisation group calculations we derive the effective low-energy theories describing the strong coupling fixed points. In the band representation we find the zero-temperature phase diagram and analyse the predominant fluctuations in each phase, showing that part of the strong coupling phase has quasi-long-range order described by fluctuations which are of a superconducting type and which carry a finite wave vector, the one-dimensional analogue of FFLO superconductivity. Section 2.4 summarises the density matrix renormalisation group algorithm, before presenting data in intermediate parameter regimes. Section 2.5 contains the conclusions and a number of technical points are

discussed in several appendices.

2.2 Lattice model and low-energy description

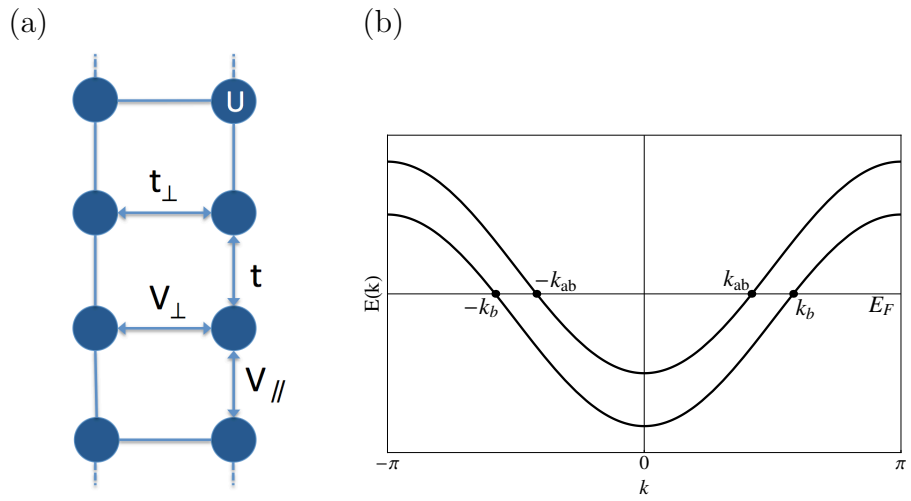

Figure 2.2: (a) Extended Hubbard ladder with different leg and rung hopping amplitudes and density-density interactions. (b) The non-interacting band structure for the tight-binding model on the ladder, with the Fermi wave vectors labelled.

In the following we consider spin–1/2 fermions on a two-leg ladder (Figure 2.2 shows schematically the ladder geometry) with Hubbard and nearest-neighbour density-density interactions. In addition we allow an external periodic potential to be present, the physical origin of which is discussed in Sec. 2.1.1. The Hamiltonian is given by

$$\begin{aligned} H_{\rm ladd}(K) &= -t\sum_{m,\sigma}\sum_{\ell=1}^{2}(a^{\dagger}_{\ell,m+1,\sigma}a_{\ell,m,\sigma}+a^{\dagger}_{\ell,m,\sigma}a_{\ell,m+1,\sigma})+U\sum_{m}\sum_{\ell=1}^{2}n_{\ell,m,\uparrow}n_{\ell,m,\downarrow} \\ &- t_{\perp}\sum_{m,\alpha}(a^{\dagger}_{1,m,\sigma}a_{2,m,\sigma}+a^{\dagger}_{2,m,\sigma}a_{1,m,\sigma})+V_{\perp}\sum_{m}n_{1,m}n_{2,m} \\ &+ V_{\parallel}\sum_{m}\sum_{\ell=1}^{2}n_{\ell,m}n_{\ell,m+1}+\sum_{m}\sum_{\ell=1}^{2}W_{\ell}\cos(Kl)\;n_{\ell,m}, \end{aligned} \tag{2.5}$$

where $a_{\ell,m,\sigma}$ are annihilation operators for spin–σ electrons on site m of leg ℓ of the ladder and $n_{\ell,m,\sigma} = a^{\dagger}_{\ell,m,\sigma}a_{\ell,m,\sigma}$. U is the Hubbard interaction strength, $V_{\perp}$ and $V_{\parallel}$ are the density-density interaction strengths along the rung and leg directions respectively and the periodic potential is characterised by its strength on each leg $W_{1,2}$ and the wavenumber of its modulation, K. The lattice model (2.5) has $U(1)\times SU(2)$

symmetry, with an additional $\mathbb{Z}_2$ symmetry if $W_1 = W_2$. It is useful to rewrite the periodic potential term as

$$\sum_m \cos(Km)\Big[W_+(n_{1,m}+n_{2,m})+W_-(n_{1,m}-n_{2,m})\Big], \tag{2.6}$$

where $W_\pm = (W_1 \pm W_2)/2$. A non-zero W_- breaks the symmetry between the two legs of the ladder. In the following we will only consider terms which do not break the leg symmetry and so we set $W_- = 0$. In order to see which wave numbers K will lead to the most pronounced effects for weak interactions and small $W_{1,2}$ it is useful to consider the band structure of H_{ladd} in the absence of interactions. We introduce the bonding (b) and antibonding (ab) variables by

$$c_{b,n,\sigma} = \frac{1}{\sqrt{2}}\left(a_{1,n,\sigma}+a_{2,n,\sigma}\right), \qquad c_{ab,n,\sigma} = \frac{1}{\sqrt{2}}\left(a_{1,n,\sigma}-a_{2,n,\sigma}\right), \tag{2.7}$$

as in terms of these operators the non-interacting tight-binding Hamiltonian $H_{\text{ladd},0}$ is diagonal in momentum space

$$H_{\text{ladd},0} = \sum_{j=1}^{2}\sum_k \epsilon_j(k) c^\dagger_{j,\sigma}(k) c_{j,\sigma}(k), \tag{2.8}$$

where $j = 1,2 = b, ab$, $c_{j,\sigma}(k) = L^{-1/2}\sum_n e^{ikn} c_{j,n,\sigma}$ and

$$\epsilon_1(k) = -2t\cos(k) - t_\perp, \quad \epsilon_2(k) = -2t\cos(k) + t_\perp. \tag{2.9}$$

The corresponding band structure is shown in Fig. 2.2(b). For weak interactions the low energy degrees of freedom occur in the vicinities of nk_b and nk_{ab} where n is an integer and k_b, k_{ab} are the Fermi momenta of the bonding and antibonding bands respectively, see also Sec. 1.1.3.1. It is then clear that external potentials with wave numbers $K = n_1 k_b + n_2 k_{ab}$ will affect the low-energy degrees of freedom most strongly. In the following we concentrate on the case with $K = 4k_b$. As we will see, in the case of strong interactions but small $t_\perp$ an analogous picture applies.

There are two complementary limits in which one can derive a field theory for the lattice Hamiltonian (2.5). Firstly, one may start from the non-interacting tight-binding Hamiltonian, diagonalise it by transforming to bonding and antibonding variables and subsequently treat the interactions perturbatively using RG methods [66, 77, 78, 79]. Hereinafter this approach will be called the "band representation".

Secondly, one starts from a model of two strongly interacting uncoupled chains and treats the across rung hopping $t_\perp$ and density-density interactions $V_\perp$ as perturbations [80, 81]. We call this approach the "chain representation". In the following subsections we summarise the two approaches in turn.

2.2.1 The band representation $U, V_j \ll t, t_\perp$

Here we start from the tight-binding model obtained by setting $U, V_j = 0$ in the Hamiltonian (2.5). The non-interacting Hamiltonian is diagonalised by the transformation (2.7) to bonding/antibonding (b/ab) variables and has split bonding and antibonding bands (2.8), depicted in Fig. 2.2(b). As our interest is in the low-energy behaviour of the system, we linearise the spectrum about the Fermi points (under the assumption that the Fermi level is away from the top/bottom of a band), see Fig. 1.3. The low-energy projections of the lattice fermion operator are then

$$c_{j,n,\sigma} \sim \sqrt{a_0}\left[R_{j,\sigma}(x)e^{ik_j x} + L_{j,\sigma}(x)e^{-ik_j x}\right], \tag{2.10}$$

where $x = na_0$, $L(x)$ and $R(x)$ are left and right moving fermion fields close to the Fermi points, k_b (k_{ab}) is the Fermi wave vector in the bonding (antibonding) band and a_0 is the lattice spacing, which serves as the short-distance cut-off of the theory. The interactions are conveniently expressed in terms of currents [66], which following Ref. [82] we define as

$$I^R_{ij} = \frac{1}{2}R_{i,\sigma}\ \epsilon_{\sigma\sigma'}\ R_{j,\sigma'}, \qquad I^{aR}_{ij} = \frac{1}{2}R_{i,\sigma}(\epsilon\sigma^a)_{\sigma\sigma'}R_{j,\sigma'}, \tag{2.11}$$

$$J^R_{ij} = \frac{1}{2}R^\dagger_{i,\sigma}\ R_{j,\sigma}, \qquad J^{aR}_{ij} = \frac{1}{2}R^\dagger_{i,\sigma}\sigma^a_{\sigma\sigma'}R_{j,\sigma'}, \tag{2.12}$$

and similarly for left-moving fermion fields with $R \leftrightarrow L$.

The low-energy Hamiltonian then takes the form $H = \int dx\ [\mathcal{H}_0 + \mathcal{H}_U + \mathcal{H}_W]$

$$\begin{aligned}
\mathcal{H}_0 &= \sum_{j=1}^{2} v_j\Big(-iR^\dagger_{j,\sigma}\partial_x R_{j,\sigma} + iL^\dagger_{j,\sigma}\partial_x L_{j,\sigma}\Big),\\
\mathcal{H}_U &= \sum_{i,j}\tilde{c}^\rho_{ij}J^R_{ij}J^L_{ij} - \tilde{c}^\sigma_{ij}J^{aR}_{ij}J^{aL}_{ij} + \sum_{i\neq j}\tilde{f}^\rho_{ij}J^R_{ii}J^L_{jj} - \tilde{f}^\sigma_{ij}J^{aR}_{ii}J^{aL}_{jj},\\
\mathcal{H}_W &= \sum_{P\in S}\sum_{\gamma=\pm} W_{\gamma,P}\ \delta_{K,P}\left[\rho^{(\gamma)}_P(x) + \text{h.c.}\right].
\end{aligned} \tag{2.13}$$

Here $\rho_P^{(\gamma)}(x)$ are the Fourier components of the low-energy projection of the density $n_{1,l} \pm n_{2,l}$, which arise from the external periodic potential (see Sec. 2.1.1 for a discussion of why such a potential may arise). These Fourier components are discussed in detail in Appendices 2.A and 2.B where we derive the form of the "$2k_F$" and "$4k_F$" components. In the ladder system, the $4k_F$ components of the density operator include the harmonics $S = \{2k_b + 2k_{ab},\ 4k_b,\ 4k_{ab},\ 3k_b + k_{ab},\ 3k_{ab} + k_b\}$ – we focus on the particular case of $P = 4k_b$ in this thesis ($P = 4k_{ab}$ follows similarly from an exchange of band indices). In Ref. [1] we also made some progress in understanding the $3k_b + k_{ab}$ and $3k_{ab} + k_b$ terms, which break the $\mathbb{Z}_2$ symmetry between the legs of the ladder. The "$4k_F$" Fourier components of the density operator are derived by performing a renormalisation group (RG) procedure on the density operator (integrating out high-energy degrees of freedom perturbatively in U) which we perform in Appendix 2.B. In terms of the currents, the density components are:

$$\begin{aligned}
\rho^{(+)}_{4k_b}(x) + \text{h.c.} &= \left(I^L_{11}\right)^\dagger I^R_{11} + \left(I^R_{11}\right)^\dagger I^L_{11}\ , \quad \rho^{(+)}_{4k_{ab}}(x) + \text{h.c.} = \left(I^L_{22}\right)^\dagger I^R_{22} + \left(I^R_{22}\right)^\dagger I^L_{22}\ , \\
\rho^{(+)}_{2k_b+2k_{ab}}(x) + \text{h.c.} &= 8\left\{\left(I^L_{12}\right)^\dagger I^R_{21} + \left(I^R_{21}\right)^\dagger I^L_{12}\right\}, \\
\rho^{(-)}_{k_b+3k_{ab}}(x) + \text{h.c.} &= 2\left\{\left(I^L_{22}\right)^\dagger I^R_{21} + \left(I^L_{21}\right)^\dagger I^R_{22} + \left(I^R_{22}\right)^\dagger I^L_{21} + \left(I^R_{21}\right)^\dagger I^L_{22}\right\}\ , \\
\rho^{(-)}_{3k_b+k_{ab}}(x) + \text{h.c.} &= 2\left\{\left(I^L_{11}\right)^\dagger I^R_{12} + \left(I^L_{12}\right)^\dagger I^R_{11} + \left(I^R_{11}\right)^\dagger I^L_{12} + \left(I^R_{12}\right)^\dagger I^L_{11}\right\}. \qquad (2.14)
\end{aligned}$$

The initial conditions for the coupling constants defined in (2.13) for the extended Hubbard model are

$$\begin{aligned}
\tilde{c}^\rho_{ii} &= U + V_\perp + 4V_\parallel\left[1 - \frac{1}{2}\cos(2k_i a_0)\right], \\
\tilde{c}^\rho_{ij} &= U - V_\perp + 4V_\parallel\left[\cos((k_b - k_{ab})a_0) - \frac{1}{2}\cos((k_b + k_{ab})a_0)\right], \\
\tilde{f}^\rho_{ij} &= U + 3V_\perp + 4V_\parallel\left[1 - \frac{1}{2}\cos((k_b + k_{ab})a_0)\right], \\
\tilde{c}^\sigma_{ii} &= U + V_\perp + 2V_\parallel\cos(2k_i a_0), \\
\tilde{f}^\sigma_{ij} &= \tilde{c}^\sigma_{ij} = U - V_\perp + 2V_\parallel\cos((k_b + k_{ab})a_0).
\end{aligned}$$

2.2.1.1 Bosonisation

To carry out our analysis in the band representation we will bosonise the Hamiltonian. We begin by briefly introducing the technique of bosonisation, starting from the

bosonisation identity and highlighting our conventions. We bosonise the fermion fields according to

$$R_{d,\sigma} \sim \frac{\kappa_{d,\sigma}}{\sqrt{2\pi a_0}} : e^{i\sqrt{4\pi}\varphi_{d,\sigma}} :, \quad L_{d,\sigma} \sim \frac{\kappa_{d,\sigma}}{\sqrt{2\pi a_0}} : e^{-i\sqrt{4\pi}\bar{\varphi}_{d,\sigma}} :, \quad d = 1, 2 = b, ab, \quad (2.15)$$

where : : denotes normal ordering, $\varphi_{d,\sigma}$ ($\bar{\varphi}_{d,\sigma}$) is the right (left) chiral component of a canonical boson field and $\{\kappa_{d,\sigma}, \kappa_{d',\sigma'}\} = 2\delta_{d,d'}\delta_{\sigma,\sigma'}$ are Klein factors to ensure the anti-commutation of different species of fermions. The bosonic fields obey the "infinite line" quantisation scheme which ensures the anti-commutation of fermions of the same species:

$$[\varphi_{d,\sigma}(x), \varphi_{d',\sigma'}(x')] = -[\bar{\varphi}_{d,\sigma}(x), \bar{\varphi}_{d',\sigma'}(x')] = \frac{i}{4}\mathrm{sgn}(x - x')\delta_{d,d'}\delta_{\sigma,\sigma'},$$

$$[\varphi_{d,\sigma}(x), \bar{\varphi}_{d',\sigma'}(x')] = \frac{i}{4}\delta_{d,d'}\delta_{\sigma,\sigma'} \ .$$

Normal ordering of the vertex operators is introduced to remove explicit divergences in system size L which arise in the thermodynamic limit. Normal ordered vertex operators multiply in the following manner:

$$: e^{i\alpha\varphi(x)} :: e^{i\beta\varphi(y)} :=: e^{i\alpha\varphi(x)}e^{i\beta\varphi(y)} : \left(\frac{ia_0}{x - y}\right)^{-\alpha\beta/4\pi},$$

where we've suppressed indices on the fields and we use that the two-point function of free bosonic fields is

$$\langle\varphi(x)\varphi(y)\rangle = -\frac{1}{4\pi}\log\left(\frac{x - y}{ia_0}\right) \ ,$$

which follows from the mode expansion of the bosonic fields. The vertex operators inside the normal ordering can now be combined using the Campbell-Baker-Hausdorff formula

$$e^A e^B = e^{A+B}e^{\frac{1}{2}[A,B]}, \qquad \text{if } [A, B] = \text{constant}.$$

Taking the expectation value of the normal ordered vertex operators, the zero-mode enforces $\alpha = -\beta$ and hence

$$\langle : e^{i\alpha\varphi(x)+i\beta\varphi(y)} : \rangle = \delta_{\alpha,-\beta}$$

It follows that the two-point function of normal-ordered vertex functions is given by

$$\langle : e^{i\alpha\varphi(x)} :: e^{i\beta\varphi(y)} : \rangle = \delta_{\alpha,-\beta}\left(\frac{ia_0}{x - y}\right)^{\frac{\alpha^2}{4\pi}},$$

and so the two-point functions of fermionic fields are recovered with $\alpha = \sqrt{4\pi}$ and rescaling the vertex operators by a factor $1/\sqrt{2\pi a_0}$, recovering the bosonisation identities (2.15).

When bosonising fermion bilinears, we employ the point-splitting procedure of quantum field theory, which we illustrate explicitly for the density operator (with indices suppressed)

$$\begin{aligned} R^\dagger(x)R(x) &= \lim_{\epsilon\to 0} R^\dagger(x+\epsilon)R(x-\epsilon) - \langle R^\dagger(x+\epsilon)R(x-\epsilon)\rangle \\ &= \lim_{\epsilon\to 0}\Big[\frac{1}{2\pi a_0} : e^{-i\sqrt{4\pi}\varphi(x+\epsilon)} :: e^{i\sqrt{4\pi}\varphi(x-\epsilon)} : + \frac{1}{2\pi i}\frac{1}{2\epsilon}\Big], \\ &= \lim_{\epsilon\to 0}\frac{i}{4\pi\epsilon}\Big[: e^{-i\sqrt{4\pi}(\varphi(x+\epsilon)-\varphi(x-\epsilon))} : -1\Big], \\ &= \lim_{\epsilon\to 0}\frac{i}{4\pi\epsilon}\Big[1 - 2i\epsilon\sqrt{4\pi} : \partial_x\varphi(x) : + \mathcal{O}(\epsilon^2) - 1\Big]. \end{aligned}$$

It is now safe to take the limit $\epsilon \to 0$ as the point-splitting procedure cancels the divergence and we obtain the bosonised expression for the density operator

$$R^\dagger(x)R(x) = \frac{1}{\sqrt{\pi}} : \partial_x\varphi(x) : \ .$$

2.2.1.2 Bosonisation of the band representation Hamiltonian

We bosonise the Hamiltonian (2.13) by direct use of the bosonisation identities (2.15) and application of the point-splitting procedure. Introducing new bosonic fields ("spin" and "charge" bosons) which are linear combinations of the previous fields

$$\begin{aligned} \Phi_{d,c} &= \frac{1}{\sqrt{2}}\left[\varphi_{d,\uparrow} + \varphi_{d,\downarrow} + \bar\varphi_{d,\uparrow} + \bar\varphi_{d,\downarrow}\right], \quad \Phi_{d,s} = \frac{1}{\sqrt{2}}\left[\varphi_{d,\uparrow} - \varphi_{d,\downarrow} + \bar\varphi_{d,\uparrow} - \bar\varphi_{d,\downarrow}\right], \\ \Theta_{d,c} &= \frac{1}{\sqrt{2}}\left[\varphi_{d,\uparrow} + \varphi_{d,\downarrow} - \bar\varphi_{d,\uparrow} - \bar\varphi_{d,\downarrow}\right], \quad \Theta_{d,s} = \frac{1}{\sqrt{2}}\left[\varphi_{d,\uparrow} - \varphi_{d,\downarrow} - \bar\varphi_{d,\uparrow} + \bar\varphi_{d,\downarrow}\right], \end{aligned} \tag{2.16}$$

where Φ and Θ are dual fields obeying $[\partial_x\Theta(x),\Phi(x')]=i\delta(x-x')$, we find that the resulting bosonised Hamiltonian is given by

$$\begin{aligned}
\mathcal{H}_0+\mathcal{H}_U &= \sum_{d=1}^{2} v_d \sum_{\gamma=c,s}\left[(\partial_x\Phi_{d,\gamma})^2+(\partial_x\Theta_{d,\gamma})^2\right]+\frac{\tilde{c}^{\rho}_{dd}}{8\pi}\left[(\partial_x\Phi_{d,c})^2-(\partial_x\Theta_{d,c})^2\right]\\
&+ \frac{\tilde{f}^{\rho}_{12}}{4\pi}\left[\partial_x\Phi_{1,c}\partial_x\Phi_{2,c}-\partial_x\Theta_{1,c}\partial_x\Theta_{2,c}\right]\\
&+ \sum_{d=1}^{2}\tilde{c}^{\sigma}_{dd}\left[\frac{1}{(2\pi a_0)^2}\cos\left(\sqrt{8\pi}\Phi_{d,s}\right)-\frac{1}{8\pi}\left[(\partial_x\Phi_{d,s})^2-(\partial_x\Theta_{d,s})^2\right]\right]\\
&+ 2\tilde{f}^{\sigma}_{12}\left[\frac{1}{(2\pi a_0)^2}\cos\left(\sqrt{2\pi}\big(\Phi_{1,s}+\Phi_{2,s}\big)\right)\cos\left(\sqrt{2\pi}\big(\Theta_{1,s}-\Theta_{2,s}\big)\right)\right.\\
&\qquad\left.-\frac{1}{8\pi}\Big(\partial_x\Phi_{1,s}\partial_x\Phi_{2,s}-\partial_x\Theta_{1,s}\partial_x\Theta_{2,s}\Big)\right]\\
&+ \left[\frac{\tilde{c}^{\rho}_{12}-\tilde{c}^{\sigma}_{12}}{(2\pi a_0)^2}\cos\left(\sqrt{2\pi}\big(\Theta_{1,s}-\Theta_{2,s}\big)\right)-\frac{\tilde{c}^{\rho}_{12}+\tilde{c}^{\sigma}_{12}}{(2\pi a_0)^2}\cos\left(\sqrt{2\pi}\big(\Phi_{1,s}-\Phi_{2,s}\big)\right)\right]\\
&\qquad\times\cos\left(\sqrt{2\pi}\big(\Theta_{1,c}-\Theta_{2,c}\big)\right)\\
&- \frac{2\tilde{c}^{\sigma}_{12}}{(2\pi a_0)^2}\cos\left(\sqrt{2\pi}\big(\Theta_{1,c}-\Theta_{2,c}\big)\right)\cos\left(\sqrt{2\pi}\big(\Phi_{1,s}+\Phi_{2,s}\big)\right)\,, \qquad (2.17)
\end{aligned}$$

where hereinafter we drop the explicit notation for normal ordering.

In the following, we will use a convenient notation for classifying the ground state phases of the ladder in terms of the spin and charge bosons (2.16). Following Ref. [66] we will classify phases by the number of spin and charge bosons which remain gapless: we use the notation $CmSn$ where m (n) is the number of gapless charge (spin) bosons.

2.2.2 The chain representation $t_\perp \ll t, U, t^2/U$

A detailed derivation of the field theory for the chain representation is given in Ref. [81], here we outline the succession of steps. We begin first by stating an important advantage of the chain representation: longer range density-density interactions along the chain

$$\sum_{j,l}\sum_{m\geq 2} V_{\parallel,m} n_{j,l} n_{j,l+m}\,, \qquad (2.18)$$

can be easily accommodated. Provided that $V_{\parallel,m}$ are decreasing with m and sufficiently small (to avoid pushing the system immediately into a ground state with translation symmetry broken by charge ordering) the main effect of the extended interactions is to decrease the Luttinger parameter in the charge sector K_c in (2.20) and (2.23). This will be a useful device for tuning K_c in the following.

The main assumption of the derivation is that the interchain hopping $t_\perp$ is small in comparison to the high-energy cutoffs, which for $V_\perp, V_\parallel \ll U$ are given by the single chain band-width and the exchange energy scale ($\sim t^2/U$ at large U). We start from two uncoupled chains $t_\perp = V_\perp = 0$ with no external potential $W_{1,2} = 0$; the Hamiltonian is bosonised using standard results for the one-dimensional (extended) Hubbard model [7, 11]. Provided that $V_\parallel$ is not too large, the resulting theory is the sum of four Gaussian models for the charge and spin bosons in each chain (we denote these fields by $\Phi_j^{(i)}$ with $i = c, s$ for charge/spin fields and $j = 1, 2$ labelling the chains).

We now proceed to add back in the interchain terms $V_\perp, t_\perp$ — to start we define the following symmetric/antisymmetric combinations of fields

$$\begin{aligned}\Phi_c &= \frac{1}{\sqrt{2}}(\Phi_1^{(c)} + \Phi_2^{(c)}), \quad \Phi_f = \frac{1}{\sqrt{2}}(\Phi_1^{(c)} - \Phi_2^{(c)}),\\ \Phi_s &= \frac{1}{\sqrt{2}}(\Phi_1^{(s)} + \Phi_2^{(s)}), \quad \Phi_{sf} = \frac{1}{\sqrt{2}}(\Phi_1^{(s)} - \Phi_2^{(s)}).\end{aligned} \tag{2.19}$$

In the absence of the periodic potential and away from commensurate fillings, the Φ_c fields completely decouples from all interactions (including those which couple the chains). The resulting sector of the theory is described by a Gaussian (Tomanaga-Luttinger) theory with Hamiltonian density

$$\mathcal{H}_c = \frac{v_c}{2}\Big[K_c(\partial_x\Theta_c)^2 + K_c^{-1}(\partial_x\Phi_c)^2\Big], \tag{2.20}$$

where Θ_c is the dual field to Φ_c, $K_c < 1$ is the Luttinger parameter in the charge sector and v_c is the charge velocity. Determining the value of the charge velocity v_c and the Luttinger parameter K_c from the microscopic parameters of the theory is very complicated, for $V_\parallel = 0$ these may be extracted from the exact solution of the one-dimensional Hubbard model [11, 83].

The remaining bosonic fields are split into their chiral components $\Phi_a = \phi_a + \bar{\phi}_a$, $\Theta_a = \phi_a - \bar{\phi}_a$, which are refermionised in terms of six Majorana fermion fields:

$$\begin{aligned}\chi_R^0 &= \frac{\kappa_{sf}}{\sqrt{\pi a_0}}\sin(\sqrt{4\pi}\phi_{sf}),\ \chi_R^3 = \frac{\kappa_{sf}}{\sqrt{\pi a_0}}\cos(\sqrt{4\pi}\phi_{sf}),\ \xi_R^3 = \frac{\kappa_f}{\sqrt{\pi a_0}}\sin(\sqrt{4\pi}\phi_f),\\ \chi_R^1 &= \frac{\kappa_s}{\sqrt{\pi a_0}}\sin(\sqrt{4\pi}\phi_s),\ \chi_R^2 = \frac{\kappa_s}{\sqrt{\pi a_0}}\cos(\sqrt{4\pi}\phi_s),\ \eta_R = \frac{\kappa_f}{\sqrt{\pi a_0}}\cos(\sqrt{4\pi}\phi_f)\ ,\end{aligned} \tag{2.21}$$

where κ_a are Klein factors fulfilling $\{\kappa_a, \kappa_b\} = 2\delta_{a,b}$. Analogous expressions for left moving Majorana fields hold with R replaced by L and ϕ by $\bar{\phi}$.

The interchain hopping $t_\perp$ induces a hybridisation of the η and χ^0 Majoranas: the quadratic part of the Hamiltonian for these fields becomes

$$H' = \sum_{k>0} \Big\{ v_c k \eta_R(k)^\dagger \eta_R(k) + v_s k \chi_R^{0\dagger}(k)\chi_R^0(k) + t_\perp \Big[\chi_R^{0\dagger}(k)\eta_R(k) + \eta_R^\dagger(k)\chi_R^0(k) \Big] \Big\}$$

for right movers (and similarly for left movers). Following Tsvelik [81] we perform the rotation of Majoranas that diagonalises this Hamiltonian and subsequently linearise the spectrum about $Q = t_\perp/\sqrt{v_c v_s}$ (where $E(Q) = 0$)

$$\begin{aligned}
\begin{pmatrix} \chi_R^0 \\ \eta_R \end{pmatrix} &= \sqrt{\frac{2}{v_s+v_c}} \begin{pmatrix} \sqrt{v_c}\cos(Qx) & \sqrt{v_c}\sin(Qx) \\ -\sqrt{v_s}\sin(Qx) & \sqrt{v_s}\cos(Qx) \end{pmatrix} \begin{pmatrix} \xi_R^1 \\ \xi_R^2 \end{pmatrix} , \\
\begin{pmatrix} \chi_L^0 \\ \eta_L \end{pmatrix} &= \sqrt{\frac{2}{v_s+v_c}} \begin{pmatrix} \sqrt{v_c}\cos(Qx) & -\sqrt{v_c}\sin(Qx) \\ \sqrt{v_s}\sin(Qx) & \sqrt{v_s}\cos(Qx) \end{pmatrix} \begin{pmatrix} \xi_L^1 \\ \xi_L^2 \end{pmatrix} .
\end{aligned} \tag{2.22}$$

Rewriting the Hamiltonian in terms of the new degrees of freedom, we obtain the low-energy "chain representation" Hamiltonian

$$\mathcal{H} = \mathcal{H}_c + \mathcal{H}_0 + \mathcal{V}_{\rm int} + \mathcal{H}_W, \tag{2.23}$$

$$\mathcal{H}_c = \frac{v_c}{2}\Big[K_c (\partial_x \Theta_c)^2 + K_c^{-1} (\partial_x \Phi_c)^2 \Big], \tag{2.24}$$

$$\begin{aligned}
\mathcal{H}_0 &= \frac{\mathrm{i}v_c}{2}(\xi_L^3 \partial_x \xi_L^3 - \xi_R^3 \partial_x \xi_R^3) + \frac{\mathrm{i}u}{2}\sum_{a=1,2}(\xi_L^a \partial_x \xi_L^a - \xi_R^a \partial_x \xi_R^a) \\
&\quad + \frac{\mathrm{i}v_s}{2}\sum_{a=1}^{3}(\chi_L^a \partial_x \chi_L^a - \chi_R^a \partial_x \chi_R^a) ,
\end{aligned} \tag{2.25}$$

$$\begin{aligned}
\mathcal{V}_{\rm int} &= -2(\xi_R^3 \xi_L^3)\Big[g_{\sigma,-}(\chi_R^a \chi_L^a) + g_{c,ss}(\xi_R^1 \xi_L^1 - \xi_R^2 \xi_L^2) \Big] - g_{\rho,-}(\xi_R^1 \xi_L^1 - \xi_R^2 \xi_L^2)^2 \\
&\quad - 2g_{c,st}(\xi_R^1 \xi_L^1 - \xi_R^2 \xi_L^2)\sum_{a=1}^{3}(\chi_R^a \chi_L^a) - 2g_{\sigma,+}\sum_{a>b,a,b=1}^{3}(\chi_R^a \chi_L^a)(\chi_R^b \chi_L^b) ,
\end{aligned} \tag{2.26}$$

$$\mathcal{H}_W = \sum_{P\in S}\sum_{\sigma=\pm} W_{\sigma,P}\ \delta_{K,P}\left[\rho_P^{(\sigma)}(x) + \text{h.c.} \right]. \tag{2.27}$$

Here $S = \{4k_F, 4k_F \pm Q, 4k_F \pm 2Q\}$ and $u = 2v_c v_s/(v_s+v_c)$. The low-energy projection of the periodic potential induces the Fourier components of the density which are

derived in Appendix 2.B.1 and are given by

$$\rho^{(+)}_{4k_F}(x) \sim \frac{\mathrm{i}F}{2} e^{i\sqrt{4\pi}\Phi_c}\left\{\xi^3_R\xi^3_L + \frac{v_s}{(v_s+v_c)}[\xi^1_R\xi^1_L - \xi^2_R\xi^2_L]\right\}, \tag{2.28}$$

$$\rho^{(+)}_{4k_F\pm 2Q}(x) \sim \frac{\pm i v_s F}{2(v_s+v_c)} e^{i\sqrt{4\pi}\Phi_c}\,(\xi^1_R \mp \mathrm{i}\xi^2_R)(\xi^1_L \pm \mathrm{i}\xi^2_L)\,, \tag{2.29}$$

$$\rho^{(-)}_{4k_F\pm Q}(x) = -iF\sqrt{\frac{v_s}{2\,(v_s+v_c)}} e^{i\sqrt{4\pi}\Phi_c}\left[\left(\xi^1_R \mp i\xi^2_R\right)\xi^3_L + \xi^3_R\left(\xi^1_L \pm i\xi^2_L\right)\right], \tag{2.30}$$

and we note that $\rho^{(+)}_{4k_F}(x)$ and $\rho^{(+)}_{4k_F\pm 2Q}(x)$ are even under interchange of the chain indices, while $\rho^{(-)}_{4k_F\pm Q}(x)$ are odd.

As required, the Hamiltonian $\mathcal{H}_c + \mathcal{H}_0 + \mathcal{V}_{\rm int}$ has the same symmetry $U(1) \times SU(2) \times \mathbb{Z}_2$ as the underlying lattice model for $W_{1,2} = 0$. The coupling parameters of the continuum Hamiltonian are determined by the underlying lattice model (2.5)

$$\begin{aligned} g_{\sigma-} &= \frac{\alpha_0 V_\perp}{2}, \qquad g_{\sigma+} = \frac{1}{2}\pi v_s g_\lambda, \qquad g_{c,ss} = u\left(\frac{\alpha_0}{v_s}V_\perp - 2g_k\right), \\ g_{c,st} &= u\left(\frac{\alpha_0}{v_c}V_\perp + \pi g_\lambda\right), \qquad g_{\rho,-} = \frac{v_s v_c}{(v_s+v_c)^2}\alpha_0 V_\perp, \end{aligned} \tag{2.31}$$

where α_0 is a short-distance cut-off, g_k characterises the four-fermion interaction in the Φ_f sector, which for $|K_c - 1| \ll 1$ is given by $g_k \approx 2\pi\,(1/K_c - 1)$, and g_λ is the strength of the marginally irrelevant spin-current interaction for a single extended Hubbard chain, which is known only for small U and $V_\parallel$.

The notable differences between the chain representation and the band representation (see the previous subsection) is the presence of several different velocities $v_c \neq v_s \neq u$; for large intrachain interactions these differences can be significant. The low-energy projection of the periodic potential for the two complementary field theory limits has the following correspondence:

$$\begin{aligned} &4k_F + 2Q \leftrightarrow 4k_b\,, \qquad 4k_F + Q \leftrightarrow 3k_b + k_{ab}\,, \qquad 4k_F \leftrightarrow 2(k_b + k_{ab})\,, \\ &4k_F - 2Q \leftrightarrow 4k_{ab}\,, \qquad 4k_F - Q \leftrightarrow 3k_{ab} + k_b\,. \end{aligned} \tag{2.32}$$

2.3 Effect of the $4k_b$ umklapp term

In this section we consider the $4k_b$ umklapp scattering process, which may be activated by commensurate filling of the bonding band [66] or at generic fillings for an applied external potential modulated at $4k_b$ (see Sec. 2.1.1). In the following, we analyse the

band and chain limit of (2.5) in turn and discuss the zero-temperature phase diagram. Our main result of this analysis is the existence of a pair density wave phase, similar in form to the unusual superconducting phase of the Kondo-Heisenberg model discussed in Sec. 2.1.2.

2.3.1 Band representation

In the band representation, we use that the interaction parameters $U, V_j \ll t$ and we approach the problem through the one-loop perturbative renormalisation group. In the following we derive the one-loop RG equations in the presence of the $4k_b$ umklapp term and we proceed to integrate these equations. We obtain the fixed point low-energy effective theory and analyse its phase diagram.

2.3.1.1 The one-loop renormalisation group equations

We begin by illustrating the procedure for deriving the one-loop RG equations. To derive the RG equations we will make use of the *operator product expansion* (OPE) for the fermion operators:

$$R_{i,\sigma}(x,\tau)R^{\dagger}_{j,\sigma'}(0,0) \sim \frac{\delta_{i,j}\delta_{\sigma,\sigma'}}{2\pi z_i}, \qquad L_{i,\sigma}(x,\tau)L^{\dagger}_{j,\sigma'}(0,0) \sim \frac{\delta_{i,j}\delta_{\sigma,\sigma'}}{2\pi \bar{z}_i}, \tag{2.33}$$

where $z_j = v_j\tau - ix$ and $\bar{z}_j = v_j\tau + ix$. Here $\sim$ signifies that we show only the singular terms of the expansion.

The one-loop RG equations are derived in the following manner (cf. Ref. [61]):

1. We begin by considering the action S_0 of the non-interacting theory perturbed by a set of operators to form the full action $S = S_0 + \sum_a g_a \int \mathrm{d}x\mathrm{d}\tau\ \mathcal{O}_a(x,\tau)$.

2. We then partition space-time into tiles of size $\ell \times \ell$ and average over the coordinates within the tile to obtain tile degrees of freedom. The effective action for these new "long-wavelength" degrees of freedom is then obtained by expanding the partition function:

$$e^{-S_{\text{eff}}} \approx e^{-S_0}\Big\{1 - \sum_a g_a \int \mathrm{d}\mathbf{x}\langle\mathcal{O}_a(\mathbf{x})\rangle_> + \frac{1}{2}\sum_{a,b} g_a g_b \iint \mathrm{d}\mathbf{x}\mathrm{d}\mathbf{x}'\langle\mathcal{O}_a(\mathbf{x})\mathcal{O}_b(\mathbf{x}')\rangle_> + \dots\Big\} \tag{2.34}$$

where $\langle\dots\rangle_>$ denotes averaging over the short distance degrees of freedom.

3. The first order term is given by dimensional analysis:

$$-\sum_a g_a \int \mathrm{d}\mathbf{x} \langle \mathcal{O}_a(\mathbf{x}) \rangle_> = -\sum_a g_a \ell^{2-\Delta_i} \int \mathrm{d}\mathbf{X}\ \mathcal{O}_a(\mathbf{X}), \tag{2.35}$$

where Δ_a is the scaling dimension of the operator $\mathcal{O}_a(\mathbf{x})$ and $\mathbf{X}$ is the coordinate of the tile degrees of freedom.

4. The second order term will be dominated by the most singular terms in the averaging procedure: these are given by the OPE. In the expectation value we make the replacement

$$\langle \mathcal{O}_a(\mathbf{x}) \mathcal{O}_b(\mathbf{x}') \rangle_> = \sum_d \frac{c_{ab}^d \langle \mathcal{O}_d(\mathbf{x}') \rangle_>}{|\mathbf{x}-\mathbf{x}'|^{\Delta_a+\Delta_b-\Delta_d}},$$

where c_{ab}^d are c-numbers. Dimensional analysis gives Eq. (2.35) and

$$\iint \mathrm{d}\mathbf{x}\mathrm{d}\mathbf{x}' \frac{1}{|\mathbf{x}-\mathbf{x}'|^{\Delta_a+\Delta_b-\Delta_d}} \sim \begin{cases} \ell^{2-\Delta_a-\Delta_b+\Delta_d} & \text{if } 2-\Delta_a-\Delta_b+\Delta_d \neq 0 \\ \log(\ell) & \text{otherwise.} \end{cases}$$

5. Inserting these expressions into the expansion (2.34) and collecting terms we define the renormalised coupling:

$$g_a' = g_a \ell^{2-\Delta_a} - \frac{1}{2} \sum_{b,d} g_b g_d c_{bd}^a \begin{cases} \ell^{2-\Delta_b-\Delta_d+\Delta_a} \\ \log(\ell) \end{cases} \ell^{2-\Delta_a},$$

where ℓ is the new lattice spacing. Taking the limit $\ell \to 1$ recovers the infinitesimal transformation. In this limit, if $\Delta_a \neq 2$ the first term dominates and we get (for $\ell = e^L$, $L \to 0$)

$$\frac{\mathrm{d}g_a}{\mathrm{d}L} = (2-\Delta_a) g_a,$$

the generic RG flow for relevant ($\Delta_a < 2$) and irrelevant ($\Delta_a > 2$) perturbations.

6. For the marginal case of $\Delta_a = 2$, which is the case for all four-fermion interaction terms (as the naïve scaling dimension of a fermion in 1+1D is $\frac{1}{2}$), we get

$$\frac{\mathrm{d}g_a}{\mathrm{d}L} = -\frac{1}{2} \sum_{b,d} c_{bd}^a g_b g_d,$$

which is the one-loop RG equation for the interaction parameter g_a.

7. We note that the set of operators $\mathcal{O}_a(\mathbf{x})$ generally do not form a closed algebra and additional operators maybe generated under the RG procedure (from the above, these must be second order in the couplings g_a).

2.3.1.2 Renormalisation group flow and low energy effective theory

In the field theory limit the $4k_b$ umklapp term becomes

$$\mathcal{H}_W = \frac{\tilde{u}^\rho_{11}}{2}\left[(I^L_{11})^\dagger I^R_{11} + (I^R_{11})^\dagger I^L_{11}\right] = -\frac{u^\rho_{11}}{(2\pi a_0)^2}\cos\left(\sqrt{8\pi}\Phi_{1,c}\right).$$

Following the procedure outlined above, we obtain the full one-loop RG equations in the presence of the $4k_b$ umklapp term. In the notations of Refs. [79, 82], these are

$$\begin{aligned}
\dot{c}^\rho_{11} &= -\frac{\alpha_1}{4}\left[(c^\rho_{12})^2 + 3(c^\sigma_{12})^2\right] + \left(u^\rho_{11}\right)^2 , \\
\dot{c}^\rho_{12} &= -\frac{1}{4}\left[c^\rho_{12}(c^\rho_{11} + c^\rho_{22}) + 3c^\sigma_{12}(c^\sigma_{11} + c^\sigma_{22})\right] + \frac{1}{2}\left[c^\rho_{12}f^\rho_{12} + 3c^\sigma_{12}f^\sigma_{12}\right] , \\
\dot{c}^\rho_{22} &= -\frac{\alpha_1}{4}\left[(c^\rho_{21})^2 + 3(c^\sigma_{21})^2\right] , \\
\dot{c}^\sigma_{dd} &= -(c^\sigma_{dd})^2 - \frac{\alpha_1}{2}c^\sigma_{12}(c^\rho_{12} + c^\sigma_{12}) , \quad (\text{for } d = 1, 2) \\
\dot{c}^\sigma_{12} &= -\frac{1}{4}\left[(c^\rho_{11} + c^\rho_{22})c^\sigma_{12} + (c^\rho_{12} + 2c^\sigma_{12})(c^\sigma_{11} + c^\sigma_{22})\right] + \frac{1}{2}\left[c^\rho_{12}f^\sigma_{12} + c^\sigma_{12}f^\rho_{12} - 2c^\sigma_{12}f^\sigma_{12}\right] , \\
\dot{f}^\rho_{12} &= \frac{1}{4}\left[(c^\rho_{12})^2 + 3(c^\sigma_{12})^2\right] , \\
\dot{f}^\sigma_{12} &= -(f^\sigma_{12})^2 + \frac{1}{2}c^\sigma_{12}(c^\rho_{12} - c^\sigma_{12}) , \\
\dot{u}^\rho_{11} &= c^\rho_{11}\, u^\rho_{11},
\end{aligned} \tag{2.36}$$

where $\alpha_1 = (v_1 + v_2)^2/(4v_1v_2)$ and the coupling constants have been rescaled by $\tilde{g}_{ij} = g_{ij}\pi(v_1+v_2)$. Equations (2.36) agree with the RG equations reported by Balents and Fisher in Ref. [66] up to a factor of 2 in the equation for u^ρ_{11}.

Further progress is made by numerically integrating these equations. We consider the case when the umklapp interaction arises from commensurate filling of the bonding band, which corresponds to some particular doping of the extended Hubbard ladder. We further restrict ourselves to discussing (sufficiently) small values of $V_\perp/U$ and $V_\parallel/U$ such that translational invariance of the system is not broken by forced charge ordering. Under these restrictions, we observe that the numerical integration of Eqs. (2.36) gives

$$c^\rho_{11}, u^\rho_{11} \to \infty, \quad \text{with} \quad c^\rho_{11}/u^\rho_{11} \to 1,$$

whilst all other couplings remain small (their ratios to c^ρ_{11} vanish).

The fixed point of the RG flow is particularly amenable to further study as the coupling constants which flow to strong coupling are solely within the bonding charge

$(1,c)$ sector of the Hamiltonian (2.17). The RG flow causes the $\Phi_{1,c}$ boson to become massive: the umklapp term pins the bosonic field to its minima $\Phi_{1,c}^{(0)} = 0$ and small fluctuations $\delta\Phi_{1,c}$ about this pinned value appear as quadratic terms:

$$-\frac{u_{11}^{\rho}}{(2\pi a_0)^2}\cos[\sqrt{8\pi}(\Phi_{1,c}^{(0)}+\delta\Phi_{1,c})] \approx -\frac{u_{11}^{\rho}}{(2\pi a_0)^2} + \tilde{m}(\delta\Phi_{1,c})^2 \ .$$

We now employ two-cutoff scaling [7], where we integrate out the massive boson $\Phi_{1,c}$ and its disordered dual field $\Theta_{1,c}$ perturbatively in the remaining small parameters. We obtain an effective action by expanding the partition function to second order in the small couplings

$$S_{\rm eff} \approx \tilde{S}_0 + \langle \tilde{S}_{\rm int}\rangle_{1,c} - \frac{1}{2}\left[\langle \tilde{S}_{\rm int}^2\rangle_{1,c} - \langle \tilde{S}_{\rm int}\rangle_{1,c}^2\right] + \ldots,$$

with

$$\langle \mathcal{O}\rangle_{1,c} \;=\; \int \mathcal{D}\Phi_{1,c}\; e^{-S_{1,c}}\; \mathcal{O},$$

$$\begin{aligned} S_{1,c} \;=\; \int \mathrm{d}x\mathrm{d}\tau \Bigg\{ &\left(1+\frac{c_{11}^{\rho}}{8\pi v_1}\right)\left[v_1\left(\partial_x\Phi_{1,c}\right)^2 + \frac{1}{v_1}\left(\partial_\tau\Phi_{1,c}\right)^2\right] \\ &-\frac{u_{11}^{\rho}}{(2\pi a_0)^2}\cos\sqrt{8\pi}\Phi_{1,c}\Bigg\}, \end{aligned}$$

$$\begin{aligned} \tilde{S}_{\rm int} \;=\; \int dx d\tau \Bigg\{ &\frac{f_{12}^{\rho}}{4\pi}\left[\partial_x\Phi_{1,c}\partial_x\Phi_{2,c} + \frac{1}{v_1 v_2}\partial_\tau\Phi_{1,c}\partial_\tau\Phi_{2,c}\right] \\ &+\frac{c_{12}^{\rho}-c_{12}^{\sigma}}{(2\pi a_0)^2}\cos\left(\sqrt{2\pi}\left(\Theta_{1,c}-\Theta_{2,c}\right)\right)\ \cos\left(\sqrt{2\pi}\left(\Theta_{1,s}-\Theta_{2,s}\right)\right) \\ &-\frac{c_{12}^{\rho}+c_{12}^{\sigma}}{(2\pi a_0)^2}\cos\left(\sqrt{2\pi}\left(\Theta_{1,c}-\Theta_{2,c}\right)\right)\ \cos\left(\sqrt{2\pi}\left(\Phi_{1,s}-\Phi_{2,s}\right)\right) \\ &-2\frac{c_{12}^{\sigma}}{(2\pi a_0)^2}\cos\left(\sqrt{2\pi}\left(\Theta_{1,c}-\Theta_{2,c}\right)\right)\ \cos\left(\sqrt{2\pi}\left(\Phi_{1,s}+\Phi_{2,s}\right)\right)\Bigg\}, \end{aligned}$$

and $\tilde{S}_0$ describes all other terms in the action which do not feature $1,c$ bosons.

The action for $S_{1,c}$ is an effective sine-Gordon model [7] and we use that $\langle\Phi_{1,c}\rangle_{1,c} = 0$ and the two-point functions obey:

$$\begin{aligned} \left\langle e^{i\beta\Theta_{1,c}(\tau,x)}e^{-i\beta'\Theta_{1,c}(\tau',x')}\right\rangle_{1,c} &\propto \delta_{\beta,\beta'}e^{-r_1/\xi}, \\ \langle\partial_y\Phi_{1,c}(\tau,x)\partial_{y'}\Phi_{1,c}(\tau',x')\rangle_{1,c} &\propto \partial_y\partial_{y'}\frac{e^{-2r_1/\xi}}{(2r_1/\xi)^2}, \\ \left\langle\partial_y\Phi_{1,c}(\tau,x)e^{-i\beta'\Theta_{1,c}(\tau',x')}\right\rangle_{1,c} &= 0, \end{aligned}$$

where $y = x, v_1\tau$ and $r_1^2 = v_1^2(\tau-\tau')^2 + (x-x')^2$. The first expression follows from the ordering of $\Phi_{1,c}$: the dual field becomes disordered and decays exponentially. The second relation follows from the $(1,c)$ boson becoming massive under the RG flow. For all other operator product expansions we use those of the corresponding Gaussian models (which is valid due to all other couplings having ratios with c_{11}^{ρ} which vanish).

Following integrating out the $(1,c)$ boson to second order in the perturbative expansion, we obtain a low-energy (at energies much below the mass gap of the $(1,c)$ boson) effective Hamiltonian density

$$\begin{aligned}
\mathcal{H}_{\text{eff}} &= \bar{v}_2 \left[\frac{1}{K_{2,c}} \left(\partial_x \Phi_{2,c}\right)^2 + K_{2,c} \left(\partial_x \Theta_{2,c}\right)^2 \right] + \sum_{d=1}^{2} \frac{\bar{v}_d}{2\pi} \left[\left(\partial_x \Phi_{d,s}\right)^2 + \left(\partial_x \Theta_{d,s}\right)^2 \right] \\
&+ \bar{c}_{dd}^{\sigma} \left[\frac{1}{(2\pi a_0)^2} \cos\left(\sqrt{8\pi}\Phi_{d,s}\right) - \frac{1}{8\pi} \left[\left(\partial_x \Phi_{d,s}\right)^2 - \left(\partial_x \Theta_{d,s}\right)^2 \right] \right] \\
&+ 2\bar{f}_{12}^{\sigma} \left[\frac{1}{(2\pi a_0)^2} \cos\left(\sqrt{4\pi}\Phi_{+,s}\right) \cos\left(\sqrt{4\pi}\Theta_{-s}\right) \right. \\
&\qquad \left. - \frac{1}{8\pi} \left(\partial_x \Phi_{1,s} \partial_x \Phi_{2,s} - \partial_x \Theta_{1,s} \partial_x \Theta_{2,s} \right) \right] \\
&+ \lambda \cos\left(\sqrt{4\pi}\Phi_{-,s}\right) \cos\left(\sqrt{4\pi}\Theta_{-,s}\right), \qquad (2.37)
\end{aligned}$$

where $\Phi_{\pm,s} = (\Phi_{1,s} \pm \Phi_{2,s})/\sqrt{2}$ (and similarly for $\Theta_{\pm,s}$) and λ is a coupling constant generated in the RG procedure, which is second order in the remaining small couplings. The λ term carries conformal spin and as a result only has minor effects at weak coupling [72].

The structure of the low-energy effective field theory $\mathcal{H}_{\text{eff}}$ is the same as for the Kondo-Heisenberg model (see Eqs. (2.3)). At first this may seem surprising, given our discussion of the KHM in Sec. 2.1.2 where we study a ladder with inequivalent legs. However, in the above effective theory, the role of the legs in the KHM (2.3) is played by the bands: if we think only in terms of the bands, we have a very natural "two-leg ladder" with inequivalent legs. Commensurate filling of the bonding band plays the same part as the half-filling of one of the legs of the ladder in the KHM and the low-energy effective theories (2.3) and (2.37) have the same structure.

Having recovered the low-energy structure of the KHM, we therefore take over the RG analysis of [84] in order to infer the phase diagram. In the KHM with non-interacting 1DEG there are two distinct phases: with ferromagnetic across-rung exchange the RG flow is to weak coupling and a $C1S2$ fixed point described by a

three-component Luttinger liquid for the $\Phi_{2,c}$, $\Phi_{1,s}$ and $\Phi_{2,s}$ bosons. On the other hand, antiferromagnetic across-rung interactions result in RG flow towards strong coupling, where a spin gap opens in both the bands and the remaining charge degree of freedom is massless, a $C1S0$ phase. Which of these phases is realised (and the exact details of the predominant fluctuations) depends on the values of the bare parameters $U, V_\parallel/U$ and $V_\perp/U$.

We will discuss the $C1S2$ and $C1S0$ phases in detail, following a discussion of the order parameters in which we will be interested.

2.3.1.3 Order parameters

Here we define the lattice order parameters in which we will be interested:
(1) The bonding charge density wave (bCDW) order parameter

$$\mathcal{O}_{\mathrm{bCDW}}(n) = \frac{1}{2}\sum_{\sigma=\uparrow,\downarrow}\left(a^\dagger_{1,n,\sigma} + a^\dagger_{2,n,\sigma}\right)\left(a_{1,n,\sigma} + a_{2,n,\sigma}\right). \tag{2.38}$$

(2) The charge density wave (CDW) order parameter

$$\mathcal{O}_{\mathrm{CDW}}(n) = \sum_{\sigma=\uparrow,\downarrow} a^\dagger_{1,n,\sigma}a_{1,n,\sigma} + a^\dagger_{2,n,\sigma}a_{2,n,\sigma}. \tag{2.39}$$

(3) The d–wave superconductivity (SCd) order parameter

$$\mathcal{O}_{\mathrm{SCd}}(n) = a_{1,n,\uparrow}a_{2,n,\downarrow} + a_{2,n,\uparrow}a_{1,n,\downarrow}. \tag{2.40}$$

(4) The antibonding pairing (abP) order parameter

$$\mathcal{O}_{\mathrm{abP}}(n) = (a^\dagger_{1,n,\uparrow} - a^\dagger_{2,n,\uparrow})(a^\dagger_{1,n+1,\downarrow} - a^\dagger_{2,n+1,\downarrow}) - (a^\dagger_{1,n,\downarrow} - a^\dagger_{2,n,\downarrow})(a^\dagger_{1,n+1,\uparrow} - a^\dagger_{2,n+1,\uparrow}). \tag{2.41}$$

2.3.1.4 The $C1S2$ Phase

From numerical integration of the RG equations (2.36) with extended Hubbard model initial conditions (2.15) at half-filling of the bonding band, we observe that the RG flow is to the $C1S2$ phase provided the coupling $\check{f}^\sigma_{12} > 0$, where $\check{f}^\sigma_{12}$ is the coupling after the two cut-off RG scheme. When $V_\parallel/U$ and $V_\perp/U$ are sufficiently small we find $f^\sigma_{12} > 0$ quite generally after integrating the RG equations. We assume that this also holds for $\check{f}^\sigma_{12}$, as it is only modified at second order by the two-cutoff procedure.

Hubbard model initial conditions ($V_{\parallel} = V_{\perp} = 0$) have RG flow that is *always* towards weak coupling, as discussed by Balents and Fisher [66].

At low energies, the $C1S2$ fixed point is governed by the Gaussian Hamiltonian

$$\begin{aligned}\mathcal{H}_{C1S2} &= \tilde{v}_2 \left[\frac{1}{\tilde{K}_{2,c}} \left(\partial_x \Phi_{2,c}\right)^2 + \tilde{K}_{2,c} \left(\partial_x \Theta_{2,c}\right)^2 \right] \\ &\quad + \sum_{d=1}^{2} \tilde{v}_d \left[\frac{1}{\tilde{K}_{d,s}} \left(\partial_x \Phi_{d,s}\right)^2 + \tilde{K}_{d,s} \left(\partial_x \Theta_{d,s}\right)^2 \right] ,\end{aligned}$$

where the spin Luttinger parameters $\tilde{K}_{d,s} = 1$ if $SU(2)$ symmetry is preserved. The calculation of correlation functions follows from bosonising the order parameters (see e.g. Sec. 1.1.3.2) bearing in mind that the $(1, c)$ boson is massive, so the correlation functions of e.g. the bCDW order parameter (2.38) decay exponentially (at $2k_F$).

2.3.1.5 The $C1S0$ Phase

Using the interpretation of (2.37) as the low-energy limit of a KHM, there is a second parameter regime, namely the one corresponding to *antiferromagnetic* exchange interaction between the spin chain and the 1DEG. Here it is known that the RG flow is towards a strong coupling phase in which both spin bosons become gapped [72]. This phase occurs when $\check{f}_{12}^{\sigma} < 0$. Following the same arguments as in the $C1S2$ case, we conclude that the resulting $C1S0$ phase occurs when $V_{\parallel}/U$, $V_{\perp}/U$ are sufficiently large. In other words, the Coulomb interactions should not be screened too strongly in order for the $C1S0$ phase to exist.

As the strong coupling phase is physically the most interesting, we now turn to characterising the properties of this phase. Here we are guided by the existing field theory [72, 73] and numerical [73] studies of the KHM. We know, in particular, that the KHM exhibits unconventional finite wave vector pairing (see the discussion of Sec. 2.1.2). The strong coupling phase is characterised by [72]

$$\langle \cos\left(\sqrt{8\pi}\Phi_{1,c}\right)\rangle \neq 0 \ , \quad \langle \cos\left(\sqrt{4\pi}\Phi_{+,s}\right)\rangle \neq 0 \ , \quad \langle \cos\left(\sqrt{4\pi}\Theta_{-,s}\right)\rangle \neq 0. \tag{2.42}$$

Concomitantly $\Theta_{1,c}$, $\Theta_{+,s}$ and $\Phi_{-,s}$ are fluctuating fields, i.e. one-point functions of vertex operators of these fields vanish and (appropriate) two-point functions decay exponentially. This follows from the canonical commutation relations which exist between the field Φ and its dual field Θ: $[\partial_x \Theta(x), \Phi(x')] = i\delta(x - x')$.

Using that the above expectation values are non-zero and that there is only a single remaining gapless degree of freedom, the $\Phi_{2,c}$ boson, we can establish the dominant quasi-long-range order in the $C1S0$ phase. To this end we study the order parameters defined in Sec. 2.3.1.3 and proceed by bosonising them:

(1) bonding charge density wave (bCDW)

$$\mathcal{O}_{\mathrm{bCDW}}(x) \sim a_0 \sqrt{\frac{2}{\pi}} \partial_x \Phi_{1,c} - \frac{1}{\pi} \sin(2k_b x + \sqrt{2\pi}\Phi_{1,c}) \cos(\sqrt{2\pi}\Phi_{1,s}) + \dots$$

(2) charge density wave (CDW)

$$\begin{aligned} \mathcal{O}_{\mathrm{CDW}}(n) \sim\ & a_0 \sqrt{\frac{2}{\pi}} \partial_x (\Phi_{1,c} + \Phi_{2,c}) - \frac{1}{\pi} \cos\left(\sqrt{2\pi}\Phi_{1,s}\right) \sin\left(2k_b x + \sqrt{2\pi}\Phi_{1,c}\right) \\ & - \frac{1}{\pi} \cos\left(\sqrt{2\pi}\Phi_{2,s}\right) \sin\left(2k_{ab} x + \sqrt{2\pi}\Phi_{2,c}\right) + \\ & + \mathcal{A} e^{i\sqrt{2\pi}(\Phi_{1,c}+\Phi_{2,c})} \cos\left(\sqrt{4\pi}\Theta_{-,s}\right) \cos\left(2(k_{ab}+k_b)x\right) + \dots \end{aligned}$$

where $\mathcal{A}$ is an amplitude which vanishes in the $U \to 0$ limit. We derive the interaction induced term for the CDW operator in Appendix 2.B. Using that certain bosonic fields become pinned (2.42), the leading contribution in the $C1S0$ phase is

$$\mathcal{O}_{\mathrm{CDW}}(n)\Big|_{C1S0} \sim \tilde{\mathcal{A}} \cos\left(2(k_b + k_{ab})n\right) e^{i\sqrt{2\pi}\Phi_{2,c}} + \dots$$

(3) d-wave superconductivity (SCd)

$$\begin{aligned} \mathcal{O}_{\mathrm{SCd}}(n) \sim\ & 2e^{i\sqrt{2\pi}\Theta_{1,c}} \cos(\sqrt{2\pi}\Phi_{1,s}) - 2e^{i\sqrt{2\pi}\Theta_{2,c}} \cos(\sqrt{2\pi}\Phi_{2,s}) \\ & + 2e^{i\sqrt{2\pi}\Theta_{1,c}} \cos\left(2k_b x + \sqrt{2\pi}\Phi_{1,c}\right) - 2e^{i\sqrt{2\pi}\Theta_{2,c}} \cos\left(2k_{ab} x + \sqrt{2\pi}\Phi_{2,c}\right) + \dots \end{aligned}$$

(4) antibonding pairing (abP)

$$\begin{aligned} \mathcal{O}_{\mathrm{abP}}(n) \sim\ & \mathcal{A}_0 e^{-i\sqrt{2\pi}\Theta_{2,c}} \left[\cos\left(2k_{ab}(x + \frac{a_0}{2}) + \sqrt{2\pi}\Phi_{2,c}\right) + \cos\left(\sqrt{2\pi}\Phi_{2,s}\right) \sin(k_{ab} a_0)\right] \\ & + e^{i\sqrt{2\pi}\Theta_{2,c}} \Bigg\{ \left[\mathcal{C}_1 \cos\left(\sqrt{4\pi}\Phi_{+,s}\right) - \mathcal{C}_3 \cos\left(\sqrt{4\pi}\Theta_{-,s}\right)\right] \cos\left(\sqrt{2\pi}\Phi_{1,c} + 2k_b x\right) + \\ & \left[\mathcal{C}_2 \cos\left(\sqrt{4\pi}\Phi_{+,s}\right) - \mathcal{C}_4 \cos\left(\sqrt{4\pi}\Theta_{-,s}\right)\right] \sin\left(\sqrt{2\pi}\Phi_{1,c} + 2k_b x\right) \Bigg\} + \dots \end{aligned} \tag{2.43}$$

where the amplitudes $\mathcal{C}_a$ vanish in the $U \to 0$ limit. The interaction induced contribution to (2.43) is derived in Appendix 2.C. Once again, we can use that certain

bosonic fields become pinned to find the leading contribution in the $C1S0$ phase

$$\mathcal{O}_{\mathrm{abP}}(n)\Big|_{C1S0} \sim (-1)^n \tilde{\mathcal{C}} e^{i\sqrt{2\pi}\Theta_{2,c}} + \dots \tag{2.44}$$

The bosonised form (2.44) of $\mathcal{O}_{\mathrm{abP}}(n)$ coincides with the PDW order parameter identified by Berg *et al.* in the low-energy description of the KHM [73], and with the analogous order parameter $\mathcal{O}_{\mathrm{PDW}}$ proposed by Jaefari and Fradkin for the doped two-leg ladder [76].

Using the above expressions for the bosonised order parameters and Eqs. (2.42), we find the long-distance asymptotics of two-point functions in the $C1S0$ phase

$$\begin{aligned}
\langle \mathcal{O}_{\mathrm{CDW}}(x)\ \mathcal{O}^{\dagger}_{\mathrm{CDW}}(0)\rangle &\propto x^{-2} + \cos\left(2(k_b+k_{ab})x\right)\frac{\mathcal{A}}{|x|^{K_{2,c}}} + \dots, \\
\langle \mathcal{O}_{\mathrm{bCDW}}(x)\ \mathcal{O}^{\dagger}_{\mathrm{bCDW}}(0)\rangle &\propto e^{-|x|/\xi_b}\ \ (\text{at } 2k_b) + \dots, \\
\langle \mathcal{O}_{\mathrm{SCd}}(x)\ \mathcal{O}^{\dagger}_{\mathrm{SCd}}(0)\rangle &\propto \cos(2k_{ab}x)\frac{1}{|x|^{K_{2,c}}}\frac{1}{|x|^{1/K_{2,c}}} + \dots\ , \\
\langle \mathcal{O}_{\mathrm{abP}}(x)\ \mathcal{O}^{\dagger}_{\mathrm{abP}}(0)\rangle &\propto \frac{(-1)^{x/a_0}}{|x|^{1/K_{2,c}}} + \dots\ ,
\end{aligned} \tag{2.45}$$

where ξ_b is correlation length for the bonding charge boson and $K_{2,c}$ is the Luttinger parameter for the charge sector of the antibonding band.

Unlike the Kondo-Heisenberg model discussed in Sec. 2.1.2 (with a non-interacting 1DEG), we find that we have two different regimes within the $C1S0$ phase:

1. $K_{2,c} < 1$

   For effective repulsive interactions, the slowest decaying correlation function is between the $2k_{ab} + 2k_b$ components of the CDW order parameter. We identify this region of the $C1S0$ phase as an incommensurate charge density wave.

2. $K_{2,c} > 1$

   For effective attractive interactions, the staggered components of the antibonding pairing order parameter exhibit the slowest decay and hence the $C1S0$ phase exhibits unconventional fluctuation superconductivity with finite wave vector pairing. This is the same "pair density wave phase" identified in Ref. [76].

The precise regime which is realised depends on the values of the microscopic parameter $V_\perp$, $V_\parallel$; from integration of the RG equations we find both regimes of $K_{2,c}$ can be realised, although $K_{2,c} < 1$ appears to be the more generic case.

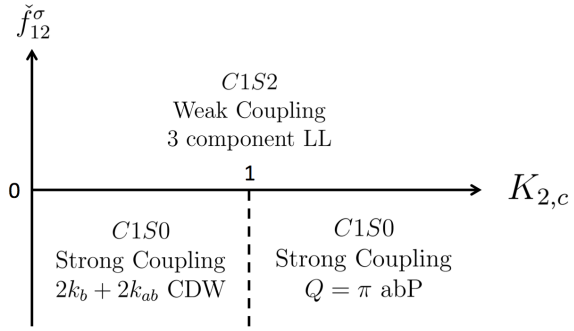

Figure 2.3: Zero-temperature phase diagram of the $4k_b$ Mott insulator. $\check{f}_{12}^{\sigma}$ is the effective across-rung exchange parameter in the KHM picture and $K_{2,c}$ is the Luttinger parameter of the antibonding charge boson.

The above analysis pertains to the case with the bonding band half-filled. In the case where umklapp scattering is induced by an external periodic potential (away from commensurate filling) we expect the same low-energy physics to emerge and both $C1S2$ and $C1S0$ phases to exist. We summarise the zero-temperature phase diagram in Fig. 2.3.

2.3.2 Chain representation

We now consider the $4k_b$ umklapp interaction in the chain representation. To simplify the analysis we consider the case with extended density-density interactions along the chain, which decrease the value of K_c (see the discussion at the beginning of Sec. 2.2.2). The low-energy projection of the umklapp term is

$$H_W = \lambda \int dx \left[i e^{i\sqrt{4\pi K_c}\Phi_c} \left(\xi_R^1 - i\xi_2^R\right)\left(\xi_L^1 + i\xi_L^2\right) + \text{h.c.} \right],$$

where we have rescaled the boson field $\Phi_c \to \sqrt{K_c}\Phi_c$ to absorb the Luttinger parameter in the kinetic term of the Hamiltonian.

For generic repulsive interactions, the umklapp term H_W is *relevant* in the RG sense, with scaling dimension $d = 1 + K_c < 2$. For long-range interactions along the chain, the Luttinger parameter becomes small $K_c \ll 1$ and the umklapp term becomes *strongly* relevant, dominating the marginal four-fermion interactions in the Hamiltonian (2.23). We should therefore treat the umklapp term first: we begin by combining Majorana fermions into a complex Dirac fermion $\mathcal{R} = (\xi_1^R + i\xi_2^R)/\sqrt{2}$ and $\mathcal{L}^\dagger = (\xi_L^1 - i\xi_L^2)/\sqrt{2}$. We then bosonise the fermions $\mathcal{R}$, L in terms of the bosonic field $\bar{\Phi}$ and its dual $\bar{\Theta}$ following Ref. [7]. The umklapp term becomes

$$H_W = \frac{2\lambda}{\pi} \int dx \ \cos\left[\sqrt{4\pi}(\sqrt{K_c}\Phi_c + \bar{\Phi})\right].$$

Following the canonical transformation

$$\Phi_\pm = \frac{1}{\sqrt{2}}(\sqrt{K_c}\Phi_c \pm \bar{\Phi}), \qquad \Theta_\pm = \frac{1}{\sqrt{2}}(\Theta_c/\sqrt{K_c} \pm \bar{\Theta}), \tag{2.46}$$

the Hamiltonian density can be written as

$$\begin{aligned}
\mathcal{H} &= \frac{v}{2}\left[K\left(\partial_x\Theta_+\right)^2 + K^{-1}\left(\partial_x\Phi_+\right)^2\right] + m\cos\left(\sqrt{8\pi}\Phi_+\right) \\
&+\frac{v}{2}\left[K\left(\partial_x\Theta_-\right)^2 + K^{-1}\left(\partial_x\Phi_-\right)^2\right] + g_1\partial_x\Theta_+\partial_x\Theta_- + g_2\partial_x\Phi_+\partial_x\Phi_- \\
&+\frac{iv_c}{2}\left(\xi^3_L\partial_x\xi^3_L - \xi^3_R\partial_x\xi^3_R\right) + \frac{iv_s}{2}\sum_a\left(\chi^a_L\partial_x\chi^a_L - \chi^a_R\partial_x\chi^a_R\right) \\
&-2g_{\sigma-}\left(\xi^3_R\xi^3_L\right)\sum_a\left(\chi^a_R\chi^a_L\right) - 2g_{\sigma+}\sum_{a>b}\left(\chi^a_R\chi^a_L\right)\left(\chi^b_R\chi^b_L\right) \\
&-\left(\xi^1_R\xi^1_L - \xi^2_R\xi^2_L\right)\left[2g_{c,ss}\left(\xi^3_R\xi^3_L\right) + g_{\rho,-}\left(\xi^1_R\xi^1_L - \xi^2_R\xi^2_L\right) + 2g_{c,st}\sum_a\left(\chi^a_R\chi^a_L\right)\right],
\end{aligned}$$

where $g_{1,2}$ and m are redefined coupling constants and

$$v = \frac{1}{2}\sqrt{\left(v_c + \tilde{u}/K_c\right)\left(v_c + \tilde{u}K_c\right)}\ , \quad K^2 = K_c\frac{\tilde{u} + v_cK_c}{v_c + \tilde{u}K_c}. \tag{2.47}$$

Now the story becomes similar to the band representation: as we consider $K \ll 1$, the cosine term in the sine-Gordon model for Φ_+ is strongly relevant and flows to strong coupling before any other coupling becomes large. The umklapp-induced gap in the Φ_+ sector will be large compared to all other low-energy scales and we proceed to integrate out the Φ_+ boson.

The four-fermion interactions that involve $\xi^{1,2}$ can also be bosonised, giving

$$\begin{aligned}
\left(\xi^1_R\xi^1_L - \xi^2_R\xi^2_L\right) &= \frac{1}{2}\left[\left(\xi^1_R + i\xi^2_R\right)\left(\xi^1_L + i\xi^2_L\right) + \left(\xi^1_R - i\xi^2_R\right)\left(\xi^1_L - i\xi^2_L\right)\right], \\
&= \mathcal{R}^\dagger\mathcal{L}^\dagger + \mathcal{R}\mathcal{L} \sim \frac{i}{2\pi}\cos\left[\sqrt{2\pi}\left(\Theta_+ + \Theta_-\right)\right].
\end{aligned}$$

When integrating out the Φ_+ boson we therefore only generate interactions proportional to $\cos\left(\sqrt{8\pi}\Theta_-\right)$, which are irrelevant as $K \ll 1$. At energies small compared to the mass gap of the Φ_+ boson, the effective Hamiltonian density has the form

$$\begin{aligned}
\mathcal{H}_{\text{eff}} &= \frac{\tilde{v}}{2}\left[\tilde{K}\left(\partial_x\Theta_-\right)^2 + \tilde{K}^{-1}\left(\partial_x\Phi_-\right)^2\right] + \frac{iv_c}{2}\left[\xi^3_L\partial_x\xi^3_L - \xi^3_R\partial_x\xi^3_R\right] + \\
&\frac{iv_s}{2}\left[\chi^a_L\partial_x\chi^a_L - \chi^a_R\partial_x\chi^a_R\right] - 2\tilde{g}_{\sigma-}\left(\xi^3_R\xi^3_L\right)\sum_a\left(\chi^a_R\chi^a_L\right) \\
&-2\tilde{g}_{\sigma+}\sum_{a>b}\left(\chi^a_R\chi^a_L\right)\left(\chi^b_R\chi^b_L\right),
\end{aligned} \tag{2.48}$$

where $\tilde{g}$ are renormalised couplings, $\tilde{v}$ is the renormalised velocity and $\tilde{K}$ is the renormalised Luttinger parameter.

The effective Hamiltonian (2.48) is also remarkably similar in form to the field theory of the KHM, with the small difference that the single and triplet Majorana modes have differing velocities. To analyse this effective theory (2.48) further we carry out a RG analysis, which gives

$$\dot{\tilde{g}}_{\sigma-} = -\frac{2}{\pi v_s}\tilde{g}_{\sigma-}\tilde{g}_{\sigma+} \ , \qquad \dot{\tilde{g}}_{\sigma+} = -\frac{\tilde{g}_{\sigma-}^2}{\pi v_c} - \frac{\tilde{g}_{\sigma+}^2}{\pi v_s} \ . \tag{2.49}$$

Defining rescaled combinations of the couplings $g_\pm = \frac{\tilde{g}_{\sigma-}}{\pi\sqrt{v_c v_s}} \pm \frac{\tilde{g}_{\sigma+}}{\pi v_s}$, the RG Eqs. (2.49) become $\dot{g}_\pm = \mp g_\pm^2$, which have the solution

$$g_\pm(l) = \frac{g_\pm(l_0)}{1 \pm g_\pm(l_0)(l - l_0)}.$$

If we assume that the couplings $g_{\sigma\pm}$ renormalise only weakly by the time at which m (the sine-Gordon coupling) reaches strong coupling, we conclude that $\tilde{g}_{\sigma\pm}(l_0) > 0$. The subsequent RG flow of g_+ is then toward weak coupling. One the other hand, g_- flows to a $C1S0$ strong coupling fixed point if

$$\tilde{g}_{\sigma-}(l_0) > \tilde{g}_{\sigma+}(l_0)\sqrt{\frac{v_c}{v_s}}, \tag{2.50}$$

To get a feel for what this requirement implies in terms of couplings in the microscopic theory we consider the case when $\tilde{g}_{\sigma\pm}$ are close to their bare values (e.g. they have renormalised very weakly) and when $U, V_\parallel, V_\perp$ are small. In this case the couplings are given by

$$g_{\sigma-} \sim \frac{V_\perp a_0}{2} \ , \quad g_{\sigma+} \sim a_0\big(U + 2\cos(2k_F a_0)V_\parallel\big),$$

where a_0 is the lattice spacing and $k_F \approx \pi/2$. The RG flow is towards the strong coupling fixed point when

$$V_\perp \gtrsim 2\sqrt{\frac{v_c}{v_s}}\big(U - 2V_\parallel\big).$$

So, we see that the repulsive interactions between neighbouring sites is crucial for driving the system to the $C1S0$ fixed point, as was the case in the weak-coupling analysis of the previous subsection. Having established the existence of a $C1S0$ phase in the chain representation, the next step would be to determine which correlations are dominant. This is difficult for the following reason: general local observables

can be expressed in terms of Ising models, but it remains an open problem to determine how products of Ising order and disorder operators transform under Tsvelik's transformation (2.22).

2.4 Numerical results: DMRG

In this section we numerically study the extended Hubbard model on the two-leg ladder using the density matrix renormalisation group (DMRG) algorithm [18, 19]. Hubbard-like models have been studied extensively using DMRG, both on single chain and multiple leg ladders [90, 91, 92, 93, 94, 95, 96, 97]. We begin this section by summarising the DMRG algorithm, before first considering the case where umklapp interactions are absent, the "generic strong coupling regime" in Section 2.4.2. Having established the properties of this generic regime, we turn to the case when the umklapp interaction is marginally relevant and study the resulting phases.

2.4.1 The DMRG algorithm

The DMRG algorithm has become the standard technique for studying the ground state properties of quasi-one-dimensional quantum systems with short range interactions. Extensive reviews of the algorithm and its relation to matrix product states can be found in Refs. [19, 98]. The essential ideas behind the DMRG algorithm are as follow: if we start with a two site system and grow the system following a set procedure (which we will discuss shortly) the size of the Hilbert space increases exponentially with the system size and just simply storing a single eigenvector rapidly becomes unfeasible (e.g. an eigenvector of a spin–1/2 fermion system with 16 sites has 4^{16} elements = 64Gb of data). Clearly if we are going to grow our system to large sizes we need to truncate the Hilbert space: the DMRG algorithm does exactly this decimation procedure by truncating the Hilbert space according to eigenstates of a particular reduced density matrix.

We begin by discussing the infinite system algorithm, which is used to grow the system from e.g. two sites to L sites, when it is then terminated. We will follow this discussion by a description of the finite-size algorithm which is subsequently iterated until the wave function for the ground state has converged. For convenience we will

discuss the DMRG algorithm for the one-dimensional chain.

2.4.1.1 The infinite size DMRG algorithm

The infinite size DMRG algorithm is used to grow the size of the system in a sequence of steps, such that the system size $\ell = 2, 4, 6, \ldots$ continuing until we reach the desired system size L. Of course, in this procedure the size of the Hilbert space is increasing exponentially, so we must perform some truncation in order to keep the size of the state space m manageable.

The infinite size DMRG algorithm performs the growth in the following manner:

1. Take your system of size ℓ and define two *blocks* A and B that equipartition the system.

2. Insert two new sites $\bullet\bullet$ between the blocks A and B to obtain the *superblock* $A \bullet \bullet B$ (following the notation of Schollwoeck [98]).

3. A generic state in the superblock can be written in the form

$$|\phi\rangle_{A\bullet\bullet B} = \sum_{\psi_A,\sigma_A,\sigma_B,\psi_B} \phi_{\psi_A\sigma_A\sigma_B\psi_B} |\psi_A\rangle \otimes |\sigma_A\rangle \otimes |\sigma_B\rangle \otimes |\psi_B\rangle,$$

   where $|\psi_{A,B}\rangle$ is a state on the A, B block (which span a Hilbert space of dimension m[†]) and $\{|\sigma_{A,B}\rangle\}$ are the sets of vectors that span the local state space of the added site $\bullet$ next to A, B (of dimension $d = 4$ for spin–1/2 fermions).

4. The ground state of the superblock Hamiltonian is found by numerical diagonalisation (e.g. the Lanczos algorithm[‡]) and is denoted by $|\phi_0\rangle$.

5. We take the set of states $\{|\phi_A\rangle\} \equiv \{|\psi_A\rangle \otimes |\sigma_A\rangle\}$ as the basis of the block $A\bullet$. The ground state vector can be expressed as:

$$|\phi_0\rangle = \sum_{\phi_A\phi_B} \psi_{\phi_A\phi_B} |\phi_A\rangle \otimes |\phi_B\rangle.$$

[†] We assume that ℓ is already large enough that the Hilbert space $d^\ell > m$ and that truncation has occurred in a previous step. Clearly one does not have to perform the truncation until the system is sufficiently large.

[‡]See the next chapter.

6. The set of states $\{|\phi_A\rangle\}$ has dimension dm – we must truncate this set of states back to size m to avoid exponential growth of the Hilbert space. We perform this truncation by keeping only the m highest weight eigenvectors $\{|\varphi\rangle_A\}$ of the reduced density matrix

$$\varrho_{A\bullet} = \mathrm{Tr}_{\bullet B}|\phi_0\rangle\langle\phi_0|, \qquad (\varrho_{A\bullet})_{ij} = \sum_k \psi_{ik}\psi^*_{jk}.$$

which are determined by exact diagonalisation. A measure of the severity of this decimation is the truncation error $\epsilon = 1 - \sum_{a=1}^{m} w_a$ (also called the discarded weight).

7. Iterate the above steps, performing the appropriate change of basis to eigenstates of the reduced density matrix after each truncation. Stop the algorithm when $\ell = L$ the system size you wish to consider.

2.4.1.2 Finite size DMRG algorithm

The infinite size DMRG algorithm has now been used to grow the system to size L, but the resulting "ground state" given by this procedure is not correct, stemming from the choices of basis for small initial system sizes which do not well describe the large system. This can, however, be corrected using the finite size DMRG algorithm, which performs the following steps:

1. We continue the growth process of one of the blocks (say A) by adding two sites. However, at the same time we *shrink* the size of the other block (B) to maintain the total system size L.

2. The basis of the reduced block B is the basis generated in the infinite size algorithm for the same block size (which is stored for this purpose).

3. The ground state of the superblock $A^{(\ell)} \bullet\bullet B^{(\bar{\ell})}$ (where $\bar{\ell}$ is the complement of $A^{(\ell)} \bullet\bullet$ and ℓ is the block size of A) is determined by numerical diagonalisation.

4. We construct the basis of $A\bullet$ in the same manner as in the infinite size algorithm, and truncate according to the eigenstates of the reduced density matrix $\varrho_{A\bullet}$.

5. The block $A^{(\ell)}$ is grown until $B^{(\bar{\ell})}$ is small enough that for the reduced Hilbert space size m, B is exactly solved.

6. The growth procedure is then reversed, with B growing until A is small enough to be exactly solved.

7. The procedure is then once more reversed, until we return to the initial configuration of equisized blocks A and B.

8. This process of *sweeps* is continued until the ground state wave function of the system of size L has converged.

We now continue to discuss our DMRG results for the extended Hubbard model on the two-leg ladder. The DMRG algorithm is used to construct the (approximate) ground state of the $L \times 2$ ladder for a fixed number m of density matrix eigenstates (computational resources constrain us to $m \leq 2000$). To ascertain the quality of the approximation we calculate the relative error between the ground state energy per site with m density matrix eigenstates and the (extrapolated) $m = 4^{2L}$ result. This relative error gives a useful order-of-magnitude estimate for the error in observables, such as the correlation functions.

2.4.2 "Generic" strong coupling regime

We begin by discussing the case where the umklapp term is absent; in this case for sufficiently small extended interactions, a weak coupling RG analysis generically flows towards a strong-coupling fixed point with

$$\tilde{c}^{\rho}_{12} = \tilde{c}^{\sigma}_{12} = 2\tilde{f}^{\rho}_{12} = -2\tilde{c}^{\rho}_{11} = -2\tilde{c}^{\rho}_{22} = -\tilde{c}^{\sigma}_{11} = -\tilde{c}^{\sigma}_{22} = g > 0, \qquad \tilde{f}^{\sigma}_{12} = 0 \ .$$

The fixed point is described by a theory with an enlarged symmetry group, the $SO(6)$ Gross-Neveu model [66, 77, 79, 85, 86]. Three of the bosons $\Theta_{-,c}$, $\Phi_{+,s}$ and $\Phi_{-,s}$ becomes massive under the RG flow, whilst the remaining charge boson $\Phi_{+,c}$ is described by a $U(1)$ Luttinger liquid. The interaction term responsible for the bosons becoming massive takes the form

$$-2g\Big\{\cos(\sqrt{4\pi}\Phi_{+,s})\cos(\sqrt{4\pi}\Phi_{-,s}) + \cos(\sqrt{4\pi}\Theta_{-,c})\Big[\cos(\sqrt{4\pi}\Phi_{-s}) + \cos(\sqrt{4\pi}\Phi_{+,s})\Big]\Big\}.$$

A classical analysis of this potential gives the values to which the bosons become pinned

$$\Theta_{-,c} = \Phi_{+,s} = \Phi_{-,s} = 2n\sqrt{\frac{\pi}{4}}, \quad \text{or} \quad (2n+1)\sqrt{\frac{\pi}{4}} \quad \text{with } n \in \mathbb{Z}$$

(in the same way as we determined the pinned value in the $4k_b$ Mott insulator $C1S0$ phase). From knowledge of these pinned values, it follows that the two-point functions of order parameters (defined in Sec. 2.3.1.3) have the asymptotic form [66, 86]

$$\begin{aligned} \langle \mathcal{O}_{\mathrm{SCd}}(x)\mathcal{O}^{\dagger}_{\mathrm{SCd}}(0)\rangle_{\mathrm{Generic}} &\propto |x|^{-1/2K_c}, \quad \langle \mathcal{O}_{\mathrm{abP}}(x)\mathcal{O}^{\dagger}_{\mathrm{abP}}(0)\rangle_{\mathrm{Generic}} \propto |x|^{-1/2K_c}, \\ \langle \mathcal{O}_{\mathrm{CDW}}(x)\ \mathcal{O}^{\dagger}_{\mathrm{CDW}}(0)\rangle_{\mathrm{Generic}} &\propto \mathcal{A}_1 x^{-2} + \mathcal{A}_2 \cos\big(2(k_b+k_{ab})x\big)x^{-2K_c}, \end{aligned} \tag{2.51}$$

where K_c is the Luttinger parameter for the $\Phi_{+,c}$ boson. As a result of the spin gap, the $2k_F$ response of the CDW order parameters (CDW, bCDW) is "blocked" (exponentially decaying), as discussed in Appendix 2.A. The second term in the two-point function of the CDW order parameter is interaction induced and vanishes in the $U \to 0$ limit. A detailed discussion of such interaction-induced terms can be found in Appendix 2.B.

We now present results in the generic strong coupling regime, for the Hamiltonian (2.5) on the 64×2 ladder with $t = t_\perp = 1$, $U = 4$ and $V_\parallel = V_\perp = W_{1,2} = 0$ and open boundary conditions.[†] We consider the system with $N = 110$ electrons and keep up to $m = 1500$ density matrix states for the reduced Hilbert space, leading to truncation errors of $\epsilon \approx 3 \times 10^{-6}$. The relative error in quantities calculated with the DMRG algorithm can be estimated from extrapolating the ground state energy to $m = 4^{\#\text{ of sites}}$ (or zero truncation error), defining ε as the relative error in the ground state energy per site E_0/L , we find $\varepsilon \approx 5 \times 10^{-4}$.

In Fig. 2.4 we show the two-point functions of the SCd and abP order parameters calculated by DMRG and appropriate power law fits. Oscillations at $2k_{ab}$ are seen in the two-point function of $\mathcal{O}_{\mathrm{abP}}$, which we attribute to a small amplitude for the power law decay term and/or a large spin correlation length, which would be consistent with a small spin gap in the system. The power law fits give the Luttinger parameter for the $\Phi_{+,c}$ boson as $K_c \approx 0.45$.

[†]This is usual in DMRG calculations: periodic boundary conditions reduce how quickly the eigenvalues of the reduced density matrix (RDM) $\varrho_{A\bullet}$ decrease and correspondingly one must include many more eigenstates of the RDM to keep the discarded weight small.

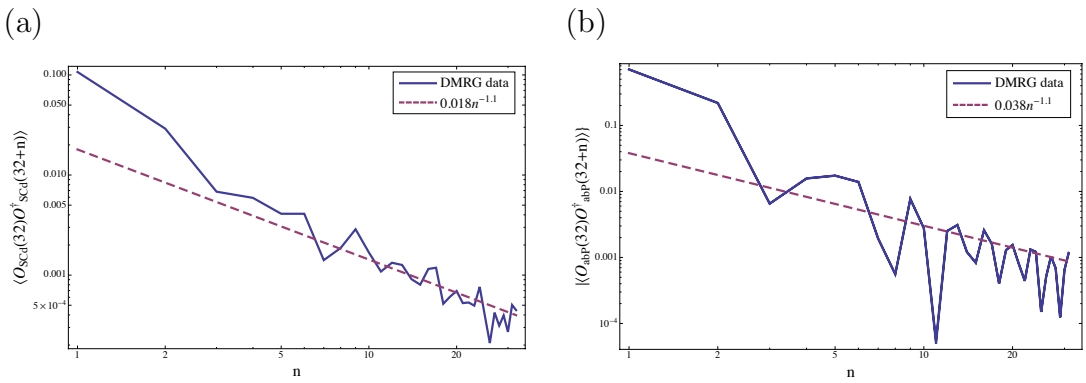

Figure 2.4: DMRG data (solid) and power law fits (dashed) in the generic strong coupling phase for (a) the superconducting d-wave order parameter $\mathcal{O}_{SCd}$, and (b) the antibonding pairing order parameter $\mathcal{O}_{abP}$.

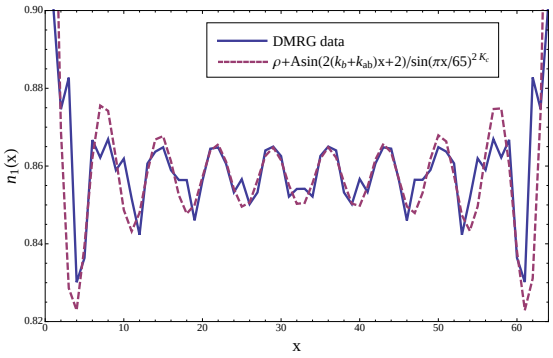

Figure 2.5: DMRG data (solid) and fit (dashed) for the density across one leg of the ladder in the generic strong coupling phase. The "Wigner crystal" oscillation fit used parameters $\rho = 0.857$, $A = 0.0054$ and $2K_c = 0.91$. The bonding and antibonding wave vectors are given by $k_b = 1.17\pi/2$ and $k_{ab} = 0.55\pi/2$.

We show the density across one of the legs of the ladder in Fig. 2.5. The oscillations in the density are induced by the open boundary conditions: the $2k_F$ response (Friedel oscillations) is suppressed by the spin gap and consequently we see the leading order oscillations at $4k_F = 2(k_b + k_{ab})$, known as "Wigner crystal" oscillations [99]. We fit these oscillations to the standard form [99]

$$\langle n(x)\rangle_{4k_F} = \rho + A\frac{\sin\left(4k_F x + \varphi\right)}{\sin\left(\frac{\pi}{L+1}x\right)^{2K_c}}, \tag{2.52}$$

using A and φ as fitting parameters, and ρ is the average electron density. Additional oscillations present in Fig. 2.5 are from the sub-leading contributions to the density operator (see Appendix 2.B). We use the same value for the Luttinger parameter K_c as in Fig. 2.4.

From the asymptotic form of the two-point functions (2.51), it is clear the dominant fluctuations depend upon the underlying microscopic parameter of the Hamiltonian (2.5). In this case, $K_c < 1/2$ and the leading fluctuations are CDW in nature, arising from the $2(k_b + k_{ab})$ interaction-induced component of the density operator.

2.4.3 $4k_b$ umklapp

Having established the properties of the "generic" strong coupling phase of the two-leg ladder, we now turn our attention to the case when umklapp scattering is activated. The umklapp term can be activated in two ways: (i) half-fill the bonding band; (ii) work away from half-filling and apply a periodic potential with the appropriate periodicity. We first attempted to study the half-filled band: there it turns out the analysis is extremely challenging for the following reasons. Firstly, the open boundary conditions in the DMRG calculations induce Friedel oscillations in the density across the ladder, and hence the band is never truly "half-filled". Secondly, we found quite generically that the spin and charge gaps are very small. It is then difficult to tell the difference between power law and exponential decay (with large correlation length) on the accessible system sizes[†]. In the following we instead focus on case (ii).

From the analysis of Sec. 2.3, we know that there are two possible phases when the $4k_b$ umklapp interaction is present and marginally relevant. We will consider the $C1S2$ and $C1S0$ phases in turn. To that end, we have carried out the DMRG calculations on the Hamiltonian

$$H = H_{\text{ladd}}(\pi) + \mu_- \sum_{j,\sigma} \left(c^\dagger_{1,j,\sigma} - c^\dagger_{2,j,\sigma}\right)\left(c_{1,j,\sigma} - c_{2,j,\sigma}\right), \tag{2.53}$$

where $H_{\text{ladd}}(K)$ is given by (2.5).

Let us make a few remarks about (2.53). Firstly, we consider the case with the bonding band *quarter-filled*. This is convenient as we can apply a periodic potential with wave vector π along the legs of the ladder which activates the $4k_b$ umklapp process (as discussed in Sec. 2.1.1). This applied potential gives us control of the strength of the umklapp and correspondingly the Mott gap (a sizeable Mott gap makes numerical analysis easier, as discussed above). Secondly, we have also applied an additional chemical potential to the antibonding band. This is introduced for convenience, as it allows us to vary the density of electrons in the antibonding band whilst keeping interaction parameters fixed. Nevertheless, isolating the region of phase space in which the two phases occur is challenging.

[†]Due to this, we did not find convincing evidence for the $C1S0$ phase when the band is half-filled.

2.4.3.1 $C1S2$ Phase

When extended interactions are sufficiently weak (small $V_\parallel, V_\perp$) the RG analyses of Sec. 2.3 show that the $4k_b$ umklapp drives the RG flow towards strong coupling with a $C1S2$ fixed point. The asymptotic forms of the two-point functions of order parameters have the following form in this phase:

$$\begin{aligned}
\langle \mathcal{O}_{\mathrm{CDW}}(x)\ \mathcal{O}^\dagger_{\mathrm{CDW}}(0)\rangle_{C1S2} &\propto \mathcal{A}_3 \cos(2k_{ab}x)|x|^{-K_{2,c}-K_{2,s}} \\
&\quad + \mathcal{A}_4 \cos(2k_b x)|x|^{-K_{1,s}} + \mathcal{A}_5 x^{-2} + \dots\ , \\
\langle \mathcal{O}_{\mathrm{bCDW}}(x)\ \mathcal{O}^\dagger_{\mathrm{bCDW}}(0)\rangle_{C1S2} &\propto e^{-|x|/\xi_b} \quad (\text{at } 2k_b) + \dots\ , \\
\langle \mathcal{O}_{\mathrm{SCd}}(x)\mathcal{O}^\dagger_{\mathrm{SCd}}(0)\rangle_{C1S2} &\propto \cos(2k_{ab}x)|x|^{-K_{2,c}-1/K_{2,c}} + \dots\ , \\
\langle \mathcal{O}_{\mathrm{abP}}(x)\mathcal{O}^\dagger_{\mathrm{abP}}(0)\rangle_{C1S2} &\propto \mathcal{A}_6 \cos(2k_{ab}x)|x|^{-K_{2,c}-1/K_{2,c}} \\
&\quad + \mathcal{A}_6 |x|^{-K_{2,s}-1/K_{2,c}} + \dots, \qquad (2.54)
\end{aligned}$$

where the amplitudes $\mathcal{A}_j$ are unknown, ξ_b is the correlation length of the massive $\Phi_{1,c}$ boson and K_j are the Luttinger parameters for the massless Φ_j bosons.

To access the $C1S2$ phase we consider the Hamiltonian (2.53) with $t = 2t_\perp = 1$, $U = 8V_\perp = 8V_\parallel = 4$ and $W_{1,2} = 1.5$. We tuned the chemical potential μ_- so that there are $N = 90$ electrons and the bonding band is quarter-filled. Up to $m = 1200$ density matrix states were kept in the calculations, leading to truncation errors of $\epsilon \approx 10^{-6}$ and corresponding relative error in the ground state energy per site of $\sim 10^{-4}$.

To confirm we are in the $C1S2$ phase we measure the bonding ($G_b(n)$) and antibonding ($G_{ab}(n)$) Green's function. From the RG analysis, we expect G_{ab} to decay as a power law, whilst G_b should decay as an exponential multiplied by a power law. We show G_b in Fig. 2.6(a), where we remove the leading k_b oscillations ($G_b(n) = G_{b,\mathrm{Full}}(n)/\cos(k_b n)$). We perform a similar procedure for G_{ab}, shown in Fig. 2.6(b). Both of these Green's functions take the expected form from the RG analysis, consistent with a $C1S2$ phase.

Having established that we're in the $C1S2$ phase, we now consider two-point functions of the order parameters (2.54). Figure 2.7 shows the two-point functions of the SCd and abP order parameters. Once again, we have removed the leading oscillations in these two-point functions. Both of the correlation functions show power law decay with the same exponent, which give an approximate value for the Luttinger

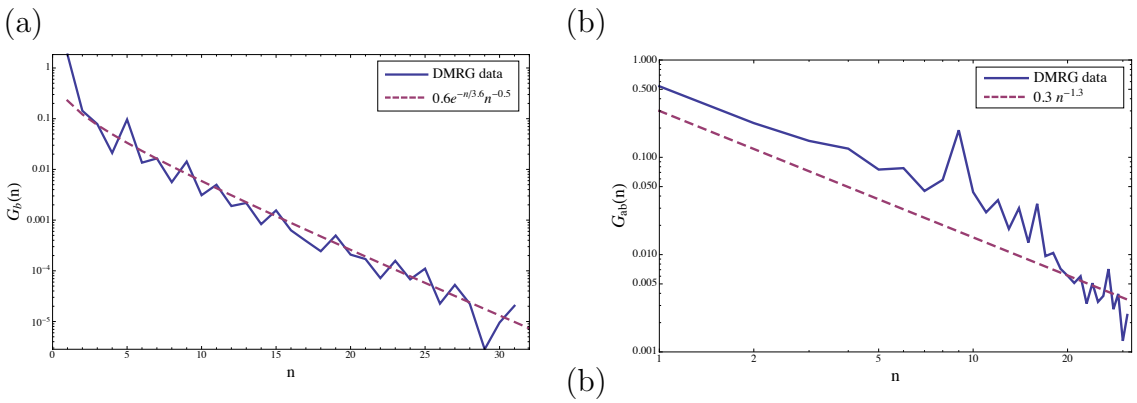

Figure 2.6: DMRG data (solid) and fits (dashed) in the $C1S2$ phase for (a) the bonding Green's function $G_b(n) = \langle c_b(32)c_b^\dagger(32+n)\rangle$ with k_b oscillations removed (see text), and (b) the antibonding Green's function $G_{ab}(n) = \langle c_{ab}(32)c_{ab}^\dagger(32+n)\rangle$ with k_{ab} oscillations removed. Fit functions are of the form predicted by the RG analysis.

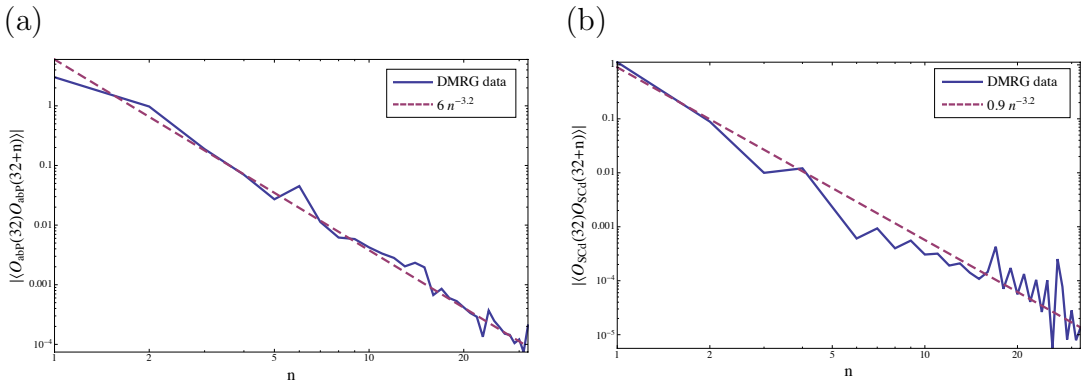

Figure 2.7: DMRG data (solid) and fit functions (dashed) in the $C1S2$ phase for (a) the two-point function of the antibonding pairing order parameter $\mathcal{O}_{\rm abP}$ with the $2k_{ab}$ oscillations removed (see text), and (b) the two-point function of the superconducting d–wave order parameter $\mathcal{O}_{\rm SCd}$ with $2k_{ab}$ oscillations removed. Fit functions are of the form given in Eqs. (2.54).

parameter $K_{2,c} \approx 0.35$. The two-point function of the CDW order parameter is shown in Fig. 2.8; the decay at intermediate distances is well described by x^{-2} and oscillates with wavenumber $2k_{ab}$, as predicted by the bosonisation analysis (2.54). Sub-leading contributions, oscillating at $4k_b$ are also observed. The long distance asymptotics are consistent with $K_{2,s} = 1$, as expected from $SU(2)$ symmetry. The dominant fluctuations in this phase are clearly of the CDW type.

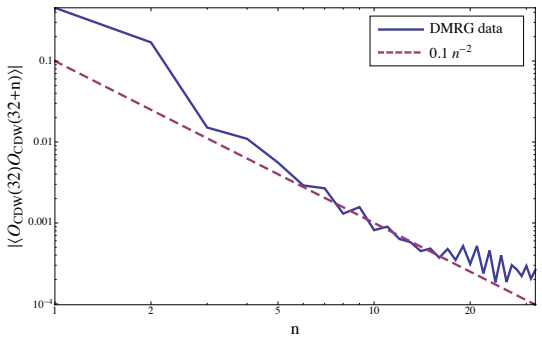

Figure 2.8: DMRG data (solid) and x^{-2} guide (dashed) in the $C1S2$ phase for the two-point function of the charge density wave order parameter $\mathcal{O}_{\rm CDW}$. Sub-x^{-2} decay is observed with oscillations at $\sim 2k_{ab}$ at large distances.

2.4.3.2 $C1S0$ $4k_b$ Mott insulator phase

In order to realise the $C1S0$ phase of the $4k_b$ Mott insulator, the inter-band exchange interaction must be *antiferromagnetic* after the initial RG procedure. This can always be achieved provided the interchain density-density interaction is large $V_\perp > U$ such that the initial condition is antiferromagnetic (it remains so under the RG flow). The $C1S0$ fixed point is characterised by the following two-point functions

$$\begin{aligned}
\langle\mathcal{O}_{\rm CDW}(x)\ \mathcal{O}^\dagger_{\rm CDW}(0)\rangle &\propto \mathcal{A}_8 x^{-2} + \mathcal{A}_9\cos\big(2(k_b+k_{ab})x\big)|x|^{-K_{2,c}} + \ldots,\\
\langle\mathcal{O}_{\rm bCDW}(x)\ \mathcal{O}^\dagger_{\rm bCDW}(0)\rangle &\propto e^{-|x|/\xi_b}\ \ (\text{at } 2k_b) + \ldots,\\
\langle\mathcal{O}_{\rm abP}(x)\ \mathcal{O}^\dagger_{\rm abP}(0)\rangle &\propto \mathcal{A}_{10}\cos(2k_{ab}x)|x|^{-K_{2,c}-1/K_{2,c}} + \mathcal{A}_{11}\cos\big(2k_b x\big)|x|^{-1/K_{2,c}} + \ldots\\
\langle\mathcal{O}_{\rm SCd}(x)\ \mathcal{O}^\dagger_{\rm SCd}(0)\rangle &\propto \cos(2k_{ab}x)|x|^{-K_{2,c}-1/K_{2,c}} + \ldots\ ,\ ,
\end{aligned} \tag{2.55}$$

where the amplitudes $\mathcal{A}_d$ are unknown.

We now present DMRG results in the $C1S0$ phase of the Hamiltonian (2.53). We work on the 96×2 ladder with $t = 2t_\perp = 1$, $V_\perp = 5$, $V_\parallel = 0$, $U = 4$ and $N = 88$ electrons, with μ_- chosen such that the bonding band is quarter-filled. We apply a periodic potential to the bonding band $W_+ = 1$ to activate the umklapp scattering. In the calculations, up to $m = 2000$ density matrix states were used, resulting in truncation errors of $\epsilon \approx 10^{-7}$ and relative error in E_0/L of $\varepsilon \approx 2\times 10^{-5}$.

As with the $C1S2$ phase, we infer the presence of a spin gap in both bands and a charge gap in the bonding band from the Green's functions shown in Fig. 2.9 and the forms of the two-point functions. As expected from the RG analysis, we see that the bonding Green's function decays exponentially, whilst the antibonding Green's function decays as an exponential multiplied by a power law. The fit of the antibonding Green's function gives a value for the Luttinger parameter $K_{2,c} \approx 0.27$.

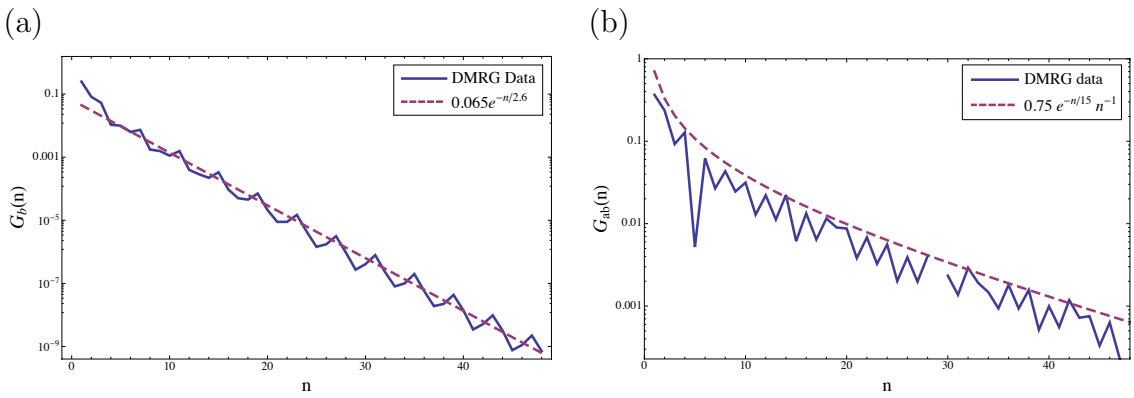

Figure 2.9: DMRG data (solid) and fit function (dashed) in the $C1S0$ phase for (a) the bonding Green's function $G_b(n) = \langle c_b(48)c_b^\dagger(48+n)\rangle$, and (b) the antibonding Green's function $G_{ab}(n) = \langle c_{ab}(48)c_{ab}^\dagger(48+n)\rangle$, with the k_{ab} oscillation removed (see text). The break in data of (b) at $n = 29$ is a remnant of removing the k_{ab} oscillations.

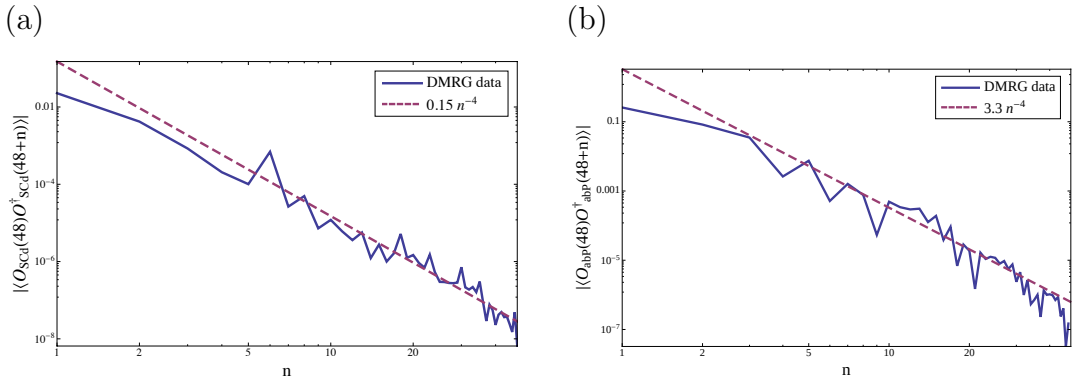

Figure 2.10: DMRG data (solid) and fit functions (dashed) in the $C1S0$ phase for (a) the absolute value of the two-point function of the superconducting d-wave order parameter $\mathcal{O}_{\mathrm{SCd}}$ with $2k_{ab}$ oscillations removed (see text), and (b) the absolute value of the two-point function of the antibonding pairing order parameter $\mathcal{O}_{\mathrm{abP}}$.

We now consider the two-point functions of the order parameters in Eqs. (2.55). The correlation functions of the SCd and abP order parameters are shown in Fig. 2.10, where leading oscillations of frequency $2k_{ab}$ have been removed. Both correlation functions are well described by power law decay consistent with $K_{2,c} \approx 0.27$ obtained from fitting the antibonding Green's function. We do not clearly see the abP component that decays with power law $1/K_{2,c}$. This may be due to the amplitude $\mathcal{A}_{11}$ being much smaller than $\mathcal{A}_{10}$, in which case the sub-leading term would dominate on the "short" length scales accessible with DMRG.

The correlation function of the CDW order parameter is shown in Fig. 2.11, where at long distances there are large wavelength oscillations with wave vector $2k_b + 2k_{ab}$

that decay at sub–x^{-2}, consistent with the bosonisation prediction. Accurate extraction of the power law of this decay is not possible – the large spin correlation length means sub-leading term decay slowly for accessible system sizes. We have similar problems with the two-point function of bCDW operator, where the long spin correlation length and unknown interaction-induced amplitudes of the $4k_F$ components (similar to Eqs. 2.57) make fitting ill-defined.

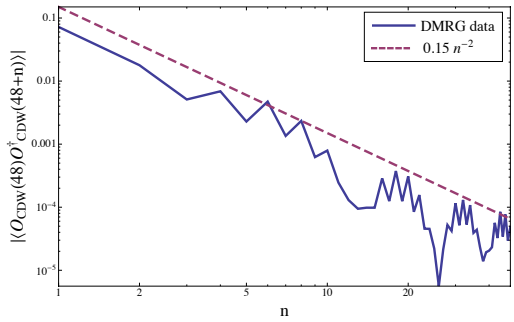

Figure 2.11: The two-point function of charge density wave order parameter $\mathcal{O}_{\rm CDW}$ (solid) and x^{-2} power law (dashed) in the $C1S0$ phase.

There are two possibilities for the dominant fluctuations in the $4k_b$ Mott insulator depending upon the Luttinger parameter $K_{2,c}$, see Fig. 2.3. For the presented data $K_{2,c} < 1$, where incommensurate $2k_b + 2k_{ab}$ CDW fluctuations dominate.

2.5 Discussion and conclusions

In this chapter we have established a mechanism for finite wave vector pairing in a doped fermionic two-leg ladder with equivalent legs. Central to this mechanism is umklapp scattering, which arises as a result of electron-electron interactions at special band fillings *or* "externally" applied periodic potentials. As we discussed in Sec. 2.1.1, the latter may arise from CDW formation driven by the (three-dimensional) long-range Coulomb interaction in realistic crystal structures. We have applied renormalisation group techniques to the low-energy description of the lattice model (2.5) in two limits: (i) weak coupling ("band representation") and (ii) and arbitrary intra-leg interaction strength and small across rung tunnelling/interactions ("chain representation"). In both limits we found that the low-energy effective theory is the same as the low-energy description of the KHM [73, 72] introduced in Sec. 2.1.2.

In particular, we have focused in this chapter on the $4k_b$ Mott insulator, analysed in detail in Sec. 2.3. This low-energy equivalence with the KHM may be anticipated

for the following reasons. The $4k_b$ umklapp process leads to a Mott gap Δ opening within the bonding band and at energies below this gap charge dynamics in the band become blocked. The bonding band can then be thought of as an effective spin–1/2 chain coupled to the antibonding band by inter-band exchange interactions. The resulting picture is an effective KHM where the inequivalent ladder legs are played by the bands of our model.

There are important differences between the low-energy effective KHM that emerges from our model and that studied previously [72, 73]. Firstly, in the lattice model (2.5) electron number in the bonding band is not conserved, so the low-energy limit is crucial for our considerations. Secondly, the effective exchange interaction between the bands is not *a priori* antiferromagnetic: for $V_\parallel = V_\perp = 0$ it is ferromagnetic and the resulting fixed point behaviour is a $C1S2$ phase. However, we found that when $V_\parallel, V_\perp$ are sufficiently strong the exchange interaction is antiferromagnetic and the RG flow is to a strong coupling $C1S0$ phase. Finally, in comparison to the KHM previously studied, we consider an interacting one-dimensional electron gas and so the dominant fluctuations of the $C1S0$ phase are controlled by the Luttinger parameter $K_{2,c}$ and are of superconducting PDW ($K_{2,c} > 1$) or CDW ($K_{2,c} < 1$) type.

An interesting question to consider beyond the present work is what is the effect of other types of umklapp scattering? In Ref. [1] we also examined the $3k_b + k_{ab}$ umklapp and found dominant fluctuations of an interesting "composite" order type which is difficult to understand. Is there some overlap between this order and a simple to understand order parameter, like in the KHM? Further work is needed to understand this and would be aided by the ability to calculate observables in the chain representation. The other types of umklapp such as the $2k_b + 2k_{ab}$ term should also be studied. It would also be interesting to study generalisations of KHM with $SU(2)$ symmetry broken in the spin chain, which may lead to a rich phase diagram.

Having studied the static properties of the two-leg ladder in this chapter using a combination of field theoretic and numeric techniques, we move to studying the dynamical properties of quasi-one-dimensional quantum systems in the next chapter. There, we will see that once again we can combine perturbative field theory and numerical computations to gain insight into material properties.

Appendix

2.A $2k_F$ components of the charge density

The number operators on each leg of the ladder can be expressed in terms of the bonding/antibonding fermions introduced in (2.7)

$$n_{1,j,\alpha} + n_{2,j,\alpha} = c^\dagger_{b,j,\alpha} c_{b,j,\alpha} + c^\dagger_{ab,j,\alpha} c_{ab,j,\alpha} \ , \quad n_{1,j,\alpha} - n_{2,j,\alpha} = c^\dagger_{b,j,\alpha} c_{ab,j,\alpha} + c^\dagger_{ab,j,\alpha} c_{b,j,\alpha} \ .$$

The low-energy projections of these operators in the continuum limit (2.10) are

$$\begin{aligned} n_{1,j,\alpha} + n_{2,j,\alpha} &\sim a_0 \rho^{(+)}_{0,\alpha}(x) + a_0 \left[\rho^{(+)}_{2k_b,\alpha}(x)\ e^{2ik_b x} + \rho^{(+)}_{2k_{ab},\alpha}(x)\ e^{2ik_b x} + \text{h.c.} \right] + \dots \ , \\ n_{1,j,\alpha} - n_{2,j,\alpha} &\sim a_0 \left[\rho^{(-)}_{k_b+k_{ab},\alpha}(x)\ e^{i(k_b+k_{ab})x} + \text{h.c.} \right] + \dots , \end{aligned}$$

where we've defined

$$\begin{aligned} \rho^{(+)}_{0,\alpha}(x) &= \sum_{d=b,ab} R^\dagger_{d,\alpha} R_{d,\alpha} + L^\dagger_{d,\alpha} L_{d,\alpha} \ , \quad \rho^{(+)}_{2k_d,\alpha}(x) = L^\dagger_{d,\alpha} R_{d,\alpha} \ , \\ \rho^{(-)}_{k_b+k_{ab},\alpha}(x) &= L^\dagger_{ab,\alpha} R_{b,\alpha} + L^\dagger_{b,\alpha} R_{ab,\alpha} \ . \end{aligned}$$

These operators can then be bosonised (see e.g. Sec. 2.2.1.1 and Ref. [7])

$$\begin{aligned} \rho^{(+)}_0(x) &= \sum_\alpha \rho^{(+)}_{0,\alpha}(x) \sim \frac{1}{\sqrt{2\pi}} \partial_x \Phi_{+,c} \ , \\ \rho^{(+)}_{2k_d}(x) &= \sum_\alpha \rho^{(+)}_{2k_d,\alpha}(x) \sim -2i\ e^{i\sqrt{2\pi}\Phi_{d,c}} \cos\left(\sqrt{2\pi}\Phi_{d,s}\right) \ , \quad d = 1,2 = b, ab \\ \rho^{(-)}_{k_b+k_{ab}}(x) &\sim -2i\ e^{i\sqrt{\pi}(\Phi_{+,c} - \Theta_{-,c})} \Big[\cos\left(\sqrt{\pi}[\Phi_{+,s} - \Theta_{-,s}]\right) - \cos\left(\sqrt{\pi}[\Phi_{+,s} + \Theta_{-,s}]\right) \Big], \end{aligned}$$

where $\Phi_{\pm,d} = (\Phi_{1,d} \pm \Phi_{2,d})/\sqrt{2}$ and $\Theta_{\pm,d} = (\Theta_{1,d} \pm \Theta_{2,d})/\sqrt{2}$ for $d = c, s$. We note that the oscillatory terms feature a spin boson – if there is a spin gap, the response of these terms is blocked (e.g. the two-point function will decay exponentially).

2.B $4k_F$ density components in the band picture

We now consider the $4k_F$ components of the charge density, which are a direct result of the presence of interaction terms in the Hamiltonian. We derive the interaction-

induced terms using an RG procedure. The on-site Hubbard interaction gives a contribution $S_{\rm int} = S_{\rm int}^{(1)} + S_{\rm int}^{(2)}$ to the action

$$\begin{aligned} S_{\rm int}^{(1)} &= -\frac{U}{2}\int d^2\mathbf{y}\left[c_{b,\uparrow}^\dagger c_{b,\uparrow} + c_{ab,\uparrow}^\dagger c_{ab,\uparrow}\right](\mathbf{y})\left[c_{b,\downarrow}^\dagger c_{b,\downarrow} + c_{ab,\downarrow}^\dagger c_{ab,\downarrow}\right](\mathbf{y}) \\ S_{\rm int}^{(2)} &= -\frac{U}{2}\int d^2\mathbf{y}\left[c_{b,\uparrow}^\dagger c_{ab,\uparrow} + c_{ab,\uparrow}^\dagger c_{b,\uparrow}\right](\mathbf{y})\left[c_{b,\downarrow}^\dagger c_{ab,\downarrow} + c_{ab,\downarrow}^\dagger c_{b,\downarrow}\right](\mathbf{y})\ . \end{aligned} \quad (2.56)$$

We decompose the continuum fields into high (>) and low (<) energy parts $c_d(x) = c_{d,<}(x) + c_{d,>}(x)$. The $4k_F$ components of the density operator are then found by taking the average $-\langle c_b^\dagger(x) c_b(x) S_{\rm int}\rangle_>$ and keeping only the $4k_F$ oscillatory terms. For example, we obtain a contribution

$$\frac{U}{2}\left\langle c_{b,\uparrow,<}^\dagger(x) c_{b,\uparrow,>}(x)\int dyd\tau\ c_{b,\uparrow,>}^\dagger c_{b,\uparrow,<}\left[c_{b,\downarrow,<}^\dagger c_{b,\downarrow,<} + c_{ab,\downarrow,<}^\dagger c_{ab,\downarrow,<}\right]\right\rangle_>,$$

where we now use that

$$\left\langle c_{b,\uparrow,>}(x)\ c_{b,\uparrow,>}^\dagger(\tau,y)\right\rangle_> = G_{b,>}(-\tau,x-y) = -\int_{k>\Lambda}\frac{dk}{2\pi}\ e^{-ik(x-y)-\epsilon_b(k)\tau}$$

is short ranged in τ, so it becomes

$$\frac{U}{2}c_{b,\uparrow,<}^\dagger(x)\int d\tau dy\ G_{b,>}(-\tau,x-y)c_{b,\uparrow,<}(y)\left[c_{b,\downarrow,<}^\dagger c_{b,\downarrow,<} + c_{ab,\downarrow,<}^\dagger c_{ab,\downarrow,<}\right](y).$$

Next we linearise about the Fermi surface (2.10) and replace the arguments of the left and right moving fermions by x, which is justified as the Green's function is also short-ranged in $x-y$. Implementing this procedure, we find the operators in Eqs. (2.14). Subsequent bosonisation gives

$$\begin{aligned} \rho_{4k_b}^{(+)}(x) &\sim -2UG_{b,>}(3k_b)\ e^{i\sqrt{4\pi}\Phi_{+,c}}\ e^{i\sqrt{4\pi}\Phi_{-,c}}\ , \\ \rho_{4k_{ab}}^{(+)}(x) &\sim -2UG_{ab,>}(3k_{ab})\ e^{i\sqrt{4\pi}\Phi_{+,c}}\ e^{-i\sqrt{4\pi}\Phi_{-,c}}\ , \\ \rho_{2k_b+2k_{ab}}^{(+)}(x) &\sim \mathcal{C}_{2k_b+2k_{ab}}\ e^{i\sqrt{4\pi}\Phi_{+,c}}\left[\cos\left(\sqrt{4\pi}\Phi_{-,s}\right) + \cos\left(\sqrt{4\pi}\Theta_{-,s}\right) - \cos\left(\sqrt{4\pi}\Theta_{-,c}\right)\right]\ , \\ \rho_{3k_b+k_{ab}}^{(-)}(x) &\sim \mathcal{C}_{3k_b+k_{ab}}e^{i\sqrt{4\pi}\Phi_{+,c}}\left[e^{-i\sqrt{\pi}\bar\varphi_{-,c}}\cos(\sqrt{\pi}\varphi_{-,s}) - e^{i\sqrt{\pi}\varphi_{-,c}}\cos(\sqrt{\pi}\bar\varphi_{-,s})\right]\ , \\ \rho_{k_b+3k_{ab}}^{(-)}(x) &\sim \mathcal{C}_{k_b+3k_{ab}}e^{i\sqrt{4\pi}\Phi_{+,c}}\left[e^{-i\sqrt{\pi}\varphi_{-,c}}\cos(\sqrt{\pi}\bar\varphi_{-,s}) - e^{i\sqrt{\pi}\bar\varphi_{-,c}}\cos(\sqrt{\pi}\varphi_{-,s})\right]\ , \end{aligned} \quad (2.57)$$

where $\mathcal{C}_p$ are non-universal pre-factors proportional to U for small interactions and the chiral fields are defined by $\Phi_{\pm,d} = \varphi_{\pm,d} + \bar\varphi_{\pm,d}$, $\Theta_{\pm,d} = \varphi_{\pm,d} - \bar\varphi_{\pm,d}$. Refermionizing in terms Majorana fermions (similar to Eq. (2.21)) makes the correspondence between band and chain pictures explicit (see Ref. [1]).

2.B.1 "$4k_F$" density components in the chain picture

To determine the $4k_F$ components of the charge density in the chain picture, we start from uncoupled chains (i.e. $t_\perp = 0 = V_\perp = W_{1,2}$), where the low-energy projection is

$$n_{1,l} \pm n_{2,l}\Big|_{t_\perp=0} \propto \sum_{n\in\mathbb{Z}} \widetilde{\rho}^{(\pm)}_{2nk_F}(x) e^{2ink_F x}.$$

The bosonised expressions for the $4k_F$ component of the charge density in the extended Hubbard *chain* is $\rho^{(\ell)}_{4k_F}(x) \sim (\tilde{F} e^{i4k_F x} \exp[i\sqrt{8\pi}\Phi^{(c)}_\ell] + \text{H.c.})$ where $\tilde{F}$ is a non-universal amplitude. In the rotated basis (2.19) this is

$$\widetilde{\rho}^{(+)}_{4k_F}(x) \sim 2\tilde{F}\cos(4k_F x + \sqrt{4\pi}\Phi_c)\cos(\sqrt{4\pi}\Phi_f). \tag{2.58}$$

This expression can be refermionised in terms of the Majoranas ξ^3, η introduced in Sec. 2.2.2, which give $\cos(\sqrt{4\pi}\Phi_f) = i\pi a_0 \left(\xi^3_R \xi^3_L + \eta_R \eta_L\right)$.

Next we take into account the non-zero $t_\perp$, which hybridises the η and χ^0 Majoranas. Performing the rotation in (2.22) we arrive at

$$\begin{aligned}\cos(\sqrt{4\pi}\Phi_f) \;\approx\; i\pi a_0 \Bigg\{ \xi^3_R \xi^3_L + \frac{v_s}{v_s+v_c}\Big[\xi^1_R\xi^1_L - \xi^2_R\xi^2_L - \frac{1}{2}e^{2iQx}\left(\xi^1_R - i\xi^2_R\right)\left(\xi^1_L + i\xi^2_L\right) \\ - \frac{1}{2}e^{-2iQx}\left(\xi^1_R + i\xi^2_R\right)\left(\xi^1_L - i\xi^2_L\right)\Big]\Bigg\}.\end{aligned} \tag{2.59}$$

Substitution of (2.59) into (2.58) gives the expression for the Fourier components

$$n_{1,l} \pm n_{2,l} \propto \sum_{P\in S_\pm} \rho^{(\pm)}_P(x) e^{iPx}, \tag{2.60}$$

where $S_+ \equiv \{4k_F, 4k_F \pm 2Q\}$, $S_- \equiv \{4k_F \pm Q\}$ and

$$\begin{aligned}\rho^{(+)}_{4k_F}(x) &\sim iFe^{i\sqrt{4\pi}\Phi_c}\left[\xi^3_R\xi^3_L + \frac{v_s}{v_s+v_c}\left(\xi^1_R\xi^1_L - \xi^2_R\xi^2_L\right)\right], \\ \rho^{(+)}_{4k_F\pm 2Q}(x) &\sim \frac{\mp iFv_s}{2(v_s+v_c)} e^{i\sqrt{4\pi}\Phi_c}\left(\xi^1_L \pm i\xi^2_L\right)\left(\xi^1_R \mp i\xi^2_R\right),\end{aligned}$$

with $F = \tilde{F}\pi a_0$ a non-universal constant. The analogous analysis for the antisymmetric combination of charge densities gives the following result

$$\rho^{(-)}_{4k_F\pm Q}(x) \;=\; -iF\sqrt{\frac{v_s}{2(v_s+v_c)}} e^{i\sqrt{4\pi}\Phi_c}\left[\left(\xi^1_R \mp i\xi^2_R\right)\xi^3_L + \xi^3_R\left(\xi^1_L \pm i\xi^2_L\right)\right],$$

where F is the same non-universal constant as in the $(+)$ component case.

2.C Higher harmonics of the bond-centred antibonding superconducting order parameter

To derive the higher harmonics of the bond-centred antibonding superconducting order parameter we follow the same procedure as for the charge density operator in Appendix 2.B. For this reason, we will be brief in this appendix. We consider the operator

$$\Phi_B(j) = c_{ab,\uparrow}(j)c_{ab,\downarrow}(j+1) - c_{ab,\downarrow}(j)c_{ab,\uparrow}(j+1), \tag{2.61}$$

where we split the fermion operators into high ($>$) and low ($<$) energy components and then we average over the high energy degrees of freedom in the presence of the onsite Hubbard interaction (2.56). As we are interested in the slowly decaying components of the order parameter in the $C1S0$ phase, we focus on the terms which contribute power law decay in this phase. These are given by fermion operators of the form

$$R_{ab,\downarrow}(x+a_0)L_{ab,\uparrow}(x)L^\dagger_{b,\downarrow}(x)R_{b,\downarrow}(x) \qquad L_{ab,\downarrow}(x+a_0)R_{ab,\uparrow}(x)R^\dagger_{b\downarrow}(x)L_{b,\downarrow}(x)\ .$$

Bosonising the subsequent expressions we find

$$\begin{aligned}
\langle \Phi_B S^{(1)}_{\rm int}\rangle_> &\sim e^{i\sqrt{2\pi}\Theta_{2,c}}\Big[\mathcal{C}_1\cos\Big(\sqrt{2\pi}\Phi_{1,c}+2k_bx\Big)+\mathcal{C}_2\sin\Big(\sqrt{2\pi}\Phi_{1,c}+2k_bx\Big)\Big] \\
&\qquad\times\cos\Big(\sqrt{4\pi}\Phi_{+,s}\Big)+\dots\ , \\
\langle \Phi_B S^{(2)}_{\rm int}\rangle_> &\sim -e^{i\sqrt{2\pi}\Theta_{2,c}}\Big[\mathcal{C}_3\cos\Big(\sqrt{2\pi}\Phi_{1,c}+2k_bx\Big)+\mathcal{C}_4\sin\Big(\sqrt{2\pi}\Phi_{1,c}+2k_bx\Big)\Big] \\
&\qquad\times\cos\Big(\sqrt{4\pi}\Theta_{-,s}\Big)+\dots\ ,
\end{aligned}$$

where the complex coefficients $\mathcal{C}_i$ are given in terms of $G_{ab,\uparrow,\pm}$. We have dropped terms which do not decay as a power law and also those which have a zero expectation value, e.g. contributions proportional to $\sin(\sqrt{4\pi}\Phi_{+,s})$ or $\sin(\sqrt{4\pi}\Theta_{-,s})$. Combining the two contributions gives the following result for the slowly decaying part of the low-energy projection of Φ_B in the $C1S0$ phase

$$\begin{aligned}
\langle \Phi_B S_{\rm int}\rangle_> \sim\ & e^{i\sqrt{2\pi}\Theta_{2,c}}\Big\{\Big[\mathcal{C}_1\cos\Big(\sqrt{4\pi}\Phi_{+,s}\Big)-\mathcal{C}_3\cos\Big(\sqrt{4\pi}\Theta_{-,s}\Big)\Big]\cos\Big(\sqrt{2\pi}\Phi_{1,c}+2k_bx\Big) \\
&+\Big[\mathcal{C}_2\cos\Big(\sqrt{4\pi}\Phi_{+,s}\Big)-\mathcal{C}_4\cos\Big(\sqrt{4\pi}\Theta_{-,s}\Big)\Big]\sin\Big(\sqrt{2\pi}\Phi_{1,c}+2k_bx\Big)\Big\}.
\end{aligned}$$

3. Quasi-particle breakdown in the quasi-one-dimensional Ising ferromagnet $CoNb_2O_6$

3.1 Background and introduction

3.1.1 Quasi-particle breakdown

Quasi-particles often play a central role in condensed matter physics: from the quasi-electrons/holes of Fermi liquid theory to Cooper pairs in conventional superconductors and magnons in a quantum magnet. In quantum magnets, spin wave theory and the conventional picture of long-lived well-defined excitations has been shown to be a good description of the static and dynamic properties of a large number of quantum magnets [100, 101, 102, 103, 104, 105, 106, 107]. However, there has recently been increasing interest [108, 109, 110, 111, 112, 113, 114, 115, 116, 117, 118, 119, 120, 121, 122, 123, 124, 125, 126, 127, 128, 129, 130] in spin systems which do not have well-defined quasi-particle excitations as a result of "quasi-particle breakdown" – a many-body quantum mechanical effect which results in the spontaneous decay of excitations.

The spontaneous decay of excitations in such spin systems has humble origins: at a given energy and momentum the single particle mode loses intensity and broadens significantly as a result of kinematically allowed decay processes into the multi-particle continua. In comparison to the finite lifetime of spin excitations caused by scattering with thermal excitations, quasi-particle breakdown can occur at zero temperature (see e.g. Ref. [128] for a recent review). The combination of kinematic considerations and the existence of matrix elements rules out quasi-particle breakdown in many of the most studied models of quantum magnetism (such as the transverse field Ising model

or the Heisenberg XXZ model) except when additional symmetry breaking terms are added [117, 118, 128].

3.1.2 $CoNb_2O_6$: an Ising ferromagnet

A paradigm of low-dimensional quantum magnetism, the transverse field Ising chain (TFIC) [20, 22, 23], has only recently been (approximately) realised in an experimental system. The quasi-one-dimensional ferromagnet $CoNb_2O_6$ is formed from weakly-coupled [131] zig-zag chains which form a triangular lattice in the plane perpendicular to the chains, see Fig. 3.1. In this material, a phase transition is observed between a spontaneously ordered magnetised state and the quantum paramagnet at an experimentally achievable critical transverse field of $B_C \approx 5.5$T. In the ordered phase, weak interchain couplings (J_1, J_2 in Fig. 3.1) give rise to a longitudinal mean field and the resulting rich spectrum of bound states, predicted 25 years ago by Zamolodchikov [132], has been observed with inelastic neutron scattering (INS) [133] and THz spectroscopy [134].

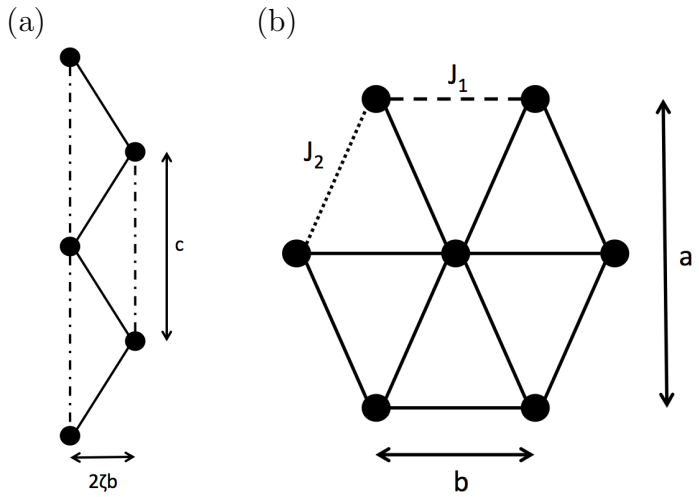

Figure 3.1: (a) The one-dimensional geometry of the Cobalt chains in $CoNb_2O_6$ along the c-axis. Nearest-neighbour bonds are shown by solid lines and next-nearest neighbour bonds are shown with dot-dashed lines. The buckling parameter $\zeta \approx 0.165$ [131]. (b) The geometry of $CoNb_2O_6$ in the a-b plane perpendicular to the chain direction c. In this chapter we consider uncoupled chains, so we approximate all the bonds shown by $J_1 = J_2 = 0$.

Just how closely $CoNb_2O_6$ realises the TFIC is still under active investigation [131, 133, 135]; the most recent INS studies [131] have focussed on the quantum param-

agnetic phase ($B > B_C$) with the aim of quantifying the interchain couplings and the extent of geometric distortion of the triangular crystal structure (see Fig. 3.1(b)). The effects of interchain couplings are predicted to be most strongly felt in the paramagnetic phase [136], whilst geometric distortion is thought to lead to a number of possibilities for long-range spin order in the a–b plane [137]. As we discussed in Chapter 1, INS in the paramagnetic phase should be dominated by a sharp high-intensity single particle mode and the remainder of the spectral weight is found in low-intensity scattering from the multi particle continuum [35]. We can think of the excitations in the paramagnetic phase as spin flips, dressed by quantum fluctuations (which are suppressed in the $B \to \infty$ limit).

The dispersion observed in INS studies suggests that additional terms must be present in the Hamiltonian, beyond the TFIC [131]. This is also consistent with numerical studies [135], the value of the critical field in comparison to the Ising exchange parameter [133] and the unusual "anomalous broadening" region seen in the INS experiments. A natural first step away from the TFIC is to consider a strongly anisotropic nearest-neighbour XXZ interaction. The zig-zag crystal structure along the c-axis, Fig. 3.1(a), also suggests that the next-nearest neighbour spin interactions should feature in the Hamiltonian. Due to the longer exchange pathway (Co–O–O–Co compared to Co–O–Co) we expect these terms to be weaker. Putting these terms together, we arrive at a "minimal spin model" for $CoNb_2O_6$:

$$\begin{aligned} H &= H_{TFIC} + H_{XY} + H_{NNN}, \\ H_{TFIC} &= J\sum_{\ell} S^z_{\ell} S^z_{\ell+1} + h\sum_{\ell} S^x_{\ell}, \\ H_{XY} &= J\sum_{\ell} \lambda_2\left(S^x_{\ell} S^x_{\ell+1} + S^y_{\ell} S^y_{\ell+1}\right), \\ H_{NNN} &= J\sum_{\ell} \lambda_1 S^z_{\ell} S^z_{\ell+2} + \lambda_3\left(S^x_{\ell} S^x_{\ell+2} + S^y_{\ell} S^y_{\ell+2}\right), \end{aligned} \tag{3.1}$$

where the λ_i are expected to be small, in keeping with the arguments presented above. The transverse field $h = g\mu_B B$ is related directly to the applied magnetic field B and the g-factor in the x direction. The buckled geometry of the Co chains in $CoNb_2O_6$ does not have an effect on the Hamiltonian (we assume no dimerisation of the exchange interactions), but can be seen in INS data.[†] Let us briefly define some

[†]The buckled geometry is responsible for a "ghost mode" appearing in the INS data when the

terminology: we will often refer to the Ising easy axis direction z as the "longitudinal" direction, whilst the applied field direction x is the "transverse" direction.

3.1.3 This chapter

In this chapter we will study the one-dimensional quantum spin Hamiltonian (3.1) and show that it captures the essential one-dimensional physics of $CoNb_2O_6$. To do so, we will begin by calculating the single particle dispersion of the model (3.1) and we fit this to the "true" dispersion extracted from INS data. Once we have fixed the exchange parameters, we will focus on understanding the physics behind the "anomalous broadening" region seen in INS data – where in part of the Brillouin zone the single particle mode is observed to broaden and lose intensity. We present high-resolution INS data from the R. Coldea group in the Clarendon Laboratory, University of Oxford, focussed on this region which shows that the single particle mode has almost vanished, so severe is the broadening. Supported by large scale exact diagonalisation studies, we attribute this broadening to the phenomena of "quasi-particle breakdown" – a small misalignment of the magnetic field and the overlap of the single particle mode with the two particle continuum conspire to allow the spontaneous decay of single particle excitations. We show that a small misalignment $\theta \approx 1.5^\circ$ is sufficient to explain the experimental observations.

This chapter is laid out as follows: in Sec. 3.2 we detail the calculation of the single-particle dispersion for the spin model (3.1) using diagrammatic perturbation theory. Section 3.3 introduces the dynamical structure factor and its relation to INS experiments, explaining how we fit the calculated dispersion to INS data. Having fit the exchange parameters, we also present the DSF of the model (3.1) calculated by exact diagonalisation. Following this, we focus on the "anomalous broadening" observed in experiment, presenting high-resolution INS data and our explanation in Sec. 3.4. This section also contains exact diagonalisation results for the DSF which clearly show the broadening of the single particle mode. Section 3.5 contains our conclusions and two appendices contain technical points of our analysis.

momentum transfer in the b direction, q_b, is non-zero. The ghost mode is shifted by $2\pi/c$ compared to the unbuckled result and has a reduced intensity, which depends on q_b.

3.2 One-dimensional quantum model of $CoNb_2O_6$

A common first approach to calculating the single particle dispersion of models such as (3.1) is linear spin wave theory (see the data parameterisation of Ref. [131]). Generally this is not a reliable approach for one-dimensional quantum systems – in this case it *can* parameterise the data at a fixed field h, but requires quite different exchange parameters at different transverse fields. This inconsistency is likely due to the higher order terms in $1/S$ not being negligible. We wish to find a *consistent* set of parameters which work for all values of the transverse field, for this reason we take a different approach to the problem and base our calculation on a self-consistent perturbative treatment of a fermionic theory [138].

We begin by performing a sequence of transformations, presented in detail in Appendix 3.A, after which we obtain a fermionic theory *exactly equivalent* to (3.1). In the fermion theory, parts of the interactions in H_{XY} and H_{NNN} have been treated exactly. The Hamiltonian now takes the form

$$\begin{aligned} H &= \sum_k E_k a_k^\dagger a_k + \frac{J}{L}\sum_{k_i} V_2(\mathbf{k}) a_{k_1}^\dagger a_{k_2}^\dagger a_{-k_3} a_{-k_4} \\ &+ \frac{J}{L}\sum_{k_i}\left\{ V_0(\mathbf{k}) a_{k_1}^\dagger a_{k_2}^\dagger a_{k_3}^\dagger a_{k_4}^\dagger + V_1(\mathbf{k}) a_{k_1}^\dagger a_{k_2}^\dagger a_{k_3}^\dagger a_{-k_4} + \text{H.c.}\right\} \end{aligned} \tag{3.2}$$

where the vertex functions $V_i(\mathbf{k}) = V_i(k_1, k_2, k_3, k_4)$ are given in Appendix 3.B, L is the system size (number of sites in the spin chain) and the single-particle dispersion relation is

$$E_k = \sqrt{\left[A_k + \sum_q \Theta_1(k,q)\right]^2 + \left[B_k + \sum_q \Theta_2(k,q)\right]^2} \tag{3.3}$$

with A_k, B_k and $\Theta_{1,2}$ defined in Appendix 3.A. In the $h \to \infty$ limit, the single particle excitations $a_k^\dagger$ are formed from spin flips in the completely polarised state $|\leftarrow_x \ldots \leftarrow_x\rangle$; at finite transverse field ($h > h_C$) these become dressed by quantum fluctuations.

The four-fermion interaction terms in the Hamiltonian (3.2) will be treated perturbatively in the following calculation, consistent with the assumption that $\lambda_i \ll 1$. It should be emphasised that this perturbative treatment is not equivalent to simply treating H_{XY} and H_{NNN} directly in perturbation theory: parts of these interaction

terms have been treated exactly through the self-consistent Bogoliubov transformation performed in Appendix 3.A. We now continue by outlining how we calculate the single particle dispersion by inverting Dyson's equation.

3.2.1 Calculation of the single particle dispersion

To zeroth order in perturbation theory, the single particle dispersion is given by Eq. (3.3). To take into account the interaction terms present within the Hamiltonian (3.2), we calculate the first order self-energy corrections to the Green's functions and obtain the modified single-particle dispersion by resumming an infinite series of diagrams by solving Dyson's equation. This perturbative calculation is well controlled provided the thermal energy $k_B T$ is smaller than the single particle gap $E_{k=0}$; we focus on the behaviour within the paramagnetic phase and away from the critical point to fulfill this criterion. We will see good agreement between the dispersion calculated by perturbation theory and that obtained from exact diagonalisation. We don't expect our calculation to predict with any great accuracy the value of the critical applied field ($B_C \approx 5.5$T) as the perturbative expansion becomes uncontrolled in the vicinity of the critical point.

We begin by discussing the formalism we use for calculating the modified single particle dispersion and following this we calculate the first order contributions to the self-energy and hence the modified single particle dispersion.

3.2.1.1 Formalism

The Hamiltonian (3.2) does not conserve the number of quasi-particles $a_k^\dagger$, so the imaginary time Green's function is given by a 2×2 matrix:

$$\mathbf{g}(i\omega_n, k) = -\int_0^\beta d\tau e^{i\omega_n \tau} \mathbf{g}(\tau, k),$$
$$\mathbf{g}(\tau, k) = \left\langle T_\tau \begin{bmatrix} a_k(\tau)a_k^\dagger(0) & a_k(\tau)a_{-k}(0) \\ a_{-k}^\dagger(\tau)a_k^\dagger(0) & a_{-k}^\dagger(\tau)a_{-k}(0) \end{bmatrix} U(\beta) \right\rangle,$$

where $\tau = it$, T_τ denotes time-ordering in imaginary time and ω_n are Matsubara frequencies. The τ-evolution operator is given by

$$U(\beta) = T_\tau \exp\left[-\int_0^\beta d\tau_1 H_{\text{int}}(\tau_1)\right]. \tag{3.4}$$

and the expectation value is

$$\langle \mathcal{O} \rangle = \frac{\mathrm{Tr}[\mathcal{O} e^{-\beta H}]}{\mathrm{Tr}[e^{-\beta H}]}, \qquad \beta = \frac{1}{k_B T}. \tag{3.5}$$

The non-interacting (zeroth-order) Green's functions are given by

$$\mathbf{g}_0(i\omega_n, k) = \begin{bmatrix} G_0(i\omega_n, k) & 0 \\ 0 & -G_0(-i\omega_n, -k) \end{bmatrix}, \tag{3.6}$$

where the bare Green's function $G_0(i\omega, k)$ takes the usual form

$$G_0(i\omega_n, k) = \frac{1}{i\omega_n - E_k}. \tag{3.7}$$

The full Green's function obeys Dyson's equation

$$\mathbf{g}^{-1}(i\omega_n, k) = \mathbf{g}_0^{-1}(i\omega_n, k) - \mathbf{\Sigma}(i\omega_n, k), \tag{3.8}$$

which defines the single-particle self-energy $\mathbf{\Sigma}$. The single-particle self-energy is formed from the same diagrams as the full Green's function with the two external legs truncated. We highlight that the solution of Dyson's equation with a truncated self-energy (e.g. only considering diagrams to a given order) corresponds to the summation of an infinite series of diagrams for the Green's function.

By inverting the Dyson equation (3.8) we obtain an expression for the full Green's function in terms of the components of the self-energy matrix $(\mathbf{\Sigma})_{ij}$

$$\begin{aligned} \mathbf{g}(i\omega_n, k) \;=\; & \begin{bmatrix} i\omega_n + E_k + (\mathbf{\Sigma})_{11} & (\mathbf{\Sigma})_{21} \\ (\mathbf{\Sigma})_{12} & i\omega_n - E_k + (\mathbf{\Sigma})_{22} \end{bmatrix} \\ & \times \frac{1}{(i\omega_n)^2 - [E_k + (\mathbf{\Sigma})_{11}]^2 - |(\mathbf{\Sigma})_{12}|^2}\ , \end{aligned} \tag{3.9}$$

where the components of the self-energy $(\mathbf{\Sigma})_{ij} \equiv (\mathbf{\Sigma}(i\omega_n, k))_{ij}$ are functions of the frequency and momentum. In Eq. (3.9) we have assumed that the self-energy matrix satisfies $(\mathbf{\Sigma})_{21} = (\mathbf{\Sigma})_{12}^* = -(\mathbf{\Sigma})_{12}$ and $(\mathbf{\Sigma})_{11} = -(\mathbf{\Sigma})_{22}$, which will be verified to first order in the subsequent calculation.

For a first order calculation, we will find that the self-energy matrix is frequency independent, and so the single-particle dispersion is given by the position of the pole in the Green's function:

$$\varepsilon_k = \sqrt{[E_k + (\mathbf{\Sigma}(k))_{11}]^2 + |(\mathbf{\Sigma}(k))_{12}|^2}\ . \tag{3.10}$$

At higher orders in perturbation theory the self-energy matrix becomes frequency dependent and has additional singularities associated with multi particle excitations. We now calculate the self-energy matrix to first order in perturbation theory.

3.2.1.2 First order self-energy corrections

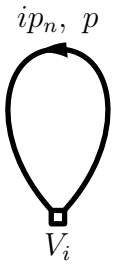

Figure 3.2: The general form of the self-energy diagram at first order. $V_i = V_2$ for $g^{dd}(i\omega_n, k)$ $(d = 1, 2)$ and $V_i = V_1$ for $g^{12}(i\omega_n, k)$.

At first order, the diagrams that contribute to the self-energy are all of the form presented in Fig. 3.2. We begin by considering the diagonal matrix elements: the vertex in the self energy diagram is then given by $V_i = V_2$. This diagram can be obtained by taking the first-order connected diagram for the propagator $\langle a_k(\tau)a_k^\dagger(0)\rangle$ and removing the external legs. The diagram corresponds to

$$\begin{aligned}(\mathbf{\Sigma}(k))_{11} &= -\sum_{ip_n,p}\frac{4J}{\beta L}V_2(k,p,-k,-p)G_0(ip_n,p)e^{ip_n0^+},\\ &= \sum_p 4JV_2(k,p,-p,-k)\frac{n_F(E_p)}{L},\end{aligned} \tag{3.11}$$

where $n_F(E_p) = 1/(\exp(\beta E_p) + 1)$ is the Fermi-Dirac distribution, which naturally arises from the Matsubara frequency summation. The remaining momentum sum in Eq. (3.11) is performed numerically as both the dispersion relation E_p and the vertex function V_2 depend upon the Bogoliubov parameter θ_k which is numerically determined from the self-consistency condition (3.24). At first order, $(\mathbf{\Sigma}(k))_{11} = -(\mathbf{\Sigma}(k))_{22}$ follows from the same diagrams contributing to both matrix elements.

The off-diagonal elements of the self-energy matrix are given by Fig. 3.2 with $V_i = V_1$ or $V_i = V_1^* = -V_1$. From this, it follows that $(\mathbf{\Sigma}(k))_{12} = -(\mathbf{\Sigma}(k))_{21}$ and the off-diagonal self-energy is given by

$$(\mathbf{\Sigma}(k))_{12} = -6\sum_p JV_1(k,-k,p,-p)\frac{n_F(E_p)}{L}. \tag{3.12}$$

From Eqs. (3.11)–(3.12) we see that the self-energy is frequency independent at first order in perturbation theory, hence Eq. (3.10) applies for calculating the modified single particle dispersion. The elements of the self-energy matrix are proportional to $J\lambda_i n_F(E_p)$; the strongest corrections to the dispersion occur close to the minima of the dispersion (e.g. in the vicinity of the single particle gap) or when the system

is at high temperatures. The single-particle dispersion with first order self-energy corrections is given by

$$\varepsilon_k = \pm\sqrt{\left(E_k + 4J\sum_p V_2(k,p,-p,-k)\frac{n_F(E_p)}{L}\right)^2 + \left|6J\sum_p V_1(k,-k,p,-p)\frac{n_F(E_p)}{L}\right|^2}. \tag{3.13}$$

We continue by discussing the dynamical structure factor, presenting a brief review of previous results before showing inelastic neutron scattering data for $CoNb_2O_6$ and explaining how we fix the exchange parameters of our model using this data.

3.3 Dynamical Structure Factor

The dynamical structure factor (DSF) $S(\omega, \mathbf{Q})$ is a frequency (ω) and momentum ($\mathbf{Q}$) resolved probe of the properties of a magnetic system

$$S^{\alpha\beta}(\omega, \mathbf{Q}) = \frac{1}{L}\int_{-\infty}^{\infty} \mathrm{d}t \sum_{\ell,\ell'} e^{i\mathbf{Q}\cdot(\mathbf{r}_\ell - \mathbf{r}_{\ell'})} e^{i\omega t}\langle S^\alpha_\ell(t) S^\beta_{\ell'}\rangle, \tag{3.14}$$

where $S^\alpha_\ell(t) = \exp(iHt)S^\alpha_\ell \exp(-iHt)$ is the time-evolved α-component of the spin operator on site $\mathbf{r}_\ell$ of the lattice and $\langle\mathcal{O}\rangle$ denotes the thermal trace (3.5). The intensity measured in inelastic neutron scattering experiments is directly proportional to the DSF [139, 140].

Analytical calculation of the DSF (3.14) is in general a very difficult task. Take the case of the transverse field Ising chain (TFIC): as was discussed in Chapter 1, the ground state properties were calculated by Pfeuty in 1970 [20] and the model can be exactly solved by Jordan-Wigner transformation. However, free fermion techniques give only the transverse component S^{xx} of the DSF (3.14) exactly [32, 33, 34] and the calculation of the other components is hindered by the non-local Jordan-Wigner strings of the other spin components in the fermion language. Calculation of the other components of the DSF in the 1D TFIC remains an area of active research [35, 36].

In recent years there has been much progress in the calculation of dynamical correlation functions in certain classes of 1D quantum integrable models, including the Heisenberg model [141] and the XXZ model [142, 143]. Certain components of the DSF may be computed numerically [17] at zero-temperature using exact results from

algebraic Bethe ansatz. In models with integrable low-energy effective field theories finite-temperature dynamical correlation functions can be computed [144, 145].

Methods not reliant upon integrability of the underlying model, such as conventional perturbation theory [138, 146], can give (perturbative) expressions for certain components of the DSF (like in the TFIC, those local in the fermion basis). Other calculable quantities of interest, such as the threshold singularities which occur at the onset of support in the (ω, Q)-plane, can sometimes be calculated phenomenologically using the non-linear Luttinger liquid theory [147].

In general, the calculation of all of the components of the DSF is reserved for numerical techniques. In quasi-one-dimensional quantum systems there are three main numerical methods of choice: (i) quantum Monte Carlo [148] with analytic continuation back to real time; (ii) the density matrix renormalization group algorithm [149, 150, 151]; (iii) exact diagonalisation [54, 153]. In the remainder of this chapter, we will restrict ourselves to small system sizes and study the dynamical properties of our model (3.1) using exact diagonalisation.

Let us now briefly recap known results of the TFIC in a strong transverse field to explain how we fit the single particle dispersion, calculated in the previous section, to the experimental inelastic neutron scattering data.

3.3.1 DSF of the transverse field Ising chain in a strong transverse field

Let us consider the DSF of the TFIC in a strong transverse field, which puts us deep within the paramagnetic phase with a single-particle gap much larger than the bandwidth of the single particle dispersion. In particular we will be interested in the DSF below the energy cost of two-particle excitations. This eliminates the need to study the transverse component, for which exact results are known [32, 33, 34], as this has only a response above the two-particle gap (as the transverse spin component is a density operator in the fermion language).

Instead we consider the remaining diagonal components of the DSF $S^{\alpha\alpha}(\omega, Q)$ with $\alpha = y, z$. Whilst there are no known exact expressions for this correlation

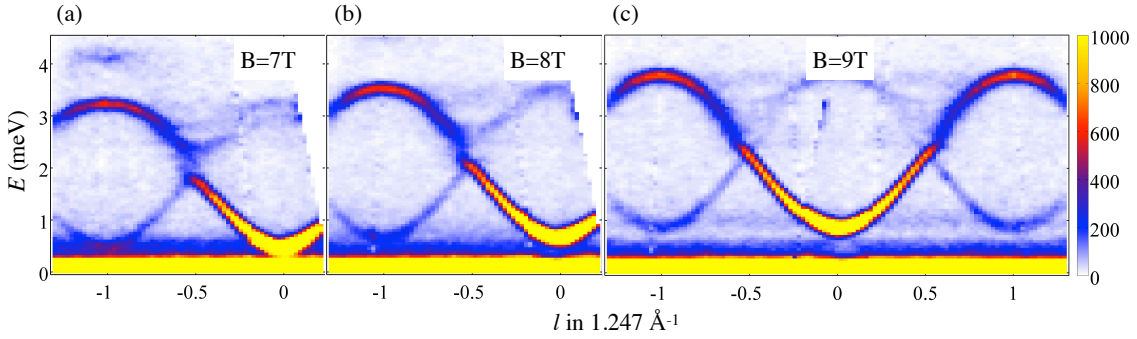

Figure 3.3: Inelastic neutron scattering data for the dispersion along the chain direction l at (a) $B = 7$T; (b) $B = 8$T; (c) $B = 9$T. From this data the single particle dispersion ("Data" in Fig. 3.4) was extracted. We highlight the"anomalous broadening region" at $l \approx -0.55$ where the dispersion loses weight and significantly broadens. The incident neutron energy was $E_i = 10$meV with a fullwidth at half-maximum resolution of $\Delta E = 0.21(1)$ meV on the elastic line.

function, the one-particle contributions are known [35]

$$S^{zz}(\omega, Q) = \left[1 - \left(\frac{J}{h}\right)^2\right]^{1/4} \frac{1}{\epsilon(Q)} \delta[\omega - \epsilon(Q)] \,, \tag{3.15}$$

$$S^{yy}(\omega, Q) = \left[1 - \left(\frac{J}{h}\right)^2\right]^{1/4} \epsilon(Q) \delta[\omega - \epsilon(Q)] \,, \tag{3.16}$$

where the single particle dispersion in the TFIC is given by

$$\epsilon(Q) = \sqrt{h^2 - hJ\cos(Q) + \frac{J^2}{4}} \,. \tag{3.17}$$

This shows that the low-energy DSF is dominated by a delta-function peak along the single particle dispersion in the (ω, Q)-plane.

We will use this fact in $CoNb_2O_6$ where we expect INS in the paramagnetic phase to have a sharp response along the single particle dispersion in the (ω, Q)-plane (in analogy to the TFIC). This allows us to extract the true single particle dispersion (to within experimental resolution) for the excitations in $CoNb_2O_6$. We can then fit the results of our perturbative calculation (3.13) to that extracted from INS data at a number of transverse field strengths to consistently fix the exchange parameters of the model (3.1).

3.3.2 Fitting the single particle dispersion to experiment

In Fig. 3.3 we present inelastic neutron scattering data for the excitations along the chains (the momentum along the chain $Q = 2\pi/cl$ with $2\pi/c = 1.247\text{Å}^{-1}$) of $CoNb_2O_6$

for an applied transverse field of $B = 7, 8, 9$T. As expected from the previous subsection, the data shows a single sharp quasi-particle excitation throughout the single unit cell Brillouin zone (except for a feature close to $l = -0.55$, which we will come to later) with additional light scattering from multi particle continua. From the INS data we extract the true single particle dispersion from the full (3D) parameterisation of the data (see e.g. Ref. [131] for such a parameterisation).

Taking the true single particle dispersion, we use a simulated annealing algorithm [154] to fit the results of our perturbative calculation (3.13) at the three different applied fields. We run the simulated annealing algorithm in the $\{\lambda_1, \lambda_2, \lambda_3\}$ parameter space, varying the values of J and $g\mu_B$ between runs and choose a set of parameters which consistently describes the single particle dispersion across the range of transverse field strengths. We find the following set of fit parameters:

$$\begin{aligned} &J = -2.88\text{meV}, \quad g = 3.21, \\ &\lambda_1 = -0.135, \quad \lambda_2 = 0.205, \quad \lambda_3 = -0.003\ . \end{aligned} \tag{3.18}$$

Comparisons between the calculated single particle dispersion (solid line), exact diagonalisation results for the Hamiltonian (3.1) with the above parameters and the extracted data from inelastic neutron scattering (Fig. 3.3) (dotted line) are shown in Figs. 3.4(a)-(c), where we see that the perturbative calculation overestimates the single particle dispersion at $l \approx 1$ for $B = 7$T, but exact diagonalisation results match very well the experimental data for all fields. The perturbative calculations allows us to estimate the critical transverse field: the parameter set (3.18) leads to a critical field strength of $h_C = 0.915$meV, corresponding to a magnetic field of $B_C \sim 4.92$T. We remind the reader that our perturbative calculation is not controlled in the vicinity of the critical point, but this value broadly agrees with the experimental estimate of the 1D critical field [133].

In the following, we will use the parameter set (3.18) in exact diagonalisation studies of the DSF. By comparing the exact diagonalisation results to the INS data, we will lend further support to our claim that the model (3.1) with fit parameters (3.18) gives a good description of the one-dimensional physics of $CoNb_2O_6$.

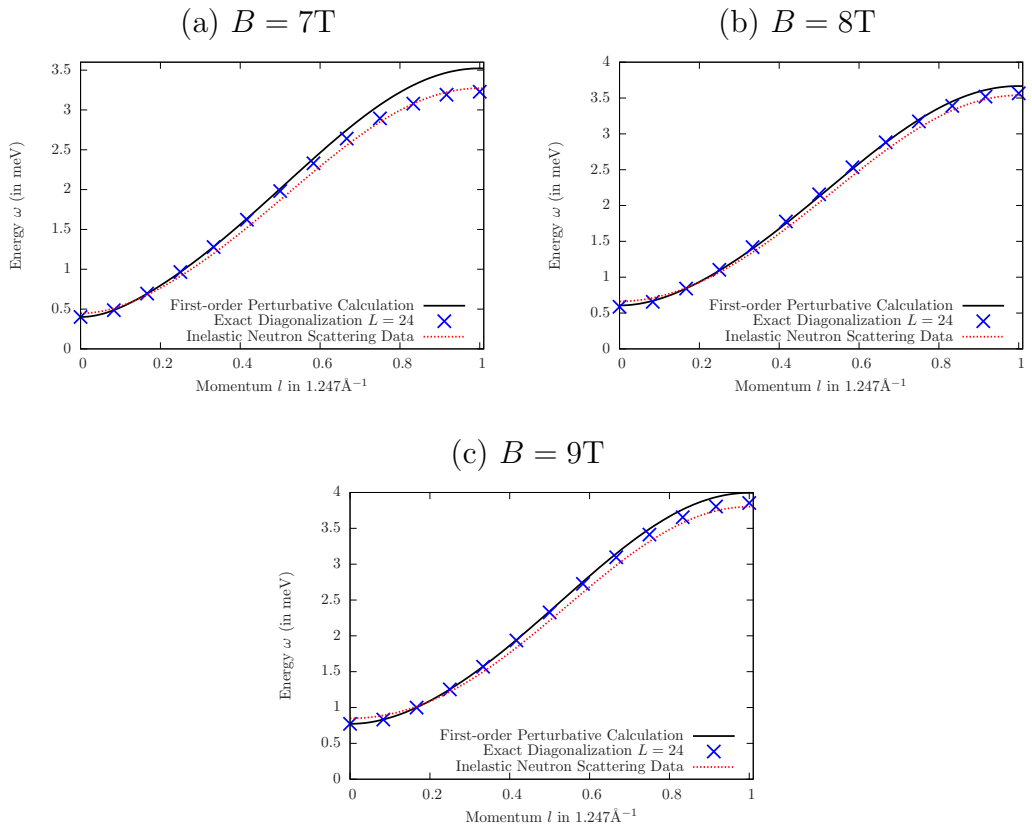

Figure 3.4: Comparison between the single particle calculated by the perturbative calculation at $T \approx 50$mK (solid line), exact diagonalisation of the $L = 24$ site system (blue crosses) and the single particle dispersion extracted from the inelastic neutron scattering data of Fig. 3.3 (dotted line).

3.3.3 Full diagonalisation: eigenvalue spectrum

Before getting to the DSF, we consider the spectrum of eigenvalues of the spin model (3.1) obtained by fully diagonalising the Hamiltonian. This will be useful in our future discussions of the DSF, particularly in describing the unusual broadening region (see Sec. 3.4). Figures 3.5(a)–(c) present the spectrum of the Hamiltonian for $B = 7, 8, 9$T, with the symmetry of each state under spin inversion $S_i^z \to -S_i^z$ labelled. The single particle mode (solid line) and the multi-particle continuum (grey shaded region) are highlighted. For all three cases we see that the single particle mode grazes the two-particle continuum in the region $l = 0.5 - 0.7$, with the three-particle continuum also close by at lower fields (within ~ 0.25meV at $B = 7$T). This overlapping of the single particle mode with the multi particle continuum is a result of physics beyond the transverse field Ising chain, where this cannot occur in the

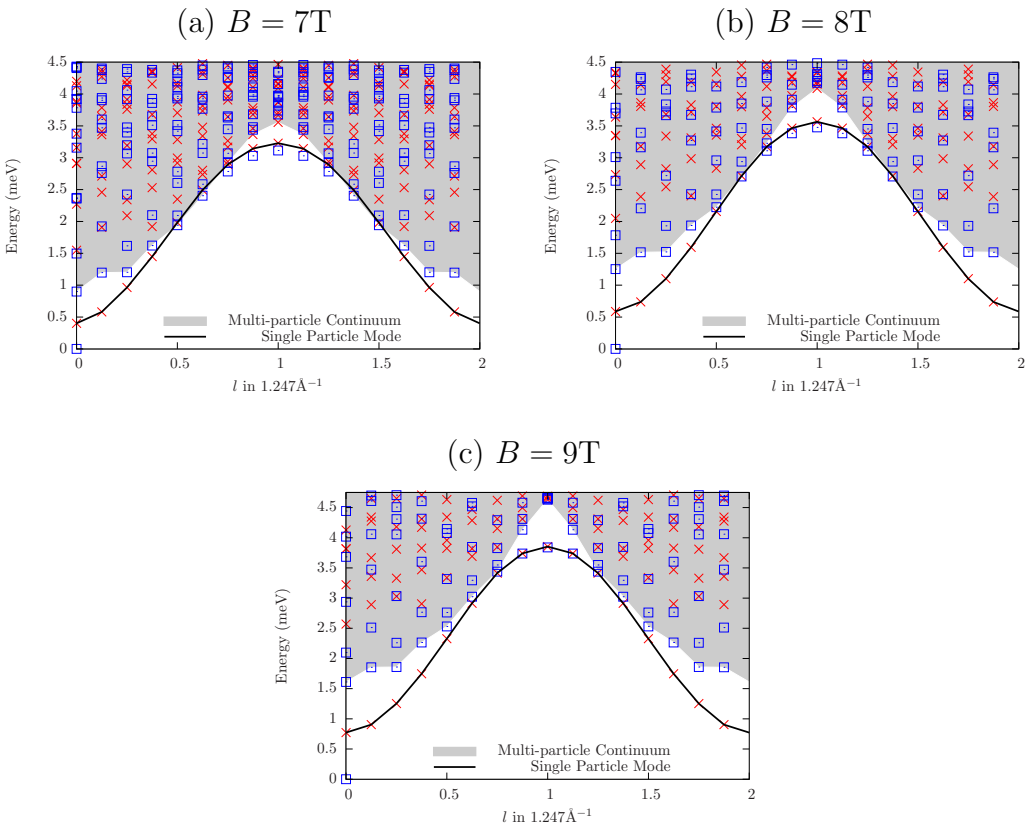

Figure 3.5: We present the spectrum of the Hamiltonian (3.1) with parameters (3.18) obtained by exact diagonalisation of the $L = 16$ chain with (a) $B = 7$T; (b) $B = 8$T and (c) $B = 9$T. The parity under spin inversion $S^z \to -S^z$ of each state is labelled by crosses (odd) and squares (even). We highlight the single particle mode (SPM) (solid line) and the multi-particle continuum (shaded region).

paramagnet due to kinematic constraints enforcing $E_k + E_{q-k} > E_k$ for all k, q.

3.3.4 Lanczos diagonalisation: the DSF

Having examined the spectrum of the Hamiltonian, we next turn our attention to the DSF. To study the DSF, we move away from full diagonalisation of the Hamiltonian and use Lanczos based techniques to iteratively diagonalise the Hamiltonian, allowing us to work on much larger system sizes (up to $L = 28$, where each momentum block of the Hamiltonian has dimension $\approx 2^{28}/28 = 9.6 \times 10^6$). This significantly increases our momentum and frequency resolution, which will be particularly useful for examining the anomalous broadening region.

3.3.4.1 The Lanczos algorithm

The exponentially increasing size of the Hilbert space with length of the spin chain means that complete diagonalisation of the Hamiltonian rapidly becomes too computationally and memory intensive to be performed. Whilst full diagonalisation gives the complete spectrum of eigenvalues and, if required, eigenvectors, this is usually much more information than we require for studying the ground state properties of a system. In such cases "iterative diagonalisation methods" can be used to target one, or a few, states of the system. Using this in combination with sparse matrix methods allows one to study spin chains approximately twice as large as those accessible with full diagonalisation.

The simplest iterative technique is the "power method" which targets the eigenvector of the matrix H with the extremal eigenvalue. We begin by taking a random vector in the Hilbert space $|v_0\rangle$; this should have a non-zero overlap with the eigenvector with extremal eigenvalue $|0\rangle$. We now repeatedly apply the matrix H to our initial vector:

$$|v_n\rangle \;=\; \sum_\ell H^n|\ell\rangle\langle\ell|v_0\rangle = \sum_\ell \lambda_\ell^n|\ell\rangle\langle\ell|v_0\rangle.$$

which in the limit $n \to \infty$ clearly converges to the eigenvector with extremal eigenvalue. The subspace formed from the vectors at each step of the power method

$$\Big\{|v_0\rangle, H|v_0\rangle, \ldots, H^n|v_0\rangle\Big\}$$

is called the nth Krylov subspace. The vectors in the Krylov subspace are not orthonormal and so do not form a basis. Orthogonalising this subspace to form a basis is the central idea of Lanczos matrix diagonalisation [152].

The Lanczos algorithm for targeting the low-energy states has the following steps:

1. Choose a vector with non-zero overlap with the ground state (normally we choose a normalised random vector $|u_0\rangle$ for this purpose).

2. Generate a basis by orthogonalising the Krylov vectors. This basis is generated recursively using

$$\begin{aligned} |u_{n+1}\rangle &= H|u_n\rangle - a_n|u_n\rangle - b_n^2|u_{n-1}\rangle, \\ a_n &= \frac{\langle u_n|H|u_n\rangle}{\langle u_n|u_n\rangle}, \qquad b_n^2 = \frac{\langle u_n|u_n\rangle}{\langle u_{n-1}|u_{n-1}\rangle}, \end{aligned} \tag{3.19}$$

with $b_0 = 0$ and $|u_{-1}\rangle = 0$.

3. Continue iterating the above until $||u_n|| < \epsilon$, where ϵ is your Lanczos tolerance.

4. The Lanczos Hamiltonian $\mathbb{T}_n$ is the tridiagonal matrix with $\{a_0, \ldots, a_n\}$ on the lead diagonal and $\{b_1, \ldots, b_n\}$ on the neighbouring diagonals. This is diagonalised using standard routines to find the energies and eigenvectors.

In a *real* numerical implementation of the Lanczos algorithm there is an additional step which significantly increases both memory usage and the computational complexity of the algorithm. The accumulation of floating point errors in the computation means that the Lanczos vectors rapidly lose orthogonality – one must reorthogonalise the vectors using e.g. Gram-Schmidt reorthogonalisation. This requires storing all the Lanczos vectors (rather than just the $n-1, n, n+1$ vectors) and performing matrix-matrix-vector multiplication.

3.3.4.2 The continued fraction representation of the DSF

One of the advantages of the Lanczos matrix diagonalisation is that it allows for easy computation of dynamical correlation by the *continued fraction representation*, which we will derive here following Ref. [54]. We wish to calculate correlation functions of the form[†]

$$I(\omega) = -\frac{1}{\pi}\lim_{\eta\to 0}\mathrm{Im}\langle\Psi_0|O^\dagger\frac{1}{\omega + E_0 + i\eta - H}O|\Psi_0\rangle,$$

where O is an operator, E_0 is the ground state energy and $|\Psi_0\rangle$ is the ground state.

Let us define the normalised state

$$|\phi_0\rangle = \frac{O|\Psi_0\rangle}{\sqrt{\langle\Psi_0|O^\dagger O|\Psi_0\rangle}},$$

and $z = \omega + E_0 - i\eta$. The correlation function is then written as

$$I(\omega) = -\frac{1}{\pi}\lim_{\eta\to 0}\mathrm{Im}\langle\phi_0|\frac{1}{z-H}|\phi_0\rangle\langle\Psi_0|O^\dagger O|\Psi_0\rangle.$$

The matrix $z - H$ trivially satisfies the identity

$$\sum_n (z-H)_{mn}(z-H)^{-1}_{np} = \delta_{m,p},$$

[†]This is formally equivalent to the Lehmann representation. Inserting a complete set of eigenstates between the operator O and the fraction leads to a sum over $(\omega + E_0 - E_n + i\eta)^{-1}$ factors. Now use the identity $\lim_{\eta\to 0} 1/(z+i\eta) = P[1/z] - i\pi\delta(z)$, where P denotes the principal part, to rewrite the fraction as a delta function

which for the special case of $p = 0$ can be written as:

$$\sum_n (z - H)_{mn} x_n = \delta_{m,0}, \qquad x_n = (z - H)^{-1}_{n0}.$$

So far this seems like a tautology, but importantly we can write the matrix $(z - H)$ in the Lanczos basis generated from the relation (3.19) with $|u_0\rangle = |\phi_0\rangle$. Then the case with $n = 0$ corresponds to $x_0 \equiv \langle\phi_0|(z - H)^{-1}|\phi_0\rangle$.

The value of x_0 can be determined by Cramer's rule: for a system of equations $Ax = b$ where $x = (x_0, \ldots, x_{N-1})$ with unique solutions x_i, the solutions can be determined from $x_i = \det A_i / \det A$ where A_i is the matrix A with the $i + 1$th column replaced by b. That is:

$$x_0 = \frac{\det(z - H)_0}{\det(z - H)} \ .$$

Now let us define D_n as the matrix $(z - H)$ with the first n rows and columns removed. From the particular symmetric tridiagonal structure of $(z - H)$ we have

$$\frac{\det D_n}{\det D_{n-1}} = \frac{1}{z - a_{n-1} - b_n^2 \frac{\det D_{n+1}}{\det D_n}},$$

and hence

$$x_0 = \cfrac{1}{z - a_0 - \cfrac{b_1^2}{z - a_1 - \cfrac{b_2^2}{z - a_2 - \cfrac{b_3^2}{\cdots}}}} \ .$$

The dynamical correlation function thus becomes a continued fraction

$$I(\omega) = -\frac{1}{\pi} \lim_{\eta \to 0} \mathrm{Im} \cfrac{\langle \Psi_0 | O^\dagger O | \Psi_0 \rangle}{\omega + E_0 + i\eta - a_0 - \cfrac{b_1^2}{\omega + E_0 + i\eta - a_1 - \cfrac{b_2^2}{\omega + E_0 + i\eta - a_2 - \cfrac{b_3^2}{\cdots}}}},$$

which may easily be computed.

Our procedure for calculating the diagonal components ($\alpha = x, y, z$) of the DSF is as follows: (i) we begin by using a Lanczos procedure to find the ground state; (ii) we construct the state obtained by acting on the ground state with the Fourier transformed spin operator; (iii) we perform an additional Lanczos procedure with the constructed state as the initial state and then calculate the DSF using the continued fraction representation [54, 153]. We have checked that the Lanczos procedure agrees with full diagonalisation for $L = 16$ sites.

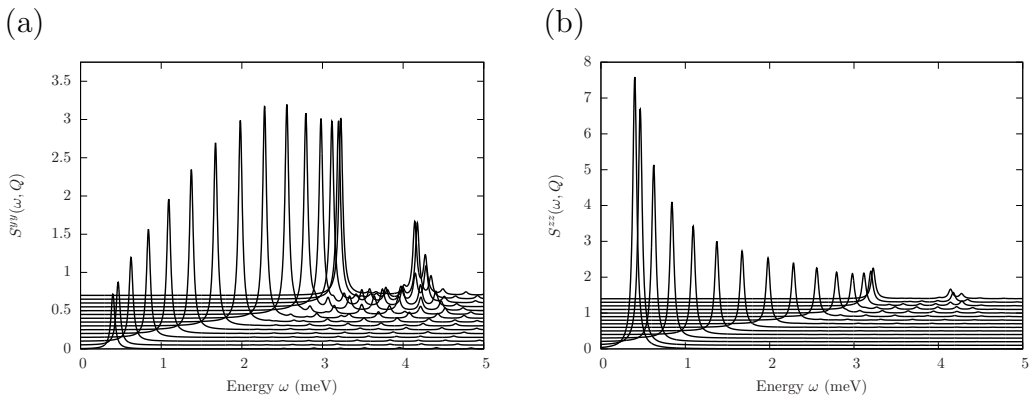

Figure 3.6: Constant $Q = 2\pi/cl$ cuts ($l = 0 \to 1$ in steps of $\delta l = 1/14$) of the dynamic structure factor $S^{\alpha\alpha}(\omega, Q = 2\pi/cl)$ for (a) $\alpha = y$ and (b) $\alpha = z$ at $B = 7T$ on the $L = 28$ chain with Hamiltonian (3.1) and exchange parameter (3.18). We have used 120 Lanczos iterations in the continued fraction and broadening parameter $\eta = 0.01J$.

3.3.4.3 Results

Following this procedure we find the DSF of the Hamiltonian (3.1) with exchange parameters (3.18) for $B = 7, 8, 9$T. We present the data for $B = 7$T in Fig. 3.6, where we have focussed on the $\alpha = y, z$ components of the DSF as these carry the majority of the spectral weight. The DSF is dominated by a single sharp mode across the Brillouin zone, with the multi particle continuum having non-negligible weight at $l \approx 1$ and $E \approx 4$meV. This should be compared to the INS data presented in Fig. 3.3, where a similar feature is observed. As seen in experiment, with increasing applied transverse field B the multi particle feature moves to higher energies and becomes less intense. The single particle mode also moves up in energy with applied transverse field, as depicted in Figs. 3.4.

We see that whilst both the general features and the quantitative behaviour with transverse field of the DSF are captured by the minimal spin model (3.1), we *do not* see the anomalous broadening region observed in experiments [131], see Fig. 3.3. In the next section we present high-resolution INS data for this phenomena and a simple possible explanation of its origin.

3.4 Anomalous broadening and quasi-particle breakdown

3.4.1 High-resolution INS: broadening region

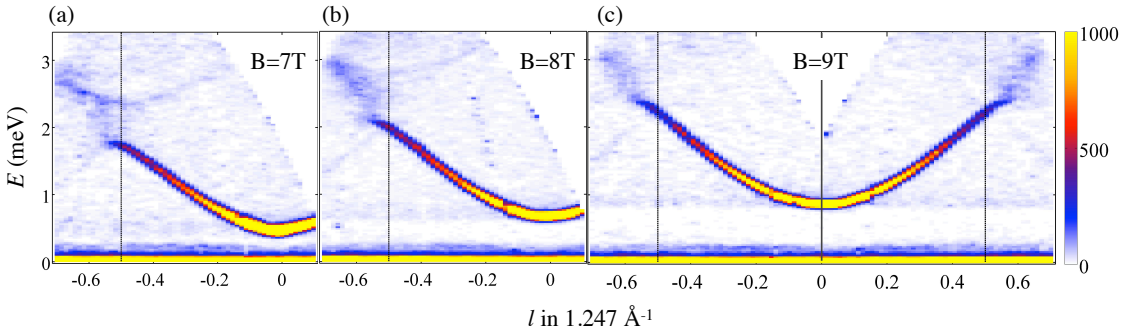

Figure 3.7: High-resolution inelastic neutron scattering data for the single particle dispersion with momentum oriented along the chain. This data was obtained for neutrons with an incident energy of $E_i = 4$meV and a corresponding resolution on the elastic line of $\Delta E = 0.051(1)$meV. Data is shown for three applied transverse field strengths: (a) $B = 7$T; (b) $B = 8$T and (c) $B = 9$T.

A surprising and interesting feature of the INS data shown in Fig. 3.3, is that close to $l \approx 0.5$ the single particle mode appears to broaden and lose a significant amount of weight. Figure 3.7 presents high-resolution INS data (with resolution on the elastic line of $\Delta E = 0.051(1)$meV) focussed on this particular feature. The broadening and lose of weight is so extreme that at $B = 7$T one might say that a gap has opened in the single particle mode; careful analysis of the data shows that this is *not* at $l = -0.5$, so cannot attributed to a dimerisation induced gap (e.g. a Peierls transition).

3.4.2 Broadening in the spin model (3.1)

In the remainder of this chapter, we focus on explaining the "anomalous broadening" region in the INS data. The spin model introduced in Sec. 3.2 and the fit parameters of Sec. 3.3.2 serve as a starting point for exact diagonalisation studies. As we have seen in the previous section, the DSF for the Hamiltonian (3.1) is dominated by a sharp mode across the whole Brillouin zone and so does not capture the physics of the broadening of the single particle mode. To go beyond this, we take inspiration from the data presented in Figs. 3.5(a)–(c), which show that the single particle mode and the multi-particle continuum overlap in the same region as the anomalous broadening

is observed in the INS data. With this in mind, we add an additional term to the Hamiltonian (3.1) which breaks the $\mathbb{Z}_2$ spin inversion symmetry $S_i^z \to -S_i^z$ of the model which previously forbid transitions between the single particle mode and two particle continuum. A natural candidate for such a term is a small *longitudinal field* $h_z = g_z \mu_B B_z$ which would arise in the experimental setting due to not having perfect alignment of the crystal with respect to the transverse field. Thus we consider the Hamiltonian modified by

$$H \to H + h_z \sum_l S_l^z \ . \tag{3.20}$$

For the inelastic neutron scattering data presented in Figs. 3.3 and 3.7, it is anticipated that the crystal is aligned to within 1° of accuracy.

3.4.2.1 Longitudinal field added to the critical transverse field Ising chain

The critical TFIC field theory perturbed by a longitudinal field was studied by Zamolodchikov [132] in the late 80s and the exact S-matrix calculated using the bootstrap method. He found that the theory has a spectrum with eight stable particles with masses $\{m_1, \ldots, m_8\}$. The heaviest 5 particles (with masses $m_4, \ldots, m_8$) lie above the threshold of the two-particle continuum ($2m_1$). The stability of these particles is not a result of an internal symmetry of the model (such as the $\mathbb{Z}_2$ spin inversion symmetry in the TFIC which forbids $1 \to 2$ particle transitions) but arises from the integrable structure of the model.

What happens when integrability is broken? This question was considered by McCoy and Wu in Refs. [155, 156] by working at $\tau = (T - T_C) \neq 0$ and $h_z \neq 0$. This corresponds to perturbing the critical TFIC field theory with both the spin and the energy density operators. They examined the structure of the poles appearing in the one-particle Green's function, ascertaining the number of particles below the two-particle continuum threshold and how the structure of poles coalesces into a branch cut starting at $2im$ at $h_z = 0$, $\tau < 0$. McCoy and Wu studied this problem using knowledge of the thermal n-point functions of the Ising model to study the problem with small h. An alternative approach, the form factor perturbation theory, was employed by Delfino, Mussardo and Simonetti [157] to study the same problem. Later work by Delfino, Grinza and Mussardo [158] computed the decay widths of

the first two particles (m_4, m_5) above the two-particle threshold, whilst Fonseca and Zamolodchikov [159] studied analytic properties of the free energy.

3.4.2.2 Longitudinal field in the minimal spin model (3.1)

Let us briefly consider the effect of adding such a longitudinal field to our spin model (3.1). As the symmetry forbidding transitions between one and two-particle states has been broken, we expect transitions between the single particle state $|1\rangle$ with energy E_1 and the two-particle continuum at a transition rate approximated by Fermi's golden rule (provided $h_z \ll J$)

$$T_{1\to 2} \approx \sum_{\substack{|2\rangle \\ E_2 \approx E_1}} \rho_2(E_2) \frac{2\pi}{\hbar} \left| h_z \sum_l \langle 2|S_l^z|1\rangle \right|^2 , \tag{3.21}$$

where $|2\rangle$ is a two-particle state with energy E_2, $\rho_2(E)$ is the density of two-particle states at energy E and the sum is taken only over two-particle states with approximately the same energy as state $|1\rangle$. The larger the rate of transition $T_{1\to 2}$, the shorter the life-time of the one-particle state and hence the broader the peak.

We note that the approximate form of the transition rate (3.21) suggests that exact diagonalisation may underestimate the broadening caused by the addition of a longitudinal magnetic field. Due to the small accessible system sizes in exact diagonalisation, we have access to a restricted number of states which are generally well-separated in energy. Thus we expect that the number of terms in the sum (3.21) is suppressed and the density of two-particle states is small. Both of these reductions can be countered by increasing the strength of the perturbation h_z and hence we expect exact diagonalisation to require larger values of h_z than those observed in experiment for the same anomalous broadening to be observed. Difficulties extracting the decay width (broadening) of excitations from numerical exact diagonalisation have also been encountered in previous works, see e.g. Ref. [158].

It is worth noting that transitions between the 1 and 3 particle states can occur without the breaking of S^z spin inversion symmetry, however as we do not see this in the DSF of previous section and Fig. 3.5(a)–(c) shows that the 3 particle states are well separated from the one particle mode, we have to conclude that this is not the origin of the anomalous broadening. We also wish to highlight the fact that the

overlap of the one-particle mode with the multi-particle continuum does not occur within the paramagnetic phase of the transverse field Ising chain: the overlap occurs due to the additional exchange interactions present in the Hamiltonian (3.1).

Let us now briefly summarise the requirements for the broadening of the single particle mode:

1. The single particle mode and the multi-particle continuum must overlap/be in very close proximity (see Figs. 3.5(a)–(c)).

2. Matrix elements must exist between the single particle mode and the (approximately) overlapping states within the multi-particle continuum. If these states are two-particle states, the S^z spin inversion symmetry must be broken to allow transitions.

3. The decay rate of the single particle mode must be sufficiently large for the broadening to become apparent.

3.4.3 Lanczos Diagonalisation (up to $L = 28$)

We now turn to exact diagonalisation results for the DSF in the presence of a small longitudinal field. As the broadening effect that we are looking for is seen in a certain area of the Brillouin zone, we use Lanczos diagonalisation (and associated continued fraction techniques [54, 153]) to extend the momentum resolution of our calculations (for full diagonalisation we are limited to $L \sim 18$ sites). We focus on the diagonal components of the DSF $S^{\alpha\alpha}(\omega, Q)$ with $\alpha = y, z$ as these carry most of the intensity. To allow us to compare the regions of anomalous broadening for different strength of the transverse field, we work with a fixed "crystal misalignment" of $\theta \sim 1.5°$, and we use $g_z = 5.9$ (we estimate from Ref. [161] that $g_z \approx 5.6 - 6.2$).

Fig. 3.8(a)–(b) shows the Lanczos results for the $\alpha = y, z$ components of the DSF in the $L = 28$ chain at $B = 7$T with a misalignment of $\theta \sim 1.5°$ ($h_z = 0.062$meV). We see that when the single particle mode brushes the continuum (at $\omega \approx 2 - 2.5$meV, cf. Fig. 3.5) the mode loses intensity and significantly broadens. This is in the same range of momenta $l \approx 0.5 - 0.7$ and frequency as the experimental observations, see

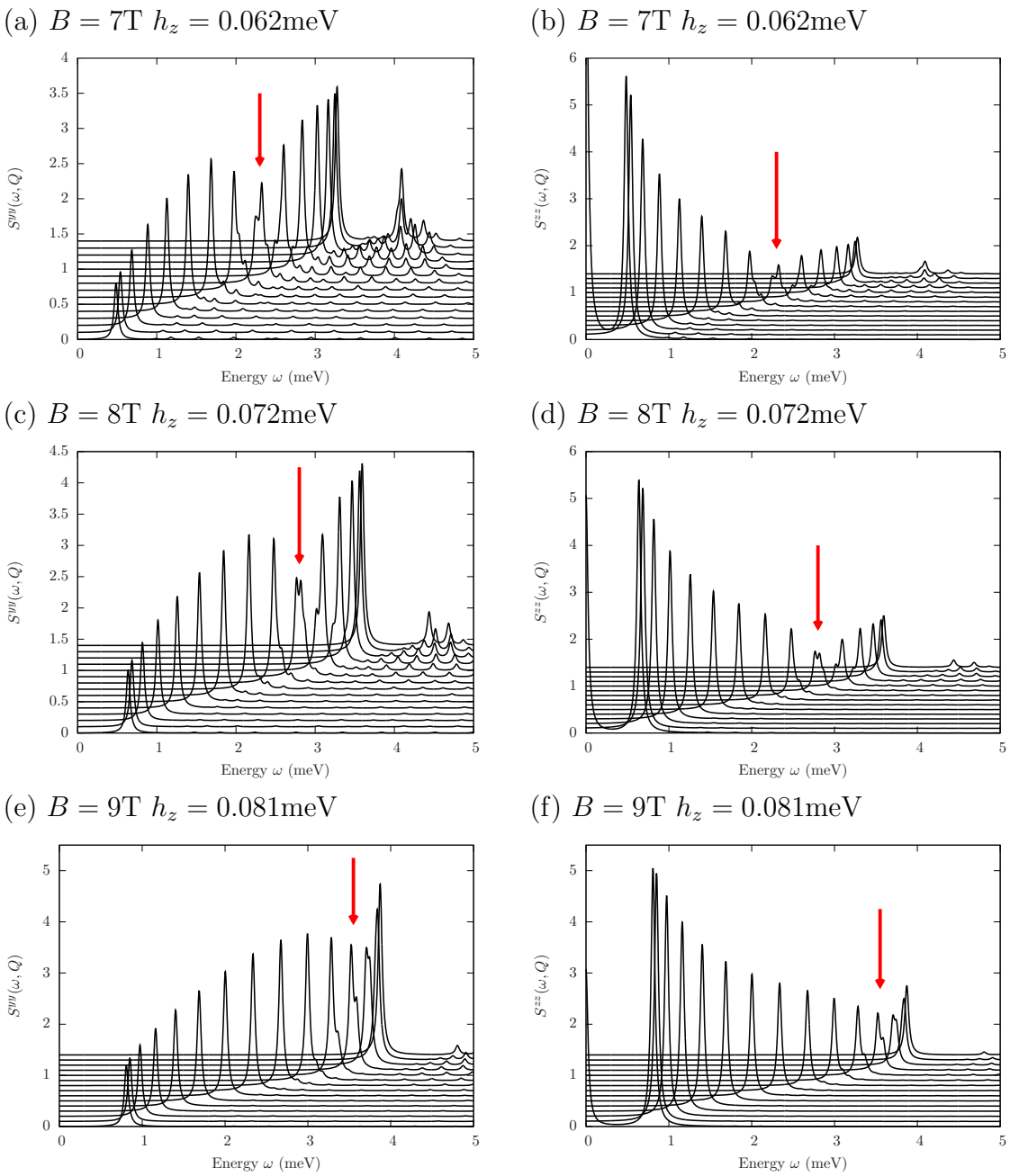

Figure 3.8: Constant $Q = 2\pi/cl$ cuts ($l = 0 \to 1$ in steps of $\delta l = 1/14$) of the dynamic structure factor $S^{\alpha\alpha}(\omega, Q = 2\pi/cl)$ for (left) $\alpha = y$ and (right) $\alpha = z$ for the $L = 28$ site Hamiltonian (3.20) with transverse field $B = 7, 8, 9\text{T}$ and misalignment of $\theta \sim 1.5°$. We have used 120 Lanczos iterations in the continued fraction and broadening parameter $\eta = 0.01J$. The arrows highlight the region of "anomalous broadening" in each case.

Figs. 3.3 and 3.7. We see that the multi particle continuum feature at $E \approx 4$meV, $l \approx 1$ persists, which is also consistent with experiment.

Analogous results for a field of $B = 8$T are shown Fig. 3.8(c)–(d). Compared to the $B = 7T$ data the region of anomalous broadening has shifted slightly in energy and momentum ($l \approx 0.55 - 0.75$) and the intensity loss is less pronounced, reflecting the decreased overlap between the single particle mode and the two-particle continuum, cf Fig. 3.5.

When increasing the field further to $B = 9$T the broadening is seen to diminish and occurs closer to the centre of the zone, as shown in Fig. 3.8(e)–(f). While there is still qualitative agreement with experiment, our theoretical computation now shows the broadening at around $l \approx 0.7$, which is shifted away from the region observed in experiment, see Fig. 3.7(c). Possible explanations for this discrepancy are that (i) the misalignment angle depends on the applied field; (ii) there are terms in the Hamiltonian beyond the ones taken into account in our model (3.1); (iii) the small system size $L = 28$ precludes an accurate description of the effect due to insufficient resolution in phase space.

3.4.4 Quasi-particle breakdown

In the above we have shown that the addition of a small longitudinal magnetic field component, consistent with small misalignment of the crystal in experiment, leads to the broadening of the single particle mode in the region $l \approx 0.5 - 0.7$ and that this broadening decreases with increased applied transverse field (for fixed misalignment). High resolution inelastic neutron scattering data in Fig. 3.7 shows that this indeed occurs in experiment, with the single particle mode becoming extremely broad and carrying little spectral weight around $l = 0.5 - 0.65$. The level of broadening observed in experiment is sufficient to say that the quasi-particles are no longer *well defined* over this region of the Brillouin zone, a phenomena known as "quasi-particle breakdown" [128].

A number of mechanisms for quasi-particle breakdown (and specifically "spontaneous magnon decay" in quantum magnets) are discussed in Refs. [113, 115, 116, 121, 124, 125, 128], including the case of field-induced decay. Most experimental observa-

tions of quasi-particle breakdown have so far been limited to the case where the single particle mode enters the two-particle continuum and terminates, such as in quasi-2D quantum magnets [112] and quasi-1D spin-1 chains [114].

In this case we observe something more unusual: two region of the Brillouin zone ($0 \leq |l| \lesssim 0.5$ and $0.7 \lesssim |l| \leq 1$) have coherent well-defined single particle excitations, whilst in the intermediate region $0.5 \lesssim |l| \lesssim 0.7$ quasi-particle breakdown occurs. For the smallest fields that we examine ($B = 7$T) this effect is particularly severe in experiments (see Fig. 3.7(a)), where one could easily believe that a gap has opened in the single particle dispersion. Compare this to a similar field-tuned effect seen in the quasi-2D quantum magnet $Ba_2MnGe_2O_7$, where the excitation is broadened, but without the severe loss of intensity [120].

The quasi-particle breakdown in $CoNb_2O_6$ is a direct result of *explicit symmetry breaking within the experimental setting*, and highlights the crucial role that symmetry breaking perturbations can play in the condensed matter setting.

3.5 Conclusions

Motivated by recent inelastic neutron scattering experiments [131], we have investigated the origin of the anomalous broadening of the single particle dispersion in the quasi-one-dimensional ferromagnet $CoNb_2O_6$. We have presented high-resolution inelastic neutron scattering data (Fig. 3.7) showing that the observed anomalous broadening has a non-trivial field dependence and is particularly severe at the small transverse field strengths (7T), where the broadening may easily be mistaken for a gap in the single particle dispersion. To understand this behaviour, we have proposed a one-dimensional spin Hamiltonian whose parameters we fix by fitting the single particle dispersion (calculated to first order in perturbation theory) to inelastic neutron scattering data presented in Fig. 3.3.

Having fixed the exchange parameters of our effective model, we add a *single* free parameter to our model – a longitudinal magnetic field. Such an addition is rather physical, as we expect a small longitudinal field to arise from slight misalignment of the crystal in experiment. Crucially, this longitudinal field breaks spin inversion symmetry ($S^z \to -S^z$) which forbids transitions between the one-particle mode and

the two-particle continuum. The breaking of this symmetry has a profound effect on the dynamical structure factor of the quantum spin model – in regions of the Brillouin zone where the two-particle continuum overlaps with the single particle mode (see Fig. 3.5) we see that the single particle mode loses weight and broadens (see Figs. 3.8(a)–(f) for exact diagonalisation data). This broadening occurs due to the longitudinal field inducing the spontaneous decay of the single particle excitation into multi particle excitations, an example of "quasi-particle breakdown" [128]. $CoNb_2O_6$ is particularly unusual in this regard as the region of quasi-particle breakdown separates two regions of coherent quasi-particle breakdown in the Brillouin zone.

Having spent the last two chapters studying the equilibrium properties of quantum systems using a combination of perturbative analytical calculations and numerical computations, in the next we study the out-of-equilibrium dynamics of a many-body quantum system. We will see once more this combined approach also works for non-equilibrium quantum systems, where we study the effect of breaking integrability.

Appendix

3.A Self-consistent Bogoliubov transformation

Starting from the Hamiltonian (3.1), we start by rotating the spin quantisation axes by $\pi/2$ about S^y to be in keeping with standard conventions. We then perform a Jordan-Wigner transformation and subsequently Fourier transform the resulting fermionic theory to obtain the momentum space Hamiltonian $H = H_0 + H_{\rm int} + E_0$, where E_0 is an additive constant that rescales the absolute energy and is neglected herein, H_0 contains only fermion bilinears and $H_{\rm int}$ is quartic in the fermion operators

$$\begin{aligned}
H_0 &= \frac{1}{2}\sum_k \begin{pmatrix} c_k^\dagger & c_{-k} \end{pmatrix} \begin{pmatrix} A_k & iB_k \\ -iB_k & -A_k \end{pmatrix} \begin{pmatrix} c_k \\ c_{-k}^\dagger \end{pmatrix}, \\
H_{\rm int} &= \frac{J}{2L}(\lambda_1 - \lambda_3) \sum_{k_i} \left[f_{(k_1,k_2,k_3)(k_4)} c_{k_1}^\dagger c_{k_2}^\dagger c_{k_3}^\dagger c_{-k_4} + \text{H.c.} \right] \\
&- \frac{J}{2L} \sum_{k_i} \left[2\lambda_2 h_{(k_1,k_2)(k_3,k_4)} + 2\lambda_3 h_{(2k_1,2k_2)(2k_3,2k_4)} \right] c_{k_1}^\dagger c_{k_2}^\dagger c_{-k_3} c_{-k_4} \\
&- \frac{J}{2L} \sum_{k_i} (\lambda_1 + \lambda_3) g_{(k_1,k_2)(k_3,k_4)} c_{k_1}^\dagger c_{k_2}^\dagger c_{-k_3} c_{-k_4} \ .
\end{aligned}$$

The matrix elements of H_0 are given by

$$\begin{aligned}
A_k &= \frac{J}{2}(1+\lambda_2)\cos(k) + \frac{J}{2}(\lambda_1+\lambda_3)\cos(2k) + h - J(\lambda_2+\lambda_3), \\
B_k &= -\frac{J}{2}(1-\lambda_2)\sin(k) - \frac{J}{2}(\lambda_1-\lambda_3)\sin(2k),
\end{aligned}$$

whilst the vertex factors appearing in $H_{\rm int}$ take the form

$$\begin{aligned}
f_{(k_1,k_2,k_3)(k_4)} &= \frac{i}{3}\left[\sin(k_3-k_1) + \sin(k_1-k_2) + \sin(k_2-k_3)\right] \delta_{\sum_j k_j, 0}, \\
g_{(k_1,k_2)(k_3,k_4)} &= \frac{1}{2}\left[\cos(k_4-k_1) - \cos(k_4-k_2) + \cos(k_3-k_2) - \cos(k_3-k_1)\right] \delta_{\sum_j k_j, 0}, \\
h_{(k_1,k_2)(k_3,k_4)} &= \frac{1}{4}\left[\cos(k_1+k_3) - \cos(k_2+k_3) + \cos(k_2+k_4) - \cos(k_1+k_4)\right] \delta_{\sum_j k_j, 0},
\end{aligned}$$

which are antisymmetric under pair-wise exchange of indices appearing within the same brackets $(\ldots)$ and impose momentum conservation.

We now diagonalise the quadratic part of the Hamiltonian by performing a self-consistent Bogoliubov transformation, details of which are given in Appendix 3.A. We define the Bogoliubov fermions a_k by

$$c_k^\dagger = -i\cos\theta_k a_k^\dagger - \sin\theta_k a_{-k}, \qquad c_k = i\cos\theta_k a_k - \sin\theta_k a_{-k}^\dagger, \tag{3.22}$$

where the Bogoliubov parameter $\theta_k = -\theta_{-k}$ satisfies the self-consistency condition $A_k \sin(2\theta_k) - B_k \cos(2\theta_k) = 0$. The quadratic part of the Hamiltonian then becomes diagonal

$$H_0 = \frac{1}{2}\sum_k \begin{pmatrix} a_k^\dagger & a_{-k} \end{pmatrix} \begin{pmatrix} \sqrt{A_k^2+B_k^2} & 0 \\ 0 & -\sqrt{A_k^2+B_k^2} \end{pmatrix} \begin{pmatrix} a_k \\ a_{-k}^\dagger \end{pmatrix}. \tag{3.23}$$

Let us now consider the action of the Bogoliubov transformation (3.22) on the interaction term of the Hamiltonian $H_{\rm int}$. It is clear that many of the transformed terms in $H_{\rm int}$ will not be normal ordered. The normal ordering of these terms will generate fermion bilinear terms that contribute to both the diagonal and off-diagonal elements of H_0 in Eq. (3.23). In order that the quadratic part of the Hamiltonian is diagonal, we impose a self-consistency condition on the Bogoliubov parameter: it must be chosen such that the off-diagonal terms that result from normal-ordering interaction terms vanish. The resulting self-consistency condition for the Bogoliubov parameter is

$$\left[A_k + \sum_q \Theta_1(k,q)\right]\sin 2\theta_k - \left[B_k + \sum_q \Theta_2(k,q)\right]\cos 2\theta_k = 0, \tag{3.24}$$

where we have defined the functions

$$\begin{aligned}
\Theta_1(k,q) &= -\frac{4J}{L}\left[\frac{1}{2}(\lambda_1+\lambda_3)g_{(k,q)(-q,-k)} + \lambda_2 h_{(k,q)(-q,-k)} + \lambda_3 h_{(2k,2q)(-2q,-2k)}\right]\sin^2\theta_q \\
&\quad + \frac{3J}{2L}(\lambda_1-\lambda_3) i f_{(k,q,-q)(-k)} \sin 2\theta_q, \\
\Theta_2(k,q) &= \frac{J}{L}\left[\frac{1}{2}(\lambda_1+\lambda_3)g_{(k,-k)(q,-q)} + \lambda_2 h_{(k,-k)(q,-q)} + \lambda_3 h_{(2k,-2k)(2q,-2q)}\right]\sin 2\theta_q \\
&\quad + \frac{3J}{L}(\lambda_1-\lambda_3) i f_{(k,q,-k)(-q)} \sin^2\theta_q,
\end{aligned} \tag{3.25}$$

which also depend upon the Bogoliubov parameter.

The self-consistency condition (3.24) perturbatively modifies the Bogoliubov parameter. Due to the complicated structure Eq. (3.24), we solve the set of non-linear

simultaneous equations numerically using standard techniques. Following the imposition of the self-consistency condition, we obtain the Hamiltonian (3.2) with dispersion relation (3.3).

3.B Vertex functions

The vertex functions $V_0,\ V_1,\ V_2$ in Eq. (3.2) are obtained by normal-ordering of the four-fermion terms after Bogoliubov transformation. By symmetry, they can be expressed in terms of summations over permutations of indices. For example

$$\begin{aligned}
&V_0(k_1,k_2,k_3,k_4)\\
&=\delta_{\sum_j k_j,0}\Bigg\{\frac{1}{96}(\lambda_3-\lambda_1)\sum_{P\in S_4}\mathrm{sgn}(P)\cos\Big[k_{P_1}-k_{P_2}+\theta_{k_{P_1}}+\theta_{k_{P_2}}+\theta_{k_{P_3}}-\theta_{k_{P_4}}\Big]\\
&+\frac{1}{96}\sum_{j=2}^{3}\lambda_j\sum_{P\in S_4}\mathrm{sgn}(P)\cos\Big[(j-1)\Big(k_{P_1}+k_{P_2}\Big)+\theta_{k_{P_1}}-\theta_{k_{P_2}}+\theta_{k_{P_3}}-\theta_{k_{P_4}}\Big]\Bigg\},
\end{aligned}$$

where P is the permutation $P:\{1,2,3,4\}\to\{P_1,P_2,P_3,P_4\}$.

The vertex which changes quasi-particle number by two is given by

$$V_1(k_1,k_2,k_3,k_4)=\delta_{\sum_j k_j,0}\Big[V_1^{(12)}(k_1,k_2,k_3,k_4)+V_1^{(23)}(k_1,k_2,k_3,k_4)+V_1^{(13)}(k_1,k_2,k_3,k_4)\Big]$$

where

$$\begin{aligned}
&V_1^{(12)}(k_1,k_2,k_3,k_4)\\
&=\frac{i}{24}(\lambda_1-\lambda_2)\sum_{Q\in S_3}\mathrm{sgn}(Q)\Bigg\{\sin\Big[k_{Q_1}-k_4+\theta_{k_{Q_1}}-\theta_{k_{Q_2}}+\theta_{k_{Q_3}}-\theta_{k_4}\Big]\\
&\qquad+\sin\Big[k_{Q_1}-k_4-\theta_{k_{Q_1}}+\theta_{k_{Q_2}}-\theta_{k_{Q_3}}+\theta_{k_4}\Big]\\
&\qquad-\sin\Big[k_{Q_1}-k_{Q_2}+\theta_{k_{Q_1}}-\theta_{k_{Q_2}}-\theta_{k_{Q_3}}+\theta_{k_4}\Big]\\
&\qquad-\sin\Big[k_{Q_1}-k_{Q_2}-\theta_{k_{Q_1}}+\theta_{k_{Q_2}}-\theta_{k_{Q_3}}+\theta_{k_4}\Big]\Bigg\},
\end{aligned}$$

$$
\begin{aligned}
&V_1^{(23)}(k_1,k_2,k_3,k_4)\\
&=-\frac{i}{24}\sum_{j=2}^{3}\lambda_j\sum_{Q\in S_3}\mathrm{sgn}(Q)\Bigg\{\sin\Big[(j-1)\Big(k_{Q_1}+k_{Q_2}\Big)-\theta_{k_{Q_1}}+\theta_{k_{Q_2}}-\theta_{k_{Q_3}}+\theta_{k_4}\Big]\\
&\qquad+\sin\Big[(j-1)\Big(k_{Q_1}+k_{Q_2}\Big)-\theta_{k_{Q_1}}+\theta_{k_{Q_2}}+\theta_{k_{Q_3}}-\theta_{k_4}\Big]\\
&\qquad+\sin\Big[(j-1)\Big(k_{Q_1}+k_4\Big)+\theta_{k_{Q_1}}-\theta_{k_{Q_2}}+\theta_{k_{Q_3}}-\theta_{k_4}\Big]\\
&\qquad+\sin\Big[(j-1)\Big(k_{Q_1}+k_4\Big)-\theta_{k_{Q_1}}-\theta_{k_{Q_2}}+\theta_{k_{Q_3}}+\theta_{k_4}\Big]\Bigg\},
\end{aligned}
$$

$$
\begin{aligned}
&V_1^{(13)}(k_1,k_2,k_3,k_4)\\
&=\frac{i}{24}(\lambda_1+\lambda_3)\sum_{Q\in S_3}\mathrm{sgn}(Q)\Bigg\{\sin\Big[k_{Q_1}-k_{Q_2}-\theta_{k_{Q_1}}+\theta_{k_{Q_2}}+\theta_{k_{Q_3}}-\theta_{k_4}\Big]\\
&\qquad-\sin\Big[k_{Q_1}-k_{Q_2}+\theta_{k_{Q_1}}-\theta_{k_{Q_2}}-\theta_{k_{Q_3}}+\theta_{k_4}\Big]\\
&\qquad+\sin\Big[k_{Q_1}-k_4+\theta_{k_{Q_1}}-\theta_{k_{Q_2}}+\theta_{k_{Q_3}}-\theta_{k_4}\Big]\\
&\qquad-\sin\Big[k_{Q_1}-k_4-\theta_{k_{Q_1}}+\theta_{k_{Q_2}}-\theta_{k_{Q_3}}+\theta_{k_4}\Big]\Bigg\},
\end{aligned}
$$

where in $V_1^{(12)}$, $V_1^{(23)}$ and $V_1^{(13)}$ the permutation Q acts as $Q:\{1,2,3\}\to\{Q_1,Q_2,Q_3\}$.

The remaining vertex function that preserves quasi-particle number is given by

$$
V_2(k_1,k_2,k_3,k_4)=\delta_{\sum_j k_j,0}\Big[V_2^{(1)}(k_1,k_2,k_3,k_4)+V_2^{(23)}(k_1,k_2,k_3,k_4)+V_2^{(3)}(k_1,k_2,k_3,k_4)\Big]
$$

with

$$
\begin{aligned}
&V_2^{(1)}(k_1,k_2,k_3,k_4)\\
&=\frac{\lambda_1}{4}\sum_{P,Q\in S_2}\mathrm{sgn}(P)\mathrm{sgn}(Q)\Bigg\{\cos\Big[k_{P_1}-k_{P_2}+\theta_{k_1}-\theta_{k_2}+\theta_{k_{Q_3}}-\theta_{k_{Q_4}}\Big]\\
&\qquad+\cos\Big[k_{Q_3}-k_{Q_4}+\theta_{k_3}-\theta_{k_4}+\theta_{k_{P_1}}-\theta_{k_{P_2}}\Big]\\
&\qquad+\cos\Big[k_{P_1}-k_{Q_3}+\theta_{k_{P_1}}+\theta_{k_{P_2}}-\theta_{k_{Q_3}}-\theta_{k_{Q_4}}\Big]\\
&\qquad+\cos\Big[k_{P_1}-k_{Q_3}+\theta_{k_{P_1}}-\theta_{k_{P_2}}-\theta_{k_{Q_3}}+\theta_{k_{Q_4}}\Big]\Bigg\}
\end{aligned}
$$

$$
\begin{aligned}
&V^{(23)}(k_1,k_2,k_3,k_4)\\
&=\frac{1}{8}\sum_{j=2}^{3}\lambda_j\sum_{P,Q\in S_2}\mathrm{sgn}(P)\mathrm{sgn}(Q)\Bigg\{\cos\Big[(j-1)\Big(k_{P_1}+k_{P_2}\Big)+\theta_{k_1}-\theta_{k_2}-\theta_{k_{Q_3}}+\theta_{k_{Q_4}}\Big]\\
&\qquad+\cos\Big[(j-1)\Big(k_{Q_3}+k_{Q_4}\Big)+\theta_{k_3}-\theta_{k_4}-\theta_{k_{P_1}}+\theta_{k_{P_2}}\Big]\\
&\qquad-\cos\Big[(j-1)\Big(k_{P_1}+k_{Q_3}\Big)+\theta_{k_{P_1}}+\theta_{k_{P_2}}-\theta_{k_{Q_3}}-\theta_{k_{Q_4}}\Big]\\
&\qquad-\cos\Big[(j-1)\Big(k_{P_1}+k_{Q_3}\Big)+\theta_{k_{P_1}}-\theta_{k_{P_2}}-\theta_{k_{Q_3}}+\theta_{k_{Q_4}}\Big]\\
&\qquad-\cos\Big[(j-1)\Big(k_{P_1}+k_{Q_3}\Big)-\theta_{k_{P_1}}-\theta_{k_{P_2}}+\theta_{k_{Q_3}}+\theta_{k_{Q_4}}\Big]\\
&\qquad-\cos\Big[(j-1)\Big(k_{P_1}+k_{Q_3}\Big)-\theta_{k_{P_1}}+\theta_{k_{P_2}}+\theta_{k_{Q_3}}-\theta_{k_{Q_4}}\Big]\Bigg\}
\end{aligned}
$$

$$
\begin{aligned}
&V_2^{(3)}(k_1,k_2,k_3,k_4)\\
&=\frac{\lambda_3}{4}\sum_{P,Q\in S_2}\mathrm{sgn}(P)\mathrm{sgn}(Q)\Bigg\{\cos\Big[k_{P_1}-k_{Q_3}-\theta_{k_{P_1}}+\theta_{k_{P_2}}+\theta_{k_{Q_3}}-\theta_{k_{Q_4}}\Big]\\
&\qquad+\cos\Big[k_{P_1}-k_{Q_3}-\theta_{k_{P_1}}-\theta_{k_{P_2}}+\theta_{k_{Q_3}}+\theta_{k_{Q_4}}\Big]\Bigg\}
\end{aligned}
$$

where P is the permutation $P:\{1,2\}\to\{P_1,P_2\}$ and Q is the permutation $Q:\{3,4\}\to\{Q_3,Q_4\}$.

4. Quench dynamics in a model with tuneable integrability breaking

4.1 Introduction and background

In the past 15 years, important advances have been made in the manipulation of cold atomic gases which mean that recent experiments [162, 163, 164, 165, 166, 167] have realised essentially unitary time-evolution for extended periods of time. Stimulated by such experiments, there has been an immense theoretical effort (see e.g. Ref. [168] for a recent review) to understand fundamental questions about the non-equilibrium dynamics of quantum systems: do observables in a subsystem relax to stationary values? If so, can the expectation values be reproduced with a thermal density matrix? What governs how and to which values expectation values relax?

4.1.1 The quantum quench and subsequent relaxation

The quantum quench is a paradigm in the study of quantum systems out-of-equilibrium. The standard "sudden quench" protocol [169] starts from the ground state $|\Psi_0\rangle$ of a Hamiltonian $H(g_0)$, where g_0 is a tuneable parameter such as the interaction strength or a magnetic field. At time $t = 0$ we change $g_0 \to g$; generically the initial state $|\Psi_0\rangle$ is not an eigenstate of $H(g)$ and we perform the subsequent time-evolution $|\Psi_0(t)\rangle = \exp[-iH(g)t]|\Psi_0\rangle$. Quantities of interest following a quantum quench include static correlation functions $\langle\Psi_0(t)|\mathcal{O}_i\mathcal{O}_j|\Psi_0(t)\rangle$ and dynamical quantities $\langle\Psi_0|\mathcal{O}_i(t')\mathcal{O}_j(t)|\Psi_0\rangle$, as well as the long-time limit of observables (e.g. stationary values, if they exist).

From the above prescription of the quantum quench, we see that the system

remains in a pure state at *all* times $|\Psi_0(t)\rangle$, so the system as a whole cannot be described by a statistical ensemble. It is also a trivial exercise to construct observables that do not relax in the long time limit: consider the operator

$$\mathcal{O}_{a,b} = |a\rangle\langle b| + |b\rangle\langle a|,$$

where $|a\rangle$ and $|b\rangle$ are eigenstates of the Hamiltonian $H(g)$ with energies $E_a \neq E_b$. In the Heisenberg picture this operator become time-dependent

$$\mathcal{O}_{a,b}(t) = e^{iH(g)t}\mathcal{O}_{a,b}e^{-iH(g)t} = e^{i(E_a-E_b)t}|a\rangle\langle b| + e^{i(E_b-E_a)t}|b\rangle\langle a|,$$

and does not approach a stationary value in the $t \to \infty$ limit.

In order to be able to discuss statistical ensembles and stationary long time limits of expectation values we focus on *local* operators which act on a finite number of sites in the system. The operator $\mathcal{O}_{a,b}$ does not meet such a requirement and is obviously a very non-local operator, acting as a projection operator between two eigenstates of $H(g)$. For operators $\mathcal{O}_\ell$ localised on a region of ℓ sites we have the following picture: the system is divided into two segments, the region ℓ and its complement $\bar{\ell}$. The complement can act as a bath for the region ℓ, allowing the exchange of probability, leading to the region ℓ being described by a mixed state. One can then construct the reduced density matrix for the region ℓ

$$\varrho_\ell(t) = \mathrm{tr}_{\bar{\ell}}\, |\Psi_0(t)\rangle\langle\Psi_0(t)|,$$

and ask questions such as does this reduced density matrix approach that of a statistical ensemble ϱ_{stat} in the long time limit?

$$\lim_{t\to\infty} \varrho_\ell(t) \stackrel{?}{=} \mathrm{tr}_{\bar{\ell}}\, \varrho_{\mathrm{stat}}. \tag{4.1}$$

If the supposition (4.1) is true, then expectation values of operators localised in the region ℓ take the form

$$\lim_{t\to\infty} \langle\Psi_0(t)|\mathcal{O}_\ell|\Psi_0(t)\rangle = \mathrm{tr}(\mathcal{O}_\ell\varrho_{\mathrm{stat}}).$$

4.1.2 The role of conservation laws

It is generally accepted that conservation laws and dimensionality play important roles in the time-evolution of isolated quantum systems. This is highlighted by the

ground-breaking experiments of Kinoshita, Wenger and Weiss [163] where it was found that a three-dimensional condensate of ^{87}Rb atoms driven out of equilibrium rapidly relaxed to a thermal state ("thermalised"), whilst a condensate constrained to move in a single spatial dimension relaxed slowly to a non-thermal ensemble. It is thought that the presence of additional (approximate) conservation laws in the one-dimensional case lies at the heart of this difference.

Two central paradigms have been established in the late time behaviour of translationally invariant models following a quantum quench:

1. Subsystems thermalise and are then described by the Gibbs ensemble (GE) [170].

2. Subsystem do not thermalise, but approach a late time stationary state described by the generalised Gibbs ensemble (GGE).

There is substantial evidence [30, 169, 171, 172, 173, 174, 175, 176, 177, 178, 179, 180, 181, 183, 182, 184, 185, 186, 187, 188, 189] that the second case applies to quenches in integrable models, as suggested in a seminal paper by Rigol *et al.* [190]. Very recently, theoretical studies suggest that in interacting integrable models the generality of the GGE may be somewhat limited [191] or the construction requires additional (previously unknown) conservation laws [192].

4.1.2.1 The generalised Gibbs ensemble (GGE)

The role of conservations laws in the time-evolution of quantum systems is well illustrated by quantum quenches in integrable models. In the thermodynamic limit integrable systems possess an *infinite* number of local conservation laws: this puts extremely strong constraints on the dynamics of such systems. These constraints on the dynamics have been shown to lead to expectation values described by the GGE in the long time limit in many cases [30, 169, 171, 172, 173, 174, 175, 176, 177, 178, 179, 180, 181, 183, 182, 184, 185, 186, 187, 188, 189].

For an integrable models with (semi) local conserved quantities I_j (with $I_0 = H$ and $[I_j, I_k] = 0\ \forall j, k$) the GGE takes the following form

$$\varrho_{\mathrm{GGE}} = \frac{1}{Z_{\mathrm{GGE}}} \exp\Big[- \sum_j \lambda_j I_j \Big], \tag{4.2}$$

where $Z_{\mathrm{GGE}} = \mathrm{tr}\exp[-\sum_j \lambda_j I_j]$ ensures normalisation and λ_j are Lagrange multipliers which are fixed by requiring that expectation values with the GGE of the conserved quantities reproduce the expectation values in the initial state $|\Psi_0\rangle$:

$$\lim_{L\to\infty} \frac{1}{L}\langle\Psi_0|I_j|\Psi_0\rangle = \lim_{L\to\infty} \frac{1}{L}\mathrm{tr}[\varrho_{\mathrm{GGE}} I_j].$$

The GGE applies to expectation values in the manner discussed in Sec. 4.1.1: the reduced density matrix of a segment ℓ coincides with the reduced density matrix of the GGE in the sense

$$\lim_{t\to\infty}\lim_{L\to\infty} \varrho_\ell(t) = \mathrm{tr}_{\bar{\ell}}\ \varrho_{\mathrm{GGE}},$$

where L is the size of the whole system and subsequently expectations values of local operators are described by

$$\lim_{t\to\infty} \langle\Psi_0(t)|\mathcal{O}|\Psi_0(t)\rangle = \mathrm{tr}[\varrho_{\mathrm{GGE}}\mathcal{O}].$$

This has been shown to be the case in non-interacting integrable models using standard free fermion techniques (see, e.g. Ref. [30]). In the interacting case, the long-time limit recovering a GGE remains a hypothesis for which there is conflicting evidence [191, 192].

In the case of free fermions, there is an alternative [171, 174, 190] but equivalent [173] construction of the GGE, which relies upon the fact that the local conservation laws can be written as a linear superposition of the mode occupation numbers $\hat{n}(k)$. Then the GGE can be written in the form

$$\varrho_{\mathrm{GGE}} = \frac{1}{Z_{\mathrm{GGE}}} \exp\Big[-\sum_k \beta_k \hat{n}(k)\Big],$$

where Lagrange multipliers β_k can be interpreted as mode dependent effective temperatures, by comparison with the Gibbs ensemble.

4.1.2.2 The Gibbs ensemble

For a generic non-integrable model, the set of operators $\{N_1, \ldots, N_\ell\}$ with (semi) local density which commute with the Hamiltonian is of fixed size ℓ, independent of the system size. The symmetries of the Hamiltonian govern which operators are found within this set, which may be empty or may include the total particle number, net

magnetisation, etc. The ensemble which is then constructed with Lagrange multipliers μ_a for each of these operators is herein called the Gibbs ensemble and takes the form

$$\varrho_{\mathrm{GE}} = \frac{1}{Z_{\mathrm{GE}}} \exp\Big[-\beta H - \sum_{a=1}^{\ell} \mu_a N_a \Big]. \tag{4.3}$$

It is generally *assumed* that the long time limit of expectation values following a quantum quench with broken integrability are reproduced by the Gibbs ensemble.[†]

4.1.3 Weak integrability breaking

The dichotomy in the dependence of stationary behaviour after a quench on integrability then poses an intriguing question: what happens if integrability is weakly broken? Does the system thermalise, and if so, how fast does it relax? Might there be an intermediate time scale still governed by the physics of integrability?

Early numerical studies [194] suggested that even with an integrability breaking term the system does not thermalise on the accessible time scales and system sizes. Studies using dynamical mean field theory (DMFT) [195] or analytical methods in $d > 2$ [196] showed that on intermediate time scales the system approaches a non-thermal quasi-stationary state (a prethermalization plateau). At later times the system is expected to thermalise [175, 197]. Prethermalization plateaux have also been observed in a somewhat artificial model of a non-integrable quantum Ising chain with long-range interactions [198]. It has been suggested recently [199], that the time scale for integrability breaking (leaving the prethermalization plateau) is not necessarily related to the strength of the integrability breaking term. Experimental evidence for the prethermalization plateau in systems of bosonic cold atoms was reported in Refs. [167, 200, 201]. In spite of the aforementioned works exhibiting prethermalization plateaux in specific models, a general understanding of if, when and how such plateaux emerge when integrability is broken remains open. Similarly, a precise characterisation of such plateaux in terms of statistical ensembles has not been achieved.

[†]This assumption seems reasonable, but showing that this statement is generally true is extremely difficult, as it requires a full treatment of non-integrable models. We will see later that perturbation theory gives very little insight into the long-time limit of the problem. Numerical studies can shed some light on the issue, for example in Ref. [193] the expectation value of the string order in a non-integrable spin-1 chain following a quantum quench is compatible with eventual thermalisation.

4.1.4 This chapter

In this chapter, we will be concerned with the effects of breaking of integrability on the dynamics following a quantum quench. Our model allows us to compare integrable quenches to those where integrability is broken by the addition of interactions. We combine analytical and numerical calculations to demonstrate the existence of prethermalization plateaux when integrability-breaking is weak. We find that on *intermediate* time-scales, expectations values of local observables relax to non-thermal values described by a GGE in which the non-interacting conserved charges have been deformed to leading order in perturbation theory. Surprisingly, these deformed charges no longer commute with the post-quench Hamiltonian.

This chapter is organised as follows. In Sec. 4.2 we introduce the model under study. In Section 4.3 we consider integrable quenches of the non-interacting Peierls insulator and compared the results from the Gibbs and generalised Gibbs ensembles. The continuous unitary transformation technique is introduced and used to study a weakly non-integrable quench of the model in Sec. 4.4. In Sec. 4.5 we establish the existence of the prethermalized regime and describe the approximately stationary behaviour in this regime by constructing a "deformed GGE". The dynamics in the presence of strong integrability-breaking interactions is studied numerically in Sec. 4.6. We present a summary and discussion of our main results in Sec. 4.7. An appendix containing a derivation of the *local* conservation laws in the Peierls insulator completes the chapter. The time-dependent density matrix renormalisation group (tDMRG) and exact diagonalisation (ED) data shown in the figures of this chapter were provided by Dr. Salvatore R. Manmana (SRM) of the University of Göttingen.

4.2 The model

To explore the physics of integrability breaking in a quantum quench, we consider the following model of spinless fermions with dimerised hopping and nearest-neighbour density-density interaction

$$H(\delta,U) \;=\; -J\sum_{l=1}^{L}\Big[1+(-1)^{l}\delta\Big]\Big(c_l^{\dagger}c_{l+1}+\text{H.c.}\Big)+U\sum_{l=1}^{L}c_l^{\dagger}c_l\,c_{l+1}^{\dagger}c_{l+1}, \qquad (4.4)$$

with periodic boundary conditions on a chain of length L. The spinless fermions obey the anti-commutation relations $\{c_l^\dagger, c_j\} = \delta_{l,j}$. We restrict our attention to the parameter regime $J > 0$, $U \geq 0$ and $0 < \delta < 1$. We work at half-filling throughout, i.e. the total number of fermions is $L/2$, which is the sector of the Hamiltonian in which the non-interacting ground state is found. In the rest of this chapter we measure time in units of J^{-1}.

One important characteristic of the Hamiltonian $H(\delta, U)$ is that the fermion number is conserved by virtue of the $U(1)$ symmetry $c_j \longrightarrow e^{i\varphi} c_j$, $\varphi \in [0, 2\pi]$. This $U(1)$ symmetry leads to the dramatic simplification of the analytical calculations and at the same time it enables us to access very late times in our time-dependent density matrix renormalisation group (tDMRG) calculations presented later in this chapter (in comparison to existing studies of other non-integrable one-dimensional models).

4.2.0.1 Equilibrium Properties

Let us briefly recap the equilibrium properties of the Hamiltonian $H(\delta, U)$. It is equivalent to a spin–1/2 Heisenberg XXZ chain with dimerised XX term, as can be shown by means of a Jordan-Wigner transformation. The model has been little studied in equilibrium[†], serving only as a model to investigate the effect of interactions on the Peierls transition [202, 203]. DMRG calculations suggested that for large values of the interaction parameter $U \gtrsim 4$, the Peierls transition to a dimerised ground state is suppressed [203].

There are several limits in which exact results for the equilibrium phase diagram of $H(\delta, U)$ are known. In the absence of interactions $U = 0$, we obtain a model of a non-interacting Peierls insulator. For vanishing δ and $U \geq 0$ the Jordan-Wigner transformation maps the Hamiltonian to the spin-1/2 Heisenberg XXZ chain, for which exact results via the Bethe ansatz are know. Finally, for small $|\delta|$ and $U < J$, the low-energy limit is given by the integrable sine-Gordon model [144, 204].

[†]Its equilibrium properties are evident: the dimerisation δ opens a gap in the spectrum and it is an insulator. For fixed δ the addition of weak repulsive interactions should not qualitatively change any behaviour – whether there exists a quantum phase transition in U is, to the best of our knowledge, unknown.

4.3 The Peierls insulator

We start by considering the non-interacting case, which describes the Peierls insulator

$$H(\delta,0) = -J\sum_{l}\Big[1+\delta(-1)^{l}\Big]\Big(c_{l}^{\dagger}c_{l+1}+\text{H.c.}\Big). \tag{4.5}$$

The Hamiltonian can be diagonalised by means of a Bogoliubov transformation

$$c_{l} = \frac{1}{\sqrt{L}}\sum_{k>0}\sum_{\alpha=\pm}\gamma_{\alpha}(l,k|\delta)a_{\alpha}(k)\ . \tag{4.6}$$

The fermion operators $a_{\alpha}(k)$ fulfil the anti-commutation relations $\{a_{\alpha}(k),a_{\beta}(q)\}=0$, $\{a_{\alpha}(k),a_{\beta}^{\dagger}(q)\}=\delta_{\alpha,\beta}\delta_{k,q}$. The coefficients in the Bogoliubov transformation are chosen as

$$\gamma_{\alpha}(l,k|\delta) = e^{-ikl}\Big[u_{\alpha}(k,\delta)+v_{\alpha}(k,\delta)(-1)^{l}\Big], \tag{4.7}$$

where we have defined

$$\begin{aligned} v_{\alpha}(k,\delta) &= \left[1+\left|\frac{2J\cos(k)-\epsilon_{\alpha}(k)}{2\delta J\sin(k)}\right|^{2}\right]^{-\frac{1}{2}}, \quad u_{\alpha}(k,\delta) = iv_{\alpha}(k)\frac{2J\cos(k)-\epsilon_{\alpha}(k)}{2\delta J\sin(k)}, \\ \epsilon_{\alpha}(k,\delta) &= 2\alpha J\sqrt{\delta^{2}+(1-\delta^{2})\cos^{2}(k)}. \end{aligned} \tag{4.8}$$

Equation (4.8) describes the single particle dispersion for particles in the $\alpha=\pm$ bands, which are separated by an energy gap of $4\delta J$. Finally, $\sum_{k>0}$ is a shorthand notation for the momentum sum

$$\sum_{k>0}f(k) = \sum_{n=1}^{L/2}f\big(\frac{2\pi n}{L}\big).$$

Following the Bogoliubov transformation, the Peierls Hamiltonian is diagonal

$$H(\delta,0) = \sum_{k>0}\epsilon_{\alpha}(k,\delta)a_{\alpha}^{\dagger}(k)a_{\alpha}(k),$$

and describes two $\alpha=\pm$ bands of non-interacting fermions. The ground state is obtained by completely filling the "$-$" band with Bogoliubov fermions

$$|\text{GS}\rangle = \prod_{k}a_{-}^{\dagger}(k)|0\rangle,$$

where $|0\rangle$ is the vacuum state defined by $a_{\alpha}(k)|0\rangle=0$ for $\alpha=\pm$ and $k\in(0,\pi]$.

4.3.1 Integrable quantum quenches in the Peierls Insulator

We will now consider the quantum quench of the dimerisation parameter δ in the non-interacting Peierls insulator. Following the standard "sudden quench" protocol discussed in Sec. 4.1.1, we prepare the system in the ground state $|\Psi_0\rangle$ of the Hamiltonian $H(\delta_i, 0)$ and at time $t = 0$ the dimerisation is suddenly quenched from $\delta_i \to \delta_f$. The system then evolves unitarily under the new Hamiltonian $H(\delta_f, 0)$.

The diagonal form of our initial Hamiltonian is

$$H(\delta_i, 0) = \sum_{\alpha=\pm} \sum_{k>0} \epsilon_\alpha(k, \delta_i) b^\dagger_\alpha(k) b_\alpha(k),$$

and the ground state is given by

$$|\Psi_0\rangle = \prod_k b^\dagger_-(k)|0\rangle, \tag{4.9}$$

At times $t > 0$ the system is in the state

$$|\Psi_0(t)\rangle = e^{-iH(\delta_f,0)t}|\Psi_0\rangle,$$

where the new Hamiltonian $H(\delta_f, 0)$ can also be diagonalised by the Bogoliubov transformation (4.6)

$$H(\delta_f, 0) = \sum_{\alpha=\pm} \sum_{k>0} \epsilon_\alpha(k, \delta_f) a^\dagger_\alpha(k) a_\alpha(k).$$

By virtue of (4.6) the Bogoliubov fermions $a^\dagger_\alpha(k)$ are *linearly* related to $b^\dagger_\alpha(k)$ by

$$a^\dagger_\alpha(k) = \sum_{\beta=\pm} S^\beta_\alpha(k) b^\dagger_\beta(k),$$

where

$$S^\beta_\alpha(k) = u_\alpha(k, \delta_f) u^*_\beta(k, \delta_i) + u \leftrightarrow v. \tag{4.10}$$

Following the Bogoliubov transformation, the time-dependent fermion Green's function is given by

$$\begin{aligned} G_0(j, \ell, t) &= \langle \Psi_0(t)| c^\dagger_j c_\ell |\Psi_0(t)\rangle \\ &= \frac{1}{L} \sum_{k>0} \sum_{\alpha\beta} \gamma^*_\alpha(j, k|\delta_f) \gamma_\beta(\ell, k|\delta_f) e^{i(\epsilon_\alpha(k) - \epsilon_\beta(k))t} S^-_\alpha(k) S^-_\beta(k)^*, \end{aligned} \tag{4.11}$$

The late-time behaviour of the Green's function can be determined by a stationary phase approximation, giving

$$\lim_{t\to\infty} G_0(j, \ell, t) \sim g_1(j, \ell) + g_2(j, \ell) t^{-3/2} + \dots \tag{4.12}$$

4.3.1.1 Generalised Gibbs ensemble (GGE)

The stationary state of the dimerisation quench is described by a GGE [190]. The Hamiltonian (4.5) after the quantum quench possess an infinite number of local conservation laws $I_a^{(n)}$ ($a = 1, 2, 3, 4$, $n \in \mathbb{N}$) in the thermodynamic limit.

$$[I_a^{(n)}, I_b^{(m)}] = 0 \ , \quad I_1^{(1)} = H(\delta_f, 0).$$

An explicit construction of these conservation laws is presented in Appendix 4.A. Given these conserved quantities, we defined the density matrix

$$\varrho_{\mathrm{GGE}} = \frac{1}{Z_{\mathrm{GGE}}} \exp\left[- \sum_{a=1}^{4} \sum_{j \geq 1} \lambda_a^{(j)} I_a^{(j)} \right],$$

where Z_{GGE} ensures normalisation[†]. The Lagrange multipliers are fixed by the requirements that the expectation values of the conserved quantities are the same in the initial state and in the GGE

$$\lim_{L\to\infty} \frac{1}{L} \langle \Psi_0 | I_a^{(j)} | \Psi_0 \rangle = \lim_{L\to\infty} \frac{1}{L} \mathrm{tr}\left[\varrho_{\mathrm{GGE}} I_a^{(j)} \right].$$

The GGE then describes expectation values of local observables in the manner discussed in Sec. 4.1.2.1.

For convenience we use an alternative [171, 174, 190] but equivalent [173] construction of the GGE based on the mode occupation numbers $\hat{n}_\alpha(k) = a_\alpha^\dagger(k) a_\alpha(k)$. These commute with the Hamiltonian $H(\delta_f, 0)$ and amongst themselves by construction, and we can express the density matrix in a particularly simple form

$$\varrho_{\mathrm{GGE}} = \frac{1}{Z_{\mathrm{GGE}}} \exp\left[- \sum_{k>0} \sum_{\alpha=\pm} \beta_k^{(\alpha)} \hat{n}_\alpha(k) \right].$$

The Lagrange multipliers are fixed by the conditions $\langle \Psi_0 | \hat{n}_\alpha(k) | \Psi_0 \rangle = \mathrm{tr}\left[\varrho_{\mathrm{GGE}} n_\alpha(k) \right]$, which are solved by

$$e^{-\beta_k^{(+)}} = \frac{|S_+^-(k)|^2}{1 - |S_+^-(k)|^2} \ , \qquad e^{-\beta_k^{(-)}} = \frac{|S_-^-(k)|^2}{1 - |S_-^-(k)|^2} \ .$$

Here the functions $S_\beta^\alpha(k)$ are defined in (4.10).

[†]In practice we consider a very large system of size L and take into account L conserved quantities.

4.3.1.2 GGE vs. thermal expectation values

In the introduction to this chapter, we discussed the dichotomy in behaviour between integrable and non-integrable system: we are now able to quantify the difference between the GGE constructed above and a Gibbs ensemble (GE)

$$\varrho_{\rm GE} = \frac{1}{Z_{\rm GE}} \exp(-\beta_{\rm eff} H(\delta_f, 0)) \ ,$$

where $\beta_{\rm eff}$ is fixed by requiring the average thermal energy density is equal to the energy density in the initial state

$$\lim_{L\to\infty} \frac{\langle \Psi_0 | H(\delta_f, 0) | \Psi_0 \rangle}{L} = \lim_{L\to\infty} \frac{{\rm tr}\left[\varrho_{\rm G}(\beta_{\rm eff})\ H(\delta_f, 0)\right]}{L}. \tag{4.13}$$

We can once again use that the fermions diagonalising $H(\delta_i, 0)$ and $H(\delta_f, 0)$ are linearly related $a^\dagger_\alpha(k) = S^\beta_\alpha(k)\ b^\dagger_\beta(k)$, to rewrite (4.13) in the form

$$\sum_{k>0} \epsilon_+(k, \delta_f) \left[|S^-_-(k)|^2 - |S^-_+(k)|^2 \right] = \sum_{k>0} \epsilon_+(k, \delta_f) \tanh \left[\frac{\beta_{\rm eff}}{2} \epsilon_+(k, \delta_f) \right],$$

which fixes the effective temperature.

To highlight the difference between the Gibbs and generalised Gibbs ensembles we consider two observables: the mode occupation numbers and the Green's function in turn. To start, the mode occupation numbers are given by

$$\langle \hat{n}_\alpha(p) \rangle \ = \ \begin{cases} \frac{1}{1+\exp\left(\beta_{\rm eff}\epsilon_\alpha(k,\delta_f)\right)} & \text{for GE,} \\ \frac{1}{1+\exp\left(\beta^{(\alpha)}_k\right)} & \text{for GGE,} \end{cases} \tag{4.14}$$

and plotted in Figs. 4.1(a)–(b). Clearly the mode occupation numbers in the two ensembles are very different.

It has been emphasised in Ref. [30] and Sec. 4.1.1, that as we are dealing with the non-equilibrium dynamics of an *isolated* quantum system, we should focus on the expectation values of local (in space) operators, as descriptions in terms of statistical ensembles most naturally apply to them (see also Refs. [173, 205]). With this in mind, it is natural to consider the fermionic Green's function in position space and its short distance properties. In the two ensembles the Green's function is given by

$$\langle c^\dagger_j c_l \rangle \ = \ \frac{1}{L} \sum_{p>0} \sum_\alpha \gamma^*_\alpha(j, p|\delta_f) \gamma_\alpha(l, p|\delta_f) \langle \hat{n}_\alpha(p) \rangle, \tag{4.15}$$

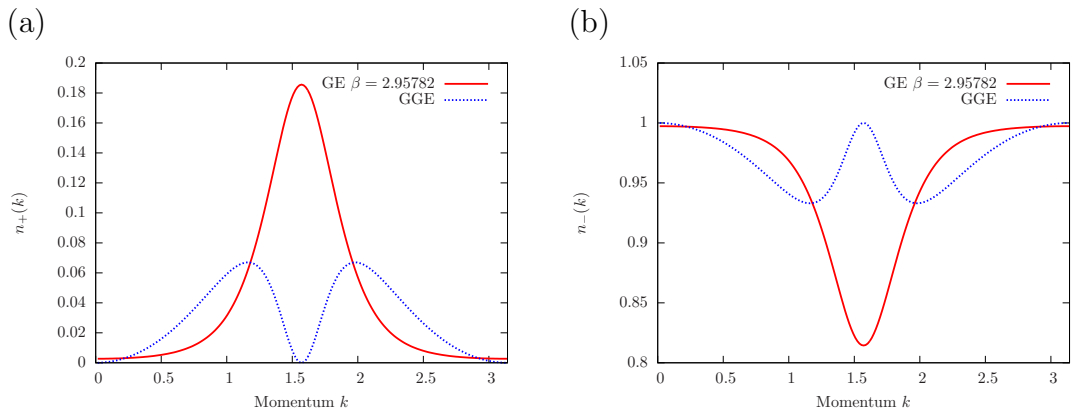

Figure 4.1: Comparison between the mode occupation numbers (a) $\langle n_+(k)\rangle$; (b) $\langle n_-(k)\rangle$ for Gibbs and generalised Gibbs ensembles for a quench with $\delta_i = 0.75$, $\delta_f = 0.25$. The effective inverse temperature for this quench is $\beta_{\text{eff}} = 2.95782J$.

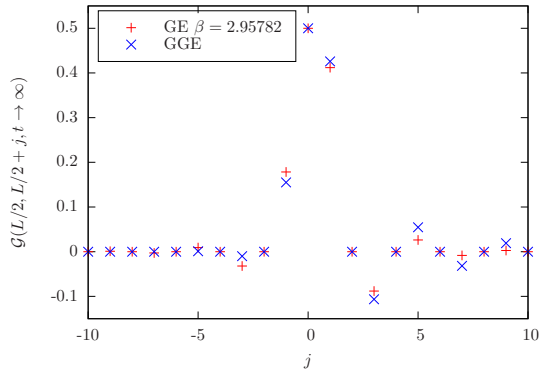

Figure 4.2: Green's function $\langle c^\dagger_{L/2} c_{L/2+j}\rangle$ calculated in the Gibbs and generalised Gibbs ensembles for a quench with $\delta_i = 0.75$, $\delta_f = 0.25$ and a lattice with $L = 100$ sites. The effective inverse temperature for this quench is $\beta_{\text{eff}} = 2.95782J$.

where the mode occupation numbers are given by (4.14). We plot the two results for the Green's function in Fig. 4.2; in contrast to the mode occupation numbers, the differences between the short distance behaviour in the two ensembles is quite small.

4.4 Quenching to a weakly interacting model

In the previous section we have examined quenches in the integrable limit of the model (4.4), where interactions have been switched off. Turning on interactions leads to a theory which is non-integrable[†]. In terms of the Bogoliubov fermions which diagonalise the Peierls insulator $H(\delta, 0)$ the interaction term becomes

$$H_{\text{int}} \;=\; U \sum_{k_j>0} V_{\alpha_1\alpha_2\alpha_3\alpha_4}(k_1,k_2,k_3,k_4) a^\dagger_{\alpha_1}(k_1) a_{\alpha_2}(k_2) a^\dagger_{\alpha_3}(k_3) a_{\alpha_4}(k_4)\ ,$$

[†]An exception is the low-energy limit for $|\delta| \ll 1$, which is described by a quantum sine-Gordon model [144, 204]. We avoid this region by considering $0.4 \le \delta \le 0.8$.

where the interaction vertices are given by

$$V_{\boldsymbol{\alpha}}(\boldsymbol{k}) = \frac{1}{L^2}\sum_{l}\gamma^*_{\alpha_1}(l,k_1|\delta)\gamma_{\alpha_2}(l,k_2|\delta)\gamma^*_{\alpha_3}(l+1,k_3|\delta)\gamma_{\alpha_4}(l+1,k_4|\delta).$$

Summing over l results in momentum-space delta-functions which conserve momentum at the vertices up to a factor of π (reflecting that the dimerisation breaks translational symmetry from one to two sites)

$$\begin{aligned} V_{\boldsymbol{\alpha}}(\boldsymbol{k}) = \frac{1}{L}e^{i(k_3-k_4)}\Big\{&\delta_{k_1+k_3,k_2+k_4}\left[w^{k_1k_2}_{\alpha_1\alpha_2}w^{k_3k_4}_{\alpha_3\alpha_4} - x^{k_1k_2}_{\alpha_1\alpha_2}x^{k_3k_4}_{\alpha_3\alpha_4}\right] \\ &+\delta_{k_1+k_3+\pi,k_2+k_4}\left[x^{k_1k_2}_{\alpha_1\alpha_2}w^{k_3k_4}_{\alpha_3\alpha_4} - w^{k_1k_2}_{\alpha_1\alpha_2}x^{k_3k_4}_{\alpha_3\alpha_4}\right]\Big\}, \end{aligned} \quad (4.16)$$

with $w^{kp}_{\alpha\beta} = u^*_\alpha(k,\delta)u_\beta(p,\delta)+v^*_\alpha(k,\delta)v_\beta(p,\delta)$ and $x^{kp}_{\alpha\beta} = u^*_\alpha(k,\delta)v_\beta(p,\delta)+v^*_\alpha(k,\delta)u_\beta(p,\delta)$.

To examine quenches in which integrability is broken, we modify our quantum quench as follows. We still start in the ground state $|\Psi_0\rangle$ of the non-interacting Peierls Hamiltonian $H(\delta_i,0)$ given by Eq. (4.9), but we quench to the $H(\delta_f,U)$ with U/J small compared to $\min(\delta_i,\delta_f)$. Our aim is to quantify how the non-zero value of U modifies the dynamics following the quench.

To tackle the quench problem in the non-integrable weakly interacting model we employ the continuous unitary transformation (CUT) technique [206, 207] which has been applied extensively to non-equilibrium problems (see, for example, Refs. [196, 208]). We provide an overview of the CUT technique in the following subsection and then proceed to calculate the time-dependent Green's function and the four-point function.

4.4.1 Time-evolution of observables by CUT

For the non-integrable interacting Hamiltonian (4.4) exact solutions are not known and it is no longer possible to calculate the time evolution exactly. This is a generic problem in gaining an analytical understanding of the out-of-equilibrium dynamics of non-integrable models and one for which there is as yet no solution. To tackle the problem of the weakly interacting model, we use the continuous unitary transformation to obtain a perturbative expansion in U of the time-evolved observables which applies to some maximal time scale (dependent on the interaction strength U).

The central idea of the CUT method is to construct a sequence of infinitesimal unitary transformations, chosen such that the Hamiltonian becomes successively more

energy-diagonal. This is achieved in the following manner: a family of unitarily equivalent Hamiltonians $H(B)$, characterised by the parameter B, can be constructed from the solutions of the differential equation

$$\frac{\mathrm{d}H(B)}{\mathrm{d}B} = \Big[\eta(B), H(B)\Big], \tag{4.17}$$

where $\eta(B)$ is an antihermitian operator which is the "generator" of the unitary transformation. The CUT method pivots on making an appropriate choice for the generator $\eta(B)$ – here we are directed by Wegner [206] to make the canonical choice $\eta(B) = [H_0(B), H_{\mathrm{int}}(B)]$ where H_0 is the diagonal quadratic part of the Hamiltonian and H_{int} the remainder. For Hamiltonians with a single particle gap, the subsequent integration of Eq. (4.17) to find $H(B = \infty)$ results in a basis where the Hamiltonian is energy diagonal. In practice one cannot directly integrate Eq. (4.17) and instead all the operators appearing in (4.17) are expressed as power series in an appropriate small parameter (in our case U) and the flow in B is solved perturbatively.

Following the sequence of infinitesimal unitary transformations with an appropriate choice of generator we have a non-integrable energy-diagonal Hamiltonian. To perform the time-evolution we have to introduce an additional approximation: we normal order the interaction term with respect to the initial state $|\Psi_0\rangle$ (see e.g. Eq. (4.28)) and neglect the normal-ordered quartic (and higher order) terms. The time-evolution operator $\mathcal{U}(t) = \exp(-iH't)$ depends only on the quadratic Hamiltonian H' whose single particle energies have $\mathcal{O}(U)$ contributions. These contributions from the normal ordering procedure are reminiscent of a first-order self-energy correction[†]. Time-evolution can then be performed. For operators, a schematic of the procedure is shown in Fig. 4.3 – we transform to the $B = \infty$ basis, perform the time-evolution and reverse the CUT to take expectation values in $B = 0$ basis.

By construction this approximate time-evolution introduces a *maximal time scale*, on which we expect our calculations to be accurate by virtue of the smallness of U. Estimating this time scale within the CUT formalism is difficult, as it requires a reliable treatment of the neglected energy diagonal interaction terms. For this reason we extensively compare our CUT results to tDMRG computations (see Sec. 4.4.5).

[†]Compare to the self-energy corrections to the single particle dispersion calculated perturbatively in Chapter (3) by inverting Dyson's equation.

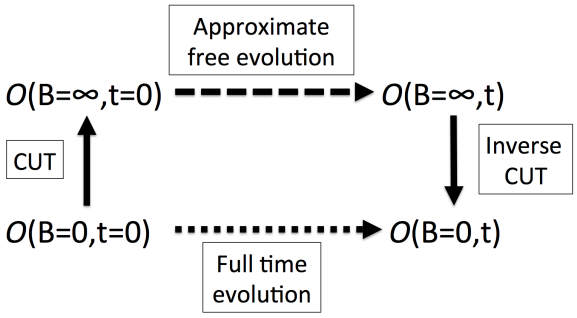

Figure 4.3: A schematic of the CUT method for finding the approximate time-evolution of O to $\mathcal{O}(U)$.

Importantly, we can perform our CUT calculations for very large systems of hundreds of sites, for which we have verified that finite-size effects do not play a role on time scales less then the revival time (the results shown below are for times less than the revival time).

4.4.2 The canonical generator and flow equations for the Hamiltonian

We now follow the general prescription laid out above for the CUT technique. We begin by constructing the "canonical generator" of the unitary transformation [207] given by $\eta(B) = [H_0(B), H_{\rm int}(B)]$. The flow-dependent operators are defined by

$$\begin{aligned} H_0(B) &= \sum_{\alpha=\pm}\sum_{k>0} \epsilon_\alpha(k|B) a^\dagger_\alpha(k) a_\alpha(k), \\ H_{\rm int}(B) &= U \sum_{k_j>0} V_{\boldsymbol{\alpha}}(\boldsymbol{k}|B) a^\dagger_{\alpha_1}(k_1) a_{\alpha_2}(k_2) a^\dagger_{\alpha_3}(k_3) a_{\alpha_4}(k_4) + \ldots \end{aligned}$$

where the functions in the Hamiltonian have been promoted to functions of the flow parameter B (with initial conditions $\epsilon_\alpha(k|B=0) = \epsilon_\alpha(k)$ and $V_{\boldsymbol{\alpha}}(\boldsymbol{k}|B=0) = V_{\boldsymbol{\alpha}}(\boldsymbol{k})$) and the ellipses indicate terms sextic and higher in creation and annihilation operators which are induced by the unitary transformation at order U^2. The canonical generator is given by

$$\eta(B) = U \sum_{k_j>0} W_{\boldsymbol{\alpha}}(\boldsymbol{k}|B) a^\dagger_{\alpha_1}(k_1) a_{\alpha_2}(k_2) a^\dagger_{\alpha_3}(k_3) a_{\alpha_4}(k_4) + \mathcal{O}(U^2), \qquad (4.18)$$

where

$$\begin{aligned} W_{\boldsymbol{\alpha}}(\boldsymbol{k}|B) &= V_{\boldsymbol{\alpha}}(\boldsymbol{k}|B) E_{\boldsymbol{\alpha}}(\boldsymbol{k}|B), \\ E_{\boldsymbol{\alpha}}(\boldsymbol{k}|B) &= \epsilon_{\alpha_1}(k_1|B) - \epsilon_{\alpha_2}(k_2|B) + \epsilon_{\alpha_3}(k_3|B) - \epsilon_{\alpha_4}(k_4|B). \end{aligned}$$

By inserting the canonical generator (4.18) and the flow Hamiltonian $H(B)$ into Eq. (4.17) we obtain the flow equations

$$\frac{\mathrm{d}\epsilon_\alpha(k|B)}{\mathrm{d}B} = 0, \qquad \frac{\mathrm{d}V_{\boldsymbol{\alpha}}(\boldsymbol{k}|B)}{\mathrm{d}B} = -E_{\boldsymbol{\alpha}}(\boldsymbol{k})^2 V_{\boldsymbol{\alpha}}(\boldsymbol{k}|B),$$

which can be directly integrated to give the flow-dependent single particle energies and interaction vertices

$$\epsilon_\alpha(k|B) = \epsilon_\alpha(k|B=0), \tag{4.19}$$

$$V_{\boldsymbol{\alpha}}(\boldsymbol{k}|B) = V_{\boldsymbol{\alpha}}(\boldsymbol{k}|B=0)e^{-BE^2_{\boldsymbol{\alpha}}(\boldsymbol{k})} \ . \tag{4.20}$$

Setting $B=\infty$ we obtain the Hamiltonian in the energy-diagonal basis

$$\begin{aligned} H(B=\infty) &= \sum_{\alpha=\pm}\sum_{k>0} \epsilon_\alpha(k) a^\dagger_\alpha(k) a_\alpha(k) \\ &+ \sum_{k_j>0} \breve{V}_{\boldsymbol{\alpha}}(\boldsymbol{k}) a^\dagger_{\alpha_1}(k_1) a_{\alpha_2}(k_2) a^\dagger_{\alpha_3}(k_3) a_{\alpha_4}(k_4) + \mathcal{O}(U^2) \ , \end{aligned} \tag{4.21}$$

where indeed the interaction vertices conserve energy

$$\breve{V}_{\boldsymbol{\alpha}}(\boldsymbol{k}) \equiv V_{\boldsymbol{\alpha}}(\boldsymbol{k}|B=\infty) = V_{\boldsymbol{\alpha}}(\boldsymbol{k})\delta_{E_{\boldsymbol{\alpha}}(\boldsymbol{k}),0} \ . \tag{4.22}$$

We note that to leading order in U the single particle energies $\epsilon_\alpha(k)$ remain unchanged by the unitary transformation. Having found the energy-diagonal form of the Hamiltonian to leading order we now consider the unitary transformation induced by the canonical generator (4.18) on the Green's function.

4.4.3 Green's function

We now wish to determine the fermion Green's function on the time-evolved initial state $G(j,l;t) = \langle \Psi_0(t)|c^\dagger_j c_l|\Psi_0(t)\rangle$. We follow the general prescription described in Sec. (4.4.1) and depicted schematically in Fig. 4.3. We transform to the final $B=\infty$ basis, time-evolve according to a (approximately) non-interacting Hamiltonian and finally reverse the unitary transformation back to the initial $B=0$ basis and take expectation values. The Green's function is expressed in terms of the Bogoliubov fermions $a_\alpha(k)$ using

$$c^\dagger_j c_l = \frac{1}{L}\sum_{k,q>0}\sum_{\alpha,\beta=\pm} \gamma^*_\alpha(j,k|\delta_f)\gamma_\beta(l,q|\delta_f)\hat{n}_{\alpha\beta}(k,q|B=0) \ , \tag{4.23}$$

where $\gamma_\alpha(j,k|\delta)$ are defined in Eq. (4.7) and $\hat{n}_{\alpha\beta}(k,q|B=0) = a^\dagger_\alpha(k)a_\beta(q)$. Hence the basic objects we need to calculate are expectation values of the "number operators" $\hat{n}_{\alpha\beta}(p,q|B=0)$.

The change of basis is performed by integrating the flow equations

$$\frac{\mathrm{d}\hat{n}_{\alpha\beta}(p,q|B)}{\mathrm{d}B} = \Big[\eta(B), \hat{n}_{\alpha\beta}(p,q|B)\Big] \ .$$

By expressing the flow operator $\hat{n}_{\alpha\beta}(p,q|B)$ in the form

$$\begin{aligned}\hat{n}_{\alpha\beta}(p,q|B) &= f_{\alpha\beta}(p,q|B)\hat{n}_{\alpha\beta}(p,q|B=0) \\ &\quad + U\sum_{\boldsymbol{k},\boldsymbol{\gamma}} g^{\boldsymbol{\gamma}}_{\alpha\beta}(\boldsymbol{k}|p,q|B)a^\dagger_{\gamma_1}(k_1)a_{\gamma_2}(k_2)a^\dagger_{\gamma_3}(k_3)a_{\gamma_4}(k_4) + \mathcal{O}(U^2),\end{aligned}$$

with $f_{\alpha\beta}(p,q|B=0)=1$ and $g^{\boldsymbol{\gamma}}_{\alpha\beta}(\boldsymbol{k}|p,q|B=0)=0$, the flow equations can be written as

$$\frac{\mathrm{d}f_{\alpha\beta}(p,q|B)}{\mathrm{d}B} = 0, \qquad \frac{\mathrm{d}g^{\boldsymbol{\gamma}}_{\alpha\beta}(\boldsymbol{k}|p,q|B)}{\mathrm{d}B} = Y^{\boldsymbol{\gamma}}_{\alpha\beta}(\boldsymbol{k}|p,q|B), \tag{4.24}$$

where

$$\begin{aligned}Y^{\boldsymbol{\gamma}}_{\alpha\beta}(\boldsymbol{k}|p,q|B) &= \delta_{k_4,q}\delta_{\gamma_4,\beta}W_{\gamma_1\gamma_2\gamma_3\alpha}(k_1,k_2,k_3,p|B) + \delta_{k_2,q}\delta_{\gamma_2,\beta}W_{\gamma_1\alpha\gamma_3\gamma_4}(k_1,p,k_3,k_4|B) \\ &\quad -\delta_{k_3,p}\delta_{\alpha_3,\alpha}W_{\gamma_1\gamma_2\beta\gamma_4}(k_1,k_2,q,k_4|B) - \delta_{k_1,p}\delta_{\alpha_1,\alpha}W_{\beta\gamma_2\gamma_3\gamma_4}(q,k_2,k_3,k_4|B)\end{aligned}$$

and $W_{\boldsymbol{\alpha}}(\boldsymbol{k}|B) = E_{\boldsymbol{\alpha}}(\boldsymbol{k})V_{\boldsymbol{\alpha}}(\boldsymbol{k}|B)$.

Integration of the flow equations (4.24) gives the flow operator

$$\begin{aligned}\hat{n}_{\alpha\beta}(k,p|B) &= \hat{n}_{\alpha\beta}(k,p|B=0) \\ &+ U\sum_{q_j>0} N^{\boldsymbol{\alpha}}_{\alpha\beta}(\boldsymbol{q}|k,p,B)a^\dagger_{\alpha_1}(q_1)a_{\alpha_2}(q_2)a^\dagger_{\alpha_3}(q_3)a_{\alpha_4}(q_4) + \mathcal{O}(U^2),\end{aligned} \tag{4.25}$$

where we have defined

$$\begin{aligned}N^{\boldsymbol{\alpha}}_{\alpha\beta}(\boldsymbol{q}|k,p,B) &= \delta_{q_4,p}\delta_{\alpha_4,\beta}\tilde{V}_{\alpha_1\alpha_2\alpha_3\alpha}(q_1,q_2,q_3,k|B) + \delta_{q_2,p}\delta_{\alpha_2,\beta}\tilde{V}_{\alpha_1\alpha\alpha_3\alpha_4}(q_1,k,q_3,q_4|B) \\ &- \delta_{q_3,k}\delta_{\alpha_3,\alpha}\tilde{V}_{\alpha_1\alpha_2\beta\alpha_4}(q_1,q_2,p,q_4|B) - \delta_{q_1,k}\delta_{\alpha_1,\alpha}\tilde{V}_{\beta\alpha_2\alpha_3\alpha_4}(p,q_2,q_3,q_4|B) \ , \\ \tilde{V}_{\boldsymbol{\alpha}}(\boldsymbol{q}|B) &= \frac{1-e^{-B[E_{\boldsymbol{\alpha}}(\boldsymbol{q})]^2}}{E_{\boldsymbol{\alpha}}(\boldsymbol{q})}V_{\boldsymbol{\alpha}}(\boldsymbol{q}).\end{aligned}$$

The next step in the procedure for calculating the time-dependent Green's function is to perform the time-evolution in the $B=\infty$ basis.

4.4.3.1 Approximate time-evolution

The Hamiltonian in the $B = \infty$ basis (4.21) is energy-diagonal to leading order in U. However, interaction terms which are difficult to deal with in the time-evolution still remain. We instead approximate the time evolution operator $\mathcal{U}(t)$

$$\mathcal{U}(t) \;=\; e^{-iH(B=\infty)t} \approx e^{-iH't} \;, \tag{4.26}$$

where the interacting Hamiltonian $H(B = \infty)$ has been replaced by the free fermion Hamiltonian

$$H' \;=\; \sum_{\alpha=\pm}\sum_{k>0} \tilde{\epsilon}_\alpha(k) a^\dagger_\alpha(k) a_\alpha(k),$$

with single particle energies $\tilde{\epsilon}_\alpha(k) = \epsilon_\alpha(k) + UP_\alpha(k)$. The correction to the single particle energies takes the form

$$\begin{aligned} P_\alpha(k) \;=\; \sum_{\gamma,\delta}\sum_{q>0} \Big[& \breve{V}_{\alpha\alpha\gamma\delta}(k,k,q,q) + \breve{V}_{\gamma\delta\alpha\alpha}(q,q,k,k) \\ & - \breve{V}_{\alpha\delta\gamma\alpha}(k,q,q,k) - \breve{V}_{\gamma\alpha\alpha\delta}(q,k,k,q) \Big] n_{\gamma\delta}(q) \;, \end{aligned}$$

where $\breve{V}_{\boldsymbol{\alpha}}(\boldsymbol{k})$ is defined in Eq. (4.22). Expectation values are taken with respect to the initial state $n_{\gamma\delta}(q) = \langle\Psi_0|\hat{n}_{\gamma\delta}(q,q)|\Psi_0\rangle$ and are given by

$$\begin{aligned} n_{--}(k) = \;& |S^-_-(k)|^2, \qquad n_{-+}(k) = S^-_-(k) S^-_+(k)^* \;, \\ n_{++}(k) = \;& |S^-_+(k)|^2, \qquad n_{+-}(k) = S^-_+(k) S^-_-(k)^*, \end{aligned} \tag{4.27}$$

with $S^\beta_\alpha(k)$ defined in Eq. (4.10).

The corrections $P_\alpha(k)$ arise from normal ordering the interaction term with respect to the initial state $|\Psi_0\rangle$. The normal ordering is performed by the following prescription

$$\begin{aligned} a^\dagger_{\alpha_1} a_{\alpha_2} a^\dagger_{\alpha_3} a_{\alpha_4} \;=\; & :a^\dagger_{\alpha_1} a_{\alpha_2} a^\dagger_{\alpha_3} a_{\alpha_4}: + n_{\alpha_1\alpha_2}(k_1)\delta_{k_1,k_2} :a^\dagger_{\alpha_3} a_{\alpha_4}: \\ - \;& n_{\alpha_1\alpha_4}(k_1)\delta_{k_1,k_4} :a^\dagger_{\alpha_3} a_{\alpha_2}: - [n_{\alpha_3\alpha_2}(k_3) - \delta_{\alpha_2,\alpha_3}]\delta_{k_2,k_3} :a^\dagger_{\alpha_1} a_{\alpha_4}: \\ + \;& n_{\alpha_3\alpha_4}(k_3)\delta_{k_3,k_4} :a^\dagger_{\alpha_1} a_{\alpha_2}: + n_{\alpha_1\alpha_2}(k_1) n_{\alpha_3\alpha_4}(k_3)\delta_{k_1,k_2}\delta_{k_3,k_4} \\ - \;& n_{\alpha_1\alpha_4}(k_1)[n_{\alpha_3\alpha_2}(k_2) - \delta_{\alpha_2,\alpha_3}]\delta_{k_1,k_4}\delta_{k_2,k_3} \;, \end{aligned} \tag{4.28}$$

and subsequently the quartic piece on the right hand side of (4.28) is neglected in the time-evolution (4.26). The correction to the single particle energies is similar in form

to the first-order self-energy correction which we calculated in a different context in the previous chapter.

Under this approximation, the time evolution results only in additional phase factors for the fermion operators

$$\mathcal{U}^\dagger(t)a^\dagger_\alpha(k)\mathcal{U}(t) = e^{i\tilde{\epsilon}_\alpha(k)t}a^\dagger_\alpha(k). \tag{4.29}$$

Using the above expression (4.29) in Eq. (4.25) gives an explicit expressions for the time-evolved flow operators $\hat{n}_{\alpha\beta}(k,p|B=\infty,t)$. The final step of the procedure for calculating the time evolution of observables, shown in Fig. (4.3), is to reverse the CUT and take expectation values on the initial state $|\Psi_0\rangle$. Reversing of the CUT is performed by integrating the flow equations (4.24) from $B=\infty$ to $B=0$ with the initial conditions

$$\begin{aligned} f_{\alpha\beta}(p,q|B=\infty;t) &= f_{\alpha\beta}(p,q|B=\infty)e^{i(\tilde{\epsilon}_\alpha-\tilde{\epsilon}_\beta)t}, \\ g^\gamma_{\alpha\beta}(\boldsymbol{k}|p,q|B=\infty;t) &= g^\gamma_{\alpha\beta}(\boldsymbol{k}|p,q|B=\infty)e^{i[\tilde{\epsilon}_{\gamma_1}(k_1)-\tilde{\epsilon}_{\gamma_2}(k_2)+\tilde{\epsilon}_{\gamma_3}(k_3)-\tilde{\epsilon}_{\gamma_4}(k_4)]t}. \end{aligned}$$

Taking the expectation value at $B=0$ on the initial state, we find

$$\langle\hat{n}_{\alpha\beta}(p,q|B=0,t)\rangle = \delta_{p,q}e^{i(\tilde{\epsilon}_\alpha(p)-\tilde{\epsilon}_\beta(q))t}n_{\alpha\beta}(p) + Uc_{\alpha\beta}(p,q|t) + \mathcal{O}(U^2), \tag{4.30}$$

where the order U piece is given by

$$\begin{aligned} c_{\alpha\beta}(p,q|t) = \sum_{q,r>0} & N^\gamma_{\alpha\beta}(r,r,q,q|p,q|t)n_{\gamma_1\gamma_2}(r)n_{\gamma_3\gamma_4}(q) \\ & -N^\gamma_{\alpha\beta}(r,q,q,r|p,q|t)n_{\gamma_1\gamma_4}(r)\big[n_{\gamma_3\gamma_2}(q)-\delta_{\gamma_2,\gamma_3}\big]. \end{aligned}$$

and we have defined

$$\begin{aligned} N^\gamma_{\alpha\beta}(\boldsymbol{k}|p,q|t) &= N^\gamma_{\alpha\beta}(\boldsymbol{k}|p,q,B=\infty)\Big[e^{i\tilde{E}_{\boldsymbol{\gamma}}(\boldsymbol{k})t} - e^{i(\tilde{\epsilon}_\alpha(p)-\tilde{\epsilon}_\beta(q))t}\Big], \\ \tilde{E}_{\boldsymbol{\gamma}}(\boldsymbol{k}) &= \tilde{\epsilon}_{\gamma_1}(k_1) - \tilde{\epsilon}_{\gamma_2}(k_2) + \tilde{\epsilon}_{\gamma_3}(k_3) - \tilde{\epsilon}_{\gamma_4}(k_4)\ . \end{aligned} \tag{4.31}$$

Substitution of the expectation values (4.30) into Eq. (4.23) and imposing the momentum conserving delta-functions in the vertices (4.16) gives the time-dependent Green's function

$$\begin{aligned} G(j,l;t) &= \langle\Psi_0(t)|c^\dagger_j c_l\,|\Psi_0(t)\rangle \\ &= \frac{1}{L}\sum_{k>0}\sum_{\alpha,\beta=\pm}\gamma^*_\alpha(j,k|\delta_f)\gamma_\beta(l,k|\delta_f)\Big[e^{i(\tilde{\epsilon}_\alpha(k)-\tilde{\epsilon}_\beta(k))t}n_{\alpha\beta}(k) + Uc_{\alpha\beta}(k,k|t)\Big] \\ &\quad +\mathcal{O}(U^2). \end{aligned} \tag{4.32}$$

The remaining momentum sum $\sum_{k>0}$ is evaluated numerically.

4.4.4 CUT results for the Green's function

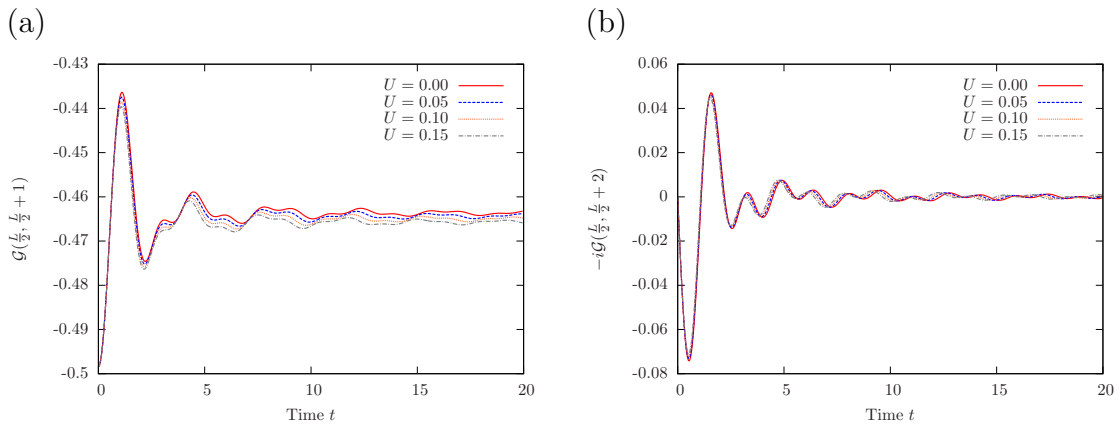

Figure 4.4: Comparison of the exact (solid) $U = 0$ solution and the CUT result for (a) $\mathcal{G}(L/2, L/2+1) = \langle c_{L/2} c^\dagger_{L/2+1} \rangle$; (b) $\mathcal{G}(L/2, L/2+2) = \langle c_{L/2} c^\dagger_{L/2+2} \rangle$ for the quench $\delta_i = 0.8 \to \delta_f = 0.4$ and $U_i = 0 \to U$ on the $L = 100$ chain.

Let us begin by comparing the $U \neq 0$ CUT result to the $U = 0$ exactly solvable case. In Figs. 4.4(a)–(b) we show the nearest and next-nearest neighbour Green's functions for the quench $\delta_i = 2\delta_f = 0.8$ and several values of U. As expected, we see that both the periodicity and the asymptotic value of the nearest neighbour Green's function are continuously deformed away from the non-interacting case. In the case of the next-nearest-neighbour Green's function only the periodicity is deformed, as the Green's function decays asymptotically to zero by symmetry.

In Figs. 4.5(a)–(b) we focus on how the CUT result for the Green's function approaches the $t \to \infty$ asymptotic value for the quench $\delta_i = 0.75 \to \delta_f = 0.5$ and $U_i = 0 \to U = 0.15$. We see that both the nearest and next-nearest neighbour Green's functions approach the asymptotic value with power-law decay of $t^{-3/2}$, as a direct consequence of the CUT result (4.32) having the same general t-dependence as the non-interacting case (4.11) (and hence the decay follows from a stationary phase argument).

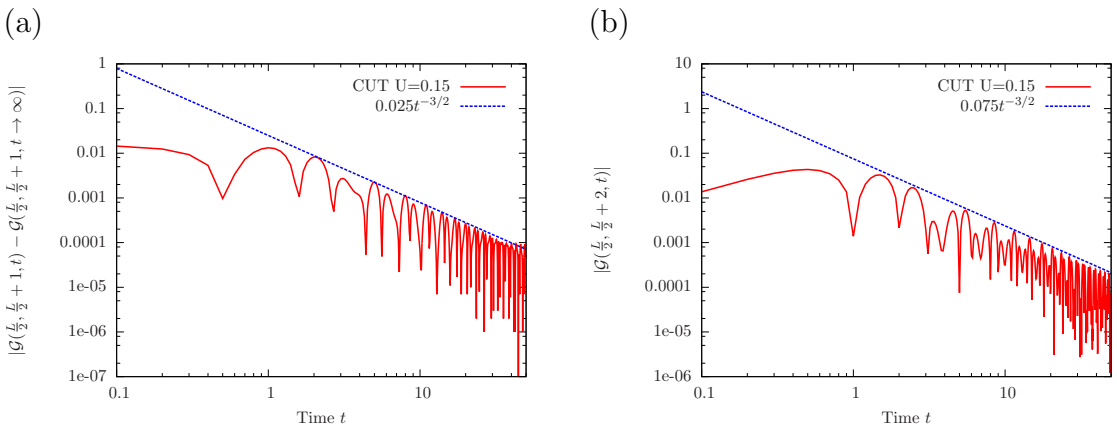

Figure 4.5: Approach of the (a) nearest-neighbour, (b) next-nearest neighbour Green's function to its asymptotic $t \to \infty$ value on the $L = 200$ chain following the quench $\delta_i = 0.75 \to \delta_f = 0.5$ and $U_i = 0 \to U = 0.15$. The dashed line shows a fit of the free fermion asymptotic form (4.12) to the CUT data. The revival time of the $L = 200$ chain is $t \sim 50$ and the asymptotic value $\mathcal{G}(100, 101, t \to \infty) = -0.482275$.

4.4.5 Accuracy of the CUT approach: comparison to time-dependent density matrix renormalisation group at small U/t

Having compared the CUT result to the non-interacting result, we now need to assess the accuracy of the CUT results for the interacting case. To do this, we have carried out extensive comparisons to numerical results obtained by the time-dependent density matrix renormalisation group (tDMRG) algorithm[†] provided by SRM. Excellent reviews of the tDMRG algorithm can be found in Refs. [209].

We carry out computations with open boundary conditions and system sizes up to $L = 200$ sites. For the purposes of comparisons with the CUT result, we choose a system size of $L = 50$ and keep up to $m = 1500$ density matrix states in the course of the time-evolution, targeting a discarded weight of $\varepsilon = 10^{-9}$. To ascertain the accuracy of the tDMRG results, we carried out comparisons to results with targeted discarded weight of 10^{-11}. In addition we also compared runs with different time steps of $\delta t = 0.005$ and $\delta t = 0.01$. We found that the difference between the results at the end of the time-evolution is $\sim 10^{-4}$ or smaller for $L = 100$ sites, hence the tDMRG errors are negligible in our comparison with the CUT results.

Beyond the tDMRG error, it is also necessary to ensure that finite-size effects

[†] A description of the DMRG algorithm in the equilibrium context can be found in Chapter 2.

are negligible in the tDMRG data. In the centre of a finite chain of non-interacting particles, the revival time τ_r for measurements is $L/2v_{\max}$, where L is the system size and $v_{\max}$ is the maximum velocity of excitations. In the small-U regime examined here, a good estimate of τ_r is provided by the $U = 0$ result and can be improved by searching for features associated with revivals at times close to the free fermion estimate. We have verified that the tDMRG data has negligible finite size effects for $t < \tau_r$ and we compare the CUT and tDMRG results only for t sufficiently smaller than τ_r. One final point to note for the tDMRG is that we have been able to reach long times ~ 200 for system sizes of $L = 50$. Whilst for short times, the error in the observable may be estimated by $\sim \sqrt{\varepsilon}$, at large times the accumulation of error in the course of each sweep needs to be taken into account, even if the discarded weight is kept constant. A comprehensive error analysis is presented in Appendix B of Ref. [2] which applies for $t > 20$.

We present a comparison between the CUT and tDMRG results for the time-dependence of the nearest-neighbour Green's function $\mathcal{G}(25, 26)$ for the length $L = 50$ chain in Figures 4.6(a)–(d). We have quenched the dimerisation parameter $\delta_i = 0.75 \to \delta = 0.5$ and the interaction strength $U = 0 \to U = 0.15, 0.25, 0.5$, respectively. We see that there is excellent quantitative agreement between the CUT and tDMRG results at small U, whilst agreement remains good even for the largest value of $U = 0.5$ tested. The remaining small discrepancies have their origin in the higher order $\mathcal{O}(U^2)$ corrections to the CUT result, as shown in Fig. 4.6(d) where the rescaled difference between the tDMRG and CUT data has been plotted for the three values of U. The oscillatory nature of these differences is a result of a "beat frequency" which arises from subtracting two oscillatory data sets where the frequencies aren't exactly matched.

The excellent agreement between the tDMRG data and the CUT result is not just restricted to the nearest-neighbour Green's function: we present $\langle (c_{L/2} c^\dagger_{L/2+j})(t) \rangle$ with $j = 2, 3, 4$ for the quench with $U = 0.15$ in Figs. 4.7(b)–(d). We will see in later sections that the good agreement between the CUT result and tDMRG extends to N–point correlation functions (in particular, we've checked $N = 4$).

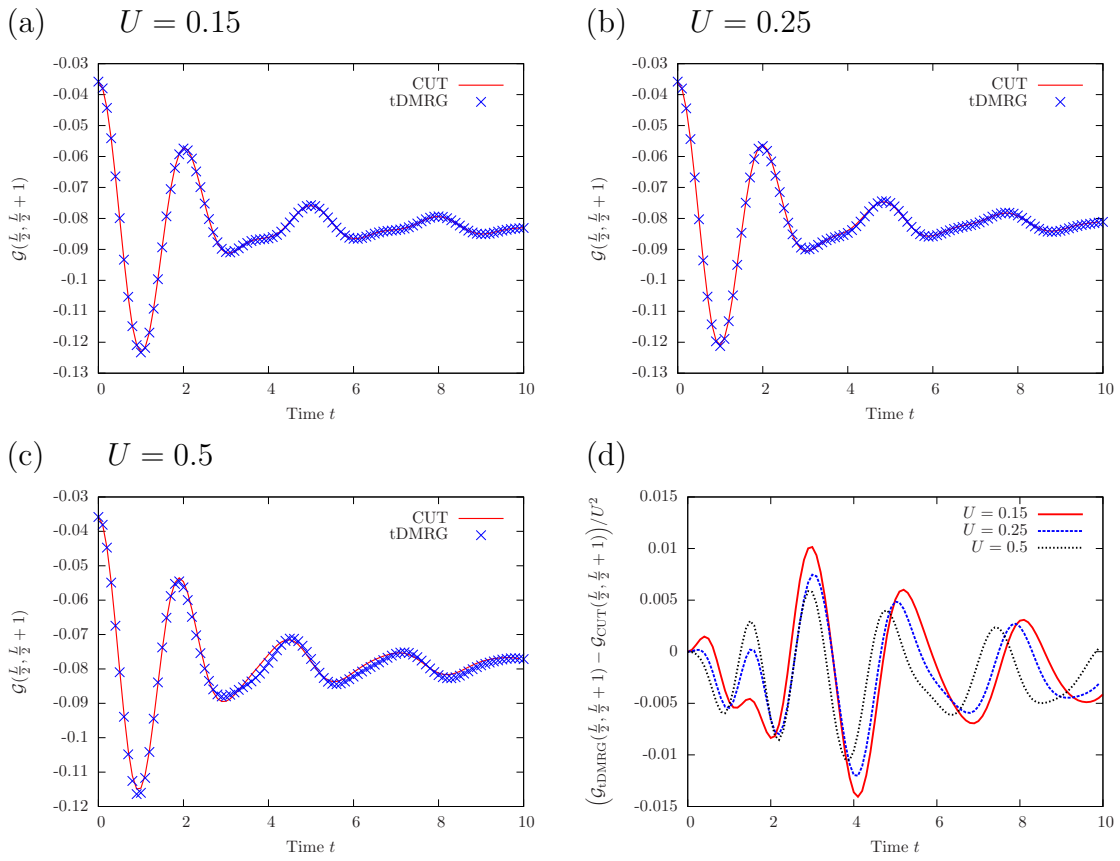

Figure 4.6: Comparison of the CUT and tDMRG results for $\mathcal{G}(L/2, L/2+1) = \langle c_{L/2} c^\dagger_{L/2+1} \rangle$ for the quench $\delta_i = 0.75 \to \delta = 0.5$ and $U_i = 0 \to$ (a) $U = 0.15$; (b) $U = 0.25$; (c) $U = 0.5$; on a $L = 50$ chain. (d) presents the relative difference between the CUT result and the tDMRG data. The revival time for the $L = 50$ system is $\tau_r \sim 13$.

4.4.6 CUT results for the four-point function

The procedure which we have outlined above for the single-particle Green's function can be generalised to N-point functions. The next non-vanishing correlation function is the four point function

$$\begin{aligned} \langle \Psi(t)| c^\dagger_j c_{j'} c^\dagger_l c_{l'} |\Psi(t)\rangle &= \frac{1}{L^2} \sum_{q_j>0} \sum_{\alpha_j=\pm} \langle \Psi_0 | \hat{A}_{\boldsymbol{\alpha}}(\boldsymbol{q}, t) | \Psi_0 \rangle \\ &\quad \times \gamma^*_{\alpha_1}(j, q_1) \gamma_{\alpha_2}(j', q_2) \gamma^*_{\alpha_3}(l, q_3) \gamma_{\alpha_4}(l', q_4), \end{aligned} \tag{4.33}$$

where $\gamma_\alpha(j,k)$ are defined in Eq. (4.7) and $\hat{A}_{\boldsymbol{\alpha}}(\boldsymbol{q}, t) = a^\dagger_{\alpha_1}(q_1, t) a_{\alpha_2}(q_2, t) a^\dagger_{\alpha_3}(q_3, t) a_{\alpha_4}(q_4, t)$. Going to the $B = \infty$ basis by applying the CUT and then time evolving with (4.26),

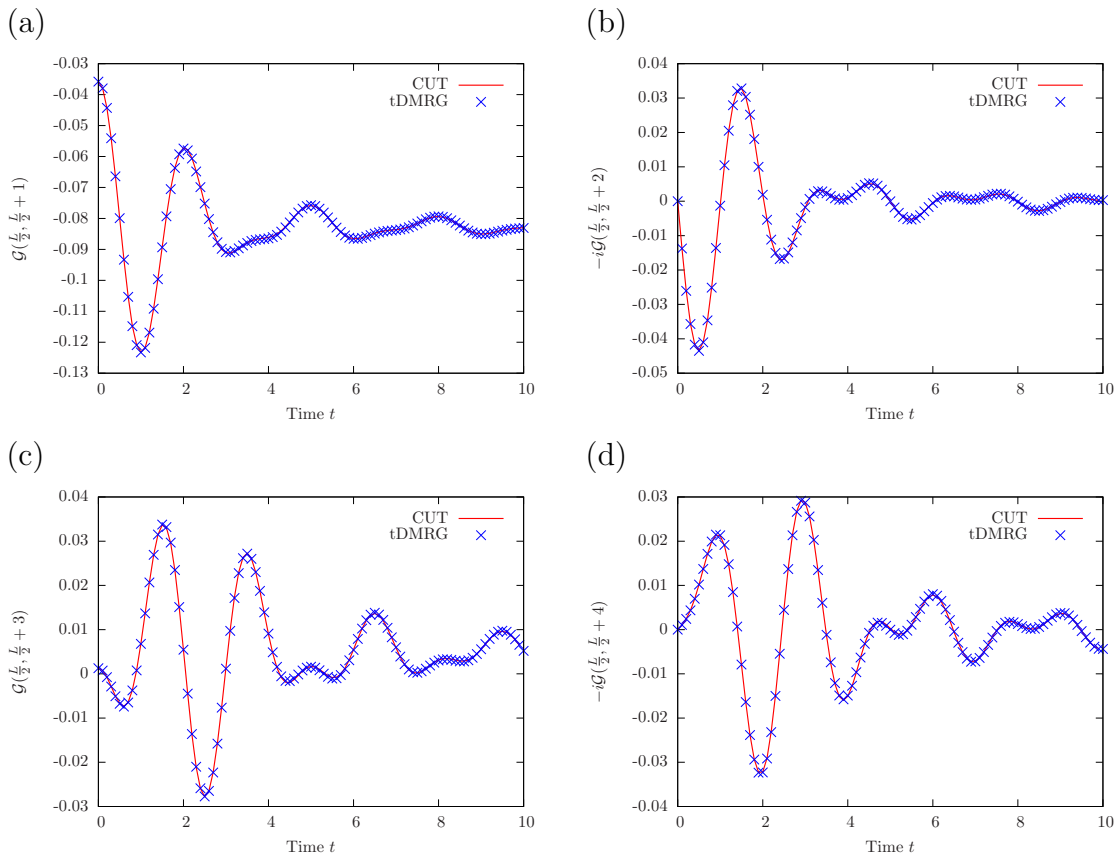

Figure 4.7: Results from the CUT calculation and tDMRG computations for (a) $\mathcal{G}(L/2, L/2+1)$; (b) $\mathcal{G}(L/2, L/2+2)$; (c) $\mathcal{G}(L/2, L/2+3)$; (d) $\mathcal{G}(L/2, L/2+4)$ for the quench $\delta_i = 0.75 \to \delta = 0.5$, $U_i = 0 \to U = 0.15$ on the $L = 50$ chain. The revival time for the $L = 50$ system is $\tau_r \sim 13$.

we obtain

$$\begin{aligned}
\hat{A}_{\boldsymbol{\alpha}}(\boldsymbol{q}, t|B=\infty) &= e^{i\tilde{E}_{\boldsymbol{\alpha}}(\boldsymbol{q})t}\hat{A}_{\boldsymbol{\alpha}}(\boldsymbol{q}, 0) \\
&+ U\sum_{k_j>0}\sum_{\gamma_j=\pm} e^{i(\tilde{\epsilon}_{\alpha_1}(q_1)-\tilde{\epsilon}_{\alpha_2}(q_2))t} N^{\gamma}_{\alpha_3\alpha_4}(\boldsymbol{k}|q_3, q_4|t) a^{\dagger}_{\alpha_1}(q_1) a_{\alpha_2}(q_2)\hat{A}_{\boldsymbol{\alpha}}(\boldsymbol{q}, 0) \\
&+ U\sum_{k_j>0}\sum_{\gamma_j=\pm} e^{i(\tilde{\epsilon}_{\alpha_3}(q_3)-\tilde{\epsilon}_{\alpha_4}(q_4))t} N^{\gamma}_{\alpha_1\alpha_2}(\boldsymbol{k}|q_1, q_2|t)\hat{A}_{\boldsymbol{\alpha}}(\boldsymbol{q}, 0) a^{\dagger}_{\alpha_3}(q_3) a_{\alpha_4}(q_4) \\
&+ \mathcal{O}(U^2), \qquad (4.34)
\end{aligned}$$

where $\tilde{E}_{\boldsymbol{\alpha}}(\boldsymbol{q})$ and $N^{\gamma}_{\alpha\beta}(\boldsymbol{k}|p, q|t)$ are defined in Eq. (4.31). Reversing the CUT, taking the expectation value of Eq. (4.34) on the initial state using Wick's theorem and substituting in to Eq. (4.33) yields the real-space four-point function. We will present data for the density-density correlation function in a subsequent section, cf Fig. 4.9.

4.5 Prethermalized regime

The CUT and tDMRG results presented in the previous section establish that the Green's function $G(j,l,t)$ after the quench $(\delta_i,0)\to(\delta_f,U)$ decays in a power-law fashion with exponent $-3/2$ to a stationary value

$$G(j,\ell,t)\longrightarrow g(j,\ell)+\mathcal{O}(t^{-3/2})\ ,\quad Jt\lesssim\tau_0,$$

in a similar manner to free fermions (4.12) for the dimerisation quench $(\delta_i,0)\to(\delta_f,0)$

$$G_0(j,\ell,t)\longrightarrow g_1(j,\ell)+\mathcal{O}(t^{-3/2})\ ,\quad Jt\lesssim\tau_0,$$

where τ_0 is some intermediate time scale. We have the following relation between the asymptotic values of the Green's function in the two cases

$$g(j,\ell)-g_1(j,\ell)=\mathcal{O}(U). \tag{4.35}$$

which follows from the excellent agreement between the tDMRG and the CUT approach, which by construction is perturbative in nature. We will now show that $g(j,\ell)$ *cannot* be described by a thermal ensemble and hence the stationary regime observed in the tDMRG is a prethermalization plateau:

1. For the non-interacting quench $(\delta_i,0)\to(\delta_f,0)$ the observed stationary value is characterised by a GGE

$$g_1(j,\ell)=\mathrm{tr}[\varrho_{\mathrm{GGE}}c_j^\dagger c_\ell]. \tag{4.36}$$

2. We showed in Sec. 4.3.1.2 that the GGE value for $g_1(j,\ell)$ is different from the thermal value at the appropriate inverse temperature β_0 for the quench

$$\mathrm{tr}[\varrho_{\mathrm{GGE}}c_j^\dagger c_\ell]-\mathrm{tr}[\varrho_{\mathrm{GE}}(\beta_0)c_j^\dagger c_\ell]=\mathcal{O}(1). \tag{4.37}$$

3. For the interacting quench $(\delta_i,0)\to(\delta_f,U)$, if the stationary state is described by the thermal ensemble then the inverse temperature β_U is set by

$$\lim_{L\to\infty}\frac{1}{L}\langle\Psi_0|H(\delta_f,U)|\Psi_0\rangle=\lim_{L\to\infty}\frac{1}{L}\mathrm{tr}\left[\varrho_{\mathrm{GE}}(\beta_U)\ H(\delta_f,U)\right].$$

Given that Wick's theorem holds in the initial state $|\Psi_0\rangle$ we find

$$\langle\Psi_0|H(\delta_f,U)|\Psi_0\rangle=\langle\Psi_0|H(\delta_f,0)|\Psi_0\rangle+\mathcal{O}(U),$$

and hence the inverse temperature $\beta_U=\beta_0+\mathcal{O}(U)$.

4. Combining $\beta_U = \beta_0 + \mathcal{O}(U)$ with (4.37) we conclude that

$$\mathrm{tr}[\varrho_{\mathrm{GGE}} c_j^\dagger c_\ell] - \mathrm{tr}[\varrho_{\mathrm{GE}}(\beta_U)\ c_j^\dagger c_\ell] = \mathcal{O}(1). \tag{4.38}$$

5. Finally, it follows from (4.35), (4.36) and (4.38) that

$$g(j,\ell) - \mathrm{tr}[\varrho_{\mathrm{G}}(\beta_U)\ c_j^\dagger c_\ell] = \mathcal{O}(1), \tag{4.39}$$

and hence $g(j,\ell)$ is not described by a thermal distribution.

4.5.1 Characterisation of the prethermalized regime through approximate conservation laws

The results of the previous section and the excellent agreement between the CUT and tDMRG results establishes the existence of a "prethermalized stationary regime". The observed relaxation on intermediate time scales is to a non-thermal quasi-stationary state – an obvious question is then how to characterise the statistical ensemble that describes the corresponding stationary values of local observables on the prethermalization plateau?

4.5.1.1 Approximate conservation laws

In this section we establish explicit expressions for the approximately conserved charges under the CUT time evolution. This is a simple exercise, as in the CUT analysis of the non-equilibrium dynamics we took the generator of the time-evolution to be

$$H' = \sum_{\alpha=\pm} \sum_{k>0} \tilde{\epsilon}_\alpha(k) a_\alpha^\dagger(k) a_\alpha(k).$$

Clearly the mode occupation number operators $a_\alpha^\dagger(k)a_\alpha(k)$ commute with H', and hence constitute conservation laws (to first order in U) within our CUT approach. Their pre-images under the CUT, accurate to order $\mathcal{O}(U)$, are simply

$$\mathcal{Q}_\alpha(k) = a_\alpha^\dagger(k)a_\alpha(k) - U \sum_{q_j>0} N^\gamma_{\alpha\alpha}(\boldsymbol{q}|k,k,B=\infty)\hat{A}_\gamma(\boldsymbol{q})\ . \tag{4.40}$$

By construction these operators commute with one another to $\mathcal{O}(U^2)$, but they *do not* in fact commute with the full $B = 0$ Hamiltonian to the same order

$$[\mathcal{Q}_\alpha(k), \mathcal{Q}_\beta(p)] = \mathcal{O}(U^2), \qquad [\mathcal{Q}_\alpha(k), H(\delta_f, U)] = \mathcal{O}(U),$$

which means that the charges (4.40) are not (approximately) conserved on the operator level, but their expectation values with respect to $|\Psi_0(t)\rangle$ *are* approximately time independent. This is a fundamental difference to the proposal put forward in Ref. [195] for describing prethermalization plateaux, where it was suggested that charges can be constructed perturbatively which commute with one another *and* the Hamiltonian to a given order in perturbation theory[†].

The charges $\mathcal{Q}_\alpha(k)$ have a very transparent physical meaning: they are the number operators for approximately conserved "quasiparticles", and the quartic terms describe the leading contribution to the dressing of the non-interacting fermions.

4.5.1.2 Approximate description by a "deformed GGE"

With knowledge of the conserved charges (4.40), it is natural to attempt a description of the prethermalization plateau in terms of a generalised Gibbs ensemble (which we called the deformed GGE, being made up of the "deformed" charges (4.40))

$$\varrho_{\mathrm{PT}} = \frac{1}{Z_{\mathrm{PT}}} \exp\left(\sum_{k,\alpha} \lambda_k^{(\alpha)} \mathcal{Q}_\alpha(k)\right). \tag{4.41}$$

As with the conventional GGE (4.2), the Lagrange multipliers $\lambda_k^{(\alpha)}$ are fixed by reproducing the expectation values on the initial state

$$\mathrm{tr}\left[\varrho_{\mathrm{PT}}\ \mathcal{Q}_\alpha(k)\right] = \langle\Psi_0|\mathcal{Q}_\alpha(k)|\Psi_0\rangle. \tag{4.42}$$

The left-hand side of (4.42) can easily be evaluated in the $B=\infty$ basis:

$$\frac{1}{Z_{\mathrm{PT}}}\mathrm{tr}\left[e^{\sum_{k,\alpha}\lambda_k^{(\alpha)}a_\alpha^\dagger(k)a_\alpha(k)}a_\alpha^\dagger(k)a_\alpha(k)\right] = \frac{1}{1+e^{-\lambda_k^{(\alpha)}}}. \tag{4.43}$$

Wick's theorem holds on the initial state, so the right-hand side of (4.42) is equal to

$$n_{\alpha\alpha}(k) - U\sum_{q_j>0} N^{\gamma}_{\alpha\alpha}(\boldsymbol{q}|k,B=\infty)\Big\{n_{\gamma_1\gamma_2}(q_1)n_{\gamma_3\gamma_4}(q_3)\delta_{q_1,q_2}\delta_{q_3,q_4} + n_{\gamma_1\gamma_4}(q_1)\left[\delta_{\gamma_2,\gamma_3} - n_{\gamma_3\gamma_2}(q_2)\right]\delta_{q_1,q_4}\delta_{q_2,q_3}\Big\}. \tag{4.44}$$

Equating (4.44) with (4.43) and using the expressions for the expectation values of number operators (4.27), we obtain the Lagrange multipliers $\lambda_k^{(\alpha)}$. The plateau value

[†] We do not believe that this construction is generically possible.

for the Green's function is found using the density matrix (4.41)

$$G_{\mathrm{PT}}(j,\ell) = \mathrm{tr}\left[\varrho_{\mathrm{PT}} c_j^\dagger c_\ell\right] = \frac{1}{L}\sum_{q>0}\sum_{\alpha=\pm}\gamma_\alpha^*(j,q|\delta_f)\gamma_\alpha(\ell,q|\delta_f)\mathrm{tr}\left[\varrho_{\mathrm{PT}} a_\alpha^\dagger(q)a_\alpha(q)\right]. \quad (4.45)$$

We now wish to show that this result is equal to the infinite time limit of the CUT result (up to order U^2 corrections)

$$G_{\mathrm{PT}}(j,\ell) = \lim_{t\to\infty} G(j,\ell;t) + \mathcal{O}(U^2). \quad (4.46)$$

The trace in (4.45) is most easily evaluated in the $B=\infty$ basis where the charges becomes mode occupation numbers $a_\alpha^\dagger(k)a_\alpha(k)$:

$$\begin{aligned}
\mathrm{tr}\left[\varrho_{\mathrm{PT}} a_\alpha^\dagger(q)a_\alpha(q)\right] &= \frac{1}{Z_{\mathrm{PT}}}\mathrm{tr}\left[e^{\sum_{k,\alpha}\lambda_k^{(\alpha)}a_\alpha^\dagger(k)a_\alpha(k)}\hat{n}_{\alpha,\alpha}(q,q|B=\infty)\right] \\
&= n_{\alpha\alpha}(q) - U\sum_{k_{1,2}>0} N^\gamma_{\alpha\alpha}(k_1,k_1,k_2,k_2|q,q,B=\infty) \\
&\quad \times n_{\gamma_1\gamma_2}(k_1)n_{\gamma_3\gamma_4}(k_2)[1-\delta_{\gamma_1,\gamma_2}\delta_{\gamma_3,\gamma_4}] \\
&\quad - U\sum_{k_{1,2}>0} N^\gamma_{\alpha\alpha}(k_1,k_2,k_2,k_1|q,q,B=\infty)n_{\gamma_1\gamma_4}(k_1) \\
&\quad \times\big(\delta_{\gamma_2,\gamma_3} - n_{\gamma_3\gamma_2}(k_2)\big)[1-\delta_{\gamma_1,\gamma_4}\delta_{\gamma_2,\gamma_3}]\,. \quad (4.47)
\end{aligned}$$

Substituting this expression (4.47) into Eq. (4.45), we obtain an expression that indeed agrees with the infinite time limit of (4.32) in the thermodynamic limit, establishing (4.46). In other words, the Green's function $G(j,\ell)$ on the prethermalization plateau is described by the GGE (4.41) with deformed charges (4.40) in the thermodynamic limit. This is consistent with a more general picture of *local* observables on the prethermalization plateau being described by a deformed GGE. It is obvious that there are *non-local* operators, such as $n_{+-}(k)$, which do not in fact relax at intermediate times and therefore cannot be described by any ensemble (without time-averaging).

4.5.1.3 "Deformed GGE" description of the four-point function

In the preceding section, we have shown that the value of the Green's function on the prethermalization is given by the deformed GGE ϱ_{PT}. We will now show that the deformed GGE also reproduces the $t\to\infty$ expectation values of the CUT result for

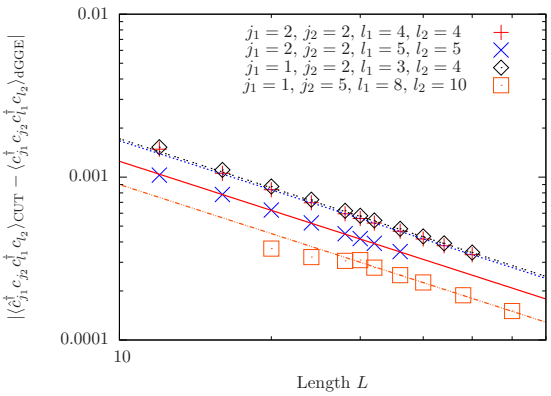

Figure 4.8: The L dependence of the difference between the deformed GGE and the $t \to \infty$ CUT result for the four point function for a number of separations. The solid lines are linear fits cL^{-1} to the data.

the four-point function (4.33). We need to calculate

$$\mathrm{tr}\Big[\varrho_{PT} c^\dagger_j c_{j'} c^\dagger_l c_{l'}\Big] = \frac{1}{L^2}\sum_{q_j>0}\sum_{\alpha_j=\pm} \gamma^*_{\alpha_1}(j,q_1)\gamma_{\alpha_2}(j',q_2)\gamma^*_{\alpha_3}(l,q_3)\gamma_{\alpha_4}(l',q_4)\mathrm{tr}\Big[\varrho_{PT}\hat{A}_{\boldsymbol{\alpha}}(\boldsymbol{q})\Big], \tag{4.48}$$

where ϱ_{PT} is given in Eq. (4.41). Once again, the trace is most easily evaluated in the $B = \infty$ basis

$$\begin{aligned}
\mathrm{tr}\Big[\varrho_{PT}\hat{A}_{\boldsymbol{\alpha}}(\boldsymbol{q})\Big] &= \frac{1}{Z_{PT}}\mathrm{tr}\Big[e^{\sum_{k,\alpha}\lambda^{(\alpha)}_k a^\dagger_\alpha(k)a_\alpha(k)}\hat{A}_{\boldsymbol{\alpha}}(\boldsymbol{q},B=\infty)\Big] \\
&= \frac{1}{Z_{PT}}\mathrm{tr}\Big[e^{\sum_{k,\alpha}\lambda^{(\alpha)}_k a^\dagger_\alpha(k)a_\alpha(k)}\hat{A}_{\boldsymbol{\alpha}}(\boldsymbol{q})\Big] \\
&+ \frac{U}{Z_{PT}}\sum_{k_j>0} N^{\gamma}_{\alpha_3\alpha_4}(\boldsymbol{k}|q_3,q_4,\infty)\mathrm{tr}\Big[e^{\sum_{k,\alpha}\lambda^{(\alpha)}_k a^\dagger_\alpha(k)a_\alpha(k)}a^\dagger_{\alpha_1}(q_1)a_{\alpha_2}(q_2)\hat{A}_{\boldsymbol{\gamma}}(\boldsymbol{k})\Big] \\
&+ \frac{U}{Z_{PT}}\sum_{k_j>0} N^{\gamma}_{\alpha_1\alpha_2}(\boldsymbol{k}|q_1,q_2,\infty)\mathrm{tr}\Big[e^{\sum_{k,\alpha}\lambda^{(\alpha)}_k a^\dagger_\alpha(k)a_\alpha(k)}\hat{A}_{\boldsymbol{\gamma}}(\boldsymbol{k})a^\dagger_{\alpha_3}(q_3)a_{\alpha_4}(q_4)\Big] \\
&+ \mathcal{O}(U^2),
\end{aligned}$$

where $\hat{A}_{\boldsymbol{\gamma}}(\boldsymbol{k}) = a^\dagger_{\gamma_1}(q_1)a_{\gamma_2}(q_2)a^\dagger_{\gamma_3}(q_3)a_{\gamma_4}(q_4)$. The GGE expectation values are easily calculated using Wick's theorem and (4.42). Retaining only terms up to $\mathcal{O}(U)$ and substituting the result back into (4.48), we obtain the deformed GGE value for the four-point function on the prethermalization plateau.

In Fig. 4.8 we plot the difference between the deformed GGE result obtained in this way and the stationary value of the CUT result (found by projecting on to the stationary terms of Eq. (4.33)) for a number of system sizes and separations. In all cases the difference between the CUT and deformed GGE results scales as $\frac{1}{L}$ and vanishes in the thermodynamic limit $L \to \infty$. This confirms that the $t \to \infty$ stationary value of the CUT four-point function is reproduced by the deformed

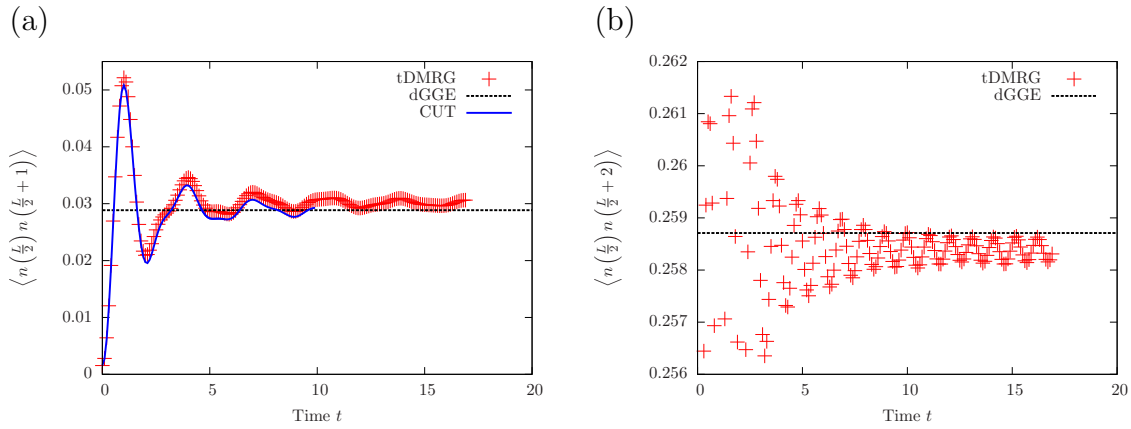

Figure 4.9: (a) Nearest-neighbour density-density correlation function $\langle n(\frac{L}{2})n(\frac{L}{2}+1)\rangle$; (b) next-nearest-neighbour density-density correlation function $\langle n(\frac{L}{2})n(\frac{L}{2}+2)\rangle$ for a quench from $\delta_i = 0.8 \to \delta_f = 0.4$ and $U = 0 \to 0.4$ computed by tDMRG for system size $L = 100$. For comparison we show CUT results for $L = 40$ and the asymptotic value predicted by the $L = 50$ deformed GGE.

GGE (4.41). This is a rather non-trivial check of our proposal that prethermalization plateaux can be described in terms of a deformed GGE.

We now present comparisons between tDMRG results and the deformed GGE predictions (4.48) for the nearest-neighbour and next-nearest-neighbour density-density correlation functions in Figs. 4.9(a)–(b). We consider the quench $\delta_i = 0.8 \to \delta_f = 0.4$ and $U = 0 \to 0.4$. Taking into account that $U = 0.4$ is not particularly small, we see quite satisfactory agreement between the two results. This supports our assertion that the deformed GGE provides a good description of local observables on the prethermalization plateau, including higher-order correlation functions. We see similarly good agreement for all separations that we explicitly checked (up to 4 sites). The deformed GGE and CUT results of Fig. 4.9(a) are calculated for $L = 40, 50$ rather than $L = 100$ due to the computational cost of carrying out the momentum sums in (4.33) increasing very rapidly with size.

4.6 tDMRG results for larger values of U and absence of thermalisation on accessible times scales

In this section we turn to numerical results obtained for quenches to final Hamiltonians with both weak and strong interactions, i.e., when $U \gtrsim |\delta_i - \delta_f|$. We will see that in

all cases the time evolution seems to reach a plateau and remains – on the accessible time scales – on this plateau. This is observed for quenches from both interacting and non-interacting initial states.

4.6.1 Extent of prethermalization plateaux

One of the first issues that we want to address is the time scale for which we observe the prethermalization plateaux. Estimating the time scale on which the CUT results may be trusted is hard as it requires proper treatment of the neglected interaction terms in the time evolution (4.26). In the previous section we found that the CUT and tDMRG results agree for the length $L = 50$ systems for times less than the revival time τ_r. Figure 4.10 shows that the prethermalization plateaux persists at much longer times in large systems and for accessible time scales there is no evidence that the system starts to deviate from the prethermalization plateau.

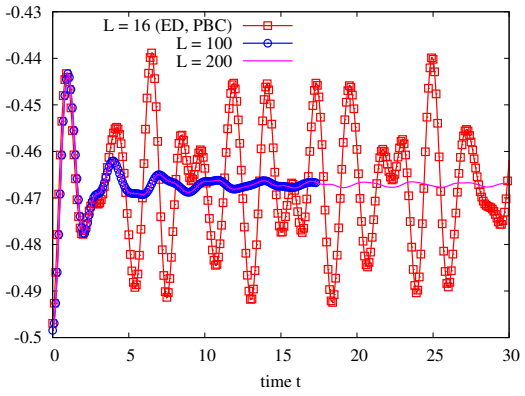

Figure 4.10: Time evolution of $\mathcal{G}(L/2, L/2+1)$ for quenches with $\delta_i = 0.8 \to \delta_f = 0.4$ and $U_i = 0 \to U = 0.4$ and system sizes $L = 16$, $L = 100$ and $L = 200$ sites. The data for $L = 16$ are ED results for systems with periodic boundary conditions (PBC) and are seen to exhibit many revivals.

4.6.1.1 Time averaged observables

One standard method for extracting stationary values of observables from data for a finite system is to *time-average* quantities

$$\overline{G\left(\frac{L}{2}, \frac{L}{2}+1\right)} = \frac{1}{T}\int_0^T dt\, G\left(\frac{L}{2}, \frac{L}{2}+1, t\right). \tag{4.49}$$

The time-averaged results of the $L = 16$ exact diagonalisation (ED) data of Fig. 4.10 is in good agreement with the plateau values for $L = 100, 200$ obtained from tDMRG. One can ask whether time-averaging reveals signs of the system deviating from the prethermalization plateau: for this reason we examined a $L = 50$ systems up to very late times of $t = 200$ with tDMRG. The result of this examination are shown in

Fig. 4.11. Time-averaging does not reveal any signs of deviations from the plateau value at late times.

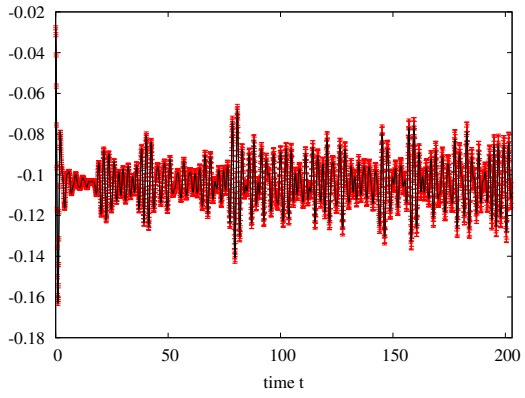

Figure 4.11: Time evolution of $\mathcal{G}(L/2, L/2+1)$ for the quench $\delta_i = 0.8 \to \delta_f = 0.4$ and $U_i = 0 \to U = 0.4$ in the $L = 50$ site system up to $t \sim 200$, with error bars estimated in Appendix B of Ref. [2].

4.6.2 The role of interactions in the $t > 0$ Hamiltonians

In this section we present results for a variety of interaction strengths $0.4 \leq U \leq 10$ in the post-quench Hamiltonian. We provide two benchmarks for comparison:

4.6.2.1 (i) The Gibbs ensemble

One useful comparison is with the appropriate Gibbs ensemble describing a putative thermal ensemble at late times. The inverse temperature β is fixed by the requirement

$$\langle \Psi_0 | H(\delta_f, U) | \Psi_0 \rangle = \mathrm{tr}[\varrho_{GE}(\beta) H(\delta_f, U)] \ . \tag{4.50}$$

We fix the inverse temperature β by calculating the left-hand side:

$$\begin{aligned} \langle \Psi_0 | H(\delta_f, U) | \Psi_0 \rangle \ = \ & \sum_{\alpha=\pm} \sum_{k>0} n_{\alpha\alpha}(k) + U \sum_{\boldsymbol{\alpha}} \sum_{k_1,k_3} V_{\boldsymbol{\alpha}}(k_1,k_1,k_3,k_4) n_{\alpha_1\alpha_2}(k_1) n_{\alpha_3\alpha_4}(k_3) \\ & + U \sum_{\boldsymbol{\alpha}} \sum_{k_1,k_3} V_{\boldsymbol{\alpha}}(k_1,k_3,k_3,k_1) n_{\alpha_1\alpha_4}(k_1) \Big[\delta_{\alpha_2\alpha_3} - n_{\alpha_3\alpha_2}(k_3) \Big], \end{aligned}$$

whilst the right-hand side is determined using a quantum Monte Carlo (QMC) algorithm from the ALPS collaboration [210], which is based on the directed loop stochastic series expansion [211]. In particular, we map the model onto a spin model using the Jordan-Wigner transformation and perform the calculation in the grand canonical ensemble where the temperature and chemical potential are fixed by ensuring the correct energy and number densities (within the QMC error). We do this

using a root finding algorithm in combination with the ALPS QMC code: the parameters are provided in Table 4.1. In our QMC simulations, we used a chain of $L = 100$ sites and we perform 5×10^7 thermalisation steps followed by 1.5×10^8 sweeps before measuring the nearest-neighbour Green's function.

U	E/L	β	μ	$\mathcal{G}(L/2, L/2+1)$	QMC Error
0.4	-0.664373	3.0741	0.4	-0.46358	1.62×10^{-3}
1	-0.589142	2.6494	1	-0.46247	2.98×10^{-4}
2	-0.463757	2.0437	2	-0.44347	6.94×10^{-5}
3	-0.338371	1.5882	3	-0.40153	6.49×10^{-5}
4	-0.212986	1.2175	4	-0.34284	3.06×10^{-4}
6	0.037784	0.7250	6	-0.23885	1.34×10^{-4}
8	0.288550	0.4868	8	-0.17441	3.15×10^{-4}
10	0.539324	0.3591	10	-0.13514	1.23×10^{-4}

Table 4.1: Summary of the effective temperature β and chemical potential μ used in the QMC to calculate the Green's function $\mathcal{G}(\frac{L}{2}, \frac{L}{2}+1)$ on the $L = 100$ chain as presented in Figs. 4.13-4.14. The energy density E/L is found by taking the expectation value of the interacting Hamiltonian $H(t > 0)$ on the initial state $|\Psi_0\rangle$.

4.6.2.2 (ii) The diagonal ensemble

The diagonal ensemble serves as the second useful benchmark. For the initial state $|\Psi_0\rangle$ we can expand in the basis of energy eigenstates $\{|n\rangle\}$, the diagonal ensemble average of an observable $\mathcal{O}$ is defined by

$$\langle \mathcal{O} \rangle_{\mathrm{DE}} = \sum_n \langle n|\mathcal{O}|n\rangle \ |\langle n|\Psi_0\rangle|^2. \tag{4.51}$$

The diagonal ensemble average is equal to the long-time average (Eq. (4.49) with $T \to \infty$) in finite systems. Due to the sum over energy eigenstates, computation of the diagonal ensemble is restricted to small systems and we compute it by exact diagonalisation for $L = 16$ sites.

4.6.2.3 Difference between diagonal and Gibbs averages

We examine how the difference between diagonal and Gibbs ensembles results for the nearest-neighbour Green's function $\mathcal{G}(L/2, L/2+1)$ changes with U_f in Figure 4.12. As the diagonal ensemble is available only for system size $L = 16$, we display the

quantities

$$\langle c^\dagger_{L/2} c_{L/2+1} \rangle_{\text{DE,L=16}} - \langle c^\dagger_{L/2} c_{L/2+1} \rangle_{\text{Gibbs,L=16}} \ ,$$
$$\langle c^\dagger_{L/2} c_{L/2+1} \rangle_{\text{DE,L=16}} - \langle c^\dagger_{L/2} c_{L/2+1} \rangle_{\text{Gibbs,L=100}} . \tag{4.52}$$

We see that for small values U_f the two averages are close to one another, but for large U_f they become very different.

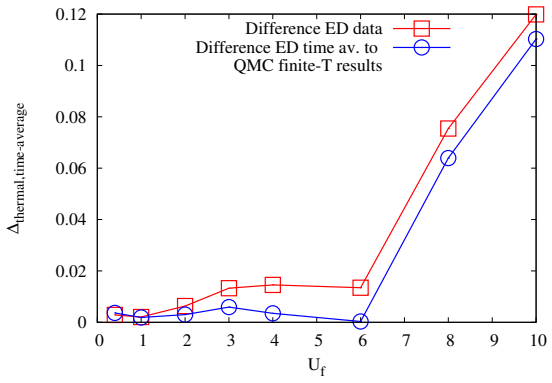

Figure 4.12: The differences between (i) thermal ED and time-averaged ED; (ii) thermal QMC and time-averaged ED for the nearest neighbour Green's function $\mathcal{G}(L/2, L/2+1)$ for the quench $\delta_i = 0.8 \to \delta_f = 0.4$ and $U_i = 0 \to U = 0.4$. QMC data is for $L = 100$ and ED data is for $L = 16$. Finite size effects are less pronounced for small values of U_f, but prominent for $U_f > 1$. The intermediate region $1 \leq U_f < 8$ is the best candidate to obtain thermalisation on long time scales.

4.6.2.4 Results

We present the results of numerical calculations in Figures. 4.13(a)–(d) and 4.14(a)–(d). We see clear evidence for the Green's function from tDMRG approaching plateaux values at small (Fig. 4.13(a)) and large (Figs. 4.14(c)–(d)) values of the interaction parameter U, which are compatible with the diagonal ensemble (given that this was calculated at $L = 16$) but *not* the Gibbs ensemble. This is clear evidence for prethermalization on accessible time scales in both the weak and strong coupling regimes.

On the other hand, at intermediate couplings $U \approx 2$ the plateau values are compatible with the thermal ensemble for accessible time scales. We have the following explanation for these observations:

1. The weakly interacting small U regime is described by a prethermalization plateau, as discussed in Sec. 4.5. The plateau can be understood in terms of a deformation of the generalised Gibbs ensemble characterising the stationary state of the $U = 0$ quench.

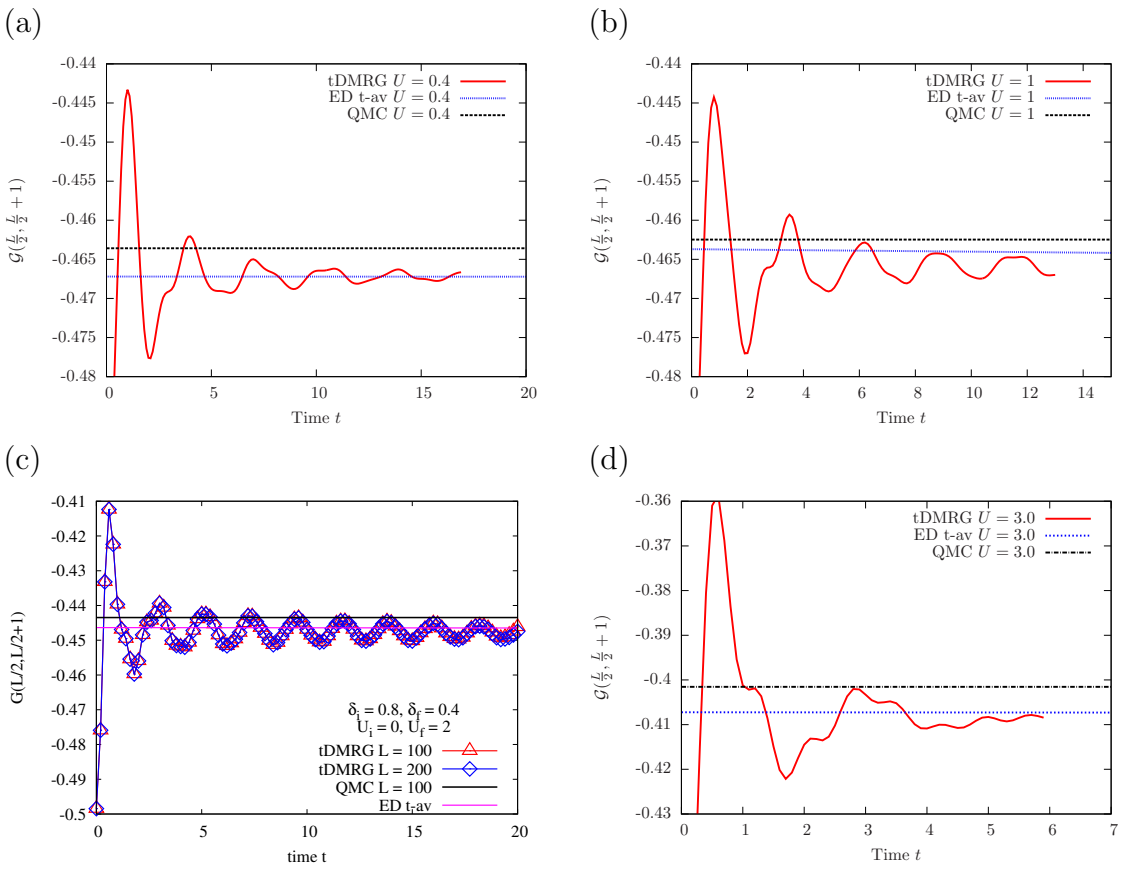

Figure 4.13: Comparison of the diagonal ensemble [time-averaged (t-av) ED], the Gibbs ensemble (QMC), and the full-time evolution obtained by tDMRG for times t after the quench $\delta_i = 0.8 \to \delta_f = 0.4$ $U = 0 \to$ (a) $U = 0.4$; (b) $U = 1$; (c) $U = 2$; (d) $U = 3$. tDMRG and QMC results are for the $L = 100$ chain, ED for $L = 16$.

2. The large-U regime is also described by a prethermalization plateau, which reflects the vicinity of the $\delta_f = 0$ integrable point. Here the final Hamiltonian can be viewed as a perturbation of the XXZ chain in the massive regime and one expects a deformed GGE description to apply. Given that the initial state has short correlation length, expectation values of the local observables could be calculated by the method of Ref. [184].

   To test the idea of stationary values being described by a perturbation of the $\delta_f = 0$ model, we present a comparison of the $\delta_f = 0.4$ and $\delta_f = 0$ results for the quench to $U = 10$ in Fig. 4.15. We see that the correlation functions approach a value that is only very weakly dependent upon the integrability breaking parameter δ_f, supporting this interpretation.

3. In the intermediate U regime there is no prethermalization plateau and the

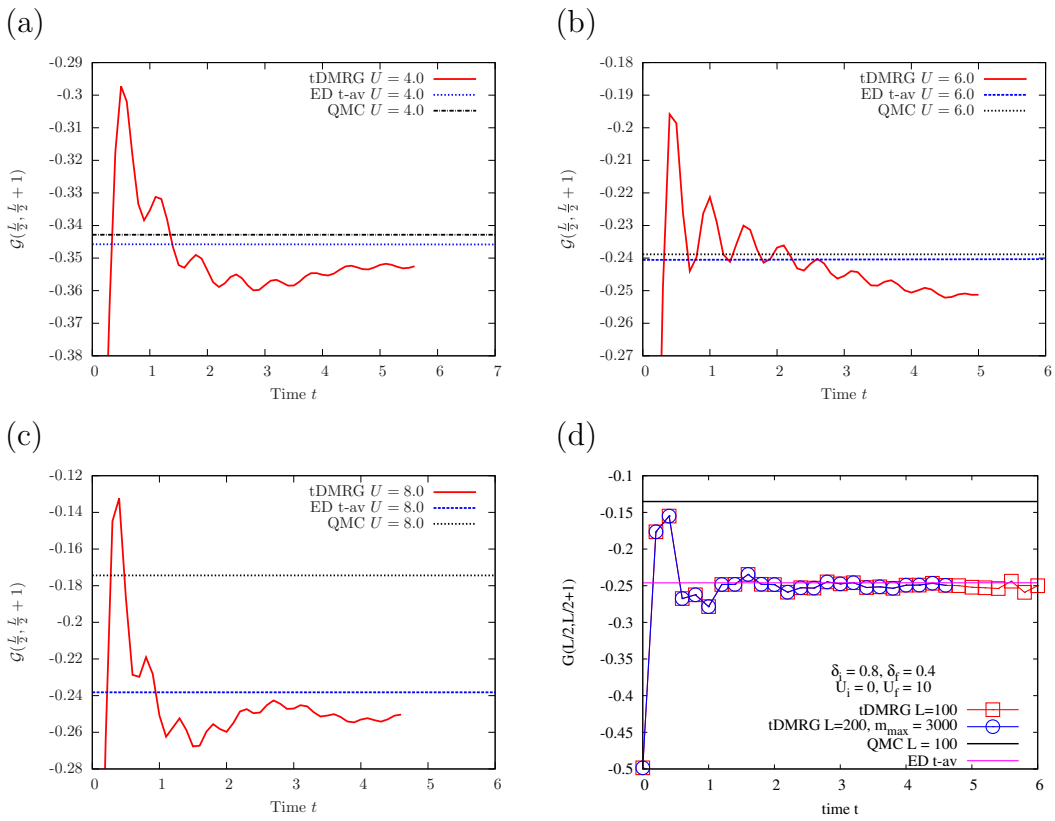

Figure 4.14: Comparison of the diagonal ensemble [time-averaged (t-av) ED], the Gibbs ensemble (QMC), and the full-time evolution obtained by tDMRG for times t after the quench $\delta_i = 0.8 \to \delta_f = 0.4$ $U = 0 \to$ (a) $U = 4$; (b) $U = 6$; (c) $U = 8$; (d) $U = 10$. tDMRG and QMC results are for the $L = 100$ chain, ED for $L = 16$.

system slowly relaxes towards a Gibbs ensemble (i.e., see Figs. 4.13(b)–(c)).

4.7 Discussion and conclusions

In this chapter, we have used a combination of analytical calculations based upon the continuous unitary transform technique and numerical tDMRG computations to establish the existence of a robust prethermalization plateau at intermediate times after a quantum quench in the weakly non-integrable Peierls insulator (4.4). The way in which we have analysed the plateau has enabled us to essentially eliminate finite-size effects and hence our results represent true "bulk" physics, avoiding revival effects. To the best of our knowledge, our work constitutes the first example of robust prethermalization plateau in a non-integrable one-dimensional fermionic model with short range interactions.

As well as establishing the existence of the prethermalization plateau, the analyt-

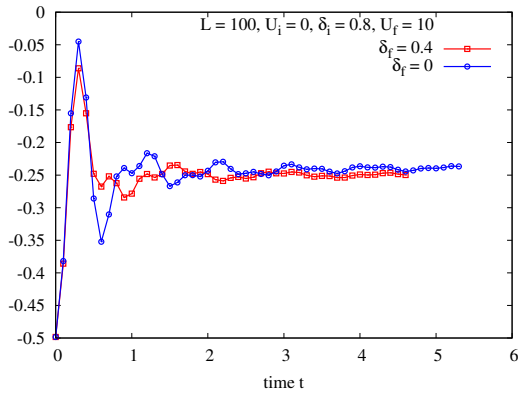

Figure 4.15: Comparison of tDMRG results for the time evolution of $\mathcal{G}(L/2, L/2+1)$ for systems with $L = 100$ sites for quenches with initial $U_i = 0$, $\delta_i = 0.8$ to values of $U_f = 10$ and $\delta_f = 0.4$ or $\delta_f = 0$, respectively. As can be seen, the expectation value for both cases is very similar.

ical approach which we use allows us to explicitly construct the statistical ensemble describing stationary values on the plateau: the so-called "deformed generalised Gibbs ensemble". The deformed GGE is constructed from the charges $\mathcal{Q}_\alpha(k)$ in Eq. (4.40), that form a mutually commuting set, but interestingly they *do not commute with the Hamiltonian.* For this reason, the charges are not conserved at an operator level, but their expectation values $\langle \mathcal{Q}_\alpha(k) \rangle$ on the time-evolved state $|\Psi_0(t)\rangle$ are (approximately) stationary. Our construction is therefore quite different to that of Ref. [195]. We conjecture the deformed GGE idea applies more widely to quantum models in one-dimension with weak integrability breaking and it would be interesting to test this conjecture on other systems.

Moving beyond the regime of weak integrability breaking, we studied our model in the limit of intermediate and strong interactions $0.4 \lesssim U \lesssim 10$ using exact diagonalisation, tDMRG and quantum Monte Carlo. At intermediate U, where integrability breaking is strongest, we observe behaviour that is compatible with thermalisation. For large U we approach another integrable limit of the model and a prethermalization plateau is once again observed on intermediate time scales. On the time scale accessible to us with tDMRG we see no evidence for a crossover from prethermalization to thermalisation.

Both the analytical CUT method and tDMRG computations are not able to access long time scales on which we do expect the system to eventually thermalise. One approach to describing the dynamics at very late times would be through a quantum Boltzmann equation (see e.g. Refs. [212]), which is currently under investigation.

Appendix

4.A Local conservation laws for H_0

To derive the local conservation laws for the non-interacting Hamiltonian $H(\delta, 0)$ we follow Appendix C of Ref. [173]. Below we give the local conservation laws and summarise the salient points of the derivation.

The Hamiltonian can be written in the form $H_0 = \sum_{i,j=0}^{2L-1} a_i \mathcal{H}_{ij} a_j$ where a_i are Majorana fermions $\{a_i, a_j\} = 2\delta_{i,j}$ defined by $a_{2n} = c_n^\dagger + c_n$, $a_{2n+1} = i(c_n^\dagger - c_n)$ and $\mathcal{H}$ is a skew-symmetric block-circulant matrix of the form

$$\mathcal{H} = \begin{bmatrix} \mathcal{Y}_0 & \mathcal{Y}_1 & \dots & \mathcal{Y}_{\tilde{L}-1} \\ \mathcal{Y}_{\tilde{L}-1} & \mathcal{Y}_0 & & \vdots \\ \vdots & & \ddots & \vdots \\ \mathcal{Y}_1 & \dots & \dots & \mathcal{Y}_0 \end{bmatrix},$$

where $\mathcal{Y}_n$ are 4×4 matrices with $\mathcal{Y}_n = -\mathcal{Y}_{\tilde{L}-n}^T$ and $\tilde{L} = L/2$. We define the Fourier transform of the block matrices as

$$\Big(\mathcal{Y}_n\Big)_{jj'} = \frac{1}{\tilde{L}} \sum_{k=1}^{\tilde{L}} e^{\frac{2\pi i k}{\tilde{L}} n} \Big(Y_k\Big)_{jj'}$$

with $(Y_k)_{jn} = -(Y_{-k})_{nj}$.

For free fermions a complete set of local conservation laws can be given by fermion bilinears $I^{(r)} = \frac{1}{2} \sum_{l,n} a_l \mathcal{I}_{ln}^{(r)} a_n$ where the matrices $\mathcal{I}^{(r)}$ must satisfy

$$\Big[\mathcal{H}, \mathcal{I}^{(r)}\Big] = 0 \quad \text{and} \quad \Big[\mathcal{I}^{(r)}, \mathcal{I}^{(r')}\Big] = 0. \tag{4.53}$$

The problem of deriving local conservation laws has now become the problem of finding a set of mutually commuting matrices that also commutes with the Hamiltonian matrix $\mathcal{H}$. At first sight the complexity of the problem does not seem to have been reduced, but we can now utilise a useful property of the Hamiltonian matrix $\mathcal{H}$: the projectors onto eigenvectors of block circulant matrices are themselves block

circulant matrices. This means one can consider $\mathcal{I}^{(r)}$ that are block circulant:

$$\mathcal{I}^{(r)} = \begin{bmatrix} \bar{\mathcal{Y}}_0^{(r)} & \bar{\mathcal{Y}}_1^{(r)} & \dots & \bar{\mathcal{Y}}_{\tilde{L}-1}^{(r)} \\ \bar{\mathcal{Y}}_{\tilde{L}-1}^{(r)} & \bar{\mathcal{Y}}_0^{(r)} & & \vdots \\ \vdots & & \ddots & \vdots \\ \bar{\mathcal{Y}}_1^{(r)} & \dots & \dots & \bar{\mathcal{Y}}_0^{(r)} \end{bmatrix} .$$

Imposing Eqs. (4.53), we obtain the conditions $\left[Y_k, \bar{Y}_k^{(r)}\right] = 0$ and $\left[\bar{Y}_k^{(r)}, \bar{Y}_k^{(r')}\right] = 0$, where $\bar{Y}_k^{(r)}$ is the Fourier transform of $\bar{\mathcal{Y}}^{(r)}$.

The construction of $\bar{Y}_k^{(r)}$ is straightforward as $Y_k = A_k \otimes \sigma^y$, where we've defined

$$A_k = \left[J(1+\delta) + J(1-\delta)\cos\left(\frac{2\pi k}{\tilde{L}}\right)\right]\sigma^x - J(1-\delta)\sin\left(\frac{2\pi k}{\tilde{L}}\right)\sigma^y \ .$$

So $\bar{Y}_k^{(r)}$ takes the form

$$\bar{Y}_k^{(r)} = \bar{q}_k^{(r)} A_k \otimes \sigma^y + q_k^{(r)} A_k \otimes \mathbb{1}_2 + \bar{\omega}_k^{(r)} \mathbb{1}_2 \otimes \sigma^y + \omega_k^{(r)} \mathbb{1}_2 \otimes \mathbb{1}_2, \tag{4.54}$$

where the functions $\omega_k^{(r)}$, $\bar{\omega}_k^{(r)}$, $q_k^{(r)}$ and $\bar{q}_k^{(r)}$ are chosen such that the Fourier transform satisfies $(\bar{Y}_k)_{jn} = -(\bar{Y}_{-k})_{jn}$.

The ambiguity in choice of functions leads to different representations of the conservation laws; following Ref. [173] we make a particular choice that ensures there is a finite real-space range r_0 of the conservation laws: $\mathcal{I}_{ln}^{(r)} = 0$ for $|l-n| > r_0$. We consider the conservation laws associated with each of the terms in $\bar{Y}_k^{(r)}$ separately and Fourier transforming back to real space we find

$$\begin{aligned} I_1^{(r)} = &-\sum_{n=0}^{\tilde{L}-1} \frac{J}{2}(1+\delta)\left[c_{2n}^\dagger c_{2n-2r+3} + c_{2n}^\dagger c_{2n+2r-1} + c_{2n+1}^\dagger c_{2n-2r+2} + c_{2n+1}^\dagger c_{2n+2r-2} + \text{H.c}\right] \\ &-\sum_{n=0}^{\tilde{L}-1} \frac{J}{2}(1-\delta)\left[c_{2n}^\dagger c_{2n-2r+1} + c_{2n}^\dagger c_{2n+2r-3} + c_{2n+1}^\dagger c_{2n-2r+4} + c_{2n+1}^\dagger c_{2n+2r} + \text{H.c.}\right], \end{aligned}$$

$$\begin{aligned} I_2^{(r)} = &-\sum_{n=0}^{\tilde{L}-1} \frac{J}{2}(1+\delta)\left[i\left(c_{2n}^\dagger c_{2n-2r+1} - c_{2n}^\dagger c_{2n+2r+1} + c_{2n+1}^\dagger c_{2n-2r} - c_{2n+1}^\dagger c_{2n+2r}\right) + \text{H.c.}\right] \\ &-\sum_{n=0}^{\tilde{L}-1} \frac{J}{2}(1-\delta)\left[i\left(c_{2n}^\dagger c_{2n-2r-1} - c_{2n}^\dagger c_{2n+2r+1} + c_{2n+1}^\dagger c_{2n-2r+2} - c_{2n+1}^\dagger c_{2n+2r+2}\right) + \text{H.c.}\right], \end{aligned}$$

$$\begin{aligned} I_3^{(r)} &= \sum_{n=0}^{\tilde{L}-1}\left[i\left(c_{2n+2r+2}^\dagger c_{2n} + c_{2n+1}^\dagger c_{2n+2r+3}\right) + \text{H.c.}\right], \\ I_4^{(r)} &= \sum_{n=0}^{\tilde{L}-1}\left[i\left(c_{2n+2r+2}^\dagger c_{2n} - c_{2n+1}^\dagger c_{2n+2r+3}\right) + \text{H.c.}\right], \end{aligned}$$

where r is a measure of the locality of the conservation laws and takes values 1 to $\tilde{L}$.

The local conservation laws $I_3^{(r)}, I_4^{(r)}$ are independent of the microscopic parameters of the theory; they arise from the $\mathbb{1}_2 \otimes \mathbb{1}_2$ and $\mathbb{1}_2 \otimes \sigma^y$ terms in $\bar{Y}_k^{(r)}$. The remaining local conservation laws are dependent on the dimerisation parameter δ. Energy conservation is also manifest in the set of local conservation laws with $I_1^{(1)} \propto H_0$.

5. Summary and outlook

Let us finish by recounting some of the topics that we have discussed and highlighting open questions.

In Chapter 2, we were motivated by experiments on the "telephone number" compounds which observed the formation of a crystal of hole pairs, likely as a result of the long-range Coulomb interaction inducing charge ordering (see Sec. 2.1.1 for a detailed discussion). The net effect of the long-range Coulomb interaction is to induce umklapp scattering at arbitrary fillings, and we study the effect of the $4k_b$ umklapp process on the ground state properties of the fermionic doped two-leg ladder with Hubbard and nearest-neighbour density-density interactions. Using the perturbative renormalisation group, we showed that the low-energy effective field theory coincides with that of the Kondo-Heisenberg model (see Sec. 2.1.2). We obtain the ground state phase diagram (Fig. 2.3) and show that there exists a region of the strong coupling phase in which the dominant fluctuations are of superconducting type and carry a finite wave vector (e.g. they are the one-dimensional analogue of Fulde-Ferrell-Larkin-Ovchinnikov superconductivity [75]).

An important question for future studies is what is the effect of other types of umklapp scattering? In Ref. [1] we made some progress on understanding the $3k_b+k_{ab}$ umklapp process, whose dominant fluctuations are of an interesting "composite" order type which is difficult to understand, but the other types of umklapp scattering were left for future studies. Another topic which requires further work is the calculation of observables in the "chain representation", which could help in understanding the phases with composite order parameters.

It would also be interesting to explore the low-energy physics of generalisations of the Kondo-Heisenberg model. Even in the simplest case (shown in Sec. 2.1.2) with a non-interacting one-dimensional electron gas and a Heisenberg spin chain the

physics is rather rich. Study of Kondo-Heisenberg-like models where the spin chain has broken $SU(2)$ symmetry from e.g. XXZ spin exchange interactions or the addition of a magnetic field may reveal some interesting phases. Another generalisation which may be interesting to study is the case of the three-leg-ladder where the central leg is spin chain and outer legs are interacting electron gases. Could there be a phase where the predominant fluctuations are of a composite superconducting type, featuring electrons from both the outer legs of the ladder?

We remained concerned with the ground state properties of quasi-one-dimensional quantum systems in Chapter 3 where we studied the dynamical structure factor of a quantum spin model with the aim of explaining inelastic neutron scattering data on the ferromagnet $CoNb_2O_6$. We presented numerical and experimental evidence for the phenomenon of *quasi-particle breakdown* occurring in the paramagnetic phase of $CoNb_2O_6$ as a direct result of the breaking of spin inversion symmetry (due to a slightly misaligned transverse field in the experiment). This phenomena manifests itself in "anomalous broadening" of the single particle mode shown clearly in the high-resolution inelastic neutron scattering data of Figure 3.7. Our claim was supported with large system (up to 28 sites) exact diagonalisation results, Figs. 3.8(a)–(f), for a spin model with the exchange parameters fitted to experimental data.

The effect of finite temperature on the quasi-particle breakdown in $CoNb_2O_6$ is an open question which can be addressed numerically with exact diagonalisation and directly compared to appropriate experiments. We also plan to investigate the dynamical structure factor for transverse fields below the critical field, where experiments observe a complicated multi particle continuum structure [213]. It is unclear to what extent quasi-particle breakdown may play a role in the ordered phase.

Moving away from the equilibrium properties of quasi-one-dimensional quantum systems, in Chapter 4 we studied the out-of-equilibrium dynamics of the interacting Peierls insulator. For the case of weak interactions, we used a combination of perturbative analytical calculations and the numerical time-dependent density matrix renormalisation group to show that there exists a robust prethermalization plateau in this model. We provide a description of the plateau in terms of a statistical ensemble constructed from charges which form a mutually commuting set and whose ex-

pectation values are (approximately) time independent, despite not commuting with the Hamiltonian. We conjecture that this construction, which we call the "deformed generalised Gibbs ensemble", applies more generally to quenches in one-dimensional quantum models with weak integrability breaking – it is important that further work checks this conjecture. It would also be interesting to generalise the perturbative procedure that we outlined to integrable *interacting* models, where the problem of constructing the deformed charges will be much more difficult.

Perhaps the most outstanding problem in the treatment of non-integrable quantum systems out-of-equilibrium is what happens in the long time limit? In Sec. 4.5 we present an argument which shows that CUT-like perturbative approach to the problem can *never* realise the thermal ensemble. Does this mean that thermalisation is a *non-perturbative* phenomena? One approach to tackling this problem is to use "kinetic equations" or the quantum Boltzmann equation [212]. It is possible to "derive" (under a given set of assumptions) such a set of equations from the Heisenberg equations of motion and this set of equations have "feedback" loops which may result in non-perturbative corrections. However, currently there exists no proof that (and few studies examining if) these equations lead to thermalisation independent of the initial conditions. Further study of the long time limit is a must for understanding how and if closed non-integrable quantum systems thermalise.

Bibliography

[1] N. J. Robinson, F. H. L. Essler, E. Jeckelmann, and A. M. Tsvelik, Phys. Rev. B **85**, 195103 (2012).

[2] F. H. L. Essler, S. Kehrein, S. R. Manmana, and N. J. Robinson, Phys. Rev. B **89**, 165104 (2014).

[3] N. J. Robinson, F. H. L. Essler, I. Cabrera, and R. Coldea, arXiv:1407.2794 (2014).

[4] P. W. Anderson, Science **177**, 393–396 (1972).

[5] S.-I. Tomanaga, Prog. Theor. Phys. **5**, 544 (1950); J. M. Luttinger, J. Math. Phys. **4**, 1154 (1963); D. C. Mattis and E. H. Lieb, J. Math. Phys. **6**, 304 (1965).

[6] A. M. Tsvelik, *Quantum Field Theory in Condensed Matter Physics* (Cambridge University Press, Cambridge, 1995); T. Giamarchi, *Quantum Physics in One-Dimension* (Clarendon Press, Oxford, 2003).

[7] A. O. Gogolin, A. A. Nersesyan, and A. M. Tsvelik, *Bosonization and Strongly Correlated Systems* (Cambridge University Press, Cambridge, 1998)

[8] C. Kim *et al.*, Phys. Rev. Lett. **77**, 4054 (1996); A. Recati *et al.*, Phys. Rev. Lett. **90**, 020401 (2003); O. M. Auslaender *et al.*, Science **308**, 88 (2005); Y. Jompol *et al.*, Science **325**, 597 (2009).

[9] H. Bethe, Z. Physik **71**, 205 (1931).

[10] M. Gaudin, *La fonction d'onde de Bethe* (Masson, Paris, 1983); M. Takahashi, *Thermodynamics of One-Dimensional Solvable Models* (Cambridge University Press, Cambridge, 1999); B. Sutherland, *Beautiful Models* (World Scientific, Singapore, 2004).

[11] F. H. L. Essler, H. Frahm, F. Göhmann, A. Klümper, and V. E. Korepin, *The One-Dimensional Hubbard Model* (Cambridge University Press, Cambridge, 2005).

[12] V. E. Korepin, N. M. Bogoliubov, and A. G. Izergin, *Quantum Inverse Scattering Method and Correlation Functions* (Cambridge University Press, Cambridge, 1993);

[13] R. J. Baxter, *Exactly Solved Models in Statistical Mechanics* (Academic Press, London, 1992).

[14] P. di Francesco, P. Mathieu and D. Sénéchal, *Conformal Field Theory* (Springer, Berlin, 1997).

[15] G. Mussardo, *Statistical Field Theory* (Oxford University Press, Oxford, 2010).

[16] V. E. Korepin, Commun. Math. Phys. **86**, 391 (1982); Commun. Math. Phys. **94**, 93 (1984); N. A. Slavnov, Teor. Mat. Fiz. **79**, 232 (1988); **82**, 389 (1990) M. Jimbo and T. Miwa, *Algebraic Analysis of Solvable Lattice Models* (AMS, Providence, 1995); T. Kojima, V. E. Korepin and N. A. Slavnov, Commun. Math. Phys. **188**, 657 (1997) N. Kitanine, J. M. Maillet, and V. Terras, Nucl. Phys. **B554**, 647 (1999); **B567**, 554 (2000).

[17] J.-S. Caux, J. Math. Phys. **50**, 095214 (2009).

[18] S. R. White, Phys. Rev. Lett. **69**, 2863 (1992).

[19] U. Schollwöck, Rev. Mod. Phys. **77**, 259 (2005) and references therein.

[20] P. Pfeuty, Ann. Phys. (New York) **57**, 79 (1970).

[21] R. B. Stinchcombe, J. Phys. C: Solid State Phys. **6**, 2459 (1973); **6**, 2484 (1973); **6** 2507 (1973).

[22] B. K. Chakrabati, A. Dutta, and P. Sen, *Quantum Ising Phases and Transitions in Transverse Ising Models* (Springer, Berlin, 1996).

[23] S. Sachdev, *Quantum Phase Transitions* (Cambridge University Press, Cambridge, 1999).

[24] P. G. de Gennes, Solid State Commun. **1**, 132 (1963).

[25] T. D. Schultz, D. C. Mattis, and E. H. Lieb, Rev. Mod. Phys. **36**, 856 (1964).

[26] R. J. Elliott, P. Pfeuty, and C. Wood, Phys. Rev. Lett. **25**, 443 (1970).

[27] P. Pfeuty and R. J. Elliott, J. Phys. C: Solid State Phys. **4**, 2370 (1971).

[28] B. McCoy, E. Barouch and D. B. Abraham, Phys. Rev. A **4**, 2331 (1971).

[29] O. Babelon and D. Bernard, Phys. Lett. B **288**, 113 (1992).

[30] P. Calabrese, F.H.L. Essler, and M. Fagotti, Phys. Rev. Lett. **106**, 227203 (2011); J. Stat. Mech. (2012) P07016; (2012) P07022.

[31] H. G. Vaidya and C. A. Tracy, Physica A **92**, 1 (1978).

[32] J. H. Taylor and G. Mller, Physica A **130**, 1 (1985).

[33] O. Derzhko and T. Krokhmalskii, Phys. Rev. B **56**, 11659 (1997).

[34] O. Derzhko *et al.*, Phys. Rev. B **73**, 214407 (2006).

[35] C. J. Hamer *et al.*, Phys. Rev. B **74**, 060402 (2006).

[36] B. Fauseweh and G. S. Uhrig, Phys. Rev. B **87**, 184406 (2013).

[37] P. Jordan and E. Wigner, Z. Phys. **47**, 631 (1928).

[38] N. D. Mermin and H. Wagner, Phys. Rev. Lett. **17**, 1133 (1966)

[39] R. E. Peierls, *More Surprises in Theoretical Physics* (Princeton University Press, Princeton, 1991).

[40] See e.g. L. M. Milne-Thomson, Chapter 17 in *"Handbook of Mathematical Functions"*, ed. M. Abramowitz and I. A. Stegun, (Dover, New York, 1965).

[41] W. P. Su, J. R. Schrieffer, and A. J. Heeger, Phys. Rev. Lett. **42**, 1698 (1979).

[42] E. Fradkin and J. E. Hirsch, Phys. Rev. B **27**, 1680 (1983).

[43] S. Kivelson and D. E. Heim, Phys. Rev. B **26**, 4278 (1982).

[44] M. J. Cohen *et al.*, Phys. Rev. B **10**, 1298 (1974); L. B. Coleman *et al.*, Solid State Commun. **12**, 125 (1973) S. Kagoshima *et al.*, J. Phys. Soc. Jpn. **39**, 1143 (1975).

[45] P. Brüesch, S. Strässler, and H. R. Zeller, Phys. Rev. B **12**, 219 (1975); T. Sambongi, *et al.*, Solid State Commun. **22**, 729 (1977); J. Pouget *et al.*, J. Physique Lett. **44**, 113 (1983); Z. Z. Wang *et al.*, J. Physique Lett. **44** 311(1983).

[46] J. W. Bray *et al.*, Phys. Rev. Lett. **35**, 744 (1975); I. S. Jacobs *et al.*, Phys. Rev. B **14**, 3036 (1976); T. Wei *et al.*, Solid State Commun. **21**, 595 (1977); S. Huizinga *et al.*, Phys. Rev. B **19**, 4723 (1979); M. Nishi, O. Fujita, and J. Akimitsu, Phys. Rev. B **50**, 6508(R) (1994).

[47] H. W. Yeom *et al.*, Phys. Rev. Lett. **82**, 4898 (1999); J. R. Ahn *et al.*, *ibid.* **91**, 196403 (2003); J. R. Ahn *et al.*, *ibid.* **93**, 106401 (2004); J. R. Ahn *et al.*, Phys. Rev. B **69**, 233311 (2004).

[48] J. R. Ahn *et al.*, Phys. Rev. Lett. **95**, 196402 (2005).

[49] J. Hubbard, Proc. R. Soc. (London) A **276**, 238 (1963).

[50] J. Kanamori, Prog. Theor. Phys. **30**, 275 (1963).

[51] M. C. Gutzwiller, Phys. Rev. Lett. **10**, 159 (1963).

[52] J. Hubbard, Proc. R. Soc. (London) A **277**, 237 (1964); **282**, 401 (1964); **285**, 542 (1965); **296**, 82 (1967); **296**, 100 (1967).

[53] See e.g. G. Castro and M. Blume, Physics Today **34**, 89 (1981); T. M. Rice, Lecture Notes in Physics **149**, 1 (1981).

[54] E. Dagotto, Rev. Mod. Phys. **66**, 763 (1994).

[55] N. F. Mott, Rev. Mod. Phys. **40**, 677 (1968).

[56] W. Nolting and W. Borgieł, Phys. Rev. B **39**, 6962 (1989).

[57] See e.g. T. Maier *et al.*, Rev. Mod. Phys. **77**, 1027 (2005); M. Aichhorn *et al.*, Phys. Rev. B **74**, 235117 (2006); J. F. Corney and P. D. Drummond, Phys. Rev. B **73**, 125112 (2006); D. Sénéchal, arXiv:0806:2690v2, unpublished (2008); D. Eichenberge, *Superconductivity and anti ferromagnetism in the two-dimensional Hubbard model*, (PhD thesis, University of Fribourg, 2008).

[58] W. Metzner and D. Vollhardt, Phys. Rev. Lett. **62**, 324 (1989).

[59] A. Georges *et al.*, Rev. Mod. Phys. **68**, 13 (1996).

[60] E. H. Lieb and F. Y. Wu, Phys. Rev. Lett. **20**, 1445 (1968); Erratum: Phys. Rev. Lett. **21**, 192 (1968).

[61] D. Sénénchal, arXiv:cond-mat/9908262, unpublished (1999).

[62] R. E. Peierls, *Bird of Passage: Recollections of a Physicist* (Princeton University Press, Princeton, 1985).

[63] H. H. Lin, L. Balents and M. P. A. Fisher, Phys. Rev. B **58**, 1794 (1998); R. M. Konik and A. W. W. Ludwig, *ibid.* **64**, 155112 (2001).

[64] M. Tsuchiizu and A. Furusaki, Phys. Rev. B **66**, 245106 (2002).

[65] C. Wu, W. V. Liu and E. Fradkin, Phys. Rev. B **68**, 115104 (2003).

[66] L. Balents and M. P. A. Fisher, Phys. Rev. B **53**, 12133 (1996).

[67] P. Abbamonte *et al.*, Nature **431**, 1078 (2004); A. Rusydi *et al.*, Phys. Rev. Lett. **97**, 016403 (2006).

[68] S. Notbohm *et al.*, Phys. Rev. Lett. **98**, 027403 (2007); T. Yoshida *et al.*, Phys. Rev. B **80**, 052504 (2009); A. Koitzsch *et al.*, *ibid.* **81**, 113110 (2010).

[69] A. Rusydi *et al.*, Phys. Rev. B **75**, 104510 (2007); A. Rusydi *et al.*, Phys. Rev. Lett. **105**, 026402 (2010).

[70] J. Almeida, G. Roux, and D. Poilblanc, Phys. Rev. B **82**, 041102 (2010).

[71] Z. Wang *et al.*, Science **327**, 552 (2010).

[72] O. Zachar and A. M. Tsvelik, Phys. Rev. B **64**, 033103 (2001).

[73] E. Berg, E. Fradkin and S. A. Kivelson, Phys. Rev. Lett. **105**, 146403 (2010).

[74] S. R. White and I. Affleck, Phys. Rev. B **54**, 9862 (1996); S. E. Sikkema, I. Affleck and S. R. White, Phys. Rev. Lett. **79**, 929 (1997).

[75] P. Fulde and R. A. Ferrell, Phys. Rev. **135**, A550 (1964); A. I. Larkin and Y. N. Ovchinnikov, Zh. Eksp. Teor. Fiz. **47**, 1136 (1964); Sov. Phys.-JETP **20**, 762 (1965) (Engl. Transl.)

[76] A. Jaefari and E. Fradkin, Phys. Rev. B **85**, 035104 (2012); arXiv:1111.6320.

[77] M. Fabrizio, Phys. Rev. B **48**, 15838 (1993).

[78] H. J. Schulz, Phys. Rev. B **53**, R2959 (1996).

[79] H. H. Lin, L. Balents and M. P. A. Fisher, Phys. Rev. B **56**, 6569 (1997).

[80] D. V. Khveshchenko and T. M. Rice, Phys. Rev. B **50**, 252 (1994).

[81] A. M. Tsvelik, Phys. Rev. B **83**, 104405 (2011).

[82] M.-S. Chang, W. Chen and H.-H. Lin, Prog. Theor. Phys. (Supplement) **160**, 79 (2005), arXiv:cond-mat/0508660.

[83] A. V. Chubukov, D. L. Maslov and F. H. L. Essler, Phys. Rev. B **77**, 161102(R) (2008).

[84] S. R. White and I. Affleck, Phys. Rev. B **54**, 9862 (1996); A. E. Sikkema, I. Affleck, and S. R. White, Phys. Rev. Lett. **79**, 929 (1997).

[85] F. H. L. Essler and R. M. Konik, Phys. Rev. B **75**, 144403 (2007).

[86] H. J. Schulz, arXiv:cond-mat/9808167, unpublished.

[87] C. M. Varma and A. Zawadowski, Phys. Rev. B **32**, 7399 (1985).

[88] D. Controzzi and A. M. Tsvelik, Phys. Rev. B **72**, 035110 (2005).

[89] H. C. Lee, P. Azaria and E. Boulat, Phys. Rev. B **69**, 155109 (2004).

[90] R. M. Noack, S. R. White and D. J. Scalapino, Phys. Rev. Lett. **73**, 882 (1994).

[91] R. M. Noack, S. R. White and D. J. Scalapino, Physica **C270**, 281 (1996).

[92] R. M. Noack *et al.* Phys. Rev. B **56**, 7162 (1997).

[93] E. Jeckelmann, D. J. Scalapino and S. R. White, Phys. Rev. B **58**, 9492 (1998).

[94] S. R. White, I. Affleck and D. J. Scalapino, Phys. Rev. B **65**, 165122 (2002).

[95] R. M. Noack *et al.* cond-mat/9808020, unpublished.

[96] Z. Weihong *et al.* J. Phys. Cond. Matt. **13**, 433 (2001).

[97] D. Poilblanc *et al.*, Phys. Rev. B **69**, 220406 (2004).

[98] T. Nishino *et al.*, Int. J. Mod. Phys. B **13**, 1 (1999); R. M. Noack and S. R. Manmana, AIP Conf. Proc. **789**, 93 (2005); U. Schollwöck, Ann. Phys. **326**, 96 (2011).

[99] S. A. Söffing *et al.*, Phys. Rev. B **79**, 195114 (2009).

[100] P. W. Anderson, Phys. Rev. **86**, 694 (1952).

[101] R. Kubo, Phys. Rev. **87**, 568 (1952); Rev. Mod. Phys. **25**, 344 (1953).

[102] F. J. Dyson, Phys. Rev. **102**, 1217 (1956); **102**, 1230 (1956).

[103] J. Van Kranendonk and J. H. Van Vleck, Rev. Mod. Phys. **30**, 1 (1958).

[104] A. I. Akhiezer, V. G. Baryakhtar, and S. V. Peletminskii, *Spin Waves* (North-Holland, Amsterdam, 1958).

[105] D. C. Mattis, *The Theory of Magnetism* (Springer, Berlin, 1981).

[106] R. Pauthenet, J. of App. Phys. **53**, 8187 (1982).

[107] E. Manousakis, Rev. Mod. Phys. **63**, 1 (1991).

[108] M. E. Zhitomirsky and A. L. Chernyshev, Phys. Rev. Lett. **82**, 4536 (1999).

[109] M. Hagiwara *et al.*, Phys. Rev. Lett. **94**, 177202 (2005).

[110] M. Y. Veillette, A. J. A. James, and F. H. L. Essler, Phys. Rev. B **72**, 134429 (2005).

[111] T. Suzuki and S.-i. Suga, Phys. Rev. B **72**, 014434 (2005).

[112] M. B. Stone *et al.*, Nature **440**, 187 (2007).

[113] M. E. Zhitomirsky, Phys. Rev. B **73**, 100404 (2006).

[114] T. Masuda *et al.*, Phys. Rev. Lett. **96**, 047210 (2006).

[115] A. Kolezhuk and S. Sachdev, Phys. Rev. Lett. **96**, 087203 (2006).

[116] P. N. Bibikov, Phys. Rev. B **76**, 174431 (2007).

[117] O. F. Syljuåsen, Phys. Rev. B **78**, 180413 (2008).

[118] A. Lüscher and A. M. Läuchli, Phys. Rev. B **79**, 195102 (2009).

[119] A. L. Chernyshev and M. E. Zhitomirsky, Phys. Rev. B **79**, 144416 (2009).

[120] T. Masuda *et al.*, Phys. Rev. B **81**, 100402 (2010).

[121] T. Fischer, S. Duffe, and G. S. Uhrig, New J. Phys. **12**, 033048 (2010).

[122] A. V. Syromyatnikov, Phys. Rev. B **82**, 024432 (2010)

[123] V. A. Stephanovich and M. E. Zhitomirsky, Europhys. Lett. **95**, 17007 (2011).

[124] T. Fischer, S. Duffe, and G. S. Uhrig, Europhys. Lett. **96**, 47001 (2011).

[125] T. Fischer, *Description of quasiparticle decay by continuous unitary transformations* (PhD thesis, TU-Dortmund, 2011).

[126] R. L. Doretto and M. Vojta, Phys. Rev. B **85**, 104416 (2012).

[127] W. T. Fuhrman *et al.*, M. Mourigal, M. E. Zhitomirsky, and A. L. Chernyshev, Phys. Rev. B **85**, 184405 (2012).

[128] M. E. Zhitomirsky and A. L. Chernyshev, Rev. Mod. Phys. **85**, 219 (2013).

[129] J. Oh *et al.*, Phys. Rev. Lett. **111**, 257202 (2013).

[130] M. Mourigal *et al.*, Phys. Rev. B **88**, 094407 (2013).

[131] I. Cabrera *et al.*, arXiv:1402.7355 (2014).

[132] A. B. Zamolodchikov, Int. J. Mod. Phys. A **4**, 4235 (1989).

[133] R. Coldea *et al.*, Science **327**, 177 (2010).

[134] C. M. Morris *et al.*, Phys. Rev. Lett. **112**, 137403 (2014).

[135] J. A. Kjäll, F. Pollmann, and J. E. Moore, Phys. Rev. B **83**, 020407 (2011).

[136] S. T. Carr and A. M. Tsvelik, Phys. Rev. Lett. **90**, 177206 (2003).

[137] S. Lee, R. K. Kaul, and L. Balents, Nature Phys. **6**, 702 (2010).

[138] A. J. A. James, W. D. Goetze, and F.H.L. Essler, Phys. Rev. B **79**, 214408 (2009).

[139] I. Zaliznyak and J. M. Tranquada, *Neutron Scattering and Its Application to Strongly Correlated Systems* (Springer, Berlin, 2013).

[140] I. Zaliznyak and J. M. Tranquada, in *Strongly Correlated Systems: Experimental Techniques*, ed. A. Avella and F. Mancini (Springer, Berlin, 2013); arXiv:1304.4214.

[141] A. Klauser, J. Mossel, and J.-S. Caux, J. Stat. Mech. (2012) P03012.

[142] J.-S. Caux, J. Mossel, and I. P. Castillo, J. Stat. Mech. (2008) P08006.

[143] J.-S. Caux *et al.*, J. Stat. Mech. (2012) P01007.

[144] F. H. L. Essler and R. M. Konik, in *From Fields to Strings: Circumnavigating Theoretical Physics*, ed. M. Shifman, A. Vainshtein, and J. Wheater (World Scientific, Singapore, 2005); cond-mat/0412421.

[145] F. H. L. Essler and R. M. Konik, J. Stat. Mech. (2009) P09018.

[146] W. D. Goetze, U. Karahasanovic, and F. H. L. Essler, Phys. Rev. B **82**, 104417 (2010).

[147] A. Imambekov, T. L. Schmidt, and L. I. Glazman, Rev. Mod. Phys. **84**, 1253 (2012).

[148] S. Grossjohann and W. Brenig, Phys. Rev. B **79**, 094409 (2009).

[149] G. Vidal, Phys. Rev. Lett. **93**, 040502 (2004).

[150] S. R. White and A. E. Feiguin, Phys. Rev. Lett. **93**, 076401 (2004).

[151] A. J. Daley *et al.*, J. Stat. Mech. (2004) P04005.

[152] See e.g. J. K. Cullum and R. A. Willoughby, *Lanczos Algorithms for Large Symmetric Eigenvalue Computations Volume 1: Theory* (SIAM, USA, 2002).

[153] E. R. Gagliano and C. A. Balseiro, Phys. Rev. Lett. **59**, 2999 (1987).

[154] W. H. Press, S. A. Teukolsky, W. T. Vetterling, and B. P. Flannery, *Numerical Recipes in C++* (Cambridge University Press, Cambridge, 2005).

[155] B. M. McCoy and T. T. Wu, Phys. Lett. **72B**, 219 (1977).

[156] B. M. McCoy and T. T. Wu, Phys. Rev. D **18**, 1259 (1978).

[157] G. Delfino, G. Mussardo and P. Simonetti, Nucl. Phys. **B473**, 469 (1996).

[158] G. Delfino, P. Grinza, and G. Mussardo, Nucl. Phys. **B737**, 291 (2006).

[159] P. Fonseca and A. Zamolodchikov, J. Stat. Phys. **110**, 527 (2003).

[160] C. Heid *et al.*, J. Magn. Magn. Mater. **151**, 123 (1995).

[161] T. Kunimoto *e*t al., J. Phys. Soc. Japan **68**, 1703 (1999).

[162] M. Greiner *et al.*, Nature **419**, 51 (2002).

[163] T. Kinoshita, T. Wenger and D. S. Weiss, Nature **440**, 900 (2006).

[164] S. Hoerberth *et al.*, Nature **449**, 324 (2007).

[165] S. Trotzky *et al.*, Nature Physics **8**, 325 (2012).

[166] M. Cheneau *et al.*, Nature **481**, 484 (2012).

[167] M. Gring *et al.*, Science **337**, 1318 (2012).

[168] A. Polkovnikov *et al.*, Rev. Mod. Phys. **83**, 863 (2011).

[169] P. Calabrese and J. Cardy, J. Stat. Mech. (2007) P06008.

[170] J. M. Deutsch, Phys. Rev. A **43**, 2046 (1991); M. Srednicki, Phys. Rev. E **50**, 888 (1994); M. Rigol, V. Dunjko, and M. Olshanii, Nature **452**, 854 (2008); E. Canovi *et al.*, New J. Phys. **14**, 095020 (2012).

[171] T. Barthel and U. Schollwöck, Phys. Rev. Lett. **100**, 100601 (2008).

[172] M. Cramer *et al.*, Phys. Rev. Lett. **100**, 030602 (2008); M. Cramer and J. Eisert, New J. Phys. **12**, 055020 (2010).

[173] M. Fagotti and F. H. L. Essler, Phys. Rev. B **87**, 245107 (2013).

[174] A. Iucci and M. A. Cazalilla, Phys. Rev. A **80**, 063619 (2009).

[175] G. Biroli, C. Kollath, and A. M. Läuchli, Phys. Rev. Lett. **105**, 250401 (2010).

[176] D. Fioretto and G. Mussardo, New J. Phys. **12**, 055015 (2010).

[177] F. H. L. Essler, S. Evangelisti and M. Fagotti, Phys. Rev. Lett. **109**, 247206 (2012);

[178] B. Pozsgay, J. Stat. Mech. (2011) P01011.

[179] A. C. Cassidy, C. W. Clark, and M. Rigol, Phys. Rev. Lett. **106**, 140405 (2011).

[180] M. A. Cazalilla, A. Iucci, and M.-C. Chung, Phys. Rev. E **85**, 011133 (2012).

[181] J.-S. Caux and R. M. Konik, Phys. Rev. Lett. **109**, 175301 (2012).

[182] J. Mossel and J.-S. Caux, New J. Phys. **14**, 075006 (2012).

[183] J.-S. Caux and F. H. L. Essler, Phys. Rev. Lett. **110**, 257203 (2013).

[184] M. Fagotti and F. H. L. Essler, J. Stat. Mech. (2013) P07012.

[185] B. Pozsgay, J. Stat. Mech. (2013) P07003.

[186] G. Mussardo, arXiv:1304.7599 (2013); Phys. Rev. Lett. **111**, 100401 (2013).

[187] M. Collura, S. Sotiriadis and P. Calabrese, Phys. Rev. Lett. **110**, 245301 (2013); J. Stat. Mech. (2013) P09025.

[188] M. Kormos, M. Collura and P. Calabrese, Phys. Rev. A **89**, 013609 (2014).

[189] M. Kormos *et al.*, Phys. Rev. B **88**, 205131 (2013).

[190] M. Rigol *et al.*, Phys. Rev. Lett. **98**, 050405 (2007).

[191] B. Wouters *et al.*, arXiv:1405.0172 (2014); B. Poszgay *et al.*, arXiv:1405:2843 (2014); G. Goldstein and N. Andrei, arXiv:1405.4224 (2014); B. Pozsgay, arXiv:1406.4613 (2014).

[192] M. Fagotti, private communication.

[193] L. Mazza *et al.*, arXiv:1311.2615 (2013).

[194] S. R. Manmana *et al.*, Phys. Rev. Lett. **98** 210405 (2007); Phys. Rev. B **79**, 155104 (2009); C. Kollath *et al.*, Phys. Rev. Lett. **98**, 180601 (2007).

[195] M. Kollar, F. A. Wolf, and M. Eckstein, Phys. Rev. B **84**, 054304 (2011).

[196] M. Moeckel and S. Kehrein, Phys. Rev. Lett. **100**, 175702 (2008); Ann. Phys. **324**, 2146 (2009); New J. Phys. **12**, 055016 (2010).

[197] M. Rigol, Phys. Rev. Lett. **103**, 100403 (2009); M. Rigol, Phys. Rev. A **80**, 053607 (2009); L. F. Santos and M. Rigol, Phys. Rev. E **81**, 036206 (2010); **82**, 031130 (2010).

[198] M. Marcuzzi *et al.*, Phys. Rev. Lett. **111**, 197203 (2013).

[199] G. Brandino, J.-S. Caux, and R. M. Konik, arXiv:1301.0308 (2013).

[200] T. Kitagawa *et al.*, New J. Phys. **13**, 073018 (2011).

[201] T. Langen *et al.*, Eur. Phys. J. Special Topics **217**, 43 (2013).

[202] V. Y. Krivnov and A. A. Ovchinnikov, Zh. Eksp. Teor. Fiz, **90**,709 (1986); Sov. Phys. JETP **63** 414 (1986).

[203] C. Schuster and U. Eckern, Eur. Phys. J. B **5**, 395 (1998).

[204] T. Nakano and H. Fukuyama, J. Phys. Soc. Jpn. **50**, 2489 (1981).

[205] J. Sirker *et al.*, Phys. Rev. A **89**, 042104 (2014)

[206] F. Wegner, Ann. Physik (Leipzig) **3**, 77 (1994); J. Phys. A **39** 8221 (2006); S. D. Glazek and K. G. Wilson, Phys. Rev. D **48**, 5863 (1993); Phys. Rev. D **49**, 4214 (1994).

[207] S. Kehrein, *The Flow Equation Approach to Many-Particle Systems* (Springer, Berlin, 2006).

[208] S. Kehrein, Phys. Rev. Lett. **95**, 056602 (2005); A. Hackl and S. Kehrein, Phys. Rev. B **78**, 092303 (2008).

[209] U. Schollwoeck and S. R. White, in "*Effective models for low-dimensional strongly correlated systems*", ed. G. G. Batrouni and D. Poilblanc (AIP, Melville, New York, 2006); G. D. Chiara *et al.*, J. Comput. Theor. Nanosci. **5**, 1277 (2008); A. E. Feguin, AIP Conf. Proc. **1419**, 5 (2011).

[210] B. Bauer *et* al. (ALPS collaboration), J. Stat. Mech. (2011) P05001.

[211] A. W. Sandvik and J. Kurkijärvi, Phys. Rev. B **43**, 5950 (1991); A. W. Sandvik, J. Phys. A **25**, 3667 (1992).

[212] L. P. Kadanoff and G. Baym, *Quantum Statistical Mechanics* (Benjamin, New York, 1962); J. Rammer and H. Smith, Rev. Mod. Phys. **58**, 323 (1986); M. L. R. Fürst *et al.*, Phys. Rev. E **86**, 031122 (2012); M. Tavora and A. Mitra, Phys. Rev. B **88**, 115144 (2013).

[213] R. Coldea and I. Cabrera, private communication.